

---

**Version 4.0**  
**May 2018**

# **WFC3 Data Handbook**



**STScI** | SPACE TELESCOPE  
SCIENCE INSTITUTE

3700 San Martin Drive  
Baltimore, Maryland 21218  
[help@stsci.edu](mailto:help@stsci.edu)

---

## User Support

Please contact the HST Help Desk for assistance. We encourage users to access the new web portal where you can submit your questions directly to the appropriate team of experts.

- **Web portal:** <http://hsthhelp.stsci.edu>
- **E-mail:** [help@stsci.edu](mailto:help@stsci.edu)
- **Phone:** (410) 338-1082 or 1-800-544-8125

## World Wide Web

Information and other resources are available on the WFC3 World Wide Web page:

- URL: <http://www.stsci.edu/hst/wfc3>

## WFC3 Revision History

Version	Date	Editor
4.0	May 2018	Mario Gennaro, et al.
3.0	January 2016	Susana Deustua, et al.
2.1	May 2011	Abhijith Rajan, et al.
2.0	October 2010	Abhijith Rajan, et al.
1.0	January 2009	Jessica Kim Quijano, Howard Bushouse, and Susana Deustua

## Contributors

This document is written and maintained by the WFC3 Team in the Instruments Division of STScI. The WFC3 Team, at the time of this writing, consists of Jay Anderson, Sylvia Baggett, Varun Bajaj, Gabriel Brammer, Matthew Bourque, Annalisa Calamida, Susana Deustua, Linda Dressel, Jules Fowler, Mario Gennaro, Harish Khandrika, Vera Khozurina-Platais, Heather Kurtz, Knox Long, Jennifer Mack, Catherine Martlin, Peter McCullough, Myles McKay, Jennifer Medina, Michele de la Pena, Norbert Pirzkal, Ryan Russell, Kailash Sahu, Clare Shanahan, Megan Sosey, Adam Riess, Elena Sabbi, Kevin Stevenson and Ben Sunnquist.

## Citation

In publications, refer to this document as:

Gennaro, M., et al. 2018, “WFC3 Data Handbook”, Version 4.0, (Baltimore: STScI).

Send comments or corrections to:  
Space Telescope Science Institute  
3700 San Martin Drive  
Baltimore, Maryland 21218  
[help@stsci.edu](mailto:help@stsci.edu)

# Acknowledgments

## Current Members of the WFC3 Team:

- Jay Anderson
- Sylvia Baggett
- Varun Bajaj
- Matthew Bourque
- Gabriel Brammer
- Annalisa Calamida
- Susana Deustua
- Linda Dressel
- Jules Fowler
- Mario Gennaro
- Harish Khandrika
- Vera Kohzurina-Platais
- Heather Kurtz
- Knox Long
- Jennifer Mack
- Catherine Martlin
- Peter McCullough
- Myles McKay
- Jennifer Medina
- Michele de la Pena
- Nor Pirzkal
- Adam Riess
- Russell Ryan
- Elena Sabbi
- Kailash Sahu
- Clare Shanahan
- Kevin Stevenson
- Ben Sunnquist

## Former Members of the WFC3 Team:

- Wayne Baggett
- Howard Bond
- Tiffany Borders Davis
- Ariel Bowers
- Tom Brown
- Howard Bushouse
- Laura Cawley
- Ed Cheng
- Thomas Dahlen
- Ilana Dashevsky
- Michael Dulude
- Meredith Durbin
- Michael Fall
- Don Figer
- Mauro Giavalisco
- Shireen Gonzaga
- Catherina Gosmeyer
- Heather Gunning
- Derek Hammer
- Christopher Hanley
- George Hartig
- Bryan Hilbert
- Ron Henry
- Jason Kaliari
- Pat Knezek
- Ray Kutina
- Janice Lee
- Casey Lisse
- Chris Long
- Olivia Lupie
- John MacKenty
- Ivelina Momcheva
- Kai Noeske
- Cheryl Pavlovski
- Jessica Kim Quijano
- Abhijit Rajan
- Neill Reid
- Massimo Robberto
- Michael Robinson
- Megan Sosey
- Massimo Stiavelli
- Dave Taylor
- Alex Viana
- Alan Welty
- Thomas Wheeler
- Michael Wong

## Thanks

The editor thanks Jennifer McFalls and Susan Rose, Senior Technical Editor, for their invaluable contributions to the editing and production of this Data Handbook.



# Preface

---

## How to Use this Handbook

This handbook is designed to provide users with an introduction on how to understand, manipulate, and analyze data from the Wide Field Camera 3 (WFC3), which was installed on-board the *Hubble Space Telescope (HST)* during the 2009 Servicing Mission 4 (SM4). It is presented as an independent and self-contained document, referred to as the “WFC3 Data Handbook.”

Information about *HST* not specific to WFC3 is not discussed here. Users are referred to a companion volume, [\*Introduction to the HST Data Handbooks\*](#), for more general information about the details of acquiring data from the *HST* archive, *HST* file formats, and general purpose software for displaying and processing *HST* data.

For detailed information about the instrument’s capabilities and design, and how to plan observations, users should refer to the [\*WFC3 Instrument Handbook\*](#).



---

## Handbook Structure

The WFC3 Data Handbook is organized in 10 chapters, which discuss the following topics:

- **Chapter 1 - WFC3 Instruments** - is a brief summary of the capabilities and design of the Wide Field Camera 3.
- **Chapter 2 - WFC3 Data Structure** - describes WFC3 data products as would be obtained from the **MAST**, file name conventions, and auxiliary files. The structure of WFC3 images is explained, and an extensive list of all the header keywords found in typical WFC3 data files is included.
- **Chapter 3 - WFC3 Data Calibration** - explains the flow of calibration steps performed on WFC3 data with the STScI software **calwf3**. It provides detailed information on what each step does with the data, and how the data header keywords are used and modified as the data are processed. It also describes when the data should be manually recalibrated and how to do it.
- **Chapter 4 - WFC3 Images: Distortion Correction and AstroDrizzle** - provides the current knowledge about WFC3 detector distortion. A brief description of what the task **AstroDrizzle** will do for WFC3 data is also presented.
- **Chapter 5 - WFC3-UVIS Sources of Error** - provides users with all the currently known error sources in the data for the UVIS detectors. Possible methods of mitigating the error sources are also discussed.
- **Chapter 6 - Charge Transfer Efficiency (CTE) in WFC3/UVIS** - describes various aspects of CTE losses and provides users with methods for mitigating CTE effects.
- **Chapter 7 - WFC3/IR Sources of Error** - provides users with all the currently known error sources in the data for the IR detector. Possible methods of mitigating the error sources are also discussed.
- **Chapter 8 - Persistence in WFC3/IR** - describes the effects of persistence on IR images, and strategies for correcting for persistence effects
- **Chapter 9 - WFC3 Data Analysis** - includes discussions for better analyzing WFC3 data. The discussions are primarily focused on photometry, astrometry and grism spectrophotometry.
- **Chapter 10 - WFC3 Spatial Scan Data** - provides some pointers on how to reduce and analyze spatial scanned images.
- For the latest information regarding WFC3 performance and calibration, users are advised to consult the WFC3 webpages located at:

<http://www.stsci.edu/hst/wfc3>

---

## Typographic Conventions

To help you understand the material in this Data Handbook, we will use a few consistent typographic conventions.

### Visual Cues

The following typographic cues are used:

- **bold** words identify **PYTHON** task or package name.
- `typewriter-like` words identify a file name, system command, or response that is typed or displayed.
- *italic* type indicates a new term, an important point, a mathematical variable, or a task parameter.
- SMALL CAPS identifies a header keyword.
- ALL CAPS identifies a table column.

### Comments

Occasional side comments point out three types of information, each identified by an icon in the left margin.




---

***Warning:*** *You could corrupt data, produce incorrect results, or create some other kind of severe problem.*

---




---

***Heads Up:*** *Here is something that is often done incorrectly or that is not obvious.*

---




---

***Tip:*** *No problems...just another way to do something or a suggestion that might make your life easier.*

---




---

***Information especially likely to be updated on the [WFC3 website](#) is indicated by this symbol.***

---

## List of Acronyms

Acronym	
A-to-D	Analog to Digital conversion
ACQ	Acquisition
ACS	Advanced Camera for Surveys
ADC	Analog-to-Digital converter
APT	Astronomer's ProposalTool
CASTLE	HST optical simulator
CSM	Channel select Mechanism
CT	Crosstalk
CTE	Charge Transfer Efficiency
CVZ	Continuous Viewing Zone
DN	Data Number
DQ	Data quality
DS9	SAOimage astronomical image visualization application
ESA	European Space Agency
ETC	Exposure Time Calculator
FGS	Fine Guidance Sensor
FITS	Flexible Image Transport System
FOV	Field of View
FSM	Filter Select Mechanism in WFC3 IR channel
HOPR	Hubble Operations Problem Report
IDC	Image distortion correction
IR	Infrared channel on WFC3
IRAF	Image Reduction and Analysis Facility
ISR	Instrument Science Report

<b>Acronym</b>	
MAST	Mikulski Archive for Space Telescopes
MULTIACCUM	Accumulation mode (multiple non-destructive reads)
NICMOS	Near Infrared Camera and Multi-Object Spectrometer
OPUS	Operational Pipeline Unified System
OS	Optical Stimulus
OTA	Optical Telescope Assembly
PAM	Pixel Area Map
POM	Pick-off Mirror
PSF	Point Spread Function
QE	Quantum efficiency
SAA	South Atlantic Anomaly
SED	Spectral Energy Distribution
SIC&DH	Science Instrument Command and Data Handling unit
SIP	Simple Image Polynomial
SMOV	Servicing Mission / Orbital Verification
SOFA	Selectable Optical Filter Assembly in WFC3 UVIS channel
ST-ECF	Space Telescope - European Coordinating Facility
STScI	Space Telescope Science Institute
STSDAS	Space Telescope Science Data Analysis Software
TIR	Technical Instrument Report
TV3	Thermal Vacuum campaign 3

---

Acronym	
UVIS	Ultraviolet-Visible channel on WFC3
WCS	World Coordinate System
WF/PC-1	Wide-field Planetary Camera 1, on-board HST Apr 1990 to Nov 1993
WFPC2	Wide-Field Planetary Camera 2, on-board HST Dec 1993 to May 2009

---

# WFC3 Instruments

**In this chapter . . .**

1.1 Instrument Overview / 1
1.2 The UVIS Channel / 3
1.3 The IR Channel / 5

## 1.1 Instrument Overview

Wide Field Camera 3 (WFC3) is a fourth-generation imaging instrument installed in 2009. It replaced the extraordinarily successful Wide Field Planetary Camera 2 (WFPC2), thereby ensuring and enhancing the imaging capability of HST in the remaining years of its observing lifetime. WFC3 is the only HST instrument developed as a facility instrument by the HST Project. WFC3 provides HST with high-sensitivity, high-resolution, wide-field survey capability covering a broad wavelength range, from the near-UV at 200 nm to the near-IR at 1700 nm. WFC3 comprises two channels, each optimized for a specific goal:

- Ultraviolet-Visible channel (UVIS):  $162 \times 162''$  field of view from 200-1000 nm with a plate scale of  $0.040''/\text{pixel}$  and a focal ratio of  $f/31$ .
- Infrared channel (IR):  $136 \times 123''$  field of view from 800-1700 nm with a plate scale of  $0.13''/\text{pixel}$  and a focal ratio of  $f/11$ .

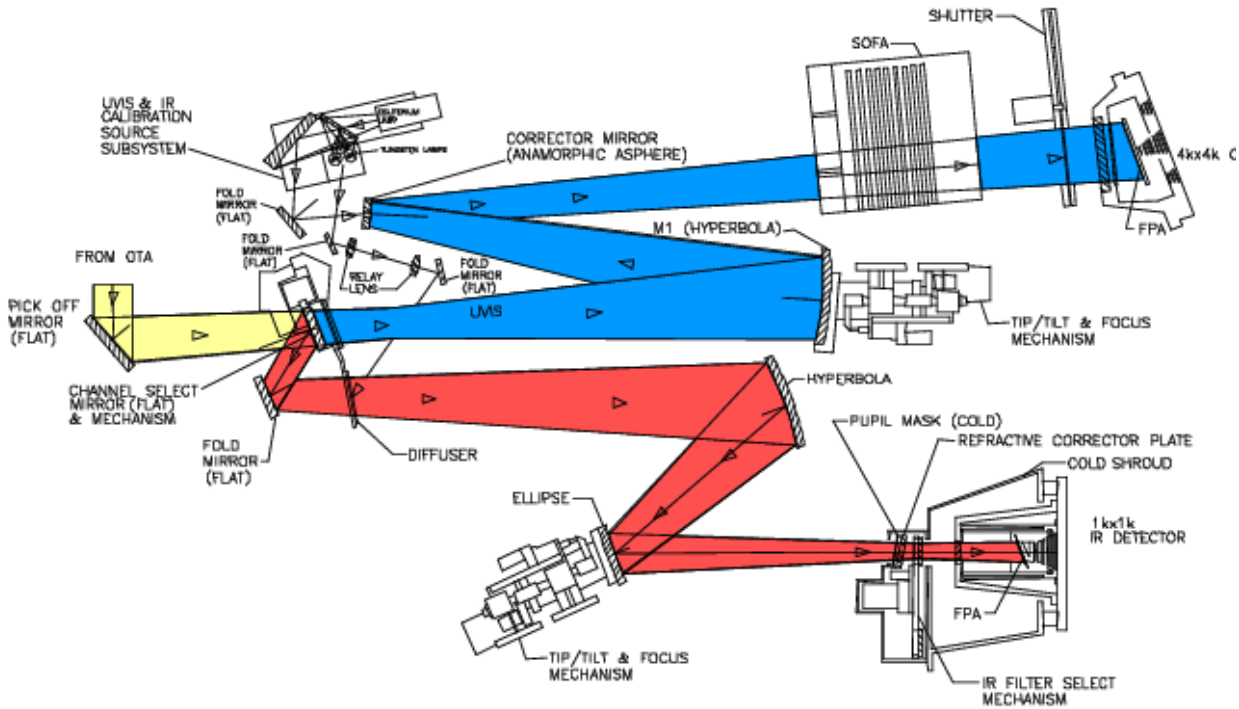
WFC3 provides the user with:

- 62 wide-, medium-, and narrow-band filters in the UVIS channel
- 15 wide-, medium-, and narrow-band filters in the IR channel
- 3 grisms: 1 in the UVIS channel and 2 in the IR channel

WFC3 occupies WFPC2's spot in HST's radial scientific-instrument bay, where it obtains on-axis direct images. Light coming from the HST Optical Telescope Assembly (OTA) is intercepted by the flat 45 degree WFC3 pick-off mirror (POM) and directed into the instrument. A channel-select mechanism (CSM) inside WFC3

then diverts the light to the IR channel via a fold mirror, or allows the light to enter the UVIS channel uninterrupted. Because of this design, only a single channel, either UVIS or IR, can be used at any one time. Figure 1.1 shows a schematic diagram of the instrument's optical and mechanical layout. The main characteristics of each channel are summarized in the following sections. For a technical description of the instrument's properties, performance, operations, and calibration, please refer to the *WFC3 Instrument Handbook*.

**Figure 1.1: Schematic optical layout of the WFC3 instrument**



For schematic simplicity, the incoming OTA beam and POM have been rotated into the plane of the optical diagram. The actual incoming OTA beam direction is into the page and then reflected by the POM into the instrument. Yellow indicates light from the OTA, which is sent into the camera by the pick-off mirror. The CSM then either allows light to pass into the UVIS channel (blue path), or directs light into the IR channel (red path). Each channel contains mechanical and optical elements which allow focusing and alignment, as well as anamorphic aspherical correctors to correct for the  $\sim 1/2$  wave spherical aberration from the HST primary mirror. Filters and grisms are contained in the UVIS selectable optical filter assembly (SOFA) and the IR filter selection mechanism (FSM). The UVIS channel has a mechanical shutter, while the IR channel is shuttered electronically by the detector, by completely resetting the whole array every  $\sim 2.9$  seconds. Light is detected by either the UVIS CCDs or the IR focal-plane array. A separate subsystem provides flat-field illumination for both channels.

## 1.2 The UVIS Channel

The UVIS channel employs a mosaic of two  $4096 \times 2051$  [Teledyne e2v](#) (formerly Marconi Applied Technologies Ltd.) CCDs, with  $\sim 0.040''/\text{pixels}$ , covering a nominal  $162 \times 162''$  field of view. These CCDs are thinned and back-illuminated devices cooled by thermo-electric cooler (TEC) stacks and housed in sealed, evacuated dewars with fused silica windows, nearly identical to the ones used for ACS. The spectral response of the UVIS CCDs is optimized for imaging from the near-UV at 200 nm to visible wavelengths at 1000 nm. The two CCDs are butted together but have a 35-pixel gap between the two chips ( $\sim 1.4''$  on the sky). Minimum UVIS exposure time is 0.5 sec. The dynamic range for a single exposure is ultimately limited by the depth of the CCD full well ( $\sim 70,000$  electrons), which determines the total amount of charge that can accumulate in any one pixel during an exposure without saturation.

The UVIS detector operates only in ACCUM mode to produce time-integrated images. Cosmic rays affect all UVIS exposures, therefore observations should be broken into multiple exposures or dither patterns whenever possible, to allow removal of cosmic rays in post-observation data processing.

WFC3 recycles hardware used in WF/PC-1 to house the complement of filters for the UVIS channel. The Selectable Optical Filter Assembly (SOFA) contains a stack of 12 wheels housing 48 physical elements covering the UV/Visible range: 42 full-frame filters, 5 quad filters ( $2 \times 2$  mosaics providing 4 different bandpasses), and 1 grism, giving a total of 63 spectral elements. Each wheel has an open slot such that when an observation is taking place, the appropriate wheel is rotated to place the desired filter in the beam, while the other wheels place the open slot in the light path.

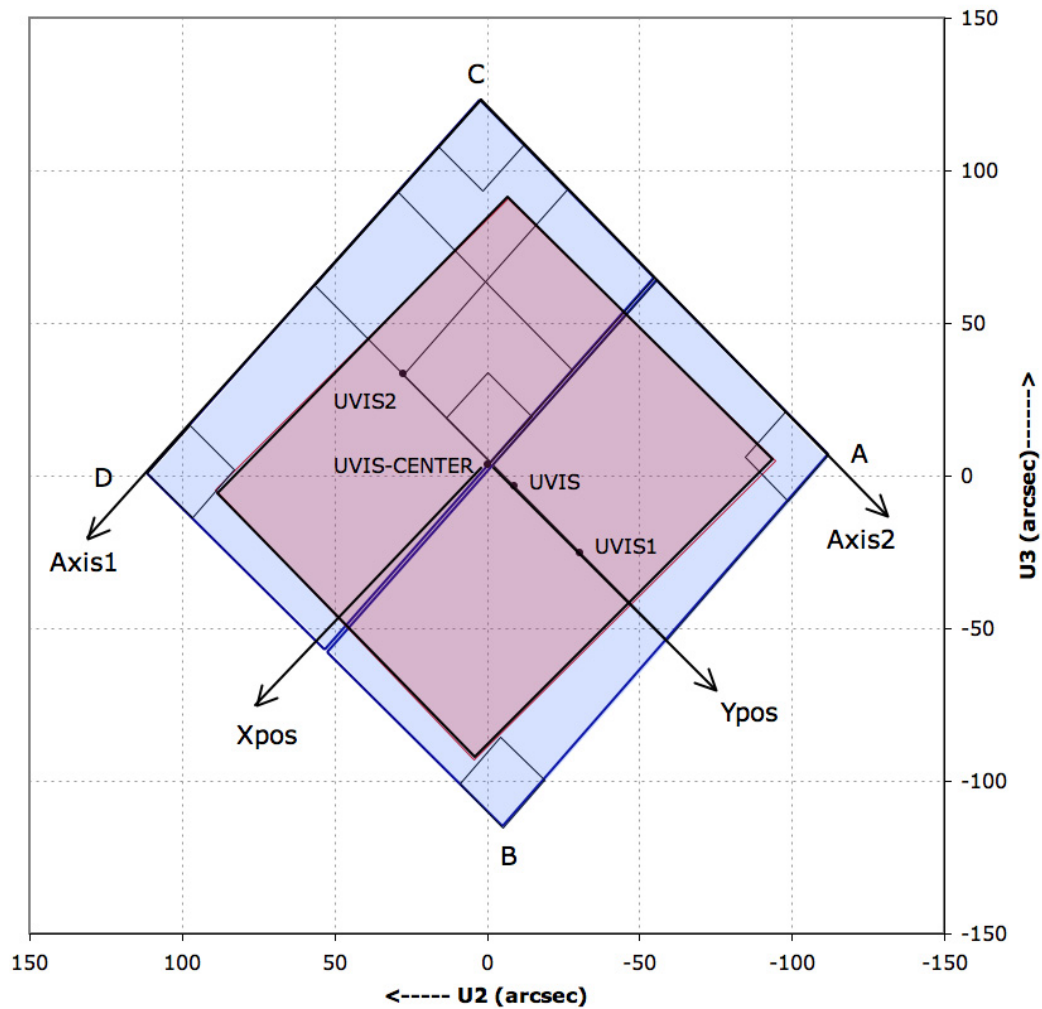
[Figure 1.2](#) shows a schematic of the UVIS channel aperture projected onto the sky with respect to the U2/U3 reference frame. (For definitions of the coordinate systems in the figure, please refer to Section 7.4.3 of the [WFC3 Instrument Handbook](#).) The WFC3 optics cause the nominally square field of view of the UVIS detector to be projected onto the sky as a skewed rhombus,  $162''$  on a side, with an angle of  $86.1$  degrees between the sides. This distortion affects both the photometric accuracy and astrometric precision of the UVIS images. For a thorough discussion of WFC3's geometric distortion, we refer the reader to [Chapter 4](#).



Figure 1.2: UVIS Aperture Diagram

Figure 1.2 illustrates the fiducial points of the full-detector apertures (UVIS, UVIS1, UVIS2, and UVIS-CENTER), and the outlines of the 2Kx2K, 1Kx1K, and 512x512 subarray apertures. Also indicated are the positions of the four readout amplifiers (A, B, C, and D). The regions imaged by the UVIS detector (represented by blue fill) and by the IR detector (represented by red fill) are also indicated. The POSition TARGET coordinate system for the UVIS-CENTER aperture, with its origin at that aperture's fiducial point, is illustrated. Although the POSition TARGET coordinate systems for the other apertures are not illustrated, they are oriented the same, but have origins at each aperture's fiducial point. ( $U2 = -V2$  and  $U3 = -V3$ ).

### WFC3/UVIS APERTURES



## 1.3 The IR Channel

The IR detector employs a  $1024 \times 1024$  Teledyne (formerly Rockwell Scientific) low noise, high quantum efficiency (QE) HgCdTe detector array with  $\sim 0.13''$ / pixels, covering a nominal  $136 \times 123''$  field of view. Only the central  $1014 \times 1014$  pixels are useful for imaging. The outer rim, of width 5 pixels, contains light-insensitive pixels that are used as reference. The HgCdTe array is actively cooled by a six-stage TEC that keeps the detector at a nominal operating temperature of 145 K. The spectral response of the IR detector is optimized for imaging at near-IR wavelengths from approximately 800 to 1700 nm.

IR detectors allow accumulated signal to be read out non-destructively multiple times, without affecting other pixels (a mode referred to as MULTIACCUM). This capability can be exploited to reduce the effective read-out noise significantly, enable recovering sources that saturate during the integration time, and enable recovering pixels affected by cosmic rays (CR), since CR hits may be recognized and removed between adjacent reads.

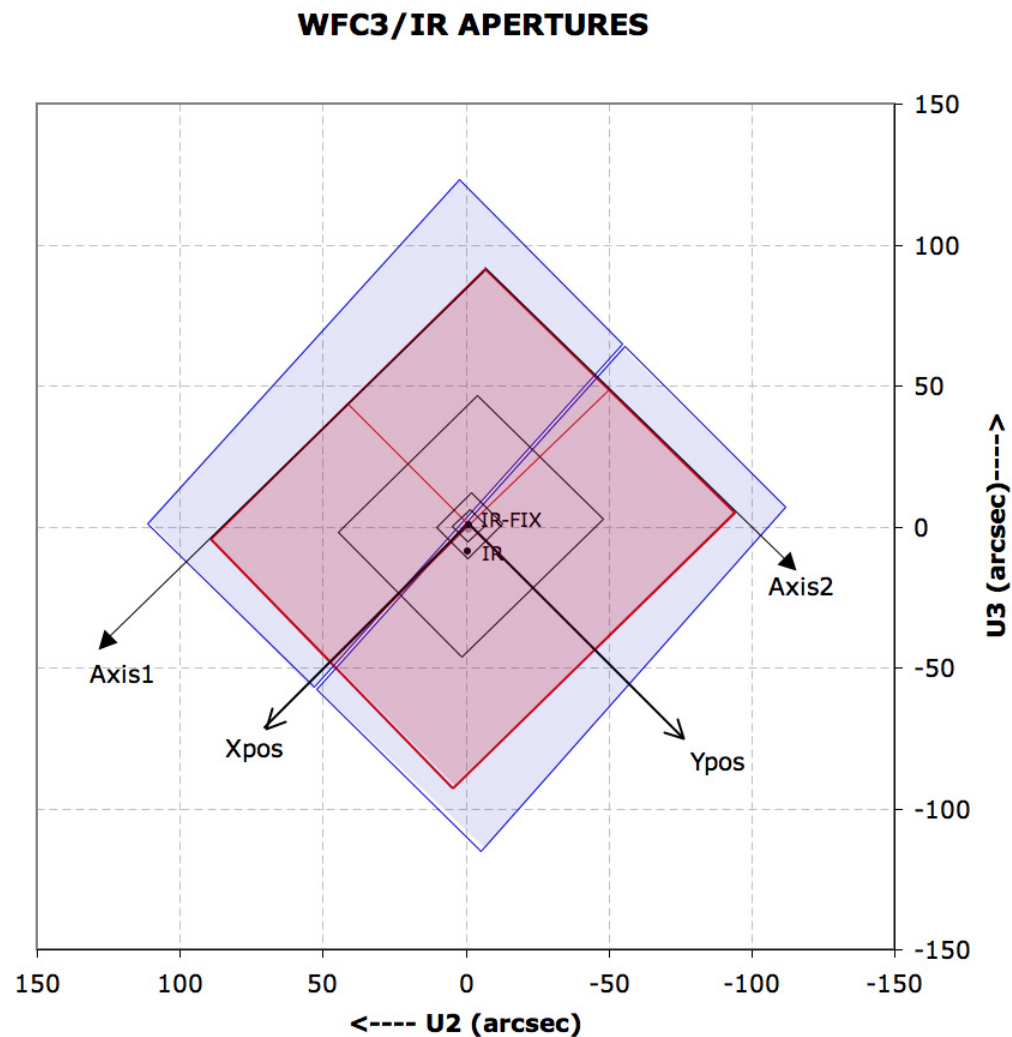
The WFC3-IR detector is immune to the charge bleeding exhibited by CCDs at high signal levels; however, saturation can still be a problem because pixels subject to the highest signal levels show higher dark current rates ("image persistence") in subsequent exposures (see [Chapter 8](#)). IR detectors do not show long-term on-orbit charge transfer efficiency (CTE) degradation, because they do not employ the charge-transfer mechanism used in CCDs. However, they are intrinsically non-linear. Nevertheless, at low and intermediate count levels, the departure from linearity is quite modest and can be well calibrated.

The IR channel has a single filter wheel housing 17 spectral elements covering the near-IR wavelengths: 15 filters and 2 grisms. An 18th slot contains an opaque blocker (called a Blank). For IR observations, the requested element is simply rotated into the light beam. The IR channel operates only in MULTIACCUM mode. The WFC3 IR channel does not have a mechanical shutter, thus when the channel is not in use, the Blank is moved into the beam to block as much light as possible from entering the detector, and the detector itself is continuously reset at the fastest possible rate for the full frame which is about 2.93 seconds.

[Figure 1.3](#) shows a schematic of the IR channel aperture projected onto the sky with respect to the U2/U3 reference frame. (For definitions of the coordinate systems in the figure, please refer to Section 6.4.3 of the *WFC3 Instrument Handbook*) The IR focal plane is tilted 22 degrees with respect to the incoming beam, thus the field of view as projected onto the sky is rectangular, with an aspect ratio of  $\sim 0.90$ . This distortion affects both the photometric accuracy and astrometric precision of the IR images. For a thorough discussion of WFC3 geometric distortion, we refer the reader to [Chapter 4](#).

Figure 1.3: IR Aperture Diagram

Figure 1.3 illustrates the fiducial points of the full-detector apertures (IR and IR-FIX), and the outlines of the concentric subarray apertures (512x512, 256x256, 128x128, and 64x64). The regions imaged by the UVIS detector (represented by blue fill) and by the IR detector (represented by red fill) are also indicated. The POSition TARGet coordinate system for the IR-FIX aperture, with its origin at that aperture's fiducial point, is illustrated. Although the POSition TARGet coordinate systems for the other apertures are not illustrated, they are oriented the same, but have origins at each aperture's fiducial point. ( $U2 = -V2$  and  $U3 = -V3$ ).



# WFC3 Data Structure

In this chapter . . .

2.1 Types of WFC3 Files / 7
2.2 WFC3 File Structure / 14
2.3 Data Storage Requirements / 22
2.4 Headers and Keywords / 22

---

## 2.1 Types of WFC3 Files

Science data taken in orbit by WFC3 are received from the Space Telescope Data Capture Facility and sent to the STScI Operational Pipeline Unified System (OPUS) pipeline, where the data are unpacked, keyword values extracted from the telemetry stream, and the science data reformatted and repackaged into raw (uncalibrated) FITS files by the Generic Conversion process (see Section 1.1.1 of the [Introduction to the HST Data Handbooks](#)). All WFC3 science data products are two-dimensional images stored in Multi-Extension FITS format files. For each exposure taken with WFC3, there is one FITS file with a unique 9-character rootname followed by a 3-character suffix: rootname\_XXX.fits. The rootname identifies the observation and the suffix denotes what type of file it is (see Chapter 5 of the [Introduction to the HST Data Handbooks](#) for more details on HST file names).

WFC3 data files are given the following definitions:

- An exposure is a single multi-extension FITS file, the atomic unit of HST data.
- A dataset is a collection of files having a common rootname.
- An association is a set of exposures that can be meaningfully combined into a single product (e.g. a set of dithered exposures, or a series of CR-SPLIT exposures)
- A sub-product is a dataset created by combining a subset of the exposures in an association.
- A product is a dataset created by combining sub-products of an association.

### 2.1.1 Data Files and Suffixes

The suffixes used for WFC3 raw and calibrated data products are described in [Table 2.1](#) and closely mimic those used by ACS and NICMOS.

**Table 2.1: WFC3 data file suffixes.**

File Suffix	Description	Units
<b>Uncalibrated</b>		
_raw	raw data	DN
<b>Distortion Corrected</b>		
_drz	UVIS and IR calibrated exposure, corrected for geometric distortion	e-/s
_drc	UVIS calibrated exposure, corrected for geometric distortion and CTE	e-/s
<b>Intermediate</b>		
_rac_tmp	UVIS CTE corrected raw data, no other calibration	DN
_blv_tmp	overscan-trimmed UVIS exposure	DN
_blc_tmp	overscan-trimmed UVIS exposure, CTE corrected exposure	DN
_crj_tmp	uncalibrated, cosmic-ray-rejected combined	DN
_crc_tmp	uncalibrated, cosmic-ray-rejected, CTE cleaned	DN
_ima	calibrated intermediate IR multiaccum image	e-/s
<b>Calibrated</b>		
_flt	UVIS calibrated exposure	e-
_flc	UVIS calibrated exposure including CTE correction	e-
_flt	IR calibrated exposure	e-/s
_flt	IR calibrated exposure (SCAN mode)	e-
_crj	UVIS calibrated, cosmic-ray-rejected image	e-
_crj	IR calibrated, cosmic-ray-rejected image	e-/s
_crc	UVIS calibrated, cr rejected, CTE cleaned image	e-
<b>Auxiliary</b>		
_asn	association file for observation set	
_spt	telescope and WFC3 telemetry and engineering data.	
_trl	trailer file contains processing messages	

The initial input files to the calibration program **calwf3** are the raw files (raw) from Generic Conversion and the association (asn) table, if applicable, for the complete observation set.

For UVIS images, temporary files are created once bias levels are subtracted and the overscan regions are trimmed. These temporary files have suffixes which also relate whether they have been corrected for Charge Transfer Efficiency (CTE) trailing. Files which have been corrected for CTE effects have a "c" as the third letter in their suffix, so it follows that "\_blv\_tmp" files have completed the BIASCORR stage but were not corrected for CTE like the "\_blc\_tmp" files. The CTE correction is the very first step in the correction process for UVIS datasets. If the save option is specified when **calwf3** is called on a "\_raw" image, then an intermediate "\_rac" file will also be saved. This contains the original data with just the CTE correction applied.

The final output files will be renamed with the "\_flt" or "\_flc" suffixes after the standard calibrations (flat fielding, dark subtraction, etc.) are complete. The "\_blv\_tmp" files serve as input for cosmic ray rejection, if required. For UVIS CR-SPLIT and REPEAT-OBS exposures, a temporary CR-combined image is created and then renamed with either the "\_crj" or "\_crc" suffix once basic calibrations of that image are complete. With the addition of the CTE correction, which is the very first step, the pipeline now follows two distinct lines of processing, one with the CTE correction applied and one without. Users running raw data through **calwf3** which has PCTECORR set to PERFORM should expect to see both sets of calibrated files when the tasks are complete.

For the IR detector, an intermediate MultiAccum (ima) file is the result after all calibrations are applied (dark subtraction, linearity correction, flat fielding, etc.) to all of the individual readouts of the IR exposure. A final step in **calwf3** processing of IR exposures produces a combined, CR-cleaned, image from the individual readouts, which is stored in an "\_flt" product file.

The final products of the **calwf3** pipeline are not corrected for geometric distortion. **AstroDrizzle** is used to correct all WFC3 images for geometric distortion, whether they are taken as single exposures or as part of an association. **Astrodrizzle** is distributed as part of the [Drizzlepac](#) package, used for aligning and combining all HST images. For CR-SPLIT and REPEAT-OBS, **AstroDrizzle** supersedes the **calwf3** cosmic-ray rejection processing and uses the individual "\_flt" or "\_flc" files directly as input, performing cosmic-ray rejection in the process of producing the final drizzled image from multiple exposures (see [Table 2.2](#)). This has significant advantages in cases where small numbers of CR-SPLIT images were obtained at a small number of different dither positions, because **AstroDrizzle** will use all the information from all the input files to produce the best cosmic-ray rejection. The resulting drizzled images should generally be useful for science, although subsequent reprocessing off-line may be desirable in some cases to optimize the data for specific scientific applications.

Table 2.2: The calwf3 and AstroDrizzle input and output products.

UVIS										
CALWF3						AstroDrizzle				
Image Type	Input	Output	CTE Corrected?	CR Rejected?	Distortion Corrected?	Input	Output	CTE Corrected?	CR Corrected?	Distortion Corrected?
Single	raw	flt	No	No	No	flt	drz	No	No	Yes
		flc	Yes	No	No	flc	drc	Yes	No	Yes
CR-SPLIT	raw, asn	crj	No	Yes	No	flt, asn	drz	No	Yes	Yes
		crc	Yes	Yes	No	flc, asn	drc	Yes	Yes	Yes
RPT-OBS	raw, asn	crj	No	Yes	No	flt, asn	drz	No	Yes	Yes
		crc	Yes	Yes	No	flc, asn	drc	Yes	Yes	Yes
Dither Pattern	raw, asn	flt	No	No	No	flt, asn	drz	No	Yes	Yes
		flc	Yes	No	No	flc, asn	drc	Yes	Yes	Yes
IR										
CALWF3						AstroDrizzle				
Image Type	Input	Output	CTE Corrected?	CR Rejected?	Distortion Corrected?	Input	Output	CTE Corrected?	CR Corrected?	Distortion Corrected?
Single	raw	ima	N/A	No	No	flt	drz	N/A	Yes	Yes
		flt	N/A	Yes	No					
RPT-OBS	raw, asn	crj	N/A	Yes	No	flt, asn	drz	N/A	Yes	Yes
Dither Pattern	raw, asn	flt	N/A	Yes	No	flt, asn	drz	N/A	Yes	Yes



*For the UVIS channel, when there are multiple exposures, AstroDrizzle supersedes the calwf3 cosmic-ray rejection processing. It uses the "flt" and "flc" files produced by calwf3 as input, and performs cosmic-ray rejection in the process of producing the final distortion-corrected drizzled image.*

*For further information on drizzle please refer to the DrizzlePac Handbook for*

*[http://documents.stsci.edu/hst/HST\\_overview/documents/DrizzlePac/DrizzlePac.cover.html](http://documents.stsci.edu/hst/HST_overview/documents/DrizzlePac/DrizzlePac.cover.html).*

## 2.1.2 Auxiliary Data Files

### Association Tables (asn)

Association tables are useful for keeping track of the complex set of relationships that can exist between exposures taken with both WFC3 channels, especially with REPEAT-OBS, CR-SPLIT, and dithered exposures. Images taken at a given dither position may be additionally CR-SPLIT into multiple exposures (e.g., UVIS observations). In these cases, associations are built to describe how each exposure relates to the desired final product. As a result, WFC3 association tables can be used to create one or more science products from the input exposures. The relationships defined in the association tables determine how far through the calibration pipeline the exposures are processed and when the calibrated exposures get combined into sub-products for further calibration.

An association file has a single extension that is a binary FITS table. That table has three columns:

- MEMNAME, the member name
- MEMTYPE, the role which that member plays in the association
- MEMPRSNT, a boolean value for whether the member is present or not.

The different MEMTYPE values are summarized in [Table 2.3](#).

**Table 2.3: Exposure types in WFC3 associations. The suffix "n" is appended to the MEMTYPE to denote multiple sets are present within a single association.**

MEMTYPE	DESCRIPTION
EXP-CRJ	Input CR-SPLIT exposure (single set)
EXP-CRn	Input CR-SPLIT exposure for CR-combined image n (multiple sets)
PROD-CRJ	CR-combined output product (single set)
PROD-CRn	CR-combined output product n (multiple sets)
EXP-RPT	Input REPEAT-OBS exposure (single set)
EXP-RPn	Input REPEAT-OBS exposure for repeated image n (multiple sets)
PROD-RPT	REPEAT-OBS combined output product (single set)
PROD-RPn	REPEAT-OBS combined output product n (multiple sets)
EXP-DTH	Input dither exposure
PROD-DTH	Dither-combined output product



A sample association table for a two-position dithered observation with CR-SPLIT=2 is presented in Table 2.4. This example shows how both MEMNAME and MEMTYPE are used to associate input and output products. The MEMTYPE for each component of the first CR-SPLIT exposure, IxxxxxECQ and IxxxxxEGQ, are given the type EXP-CR1. The sub-product Ixxxxx011 is designated in the table with a MEMTYPE of PROD-CR1. The last digit of the product filename corresponds to the output product number in the MEMTYPE. A designation of zero for the last digit in the filename is reserved for the dither-combined product.

The column MEMPRSNT indicates whether a given file already exists. For example, if cosmic ray rejection has not yet been performed by **calwf3**, the PROD-CR<sub>n</sub> files will have a MEMPRSNT value of "no". The sample association table in Table 2.4 shows the values of MEMPRSNT prior to calwf3 processing.

**Table 2.4: Sample association table ixxxxx010\_asn.**

MEMNAME	MEMTYPE	MEMPRSNT
IxxxxxECQ	EXP-CR1	Yes
IxxxxxEGQ	EXP-CR1	Yes
Ixxxxx011	PROD-CR1	No
IxxxxxEMQ	EXP-CR2	Yes
IxxxxxEOQ	EXP-CR2	Yes
Ixxxxx012	PROD-CR2	No
Ixxxxx010	PROD-DTH	No

**Table 2.5: Extensions in UVIS \_flt or \_flc files after standard processing with calwf3 and AstroDrizzle.**

Extension Number	Extension Name	Extension Description	Extension Type	Extension Dimensions	Data Format	Imset/Chip/Axis
0	Global Header					
1	[SCI,1]	Science Image	Image	4096 x 2051	Float32	Imset 1 = UVIS2 (CHIP2)
2	[ERR,1]	Error Array	Image	4096 x 2051	Float32	
3	[DQ,1]	Data Quality Array	Image	4096 x 2051	Int16	
4	[SCI,2]	Science Image	Image	4096 x 2051	Float32	Imset 2 = UVIS1 (CHIP1)
5	[ERR,2]	Error Array	Image	4096 x 2051	Float32	
6	[DQ,2]	Data Quality Array	Image	4096 x 2051	Int16	
7	[D2IMARR,1]	Filter-independent distortion correction (lithography)	Image	64 x 32	Float32	CHIP2, X axis
8	[D2IMARR,2]		Image	64 x 32	Float32	CHIP2, Y axis
9	[D2IMARR,3]		Image	64 x 32	Float32	CHIP1, X axis
10	[D2IMARR,4]		Image	64 x 32	Float32	CHIP1, Y axis
11	WCSDVARR	Filter-dependent distortion correction	Image	64 x 32	Float32	CHIP2, X axis
12	WCSDVARR		Image	64 x 32	Float32	CHIP2, Y axis
13	WCSDVARR		Image	64 x 32	Float32	CHIP1, X axis
14	WCSDVARR		Image	64 x 32	Float32	CHIP1, Y axis
15	WCSCORR	WCS change log	BINTABLE	14R x 24C		

**Note:** At the time of publishing this document, only a subset of UVIS filters have calibrated filter-dependent distortion correction, and associated NPOLFILE. These filters are F225W, F275W, F336W, F350LP, F390M, F390W, F438W, F475W, F555W, F606W, F621M, F775W, F814W, F850LP, F953N. Images produced by the calwf3 pipeline for these filters have 15 extensions, images for the remaining filters have only 11 extensions (they have no WCSDVARR). The characterization of the filter-dependent distortion correction for the remaining UVIS filters is in progress.

In order to create a geometrically correct, drizzle-combined product, PROD-DTH exposures are combined only with **Astrodrizzle**, which executes after **calwf3** has finished processing all members. PROD-RPT and PROD-CRJ products are combined using [wf3rej](#) and all output files have the “cr” extension.

### Trailer Files (trl)

Each task used by **calwf3** creates messages during processing that describe the progress of the calibration and are sent to STDOUT. In calibration pipelines written for other HST instruments, trailer files were created by simply redirecting the STDOUT to a file. Because multiple output files can be produced in a single run of **calwf3**, creating trailer files presents a unique challenge. Each task within **calwf3** must decide which trailer file should be appended with comments and automatically open, populate, and close each trailer file.

**calwf3** will always overwrite information in trailer files from previous runs of **calwf3** while preserving any comments generated by Generic Conversion. This ensures that the trailer files accurately reflect the most recent processing performed. The string "CALWF3BEG" will mark the first comment added to the trailer file. If a trailer file already exists, **calwf3** will search for this string to determine where to append processing comments. If it is not found, the string will be written at the end of the file and all comments will follow. Thus any comments from previous processing are overwritten and only the most current calibrations are recorded.

As each image is processed, an accompanying trailer file with the "\*\_trl.fits" suffix will be created. Further processing with **calwf3** will concatenate all trailer files associated with an output product into a single file. Additional messages will then be appended to this concatenated file. This duplicates some information across multiple trailer files but ensures that for any product processed within the pipeline, the trailer file will contain processing comments from all the input files.

Linking trailer files together can result in multiple occurrences of the "CALWF3BEG" string. Only the first, however, determines where **calwf3** will begin overwriting comments if an observation is reprocessed.

### Support Files (spt)

The support files contain information about the observation and engineering data from the instrument and spacecraft that was recorded at the end of the observation. A support file can have multiple FITS image extensions within the same file. Each extension holds an integer (16-bit) image containing the data that populates the \*\_spt.fits header keyword values.

---

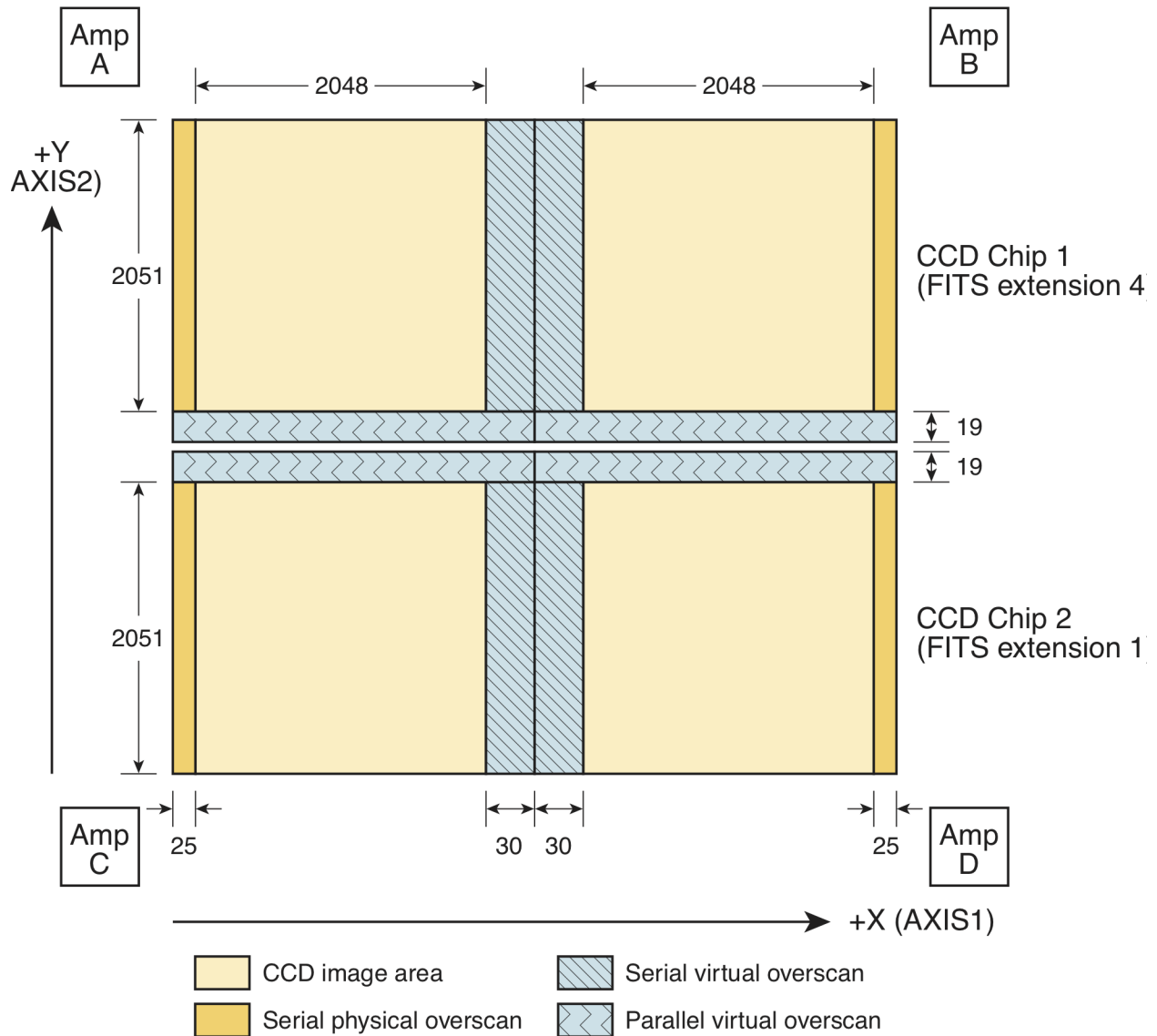
## 2.2 WFC3 File Structure

All WFC3 science data products are two-dimensional images that are stored in Multi-Extension FITS files. All images taken during an exposure are bundled in a single FITS file, with each image stored in a separate FITS image extension (see Section 2.2 of the *Introduction to the HST Data Handbooks*). The WFC3 file structure differs for UVIS and IR data, as explained in the following sections.

### 2.2.1 UVIS Channel File Structure

The WFC3 UVIS detector is similar in structure to the ACS WFC detector, with two chips butted together to form a complete detector array. As shown in [Figure 2.1](#), each chip has  $4096 \times 2051$  imaging pixels, with 19 rows and 30 columns of virtual overscan at the long and short inside edges respectively, and 25 columns of physical overscan on each side. As a result, full-frame raw images have a total of  $4206 \times 4140$  pixels, and after overscan subtraction in the calibration process, calibrated images have a total of  $4096 \times 4102$  pixels.

**Figure 2.1: Schematic of a raw, full-frame WFC3 UVIS image.**



The UVIS detector operates only in ACCUM mode to produce time-integrated images. The data read from the two chips are stored in separate image sets, or "imsets" (see Section 2.2 of the *Introduction to the HST Data Handbooks*) within a single FITS file. Each imset contains three data arrays that are stored in three separate images extensions:

- the science image (SCI)
- the error array (ERR)
- the data quality array (DQ)

When the user retrieves their data from the archive, the system delivers calibrated data which are processed by both CALWFC3 and **AstroDrizzle**. The **AstroDrizzle** step updates the header astrometric information, and adds 9 additional extensions to the final `_flt` or `_flc` files. Thus, the FITS file corresponding to a single full-frame calibrated UVIS exposure has 16 extensions, whose characteristics are summarized in [Table 2.4](#).

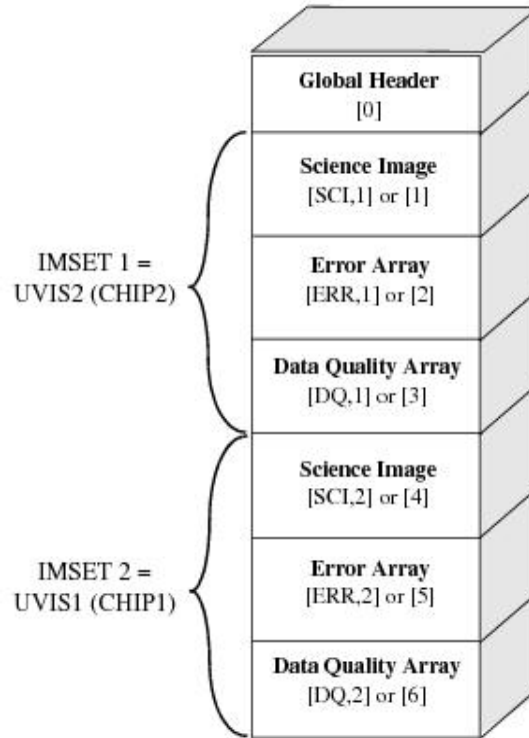
The zeroth extension is the global or primary header unit. As seen in [Figure 2.1](#) CHIP1 (UVIS1) is above CHIP2 (UVIS2) in y-pixel coordinates, but it is stored in imset 2 in the FITS file, shown graphically in [Figure 2.2](#). Thus, the chip-extension notation is counter-intuitive. To display the science image for UVIS1, the user must specify the second science extension `"file.fits[sci,2]"`. Similarly, the data quality and error arrays for UVIS1 are specified as `"[dq,2]"` and `"[err,2]"`, respectively.

The extensions from 7 to 10 are tabular data stored as imsets `[D2IMARR]` with one extension per each CCD chip's access. These imsets are filter-independent corrections for the CCD pixel-grid irregularities, an artifact of the manufacturing process imprinted on the detector itself. The lithographic-mask pattern correction is bi-linearly interpolated and used for pixel-by-pixel correction prior to correction for geometric distortion via the `IDCTAB`.

The extensions from 11 to 14 contain tabular data stored as imsets `[WCSDVARR]` with one extension per each CCD chip axis. These tabular data, which describe the fine-scale filter-dependent non-polynomial distortion corrections, are bi-linearly interpolated and used for pixel-by-pixel correction after correction for geometric distortion via the `IDCTAB`.

The 15th FITS extension called `[WCSCORR]` contains a history of WCS changes, if the data were reprocessed with a new distortion correction reference file.

**Figure 2.2: Format for the first 7 extensions of UVIS FITS files. These extensions are present in both uncalibrated and calibrated products. The final calibrated `_flc` or `_flt` files, that the user can retrieve from the archive, also have an additional 9 extensions with the astrometric information populated by AstroDrizzle.**

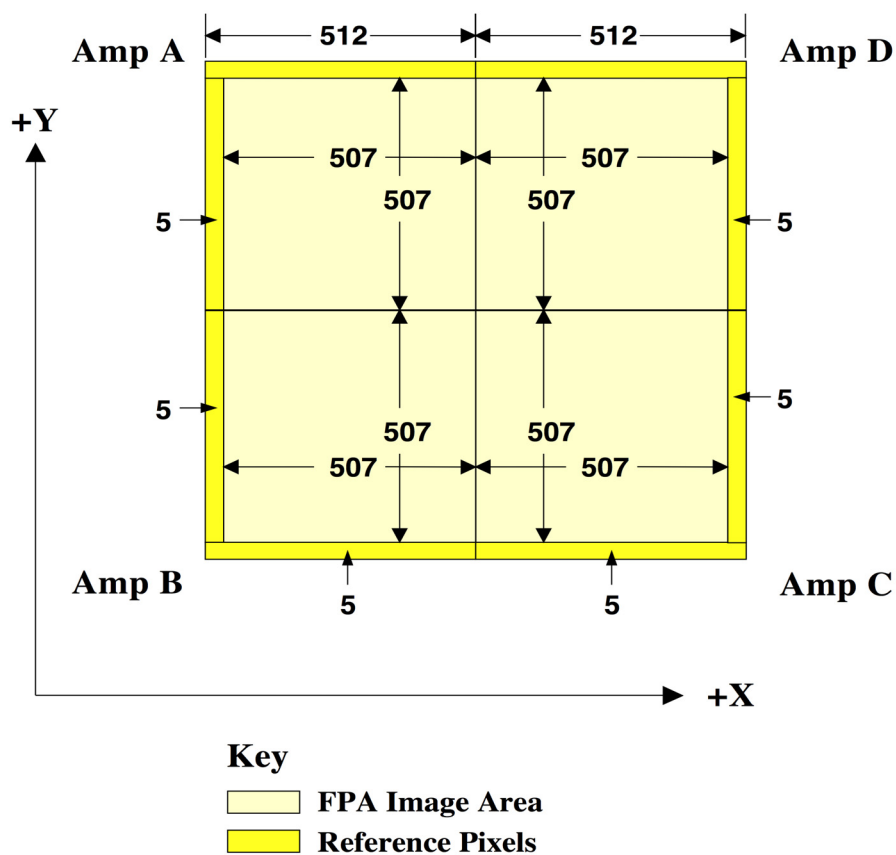


### 2.2.2 IR Channel File Structure

The WFC3 IR channel uses a  $1024 \times 1024$  pixel detector. Reference (bias) pixels occupy the 5 rows and columns on each side of the detector, thus yielding bias-trimmed images with dimensions of  $1014 \times 1014$  pixels, as shown in [Figure 2.3](#).

Like NICMOS, the IR channel operates only in MULTIACCUM mode, which starts an exposure by resetting all the detector pixels to their bias levels and recording those levels in an initial "zeroth" readout. This is then followed by  $n$  non-destructive readouts ( $n$  can be up to 15 and is set by the observer as parameter NSAMP in the Phase II proposal); the data associated with each readout are stored in a separate imset in the FITS file.

Figure 2.3: Format of a raw full WFC3 IR image.



For IR data, each imset consists of five data arrays:

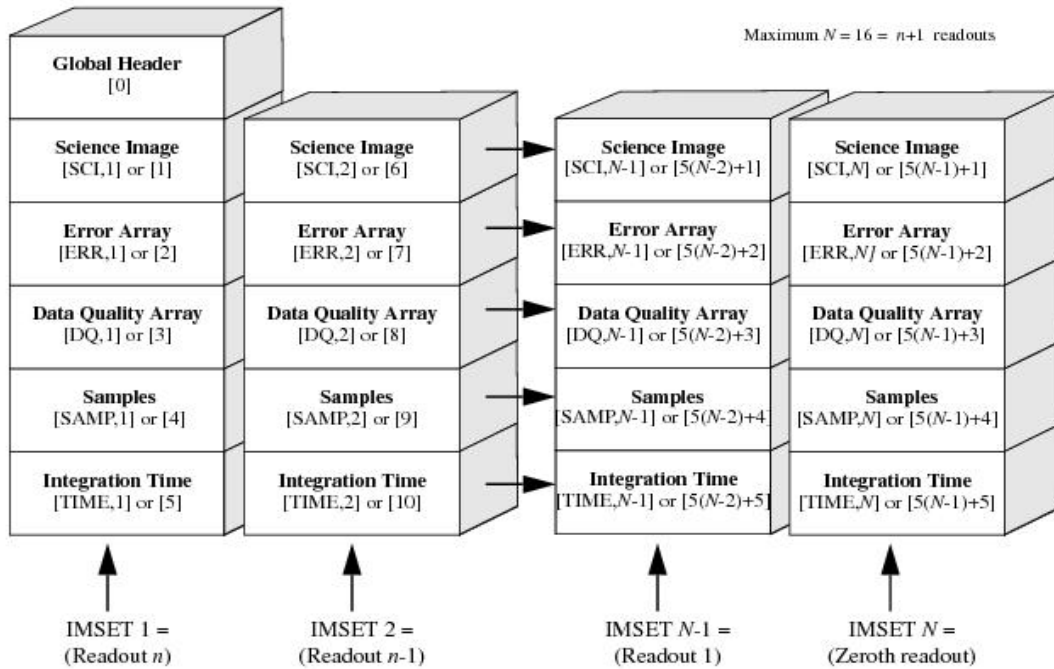
- the science image (SCI),
- the error array (ERR),
- the data quality array (DQ),
- the number of samples array (SAMP), and
- the integration time array (TIME).

An IR FITS file will therefore contain: the primary header unit and N imsets, which all together form a single IR exposure. The primary header keyword NSAMP records the total number of readouts worth of data contained in the file. Note that the value of NSAMP keyword is increased by 1 relative to proposal parameter NSAMP, because the keyword counts the zeroth read.



Also note that the order of the IR imsets in the FITS file is in reverse time order. The first imset in the file contains the result of the longest integration time (the last readout of the MULTIACCUM series). This is followed by the next-to-last readout and so on. The imset for the zeroth readout is stored last in the FITS file. This file organization has the advantage of placing the final readout first in the file, where it is easiest to access. This organization is shown graphically in [Figure 2.4](#)

**Figure 2.4: Format for WFC3 IR data.** Note that for IR data, readouts are stored in reverse chronological order.



### 2.2.3 Contents of Individual Arrays

The following sections explain the contents and origin of each of the individual arrays for WFC3 data products.

#### Science Image (SCI)

This image contains the data from the focal plane array (FPA) detectors. In raw data files, the science array is an integer (16-bit) image in units of data numbers, or DN. In calibrated data files, it is a floating-point value image in physical units of electrons (UVIS) or electrons per second (IR).



### Error Array (ERR)

This is a floating-point image that contains an estimate of the statistical uncertainty associated with each corresponding science image pixel. It is expressed as a real number of signal units or signal rates (as appropriate for the units of the science image). The values for this array are calculated during calibration with the **calwf3** task, combining detector read noise, Poisson noise in the detected signal, and uncertainties from applied calibration reference data.

### Data Quality Array (DQ)

This array contains 16 independent flags indicating various status and problem conditions associated with each corresponding pixel in the science image. Each flag has a true (set) or false (unset) state and is encoded as a bit in a 16-bit integer word. Users are advised that this word should not be interpreted as a simple integer, but must be converted to base-2 and each bit interpreted as a flag. [Table 2.6](#) lists the WFC3 data quality flags.



**Warning.** In raw data files, the *ERR* and *DQ* arrays will usually have the value of zero for all pixels, unless, for the *DQ* array, errors are detected in the down linked data. In order to reduce data volume, and, if no errors exist, both *ERR* and *DQ* extensions will contain null data arrays with *PIXVALUE* equal to zero.

**Table 2.6: WFC3 Data Quality flags.**

FLAG Value	Bit Setting	Data Quality Condition	
		UVIS	IR
0	0000 0000 0000 0000	OK	OK
1	0000 0000 0000 0001	Reed Solomon decoding error	Reed Solomon decoding error
2	0000 0000 0000 0010	Data replaced by fill value	Data missing and replaced by fill value
4	0000 0000 0000 0100	Bad detector pixel	Bad detector pixel
8	0000 0000 0000 1000	(Reserved)	Deviant zero read (bias) value
16	0000 0000 0001 0000	Hot pixel	Hot pixel
32	0000 0000 0010 0000	CTE tail	Unstable response
64	0000 0000 0100 0000	Warm pixel	Warm pixel
128	0000 0000 1000 0000	Bad pixel in bias	Bad reference pixel
256	0000 0001 0000 0000	Full well saturation	Full well saturation

**Table 2.6: WFC3 Data Quality flags. (Cont'd)**

512	0000 0010 0000 0000	Bad or uncertain flat value	Bad or uncertain flat value, including "blobs"
1024	0000 0100 0000 0000	Charge trap	(Reserved)
2048	0000 1000 0000 0000	A to D saturation	Signal in zero read
4096	0001 0000 0000 0000	Cosmic ray detected by AstroDrizzle	Cosmic ray detected by AstroDrizzle
8192	0010 0000 0000 0000	Cosmic ray detected during CR SPLIT or RPT OBS combination	Cosmic ray detected during <b>calwf3</b> up the ramp fitting
16384	0100 0000 0000 0000	Pixel affected by ghost/crosstalk	Pixel affected by ghost/crosstalk

**Note:** The CTE tail and ghost/crosstalk flags are currently not used

### Number of Samples Array (SAMP)

This array is present only for IR data. It is a 16-bit integer array and contains the number of samples used to derive the corresponding pixel values in the science image. For raw and intermediate data files, the sample values are set to the number of readouts that contributed to the science image. For calibrated files, the SAMP array contains the total number of valid samples used to compute the final science image pixel value, obtained by combining the data from all the readouts and rejecting cosmic ray hits and saturated pixels. Similarly, when multiple exposures (i.e., REPEAT-OBS) are combined to produce a single image, the SAMP array contains the total number of samples retained at each pixel for all the exposures.

### Integration Time Array (TIME)

This array is present only for IR data. This is a floating-point array that contains the effective integration time associated with each corresponding science image pixel value. For raw and intermediate data files, the time value is the total integration time of data that contributed to the science image. For calibrated datasets, the TIME array contains the combined exposure time of the valid readouts or exposures that were used to compute the final science image pixel value, after rejection of cosmic rays and saturated pixels from the intermediate data.



*In raw and intermediate data files, the SAMP and TIME arrays will each have the same value for all pixels. In order to reduce data volume, these image extensions contain null arrays, and the value of the number of samples and integration time is stored in the header keyword PIXVALUE in the SAMP and TIME extensions, respectively.*

## 2.3 Data Storage Requirements

The sizes of WFC3 data files (in MB) are given in [Table 2.7](#). The following assumptions were made when calculating these sizes:

- the ERR, DQ, SAMP, and TIME arrays are null in the raw files,
- the SAMP and TIME arrays are null in the ima files,
- IR images have the maximum of 16 MultiAccum readouts, and
- images are full-frame and unbinned.

**Table 2.7: Sizes of WFC3 data files.**

Channel	Size of FITS file			
	raw	ima	cal	drz
UVIS	35 MB		168 MB	214 MB
IR	34 MB	168 MB	17 MB	13 MB

The size of the drizzled image (\_drz) is for a single image that is drizzled only for the purpose of performing geometric corrections and for combining the two UVIS chips. It assumes that the input and output image pixels are approximately the same size (drizzle scale parameter is 1.0).

## 2.4 Headers and Keywords

Both the primary and extension headers in a WFC3 science data file contain keywords. These keywords store a wide range of information about the observations themselves (e.g., observing mode, exposure time, detector, etc.), as well as any processing done or to be done on the data.

The primary header keywords apply to all extensions in the FITS file. The extension headers carry extension-specific keywords, i.e., information relevant only to the image in a particular extension. For example, observation parameters, calibration switches, and reference file names are stored in the primary header. Exposure time and World Coordinate System information, on the other hand, are stored in the extension headers because this information can vary from one set of extensions to another.

In [Table 2.8](#) and [Table 2.9](#), we list the WFC3 keywords that appear in the primary header and SCI extension header, respectively. Columns 1 and 2 give the name of the keyword and a short description. The third column gives the format used for the value of the keyword: "L" for boolean values, "C" for characters, "R" for real values and "I" for integer values, followed by the precision of the value. Columns 4 and 5 show to which detector the keyword applies.

Table 2.10 lists the keywords that appear in the headers of the ERR, DQ, SAMP, and TIME extensions belonging to an imset in a WFC3 data file. Note that the SAMP and TIME extensions apply only to IR data.

**AstroDrizzle** adds additional keywords which are not listed in this handbook, and when it adds extensions does not update the NEXTEND keyword value. Consult the AstroDrizzle Handbook for further information. Users can use the STDAS task **catfits** (or the python task fits.info) to see all extensions in a file. The pattern keywords refer to the WFC3 dithering patterns available which are discussed in greater detail in Section 4.2.

**Table 2.8: WFC3 Primary Header Keywords**

Keyword	Description	Format	UVIS	IR
SIMPLE	data conform to FITS standard	L1	Y	Y
BITPIX	bits per data value	I2	Y	Y
NAXIS	number of data axes	I2	Y	Y
EXTEND	file may contain standard extensions	L1	Y	Y
NEXTEND	number of standard extensions	I2	Y	Y
GROUPS	image is in group format	L1	Y	Y
DATE	date this file was written (yyyy-mm-dd)	C10	Y	Y
FILENAME	name of file	C39	Y	Y
FILETYPE	type of data found in data file	C09	Y	Y
TELESCOP	telescope used to acquire data	C03	Y	Y
INSTRUME	identifier for instrument used to acquire data	C06	Y	Y
EQUINOX	equinox of celestial coordinate system	R4	Y	Y
<b>DATA DESCRIPTION KEYWORDS</b>				
ROOTNAME	rootname of the observation set	C34	Y	Y
IMAGETYP	type of exposure identifier	C18	Y	Y
PRIMESI	instrument designated as prime	C06	Y	Y
<b>TARGET INFORMATION</b>				
TARGNAME	proposer's target name	C30	Y	Y
RA_TARG	right ascension of the target (deg) (J2000)	R8	Y	Y
DEC_TARG	declination of the target (deg) (J2000)	R8	Y	Y
<b>PROPOSAL INFORMATION</b>				
PROPOSID	PEP proposal identifier	I4	Y	Y
LINENUM	proposal logsheet line number	C15	Y	Y

Table 2.8: WFC3 Primary Header Keywords (Cont'd)

PR_INV_L	last name of principal investigator	C30	Y	Y
PR_INV_F	first name of principal investigator	C20	Y	Y
PR_INV_M	middle name initial of principal investigator	C20	Y	Y
<b>EXPOSURE INFORMATION</b>				
SUNANGLE	angle between sun and V1 axis	R4	Y	Y
MOONANGL	angle between moon and V1 axis	R4	Y	Y
SUN_ALT	altitude of the sun above Earth's limb	R4	Y	Y
FGSLOCK	commanded FGS lock (FINE, COARSE, GYROS, UNKNOWN)	C18	Y	Y
GYROMODE	number of gyros scheduled for observation	C1	Y	Y
REFFRAME	guide star catalog version	C8	Y	Y
DATE-OBS	UT date of start of observation (yyyy-mm-dd)	C10	Y	Y
TIME-OBS	UT time of start of observation (hh:mm:ss)	C08	Y	Y
EXPSTART	exposure start time (Modified Julian Date)	R8	Y	Y
EXPEND	exposure end time (Modified Julian Date)	R8	Y	Y
EXPTIME	exposure duration (seconds)--calculated	R4	Y	Y
EXPFLAG	exposure interruption indicator	C13	Y	Y
QUALCOM1	data quality comment 1	C68	Y	Y
QUALCOM2	data quality comment 2	C68	Y	Y
QUALCOM3	data quality comment 3	C68	Y	Y
QUALITY	data quality summary	C68	Y	Y
<b>POINTING INFORMATION</b>				
PA_V3	position angle of V3-axis of HST (deg)	R4	Y	Y
<b>TARGET OFFSETS (POSTARGS)</b>				
POSTARG1	POSTARG in axis 1 direction	R4	Y	Y
POSTARG2	POSTARG in axis 2 direction	R4	Y	Y
<b>DIAGNOSTIC KEYWORDS</b>				
OPUS_VER	OPUS software system version number	C18	Y	Y
CAL_VER	<b>CALWF3</b> code version	C24	Y	Y
PROCTIME	pipeline processing time (MJD)	R8	Y	Y
<b>SCIENCE INSTRUMENT CONFIGURATION</b>				
OBSTYPE	observation type - imaging or spectroscopic	C14	Y	Y

**Table 2.8: WFC3 Primary Header Keywords (Cont'd)**

OBSMODE	operating mode	C10	Y	Y
SCLAMP	lamp status, NONE or name of lamp which is on	C14	Y	Y
NRPTEXP	number of repeat exposures in set: default 1	I2	Y	Y
SUBARRAY	data from a subarray (T) or full frame (F)	L1	Y	Y
DETECTOR	detector in use: UVIS or IR	C04	Y	Y
FILTER	element selected from filter wheel	C07	Y	Y
APERTURE	aperture name	C16	Y	Y
PROPAPER	proposed aperture name	C16	Y	Y
DIRIMAGE	direct image for grism or prism exposure	C09	Y	Y
NSAMP	number of MULTIACCUM samples	I2	N	Y
SAMP_SEQ	MULTIACCUM exposure time sequence name	C08	N	Y
SAMPZERO	sample time of the zeroth read (sec)	R4	N	Y
SUBTYPE	size/type of IR subarray	C08	N	Y
CTEIMAGE	type of Charge Transfer Image, if applicable	C04	Y	N
CTEDIR	serial or parallel	C08	Y	N
CRSPLIT	number of cosmic ray split exposures	I2	Y	N
<b>CTE CORRECTION PARAMETERS</b>				
CTE_NAME	name of the CTE algorithm	C23	Y	N
CTE_VER	Version number of the CTE algorithm	C23	Y	N
CTEDATE0	Date of WFC3/UVIS installation in HST (MJD)	R8	Y	N
CTEDATE1	Reference date of CTE model pinning (MJD)	R8	Y	N
PCTETLEN	Maximum length of CTE trail	R8	Y	N
PCTERNOI	Read noise amplitude	R8	Y	N
PCTENFOR	Number iterations used in CTE forward modeling	I4	Y	N
PCTENPAR	Number of iterations used in parallel transfer	I4	Y	N
PCTENSMD	read-noise mitigation algorithm	I4	Y	N
PCTETRSH	over-subtraction threshold	R8	Y	N
PCTEFRAC	Scaling of CTE model (relative to CTEDATE1)	R8	Y	N
FIXROCR	Fix readout cosmic rays	I4	Y	N
<b>SCAN KEYWORDS</b>				
SCAN_TYP	Type of scanning path	C18	Y	Y
SCAN_WID	scan width (arcsec)	R8	Y	Y

**Table 2.8: WFC3 Primary Header Keywords (Cont'd)**

ANG_SIDE	angle between sides of parallelogram (deg)	R8	Y	Y
DWELL_LN	dwelt pts/line for scan pointing	I4	Y	Y
DWELL_TM	wait time at each dwelt point (sec)	R8	Y	Y
SCAN_ANG	position angle of scan line (deg)	R8	Y	Y
SCAN_RAT	commanded rate of the line scan (arcsec/sec)	R8	Y	Y
NO_LINES	number of lines per scan	I4	Y	Y
SCAN_LEN	scan length (arcsec)	R8	Y	Y
SCAN_COR	scan coordinate frame of ref: (celestial,vehicle)	C18	Y	Y
CSMID	Channel Select Mechanism ID (UVIS/IR)	C7	Y	Y
<b>POST-SAA DARK KEYWORDS</b>				
SAA_EXIT	time of last exit from SAA contour level 23	C17	N	Y
SAA_TIME	seconds since last exit from SAA contour 23	I4	N	Y
SAA_DARK	association name for post-SAA dark exposures	C09	N	Y
SAACRMAP	SAA cosmic ray map file	C18	N	Y
<b>CALIBRATION SWITCHES: PERFORM, OMIT, COMPLETE, SKIPPED</b>				
DQICORR	data quality initialization	C08	Y	Y
BLEVCORR	subtract bias level measured from overscan, (UVIS) or reference pixels (IR)	C08	Y	Y
CRCORR	combine observations to reject cosmic rays/, identify cosmic ray hits	C08	Y	Y
DARKCORR	subtract dark image	C08	Y	Y
FLATCORR	flat-field data	C08	Y	Y
FLUXCORR	Scale the UVIS chips to get uniform flux correction	C08	Y	N
PCTECORR	Perform the pixel based CTE correction	C08	Y	N
PHOTCORR	populate photometric header keywords	C08	Y	Y
DRIZCORR	drizzle processing	C08	Y	Y
NLINCORR	correct for detector nonlinearities	C08	N	Y
RPTCORR	combine individual repeat observations	C08	N	Y
UNITCORR	convert to count rates (see also BUNIT)	C08	N	Y
ZSIGCORR	zero read signal correction	C08	N	Y
ZOFFCORR	subtract MULTIACCUM zero read	C08	N	Y
ATODCORR	correct for A to D conversion errors	C08	Y	N

**Table 2.8: WFC3 Primary Header Keywords (Cont'd)**

BIASCORR	subtract bias image	C08	Y	N
EXPSCORR	process individual observations after cr-reject	C08	Y	N
FLSHCORR	post flash correction	C08	Y	N
SHADCORR	apply shutter shading correction	C08	Y	N
<b>CALIBRATION REFERENCE FILES</b>				
BPIXTAB	bad pixel table	C23	Y	Y
CCDTAB	detector calibration parameters	C23	Y	Y
OSCNTAB	table containing overscan (UVIS) or reference pixel (IR) locations	C23	Y	Y
CRREJTAB	cosmic ray rejection parameters	C23	Y	Y
DARKFILE	superdark image file name	C23	Y	Y
PFLTFILE	pixel to pixel flat-field file name	C23	Y	Y
DFLTFILE	delta flat-field file name	C23	Y	Y
LFLTFILE	low order flat	C23	Y	Y
COMPTAB	the HST components table		Y	Y
IDCTAB	distortion coefficients table	C23	Y	Y
DGEOFILE	distortion correction image (no longer used, kept in the header for compatibility)	C23	Y	Y
MDRIZTAB	AstroDrizzle parameter table	C18	Y	Y
NLINFILE	detector nonlinearities file	C23	N	Y
ATODTAB	analog to digital correction file	C23	Y	N
BIASFILE	superbias image file name	C23	Y	N
FLSHFILE	post flash correction file name	C23	Y	N
SHADFILE	shutter shading correction file	C23	Y	N
PCTETAB	The default parameters and reference data for the CTE correction	C18	Y	N
IMPHTTAB	The default values for the photometric keywords	C18	Y	Y
DRKCFE	Superdark reference for CTE corrected files	C23	Y	N
BIACFILE	Superbias reference for CTE corrected files	C23	Y	N
SNKCFE	map of sink-pixel locations	C23	Y	N
D2IMFILE	2-D non-polynomial distortion correction table	C23	Y	N
NOPOFILE	2-D non-polynomial filter dependent distortion	C23	Y	N



**Table 2.8: WFC3 Primary Header Keywords (Cont'd)**

<b>COSMIC RAY REJECTION ALGORITHM PARAMETERS<sup>SC23</sup></b>				
MEANEXP	reference exposure time for parameters	R4	Y	Y
SCALENSE	multiplicative scale factor applied to noise	R4	Y	Y
INITGUES	initial guess method (MIN or MED)	C03	Y	Y
SKYSUB	sky value subtracted (MODE or NONE)	C04	Y	Y
SKYSUM	sky level from the sum of all constituent images	R4	Y	Y
CRSIGMAS	statistical rejection criteria	C15	Y	Y
CRRADIUS	rejection propagation radius (pixels)	R4	Y	Y
CRTHRESH	rejection propagation threshold	R4	Y	Y
BADINPDQ	data quality flag bits to reject	I2	Y	Y
REJ_RATE	rate at which pixels are affected by cosmic rays	R4	Y	Y
CRMASK	flag CR-rejected pixels in input files (T/F)	L1	Y	Y
MDRIZSKY	sky value computed by AstroDrizzle	R4	Y	Y
<b>PHOTOMETRY KEYWORDS</b>				
<b>(contained in this extension for IR, in the SCI extension for UVIS, see <a href="#">Table 2.9</a>)</b>				
PHOTMODE	observation configuration for photometric calibration	C50	N	Y
PHOTFLAM	inverse sensitivity, ergs/cm <sup>2</sup> /Ang/electron	R8	N	Y
PHOTFNU	inverse sensitivity, Jy* sec/electron	R8	N	Y
PHOTZPT	ST magnitude zero point	R4	N	Y
PHOTPLAM	pivot wavelength (Angstroms)	R4	N	Y
PHOTBW	RMS bandwidth of filter plus detector	R4	N	Y
<b>POST FLASH PARAMETERS</b>				
FLASHDUR	exposure time in seconds: 0.1 to 409.5	R4	Y	N
FLASHCUR	post flash current (zero, low, medium, high)	C07	Y	N
FLASHSTA	status: SUCCESSFUL, ABORTED, NOT PERFORMED	C16	Y	N
FLASHLVL	requested APT post flash, electrons/pixel	R4	Y	N
SHUTRPOS	shutter position: A or B	C05	Y	N
<b>CHARGE INJECTION PARAMETERS</b>				
CHINJECT	charge injection mode	C08	Y	N
<b>OTFR KEYWORDS</b>				
T_SGSTAR	OMS calculated guide star control	C18	Y	Y

**Table 2.8: WFC3 Primary Header Keywords (Cont'd)**

<b>PATTERN KEYWORDS</b>				
PATTERN1	primary pattern type	C24	Y	Y
P1_SHAPE	primary pattern shape	C18	Y	Y
P1_PURPS	primary pattern purpose	C10	Y	Y
P1_NPTS	number of points in primary pattern	I2	Y	Y
P1_PSPAC	point spacing for primary pattern (arc-sec)	R4	Y	Y
P1_LSPAC	line spacing for primary pattern (arc-sec)	R4	Y	Y
P1_ANGLE	angle between sides of parallelogram patt (deg)	R4	Y	Y
P1_FRAME	coordinate frame of primary pattern	C09	Y	Y
P1_ORINT	orientation of pattern to coordinate frame (deg)	R4	Y	Y
P1_CENTR	center pattern relative to pointing (yes/no)	C03	Y	Y
PATTERN2	secondary pattern type	C24	Y	Y
P2_SHAPE	secondary pattern shape	C18	Y	Y
P2_PURPS	secondary pattern purpose	C10	Y	Y
P2_NPTS	number of points in secondary pattern	I2	Y	Y
P2_PSPAC	point spacing for secondary pattern (arc-sec)	R4	Y	Y
P2_LSPAC	line spacing for secondary pattern (arc-sec)	R4	Y	Y
P2_ANGLE	angle between sides of parallelogram patt (deg)	R4	Y	Y
P2_FRAME	coordinate frame of secondary pattern	C09	Y	Y
P2_ORINT	orientation of pattern to coordinate frame (deg)	R4	Y	Y
P2_CENTR	center pattern relative to pointing (yes/no)	C03	Y	Y
PATTSTEP	position number of this point in the pattern	I2	Y	Y
<b>ENGINEERING PARAMETERS</b>				
CCDAMP	CCD amplifier readout configuration	C04	Y	Y
CCDGAIN	commanded gain of CCD	R4	Y	Y
CCDOFSAB	commanded CCD bias offset for amps A\&B	I4	N	Y
CCDOFSCD	commanded CCD bias offset for amps C\&D	I4	N	Y
CCDOFSTA	commanded CCD bias offset for amplifier A	I4	Y	N
CCDOFSTB	commanded CCD bias offset for amplifier B	I4	Y	N
CCDOFSTC	commanded CCD bias offset for amplifier C	I4	Y	N
CCDOFSTD	commanded CCD bias offset for amplifier D	I4	Y	N

**Table 2.8: WFC3 Primary Header Keywords (Cont'd)**

<b>CALIBRATED ENGINEERING PARAMETERS</b>				
ATODGNA	measured gain for amplifier A	R4	Y	Y
ATODGNB	measured gain for amplifier B	R4	Y	Y
ATODGNC	measured gain for amplifier C	R4	Y	Y
ATODGND	measured gain for amplifier D	R4	Y	Y
READNSEA	measured read noise for amplifier A	R4	Y	Y
READNSEB	measured read noise for amplifier B	R4	Y	Y
READNSEC	measured read noise for amplifier C	R4	Y	Y
READNSED	measured read noise for amplifier D	R4	Y	Y
BIASLEVA	bias level for amplifier A	R4	Y	Y
BIASLEVB	bias level for amplifier B	R4	Y	Y
BIASLEVC	bias level for amplifier C	R4	Y	Y
BIASLEVD	bias level for amplifier D	R4	Y	Y
<b>ASSOCIATION KEYWORDS</b>				
ASN_ID	unique identifier assigned to association	C10	Y	Y
ASN_TAB	name of the association table	C23	Y	Y
ASN_MTYP	role of the member in the association	C12	Y	Y

**Table 2.9: WFC3 SCI extension header keywords**

<b>Keyword</b>	<b>Description</b>	<b>Format</b>	<b>UVIS</b>	<b>IR</b>
XTENSION	extension type	C08	Y	Y
BITPIX	bits per data value	I2	Y	Y
NAXIS	number of data axes	I2	Y	Y
NAXIS1	length of first data axis	I4	Y	Y
NAXIS2	length of second data axis	I4	Y	Y
PCOUNT	number of group parameters	I2	Y	Y
GCOUNT	number of groups	I2	Y	Y
INHERIT	inherit the primary header	L1	Y	Y
EXTNAME	extension name	C08	Y	Y
EXTVER	extension version number	I2	Y	Y
ROOTNAME	rootname of the observation set	C34	Y	Y

**Table 2.9: WFC3 SCI extension header keywords (Cont'd)**

EXPNAME	exposure identifier	C25	Y	Y
DATAMIN	the minimum value of the data	R8	Y	Y
DATAMAX	the maximum value of the data	R8	Y	Y
BUNIT	brightness units	C18	Y	Y
BSCALE	scale factor for array value to physical value	R8	Y	Y
BZERO	physical value for an array value of zero	R8	Y	Y
<b>CCD CHIP IDENTIFICATION</b>				
CCDCHIP	CCD chip (1 or 2)	I2	Y	N
<b>WORLD COORDINATE SYSTEM AND RELATED PARAMETERS</b>				
WCSAXES	number of World Coordinate System axes	I2	Y	Y
CRPIX1	xcoordinate of reference pixel	R8	Y	Y
CRPIX2	ycoordinate of reference pixel	R8	Y	Y
CRVAL1	first axis value at reference pixel	R8	Y	Y
CRVAL2	second axis value at reference pixel	R8	Y	Y
CTYPE1	the coordinate type for the first axis	C08	Y	Y
CTYPE2	the coordinate type for the second axis	C08	Y	Y
CD1_1	partial of first axis coordinate w.r.t. x	R8	Y	Y
CD1_2	partial of first axis coordinate w.r.t. y	R8	Y	Y
CD2_1	partial of second axis coordinate w.r.t. x	R8	Y	Y
CD2_2	partial of second axis coordinate w.r.t. y	R8	Y	Y
LTV1	offset in X to subsection start	R4	Y	Y
LTV2	offset in Y to subsection start	R4	Y	Y
LTM1_1	reciprocal of sampling rate in X	R4	Y	Y
LTM2_2	reciprocal of sampling rate in Y	R4	Y	Y
PA_APER	position Angle of reference aperture center (deg)	R8	Y	Y
VAFactor	velocity aberration plate scale factor	R8	Y	Y
ORIENTAT	position angle of image y axis (degrees East of North)	R4	Y	Y
RA_APER	right ascension of aperture reference position	R8	Y	Y
DEC_APER	declination of aperture reference position	R8	Y	Y
<b>REPEATED EXPOSURES INFORMATION</b>				
NCOMBINE	number of image sets combined during CR rejection	I2	Y	Y

**Table 2.9: WFC3 SCI extension header keywords (Cont'd)**

<b>PHOTOMETRY KEYWORDS</b>					
(contained in this extension for UVIS, in the primary extension for IR, see <a href="#">Table 2.8</a> )					
PHOTMODE	observation configuration for photometric calibration	C50	Y	N	
PHOTFLAM	inverse sensitivity, ergs/cm <sup>2</sup> /Ang/electron	R8	Y	N	
PHTFLAM1	PHOTFLAM on chip 1 when scales are not uniform	R8	Y	N	
PHTFLAM2	PHOTFLAM on chip 2 when scales are not uniform	R8	Y	N	
PHTRATIO	Ratio of PHTFLAM1/PHTFLAM2	R8	Y	N	
PHOTFNU	inverse sensitivity, Jy*sec/electron	R8	Y	N	
PHOTZPT	ST magnitude zero point	R4	Y	N	
PHOTPLAM	pivot wavelength (Angstroms)	R4	Y	N	
PHOTBW	RMS bandwidth of filter plus detector	R4	Y	N	
<b>READOUT DEFINITION PARAMETERS</b>					
CENTERA1	subarray axis1 center point in unbinned detector pix	I4	Y	Y	
CENTERA2	subarray axis2 center point in unbinned detector pix	I4	Y	Y	
SIZAXIS1	subarray axis1 size in unbinned detector pixels	I4	Y	Y	
SIZAXIS2	subarray axis2 size in unbinned detector pixels	I4	Y	Y	
BINAXIS1	axis1 data bin size in unbinned detector pixels	I2	Y	Y	
BINAXIS2	axis2 data bin size in unbinned detector pixels	I2	Y	Y	
<b>READOUT PARAMETERS</b>					
SAMPNUM	MULTIACCUM sample number	I2	N	Y	
SAMPTIME	total integration time (sec)	R4	N	Y	
DELTATIM	integration time of this sample (sec)	R4	N	Y	
ROUTTIME	UT time of array readout (MJD)	R8	N	Y	
TDFTRANS	number of TDF transitions during current sample	I4	N	Y	
<b>DATA PACKET INFORMATION</b>					
FILLCNT	number of segments containing fill	I4	Y	Y	
ERRCNT	number of segments containing errors	I4	Y	Y	
PODPSFF	PODPS fill present (T/F)	L1	Y	Y	
STDCFFF	science telemetry fill data present (T/F)	L1	Y	Y	
STDCFFP	science telemetry fill pattern (hex)	C06	Y	Y	
<b>IMAGE STATISTICS AND DATA QUALITY FLAGS</b>					
NGOODPIX	number of good pixels	I4	Y	Y	

**Table 2.9: WFC3 SCI extension header keywords (Cont'd)**

SDQFLAGS	serious data quality flags	I4	Y	Y
GOODMIN	minimum value of good pixels	R4	Y	Y
GOODMAX	maximum value of good pixels	R4	Y	Y
GOODMEAN	mean value of good pixels	R4	Y	Y
SNRMIN	minimum signal to noise of good pixels	R4	Y	Y
SNRMAX	maximum signal to noise of good pixels	R4	Y	Y
NRMEAN	mean value of signal to noise of good pixels	R4	Y	Y
SOFTERRS	number of soft error pixels (DQF1)	I4	Y	Y
MEANDARK	average dark level subtracted	R4	Y	Y
MEANBLEV	average bias level subtracted	R4	Y	Y
MEANFLSH	mean number of counts in post flash exposure, DN/pixel	R4	Y	N

**Table 2.10: WFC3 extension header keywords (imset extensions 2-5)**

Keyword	Description	Format	Extension Type			
			ERR	DQ	SAMP	TIME
			(UVIS and IR)	(IR Only)		
XTENSION	extension type	C08	Y	Y	Y	Y
BITPIX	bits per data value	I2	Y	Y	Y	Y
NAXIS	number of data axes	I2	Y	Y	Y	Y
NAXIS1	length of first data axis	I4	Y	Y	Y	Y
NAXIS2	length of second data axis	I4	Y	Y	Y	Y
PCOUNT	number of group parameters	I2	Y	Y	Y	Y
GCOUNT	number of groups	I2	Y	Y	Y	Y
TFIELDS	number of fields in each table row	I2	Y	Y	Y	Y
INHERIT	inherit the primary header	L1	Y	Y	Y	Y
EXTNAME	extension name	C08	Y	Y	Y	Y
EXTVER	extension version number	I2	Y	Y	Y	Y
ROOTNAME	rootname of the observation set	C34	Y	Y	Y	Y
EXPNAME	exposure identifier	C25	Y	Y	Y	Y
DATAMIN	the minimum value of the data	R8	Y	Y	Y	Y
DATAMAX	the maximum value of the data	R8	Y	Y	Y	Y

Table 2.10: WFC3 extension header keywords (imset extensions 2-5) (Cont'd)

			Extension Type			
BUNIT	brightness units	C18	Y	Y	Y	Y
NPIX1	length of constant array axis 1	I4	Y	Y	Y	Y
NPIX2	length of constant array axis 2	I4	Y	Y	Y	Y
PIXVALUE	values of pixels in constant array	R4	Y	Y	Y	Y
<b>WORLD COORDINATE SYSTEM AND RELATED PARAMETERS</b>						
WCSAXES	number of World Coordinate System axes	I2	Y	Y	Y	Y
CRPIX1	x-coordinate of reference pixel	R8	Y	Y	Y	Y
CRPIX2	y-coordinate of reference pixel	R8	Y	Y	Y	Y
CRVAL1	first axis value at reference pixel	R8	Y	Y	Y	Y
CRVAL2	second axis value at reference pixel	R8	Y	Y	Y	Y
CTYPE1	the coordinate type for the first axis	C08	Y	Y	Y	Y
CTYPE2	the coordinate type for the second axis	C08	Y	Y	Y	Y
CD1_1	partial of first axis coordinate w.r.t. x	R8	Y	Y	Y	Y
CD1_2	partial of first axis coordinate w.r.t. y	R8	Y	Y	Y	Y
CD2_1	partial of second axis coordinate w.r.t. x	R8	Y	Y	Y	Y
CD2_2	partial of second axis coordinate w.r.t. y	R8	Y	Y	Y	Y
LTV1	offset in X to subsection start	R4	Y	Y	-	-
LTV2	offset in Y to subsection start	R4	Y	Y	-	-
LTM1_1	reciprocal of sampling rate in X	R4	Y	Y	-	-
LTM2_2	reciprocal of sampling rate in Y	R4	Y	Y	-	-
PA_APER	position angle of reference aperture center (deg)	R8	Y	Y	-	-
VAFACOR	velocity aberration plate scale factor	R8	Y	Y	-	-
<b>IMAGE STATISTICS AND DATA QUALITY FLAGS</b>						
NGOODPIX	number of good pixels	I4	Y	-	-	-
SDQFLAGS	serious data quality flags	I4	Y	-	-	-
GOODMIN	minimum value of good pixels	R4	Y	-	-	-
GOODMAX	maximum value of good pixels	R4	Y	-	-	-
GOODMEAN	mean value of good pixels	R4	Y	-	-	-

# WFC3 Data Calibration

In this chapter . . .

3.1 The calwf3 Data Processing Pipeline / 35
3.2 UVIS Data Calibration Steps / 41
3.3 IR Data Calibration Steps / 54
3.4 Pipeline Tasks / 66
3.5 Manual Recalibration of WFC3 Data / 82

## 3.1 The calwf3 Data Processing Pipeline

The main executable which processes data taken with either the UVIS or IR detectors of the WFC3 instrument onboard the Hubble Space Telescope is called **calwf3**. The code is organized into subroutines that are called by the **calwf3** executable. The subroutines may be called independently if users desire specialized processing for their dataset. The subroutines used for processing UVIS images are called **w3cte**, **wf3ccd**, and **wf32d**. The main subroutine used for processing IR images is **wf3ir**. The **wf3rej** subroutine is shared between the UVIS and IR pipelines and is used for combining CR-SPLIT or REPEAT-OBS image sets. [Figure 3.1](#) shows the flow diagram for the UVIS pipeline as a whole, while [Figure 3.3](#) contains the flow for the IR pipeline.

A detailed description of the improvements in **calwf3** v3.3, which is more generally referred to as the UVIS2.0 update, can be found in the [February 22, 2016 issue of the STAN](#) and references therein. Each WFC3 image is calibrated with reference files particular to the observing mode used. Currently, raw images and telemetry files are processed and calibrated, using the most up-to-date reference files, parameters, and software (see Section 1.1.1 of the [Introduction to the HST Data Handbooks](#)). Then the data products, as well as the raw data are stored by MAST ([Mikulski Archive for Space Telescopes](#)).

During automatic pipeline processing by the STScI archive, **Astrodrizzle** follows **calwf3**. All calibrated images are corrected for geometric distortion and associated sets of dithered images are combined into a single product.



### 3.1.1 Where to Find calwf3

**calwf3** is part of the HSTCAL package, which can be downloaded separately from its GIT repository in the [Space Telescope Area](#). Its binaries are also installed along with the STScI distributed package [Astroconda](#).

### 3.1.2 Running calwf3

**calwf3** can be run on a single input raw file or an asn table listing the members of an association. When processing an association, it retrieves calibration switch and reference file keyword settings from the first image listed in the asn table. **calwf3** does not accept a user-defined list of input images on the command line (e.g. `*raw.fits` to process all raw files in the current directory).

The **wf3ccd**, **wf32d**, **wf3cte**, **wf3ir** tasks on the other hand, will accept such user-defined input file lists, but they will not accept an association table ( `asn` ) as input.

Below are some basic examples of how to run **calwf3** in python and directly from a terminal. Pure python commands may still be used in a **PyRAF** session. More advanced usage examples are available in [Sections 3.5](#)

#### Running calwf3 from a python terminal using [wfc3tools](#)

In Python without TEAL:

```
from wfc3tools import calwf3
calwf3(filename)
```

In Python with TEAL:

```
from stsci.tools import teal
from wfc3tools import calwf3
teal.teal('calwf3')
```

#### Running many files at the same time with python

The recommended method for running **calwf3** in batch mode is to use Python and the [wfc3tools](#) package in the [Astroconda](#) distribution.

For example:

```
from wfc3tools import calwf3
from glob import glob

for fits in glob('i*_raw.fits'):
    calwf3(fits)
```

### Displaying output from calwf3 in a Jupyter Notebook

When calling **calwf3** from a Jupyter notebook using the **calwf3()** function from **wfc3tools**, informational text output from the underlying **calwf3.e** program will be passed through the **print** function as the calibration runs by default, and show up in the user's cell. This behavior can be customized by passing your own function as the **log\_func** keyword argument to **calwf3**. As output is read from the underlying program, the **calwf3** Python wrapper will call **log\_func** with the contents of each line. (**print** is an obvious choice for a log function, but this also provides a way to connect **calwf3** to the Python logging system by passing the **logging.debug** function or similar). If **log\_func=None** is passed, informational text output from the underlying program will be ignored, but the program's exit code will still be checked for successful completion.

### Command line options for the calwf3 executable

**calwf3** can also be called directly from the OS command line by supplying the executable **calwf3.e** with an input file and a list of options. This is the same executable that the **wfc3tools** package calls.

```
calwf3.e -vts iaa012wdq_raw.fits

input: str
    Name of input files
        a single filename (`iaa012wdq_raw.fits`)
        the filename of an ASN table (`*_asn.fits`)

-t : print a detailed time stamp
-s : save temporary files
-d : print optional debugging statements
-l : suppress the OpenMP parallel processing for the
UVIS CTE correction
-v : Print verbose time stamps and information
-q : Print messages only to trailer file
```

### Running many files at the same time from the command line

The command line executable only accepts one file at a time, but you can use operating system tools like **awk** or **xargs** to process everything in a directory:

```
ls *raw.fits | awk '{print "calwf3.e",$1}' | csh
```

or alternatively:

```
ls *raw.fits | xargs -I % calwf3.e %
```

### 3.1.3 Keyword Usage

**calwf3** processing is controlled by the values of keywords in the input image headers. Certain keywords, referred to as calibration switches, are used to control which calibration steps are performed. Reference file keywords indicate which reference files to use in the various calibration steps. Users who wish to perform custom reprocessing of their data may change the values of these keywords in the `_raw` FITS file primary headers and then rerun the modified file through **calwf3**.

Other keyword values record instrument and detector parameters that are used in the calibration and some record information that is computed or derived during calibration. [Table 3.1](#) provides a summary of these keywords used by **calwf3**, specifying whether they function as input or output to the task(s) listed in column 2. For a definition of each keyword see [Tables 2.7](#), [2.8](#), and [2.9](#).

**Table 3.1: WFC3 keywords used with calwf3**

Keyword	Task(s)	I/O	Header	Sample of Possible Values
APERTURE	wf3ccd,wf32d, wf3ir	Input	Primary	UVIS1,UVIS2,UVIS1-FIX,UVIS2-FIX,UVIS,IR,...
ATODGNA, ATODGNB, ATODGNC, ATODGND	wf3ccd,wf32d, wf3ir, wf3rej	Output, Input	Primary	1.56, 2.26
BIASLVA, BIASLEVB, BIASLEVC, BIASLEVD	wf3ccd	Output	Primary	2502.23, 2605.48
BINAXIS1, BINAXIS2	wf3ccd,wf32d, wf3ir	Input	SCI	1, 2, 3
CAL_VER	wf3ccd,wf32d, wf3ir	Output	Primary	2.1 (15-May-2010)
CCDAMP	wf3ccd,wf32d, wf3rej	Input	Primary	ABCD, AC, BD, A, B, C, D
CCDCHIP	wf3ccd,wf32d, wf3rej	Input	SCI	1, 2
CCDGAIN	wf3ccd,wf32d, wf3ir, wf3rej	Input	Primary	1.5, 2.5
CCDOFSTA, CCDOFSTB, CCDOFSTC, CCDOFSTD	wf3ccd,wf32d, wf3rej	Input	Primary	3
DETECTOR	wf3ccd,wf32d, wf3ir, wf3rej	Input	Primary	UVIS, IR
EXPSTART, EXPEND, EXPTIME	wf3ccd,wf32d, wf3ir, wf3rej	Input	Primary	51475.159
FILTER	wf3ccd,wf32d, wf3ir, wf3rej	Input	Primary	F606W, F160W, G102
FLASHDUR, FLASHSTA	wf3ccd,wf32d, wf3rej	Input	Primary	0.2, SUCCESSFUL
LTM1_1, LTM2_2	wf3ccd,wf3ir	Input	SCI, ERR, DQ	1.0, 0.5, 0.333
LTV1, LTV2	wf3ccd,wf32d, wf3ir	Input	SCI, ERR, DQ	0.0, 25.0, 19.0, 5.0
MEANBLEV	wf3ccd,wf3ir	Output	SCI	2554.763, 14201.36
MEANDARK	wf32d, wf3ir	Output	SCI	3.20642E-01

**Table 3.1: WFC3 keywords used with calwf3 (Continued)**

MEANFLSH	wf3ccd	Output	SCI	N/A
NEXTEND	wf3ccd,wf32d, wf3ir, wf3rej	Input	Primary	3, 6, 80
NSAMP	wf3ir	Input	Primary	2-16
OBSTYPE	wf3ccd,wf32d, wf3ir, wf3rej	Input	Primary	Imaging, Spectroscopic
PHOTMODE	wf32d, wf3ir	Output	SCI, Primary	“WFC3 UVIS1 F606W”
PHOTFLAM	wf3ir	Output	SCI, Primary	Inverse sensitivity (erg/cm-2/A/DN)
PHOTFNU	wf3ir	Output	Primary	Inverse sensitivity (Jy/sec/DN)
PHOTZPT	wf32d, wf3ir	Output	SCI, Primary	ST magnitude zero point
PHOTPLAM	wf32d, wf3ir	Output	SCI, Primary	Pivot wavelength
PHOTBW	wf32d, wf3ir	Output	SCI, Primary	rms bandwidth of filter plus detector
PHTFLAM1	wf32d	Output	SCI, Primary	Chip1 Inverse Sensitivity for infinite aperture erg/cm-2/A/DN
PHTFLAM2	wf32d	Output	SCI, Primary	Chip1 Inverse Sensitivity for infinite aperture erg/cm-2/A/DN
PHTRATIO	wf32d	Output	SCI, Primary	PHTFLAM2/PHTFLAM1 ratio
READNSEA, READNSEB, READNSEC, READNSED	wf3ccd,wf32d, wf3ir, wf3rej	Output, Input	Primary	calibrated read noise for ampli- fier A, B, C, and D (electrons)
ROOTNAME	wf3ccd,wf32d, wf3ir, wf3rej	Input	Primary	rootname of the observation set
SAMP_SEQ	wf3ir	Input	Primary	RAPID, SPARS25,...
SAMPTIME	wf3ir	Input	SCI	Total integration time (sec)
SAMPZERO	wf3ir	Input	Primary	Sample time of MULTIAC- CUM zeroth read (sec)
SDQFLAGS	wf3ccd,wf32d, wf3ir	Input	SCI	Serious data quality flags con- sidered “bad” by calwf3
SUBARRAY	wf3ccd,wf32d, wf3ir	Input	Primary	T, F
SUBTYPE	wf3ir	Input	Primary	FULLIMAG, SQ64SUB
TDFTRANS	wf3ir	Input	SCI	0, 1
<b>IMAGE STATISTICS</b>				
NGOODPIX	wf32d, wf3ir	Output	SCI, ERR	number of good pixels

**Table 3.1: WFC3 keywords used with calwf3 (Continued)**

GOODMIN, GOODMAX, GOODMEAN	wf32d, wf3ir	Output	SCI, ERR	min, max and mean values of good pixels (electrons)
SNRMIN, SNRMAX, SNRMEAN	wf32d, wf3ir	Output	SCI	min, max, and mean signal to noise of good pixels
<b>CR-REJ PARAMETERS</b>				
BADINPDQ	wf3rej	Output	Primary	data quality flag used for rejection
CRMASK	wf3rej	Output	Primary	T, F
CRRADIUS	wf3rej	Output	Primary	3.0
CRSIGMAS	wf3rej	Output	Primary	6.5, 5.5, 4.5
CRTHRESH	wf3rej	Output	Primary	rejection propagation threshold
EXPSTART, EXPEND, EXPTIME, TEXPTIME	wf3rej	Output	Primary	exposure start, and end times (modified Julian date)
EXPTIME, TEXPTIME	wf3rej	Output	Primary	total exposure duration (seconds)--calculated
INITGUES	wf3rej	Output	Primary	minimum, mode
MEANEXP	wf3rej	Output	Primary	Average exposure time (sec) for each image
NCOMBINE	wf3rej	Output	SCI	number of image sets combined during CR rejection
REJ_RATE	wf3rej	Output	Primary	rate at which pixels are affected by cosmic rays
SCALENSE	wf3rej	Output	Primary	Multiplicative term (in percent) for the noise model
SKYSUB	wf3rej	Output	Primary	Sky value subtracted (mode, none)
SKYSUM	wf3rej	Output	Primary	Sky level from the sum of all constituent images

### 3.1.4 Using CRDS To Update Reference Files

The HST Calibration Reference Data System (CRDS) is the reference file management software used by STSCI for organizing and assigning reference files to datasets. Users can query [CRDS](#) to get the best references files for their data at hand.

The WFC3 team recommends that the most up-to-date reference files be used for re-processing.



***Users should make sure that the same version of all reference files and the pipeline software is used to analyze their entire dataset.***

This is particularly important for data taken at multiple epochs. For example, if the data are retrieved from MAST at different times (e.g., after the execution of each visit), it may be possible to observe systematic differences, due to changes in the reference files, or more generally, to the whole data processing flow. Thus it is recommended that the whole dataset pertinent to the given scientific investigation is retrieved simultaneously. Alternatively, the data need to be reprocessed off-line (starting from the unprocessed raw files) using a self-consistent configuration of pipeline and reference files. Occasionally there may be an instrument mode for which there is no calibration data. In these cases there will be a placeholder reference file in CRDS that is filled with zeros or ones, as appropriate. Such reference files are identified by having their header keyword `PEDIGREE` set to `DUMMY`. When **calwf3** encounters one of these reference files it will automatically skip the calibration step for which the file is used (e.g., `DARKCORR` will be set to the value `SKIPPED` if the `DARKFILE` is dummy).

---

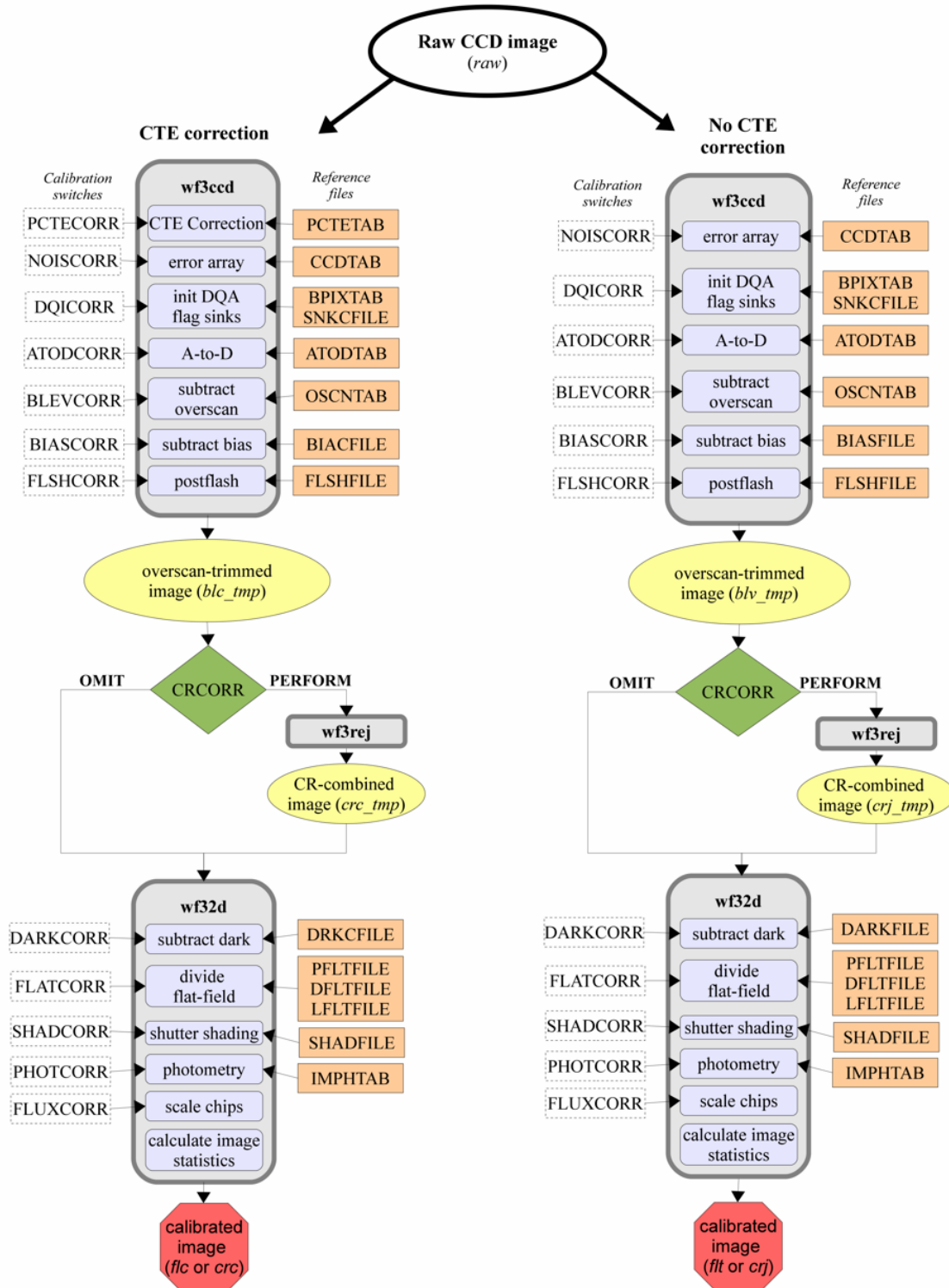
## 3.2 UVIS Data Calibration Steps

As of **calwf3** v3.3, the pipeline processes all UVIS data twice, once with the CTE correction applied as the first step, and a second time without the CTE correction. [Figure 3.1](#) shows a schematic representation of all the UVIS calibration steps, which are also briefly summarized below, in the order they are performed, with the corresponding calibration switch keyword in parenthesis:

- Calculate and remove any CTE found in the image (`PCTECORR`)
- Calculate and record a noise model for each pixel (`NOISCORR`) in the error array, `ERR`, of the header and initialize the data quality, `DQ`, array of the image (`DQICORR`). Note the (`NOISCORR`) is a calibration switch inaccessible to the user i.e. it is not listed explicitly in the image header and the correction is always performed,
- Correct for Analog-to-Digital conversion errors where necessary (`ATODCORR`)
- Subtract bias level determined from overscan regions (`BLEVCORR`)
- Subtract the bias image (`BIASCORR`)
- Detect and record SINK pixels in the `DQ` mask (`DQICORR`)
- Subtract the post-flash image if applicable (`FLSHCORR`)
- Scale and subtract the dark image (`DARKCORR`)
- Perform flat fielding (`FLATCORR`)
- Perform shutter-shading correction where necessary, currently skipped (`SHADCORR`)
- Populate photometric header keywords (`PHOTCORR`)
- Correct chips to use the same zero point (`FLUXCORR`)
- Calculate basic pixel statistics for the image and store them in relevant header keywords (No switch).

Figure 3.1: Flow diagram for the UVIS branch of the calwf3 pipeline.

The name of the reference files used at each step, as well as the calibration switches that control each step are indicated. NOISCORR is a calibration switch inaccessible to the user i.e. it is not listed explicitly in the image header and the correction is always performed by calwf3.



### 3.2.1 Correction For Charge Transfer Efficiency

- Header switch: PCTECORR
- Reference file: PCTETAB

The charge transfer efficiency (CTE) of the UVIS detector has been declining over time as on-orbit radiation damage creates charge traps in the CCDs. During the charge transfer in the CCD readout process, these traps capture photo-electrons generated in other “upstream” pixels, thus lowering the detected charge. Faint sources in particular can suffer large fractional flux losses or even be lost entirely if observations are not planned and analyzed carefully. The CTE depends on the morphology of the source, the distribution of electrons in the field of view, and the population of charge traps in the detector column between the source and the transfer register. Further details of the current understanding of the state of the WFC3/UVIS CTE are presented in [Chapter 6](#), as well as on the [WFC3 CTE webpage](#). The PCTECORR step aims to mitigate the flux loss incurred from CTE.

More information on this part of the pipeline can be found in [Section 3.4.1](#), which details the functioning of the **wf3cte** routine.

### 3.2.2 Error Array Initialization

- Header switch: NOISCORR (not listed explicitly in image header, see text)
- Reference file: CCDTAB

In this step, the image error array is initialized. The NOISCORR switch is not user-accessible and always set to PERFORM. The function examines the ERR extension of the input data to determine the state of the array. The input `_raw` image contains an empty ERR array. If the ERR array has already been expanded and contains values other than zero, then this function does nothing. Otherwise it will initialize the ERR array by assigning pixel values based on a simple noise model. The noise model uses the science (SCI) array and for each pixel calculates the error value  $\sigma$  in units of DN:

$$\sigma_{CCD} = \sqrt{\frac{SCI - bias}{gain} + \left(\frac{readnoise}{gain}\right)^2}$$

The CCDTAB reference file contains the bias, gain and readnoise values used for each CCD amplifier quadrant used in this calculation. The table contains one row for each configuration that can be used during readout, which is uniquely identified by the list of amplifiers (replicated in the CCDAMP header keyword), the particular chip being read out (CCDCHIP), the commanded gain (CCDGAIN), the commanded bias offset level (CCDOFST) and the pixel bin size (BINAXIS). These commanded values are used to find the table row that matches the characteristics of the image that is being processed and reads each amplifiers properties, including readnoise (READNSE), A-to-D gain (ATODGN) and the mean bias level (CCDBIAS).



### 3.2.3 Data Quality Array Initialization

- Header switch: DQICORR
- Reference files: CCDTAB, BPIXTAB

This step initializes the data quality array by reading a table of known bad pixels for the detector, as stored in the Bad Pixel reference table BPIXTAB. The types of bad pixels that can be flagged are indicated in [Table 3.2](#)

**Table 3.2: Data quality array flags for UVIS files**

NAME	VALUE	DESCRIPTION
GOODPIXEL	0	OK
SOFTERR	1	Reed-Solomon decoding error
DATALOST	2	data replaced by fill value
DETECTORPROB	4	bad detector pixel or beyond aperture
DATAMASKED	8	Unused in UVIS
HOTPIX	16	hot pixel
CTETAIL	32	UVIS CTE tail
WARMPPIX	64	warm pixel
BADBIAS	128	bad bias value
SATPIXEL	256	full-well or a-to-d saturated pixel
BADFLAT	512	bad flatfield value
TRAP	1024	UVIS charge trap, SINK pixel
ATODSAT	2048	a-to-d saturated pixel
CR hit	4096	reserved for Astrodrizzle CR rejection
DATAREJECT	8192	rejected during image combination UVIS, IR CR rejection
CROSSTALK	16384	ghost or crosstalk
RESERVED2	32768	can't use

Note: The DATAMASKED (8), CTETAIL (32) and CROSSTALK (16384) are not currently used.

The DQ array may already have been populated with some values to flag pixels affected by telemetry problems during downlink. Other DQ values will only be marked during further processing (such as cosmic-ray rejection). This function also checks pixel values in the SCI extension for full-well saturation, using the value of the SATURATE column in the CCD parameters table (CCDTAB). Any SCI array pixel value that is greater than the SATURATE value will be assigned the appropriate flag value in the DQ array (256). This function also checks for SCI array pixel values that

have reached the limit of the detector's 16-bit A-to-D converters, flagging any pixel with a value  $> 65534$  DN with the 'A-to-D saturation' DQ value (2048), A-to-D saturated pixels are also flagged as full-well saturated, so their DQ is actually updated (bitwise) by  $256+2048$ .

Even full-well saturated pixels (but not A-to-D saturated) could still be used for aperture photometry, since charge keeps being created in saturated pixels but it's no longer retained in the original pixel and spills over to the neighboring ones (bleeding, see also [WFC3 ISR 2010-10](#)). Users should be aware that the apertures in this case should be defined as to include all the bled charge. Users can check [Section 5.4.5](#) and [Section 5.4.6](#) of the [WFC3 Instrument handbook](#) for further details on full-well and A-to-D saturation.

DQICORR combines the DQ flags from preprocessing, BPIXTAB, and saturation tests into a single result for the particular observation. These values are combined using a bit-wise logical OR operation for each pixel. Thus, if a single pixel is affected by two DQ flags, those flag values will be added in the final DQ array. This array then becomes a mask of all pixels that had some problem coming into the calibrations, so that the calibration processing steps can ignore bad pixels during processing. The BPIXTAB reference file maintains a record of the x, y position and DQ value for all known bad pixels in each CCD chip for a given time period.

### 3.2.4 Correct for Analog-to-Digital Conversion Errors

- Header Switch: ATODCORR
- Reference File: ATODTAB

An analog-to-digital conversion correction is applied if the CCD electronic circuitry, which performs the analog-to-digital conversion, is biased toward the assignment of certain DN values. WFC3 ground test results showed that this correction is not currently needed, so the ATODCORR switch is currently always set to 'OMIT' so that this function is not performed.

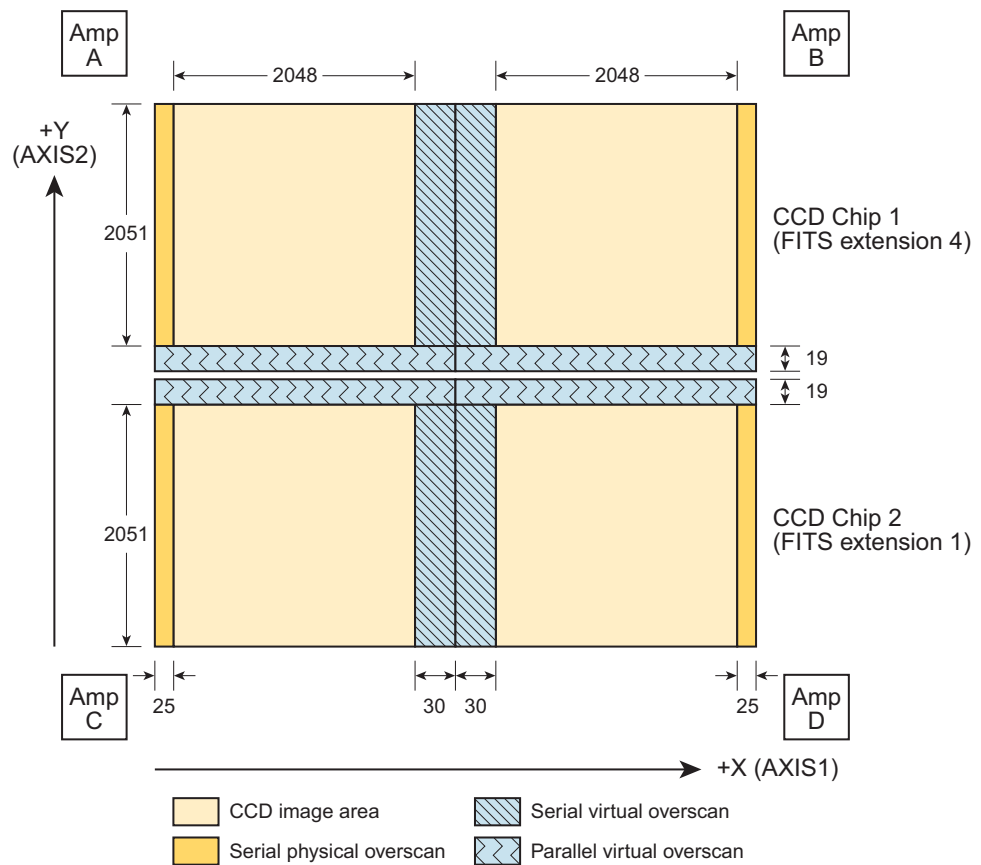
### 3.2.5 Overscan Bias Correction

- Header Switch: BLEVCORR
- Reference File: OSCNTAB

The overscan regions are used to monitor the instrument as well as provide a measure of the bias level at the time the detector was exposed (see [Figure 3.2](#)). BLEVCORR fits the bias level in the CCD overscan regions and subtracts it from the image data. The boundaries of the overscan regions are taken from the OSCNTAB reference file. With these regions defined, the serial and parallel virtual overscans are analyzed to produce a two-dimensional linear fit to the bias level. The overscan level for each row of the input image is measured within the serial virtual overscan region, utilizing sigma-clipping to reject anomalous values (e.g., cosmic-ray hits that occur in

the overscan) and a straight line is fit as a function of image line number. The same procedure is followed for the parallel overscan, resulting in a straight line fit as a function of image column number. The parallel fit is computed in the form of a correction to be added to the serial fit result, in order to remove any gradient that may exist along the x-axis direction of the image. The serial fit and the parallel correction to it are then evaluated at the coordinates of each pixel and the computed bias value is subtracted from the pixel. This is done independently for each region of the image that was read out by one of the four CCD amplifiers. The mean bias value determined for each of the amplifier quadrants is recorded in the primary header keywords `BIASLEV[ABCD]` and the overall mean bias value is computed and written to the output SCI extension header as `MEANBLEV`.

**Figure 3.2: Schematic view of the UVIS “raw” full frame, with overscan regions highlighted. See [section 6.7.2 of the WFC3 Instrument Handbook](#) for further details**



UVIS subarray images do not include virtual overscan, therefore the serial physical overscan will be used - if present - to perform the bias subtraction. If a subarray image does not include the physical overscan region of the detector, then the bias level cannot be determined. In this case a default value (`CCDBIAS` from the CCD parameters table) will be subtracted instead and a warning message is written to the processing trailer file.

The full bias level-subtracted image is retained in memory until the completion of all the processing steps in **wf3ccd**. The overscan regions will not be trimmed until the image is written to disk at the completion of **wf3ccd**.

The **OSCNTAB** reference file (Overscan Region Table) describes the overscan regions for each chip along with the regions to be used for determining the actual bias level of the observation. Each row corresponds to a specific configuration, given by the gain, amplifier used in readout, charge injection, and binning adopted. The **OSCNTAB** columns **BIASSECTAn** and **BIASSECTBn** give the range of image columns to be used for determining the bias level in the leading and trailing regions, respectively, of the serial physical overscan regions, while columns **BIASSECTCn** and **BIASSECTDn** give the range of columns to be used for determining the bias level from the serial virtual overscan regions. The parallel virtual overscan regions are defined in the **OSCNTAB** in the **VXn** and **VYn** columns. To determine which overscan regions were actually used for measuring the bias level, check the **OSCNTAB** reference file. Users may modify the overscan region definitions in the reference table for manual calibration, but the **TRIMXn** and **TRIMYn** values must not be changed.

### 3.2.6 Bias Structure Correction

- Header Switch: **BIASCORR**
- Reference File: **BIASFILE**

This step subtracts the two dimensional bias structure from the image using the superbias reference image listed in the header keyword **BIASFILE**. The dimensions of the image are used to distinguish between full and sub-array images. The **BIASFILE** has the same dimensions as a full-size science image, complete with overscan regions. Only after completion of **wf3ccd** are the science images trimmed to their final calibrated size. The same reference image is used for full-frame and subarray images, **calwf3** will extract the matching region from the full-size bias file and apply it to the subarray image.

### 3.2.7 Sink Pixel Detection and Marking

- Header Switch: **DQICORR**
- Reference File: **SNKCFIL**

Sink pixels are a detector defect. These pixels contain a number of charge traps and under-report the number of electrons that were generated in them during an exposure. These pixels can have an impact on nearby upstream or downstream pixels, though they often only impact one or two pixels when the background is high, they can impact up to 10 pixels if the background is low (see [Section 6.7](#) for more information about sink pixels detection and flagging).

Flagging of sink pixels in the DQ extension of calibrated images, controlled with the **DQICORR** header keyword, happens after the bias correction has been performed.

When set to `PERFORM`, the sink pixels are located and flagged using the `SNKCFIL` reference image. Given the reference image, the procedure for flagging the sink pixel in science data involves:

- Extraction of the MJD of the science exposure
- The reference image is examined, pixel by pixel, to find values greater than 999, pixels indicating a sink pixels. The value of the reference file pixel corresponds to the date (in MJD format) at which this pixel started exhibiting sink pixel behavior.
- If the turn-on date of the sink pixel is *after* the exposure date of the science image, then we ignore the sink pixel in this exposure and move on to the next pixel.
- If the turn-on date of the sink pixel is *before* the exposure date of the science image, then this science pixel was compromised at the time of the exposure. The corresponding pixel in the DQ extension of the science image is flagged with the "charge trap" value of 1024.
- If the pixel "downstream" of the sink pixel, along the readout direction, has a value of -1 in the reference image, then it is also flagged with the "charge trap" value in the DQ extension. We then proceed vertically "upstream" from the sink pixel and compare each pixel in the reference file to the value of the sink pixel in the science exposure at hand. The reference file contains –at the positions of the upstream pixels- estimates of the minimum charge a sink pixel has to contain, in order not to affect the nearby upstream pixel. If the value of the sink pixel in the exposure is below the value of the upstream pixel in the reference image, we flag that upstream pixel with the "charge trap" value in the DQ extension. We continue to flag upstream pixels until the value of the pixel in the reference image is zero or until the value of the sink pixel in the exposure is greater than the value of the upstream pixel in the reference image.

When originally introduced in **calwf3** version 3.3, the correction for sink pixels was only made available for images taken in full-frame mode. From **calwf3** version 3.4 onwards, sink pixels are being flagged in images taken in both full-frame and subarray observing modes.

### 3.2.8 Post-flash Correction

- Header Switch: `FLSHCORR`
- Reference File: `FLSHFILE`

WFC3 has post-flash capability to provide a means of mitigating the effects of Charge Transfer Efficiency (CTE) degradation (see [WFC3 ISR 2013-12](#)). When `FLSHCORR=PERFORM`, this routine subtracts the post-flash reference image, `FLSHFILE`, from the science image. This file has the same dimensions as a full-size

science image complete with overscan regions. `FLSHFILE` has units of electrons per second. The appropriate `FLSHFILE` has matching values of the following keywords from the image header: `DETECTOR`, `CCDAMP`, `CCDGAIN`, `FLASHCUR`, `BINAXISi`, and `SHUTRPOS`.

The success of the post-flash operation during the exposure is first verified by checking the keyword `FLASHSTA` (`ABORTED`, `SUCCESSFUL`, `NOT PERFORMED`). **calwf3** selects the reference file which matches the science image's binning, shutter position (`SHUTRPOS`) and flash current level settings (`LOW`, `MED`, `HIGH`, recorded in the `FLASHCUR` keyword), and scales it by the flash duration (stored in the `FLASHDUR` keyword). This scaled postflash image is then subtracted from the science image. The mean value of the scaled post-flash image is assigned to the `MEANFLSH` keyword in the output SCI extension header. Different members of an association can have different values of `SHUTRPOS` (indicating which shutter blade was used to reflect the postflash lamp's light into the optical path and illuminate the detector. The blade can vary by exposure). This does not constitute a problem for calibration because the reference files are populated separately for each exposure.

### 3.2.9 Dark Current Subtraction

- Header Switch: `DARKCORR`
- Reference File: `DARKFILE`, `DRKCFILE`

The dark current subtraction step subtracts the estimate of the dark current from the science image. The reference file listed under the `DARKFILE` header keyword is used in the non-CTE corrected UVIS pipeline branch, `DRKCFILE` is instead used in the CTE-corrected branch. The dark image (in units of electrons/sec) is multiplied by the exposure time, and subtracted from the input image. The mean dark value is computed from the scaled dark image and used to update the `MEANDARK` keyword in the SCI image header. The dark reference file is updated frequently to allow the tracking of hot pixels over time. The time by which the dark reference file gets multiplied is simply the exposure time in the science image; it does not include the idle time since the last flushing of the chip or the readout time. Any dark accumulation during readout time is included automatically in the `BIASFILE`.

The reference file for dark subtraction, `DARKFILE` (`DRKCFILE`), is selected based on the values of the keywords `DETECTOR`, `CCDAMP`, `CHINJECT` and `BINAXISi` in the image header. The dark correction is applied after the overscan regions are trimmed from the input science image. In a similar fashion to the `BIASCORR` step, **calwf3** requires the binning factors of the `DARKFILE` (`DRKCFILE`) and science image to match. Sub-array science images use the same reference file as a full-sized `DARKFILE` (`DRKCFILE`), **calwf3** simply extracts the appropriate region from the reference file and applies it to the sub-array input image.

### 3.2.10 Flat-field Correction

- Header Switch: `FLATCORR`
- Reference Files: `PFLTFILE`, `LFLTFILE`, `DFLTFILE`

This routine corrects for pixel-to-pixel and large-scale sensitivity variations across the detector by dividing the overscan-trimmed and dark-subtracted science image by a flat-field image.

Because of geometric distortion effects, the area of the sky seen by different pixels is not constant and therefore observations of a constant surface brightness object will have counts per pixel that vary over the detector, even if every pixel were to have the same intrinsic sensitivity. In order to produce images that appear uniform for uniform illumination, the same counts per pixel variation across the field is left in place in the flat-field images, so that when a science image is divided by the flat it makes an implicit correction for the distortion effects on photometry. A consequence of this procedure is that two point-source objects of equal brightness will not have the same total counts after the flat-fielding step.




---

*Thus, point source photometry extracted from a flat-fielded image must be multiplied by the effective pixel area map.*

---

This correction is automatically included in pipeline processing by **Astrodrizzle**, which uses the geometric distortion solution to correct all pixels to equal areas. Photometry is therefore correct for both point and extended sources in drizzled (`drz`, `drc`) images, but incorrect for point sources for `flt` or `flc` images.

Up to three separate flat-field reference files can be used: the pixel-to-pixel flat-field file (`PFLTFILE`), the low-order flat-field file (`LFLTFILE`), and the delta flat-field file (`DFLTFILE`). The `PFLTFILE` is a pixel-to-pixel flat-field correction file containing the small-scale flat-field variations. Unlike the other flat fields, the `PFLTFILE` is always used in the calibration pipeline. The `LFLTFILE` is a low-order flat that corrects for any large-scale sensitivity variations across each detector. This file can be stored as a binned image, which is then expanded when being applied by **calwf3**. Finally, the `DFLTFILE` is a delta-flat containing any needed changes to the small-scale `PFLTFILE`. If the `LFLTFILE` and `DFLTFILE` are not specified in the SCI header, only the `PFLTFILE` is used for the flat-field correction. If two or more reference files are specified, they are multiplied together to form a combined flat-field correction image. Currently the standard **calwf3** image processing uses a single flat field image, indicated by the `PFLTFILE` keyword. This image, however, does not only contain pixel-to-pixel variations but includes low order polynomial corrections as well. All flat-field reference images must have detector, amplifier, filter, and binning modes that match the observation. A sub-array science image uses the same reference file as a full-size image; **calwf3** extracts the appropriate region from the reference file and applies it to the sub-array input image.

### 3.2.11 Shutter Shading Correction

- Header Switch: SHADCORR
- Reference Files: SHADFILE

This step corrects the science image for differential exposure time across the detector caused by the amount of time it takes for the shutter to completely open and close, which is a potentially significant effect only for images with very short exposure times (less than ~5 seconds). Pixels are corrected based on the exposure time using the relation:

$$\text{corrected} = \text{uncorrected} \times \text{EXPTIME} \div (\text{EXPTIME} + \text{SHADFILE})$$

WFC3 tests have shown that the shutter shading effect is insignificant (< 1%), even for the shortest allowed UVIS exposure time of 0.5 seconds (see [WFC3 ISR 2007-17](#)). Therefore this step is set to OMIT in **calwf3** default settings.

### 3.2.12 Photometry Keywords Calculation

- Header Switch: PHOTCORR
- Reference Files: IMPHTTAB

In order to extract calibrated magnitudes (or equivalently fluxes), directly from **wfc3** images, a transformation to absolute flux units is necessary. Users that do not wish to use this feature should set the header keyword PHOTCORR to OMIT. However, users that intend to use the FLUXCORR step (see [Section 3.2.13](#)), must also set PHOTCORR to PERFORM as well.

The PHOTCORR step is performed using tables of precomputed values instead of calling SYNPHOT, to compute keyword values on-the-fly, as was done prior to November 2013. **Calwf3** version 3.1.6 and greater uses an Image Photometry reference table specified via the IMPHTTAB header keyword, where each WFC3 detector (IR or UVIS) uses a different reference file. During this process the PHOTMODE keyword string is built to reflect the configuration of the instrument for the exposure (e.g., 'WFC3, UVIS1, F814W'). **Calwf3** then uses the PHOTMODE to retrieve the keyword values from the appropriate row in the reference table and update the science data headers with the keywords listed below.

Each DETECTOR uses a different table.

- PHOTFNU: the inverse sensitivity in units of:  $\text{math: Jansky sec electron}^{-1}$
- PHOTFLAM: the inverse sensitivity in units of  $\text{ergs cm}^{-2} \text{A}^{-1} \text{electron}^{-1}$
- PHOTPLAM: the bandpass pivot wavelength in Å
- PHOTBW: the bandpass RMS width in Å
- PHTFLAM1: the inverse sensitivity in units of  $\text{ergs cm}^{-2} \text{A}^{-1} \text{electron}^{-1}$  for infinite aperture (chip1)



- PHTFLAM2: the inverse sensitivity in units of  $\text{ergs cm}^{-2} \text{A}^{-1} \text{electron}^{-1}$  for infinite aperture (chip2)

For **calwf3** version 3.3 and beyond, the value PHOTFNU is calculated for each UVIS chip (see also [Section 3.2.13](#)). The SCI headers for each chip contain the PHOTFNU keyword, which is valid for its respective chip, and is calculated as:

For UVIS 1:

$$\text{photfnu} = 3.33564e^4 * \text{PHTFLAM1} * \text{PHOTPLAM}^2$$

For UVIS 2:

$$\text{photfnu} = 3.33564e^4 * \text{PHTFLAM2} * \text{PHOTPLAM}^2$$

The IMPHTTAB file format for WFC3 UVIS is as follows:

EXT#	FITSNAME	FILENAME	EXTVE	DIMENS	BITPI	OBJECT
0	z7n21066i_imp	z7n21066i_imp.fits			16	
1	BINTABLE	PHOTFLAM	1	5F×256R		
2	BINTABLE	PHOTPLAM	1	5F×256R		
3	BINTABLE	PHOTBW	1	5F×256R		
4	BINTABLE	PHTFLAM1	1	5F×256R		
5	BINTABLE	PHTFLAM2	1	5F×256R		

where each extension contains the photometry keyword information for that specific header keyword. The rows inside the tables are split on observation mode.

### 3.2.13 Flux normalization for UVIS1 and UVIS2

- Header Switch: FLUXCORR
- Reference Files: None

The FLUXCORR step was implemented in **calwf3** v3.3 on February 23, 2016 as part of the new UVIS chip-dependent photometric calibration ([WFC3 ISR 2016-01](#)). This step multiplies the UVIS2 image (SCI, 1 in the data file) by the ratio of inverse sensitivities PHTFLAM2/PHTFLAM1 so that the same flux correction can be used for both chips. This ratio is stored for reference in the image header keyword PHTRATIO. FLUXCORR is set to PERFORM by default during **calwf3** processing, and in this case the keyword PHOTFLAM will be valid for both chips after the correction is applied. If users do not wish to perform the correction, the FLUXCORR keyword may be set to OMIT and the raw data reprocessed through **calwf3**. In this case, the keywords PHTFLAM1 and PHTFLAM2 may be used to convert to flux units in the respective chips.

Chip-dependent flat fields (from 2016 or later) must be used with **calwf3** v3.3 onwards and should not be used with older versions of the pipeline, and vice versa, otherwise the data will be scaled incorrectly.




---

*Note: In order for **FLUXCORR** to work properly, the value of **PHOTCORR** must also be set to **PERFORM** since this populates the header of the data with the keywords **FLUXCORR** requires to compute the **PHTRATIO**.*

---

### 3.2.14 Cosmic-ray Rejection

- Header Switch: **CRCORR**
- Reference Files: **CCREJTAB**

Associations with more than one member, which have been associated using either **CR-SPLIT** or **REPEAT-OBS**, will be combined using **wf3rej** (see [Section 3.4.5](#) for more details). The task uses the same statistical detection algorithm developed for ACS (**acsrej**), STIS (**ocrrj**) and WFPC2(**crrej**), providing a well-tested and robust procedure. For all associations (including dithered observations), the DRZ and DRC products will be created by **Astrodrizzle**, which performs both cosmic ray detection (in addition to **wf3rej**, for **CR-SPLIT** or **REPEAT-OBS** observations) and corrects for geometric distortion.

### 3.2.15 UVIS Image Statistics Calculation

- Header Switch: **None**
- Reference File: **None**

This routine computes several statistics for data values that are flagged as ‘good’ in the data quality array. These quantities are updated in the SCI image header: the minimum (**GOODMIN**), mean (**GOODMEAN**), and maximum (**GOODMAX**) values, as well as the minimum (**SNRMIN**), mean (**SNRMEAN**), and maximum (**SNRMAX**) signal-to-noise ratio (the ratio of the SCI and ERR pixel values). The number of good pixel is recorded in **NGOODPIX**. The minimum, mean, and maximum statistics are also computed for the ERR array.

### 3.3 IR Data Calibration Steps

The IR data reduction process begins with the raw IR image file. This contains all the non-destructive readouts from an exposure, stored in reverse time order - where the first extension corresponds to the last array read. Most of the calibration steps are applied independently to each readout. For example, the `DQICORR`, `NLINCORR`, and `FLATCORR` steps apply the same bad pixel flags, non-linearity correction coefficients, and flat-field image, respectively, to each readout. On the other hand, the `CRCORR` step, which performs the up-the-ramp fit and removes the effects of cosmic rays hits, utilizes the values from all readouts of individual pixel simultaneously. Detailed descriptions of each step are provided in the following sections.

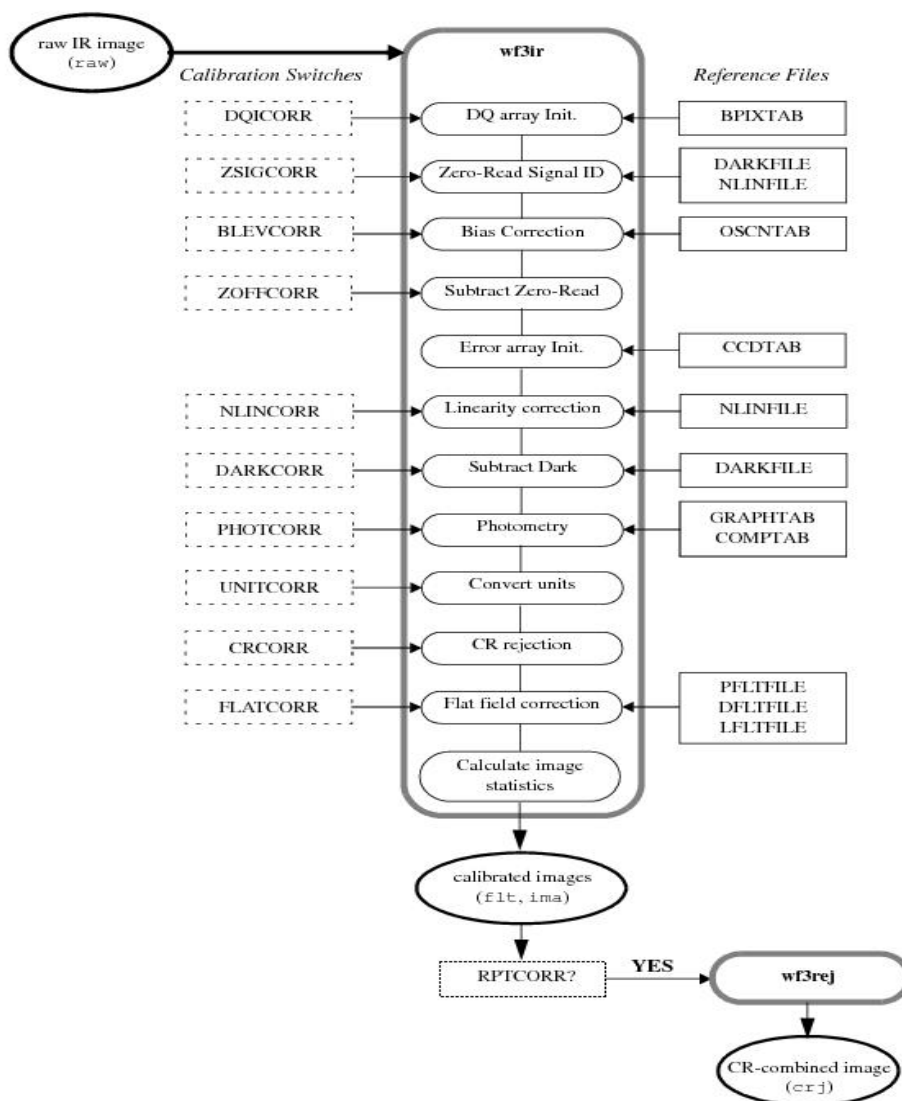
All steps up through `UNITCORR` are applied to an in-memory image stack that contains all the readouts. The `CRCORR` step produces an additional single image that gives the best-fit count rate for each pixel. The remaining steps in the process - `FLATCORR` and image statistics - are then applied to the full stack of readouts and to the single image produced by `CRCORR`.

Upon completion of the IR data calibration process, two output files are produced. The Intermediate MultiAccum (`ima`) file, which contains the full stack of calibrated readouts, and the final calibrated image (`flt`) file, which is the single image produced by `CRCORR` with subsequent flat fielding applied.

Figure 3.3 shows a schematic representation of all the IR calibration steps, which are also briefly summarized below, in the order they are performed, with the corresponding calibration switch keyword in parenthesis:

- Initialize data quality, DQ, array (`DQICORR`)
- Estimate amount of signal in zeroth-read (`ZSIGCOR`)
- Subtract bias level from reference pixels (`BLEVCORR`)
- Subtract zeroth read image (`ZOFFCORR`)
- Initialize error array, ERR (`NOISCORR`)
- Correct for detector non-linear response (`NLINCORR`)
- Subtract dark current image (`DARKCORR`)
- Compute photometric keyword values for header (`PHOTCORR`)
- Convert to units of count rate (`UNITCORR`)
- Fit accumulating signal and identify CR hits (`CRCORR`)
- Divide by flat-field image(s) and apply gain conversion (`FLATCORR`)
- Compute image statistics (No switch)

**Figure 3.3: Flow diagram for IR processing; each step, as well as the calibration switches that control each step are indicated.**



### 3.3.1 Data Quality Initialization

- Header Switch: DQICORR
- Reference File: BPIXTAB

This step populates the data quality (DQ) array in all IR readouts by reading a table of known bad pixels for the detector, stored in the 'Bad Pixel' reference table BPIXTAB; the correct BPIXTAB is selected based on the value of the DETECTOR keyword and USEAFTER.

The types of bad pixels that can be flagged are listed in [Table 3.3](#).

The DQ array is no longer updated to reflect any Take Data Flag (TDF) transition during the sample (see this issue of the [STAN](#)). Other DQ values will only be marked during further processing (such as cosmic-ray rejection).

If the users wish to update the DQ array themselves before running further processing, they should first complete the DQ initialization step, and remember that the data in the DQ extension is always in units of `UNSIGNED_INTEGER`.

**Table 3.3: Data quality array flags for IR files**

NAME	VALUE	DESCRIPTION
GOODPIXEL	0	OK
SOFTERR	1	Reed-Solomon decoding error
DATALOST	2	data replaced by fill value
DETECTORPROB	4	bad detector pixel
BADZERO	8	unstable IR zero-read pixel
HOTPIX	16	hot pixel
UNSTABLE	32	IR unstable pixel
WARMPIX	64	unused
BADBIAS	128	bad reference pixel value
SATPIXEL	256	full-well or a-to-d saturated pixel
BADFLAT	512	bad flat-field value
SPIKE	1024	CR spike detected during ramp fitting
ZEROSIG	2048	IR zero-read signal correction
TBD	4096	cosmic ray detected by Astrodrizzle
DATAREJECT	8192	rejected during up-the-ramp fitting
HIGH_CURVATURE	16384	not used
RESERVED2	32768	can't use

### 3.3.2 IR Zero-Read Signal Correction

- Header Switch: `ZSIGCORR`
- Reference Files: `DARKFILE`, `NLINFILE`

At the beginning of an IR observation the detector pixels are reset and then read out to record the bias level. An interval of approximately 2.9 seconds elapses between the time each pixel is reset and then read. Because the IR channel does not have a shutter, signal from the field of view under observation, as well as persistent signal

from previous observations, accumulates during that 2.9 second interval. When the initial (or ‘zeroth’) read is later subtracted from subsequent readouts, any signal in the zeroth read will also be subtracted. Because linearity correction and saturation checking, performed in the `NLINCORR` step described in [Section 3.3.13](#), both depend on the absolute signal level in a pixel at the time it was read, the signal in the zeroth read from bright sources can be large enough that, if neglected in the `NLINCORR` calibration step, it can lead to inaccurate linearity corrections, as well as the failure to detect saturation conditions. The `ZSIGCORR` step is used to estimate the amount of source signal in the zeroth read and to supply this estimate to the `NLINCORR` step.

Such an estimate is given by the difference between the super zero read in the linearity reference file (`NLINFILE`) and the science zero read exposure. The `ZSIGCORR` step is executed roughly as follows:

- copy the zero signal image from the linearity reference file (super zero).
- compute any subarray offsets.
- subtract the super zero read reference image from the zero read science image.
- compute the noise in the zero image.
- pixels which contain more signal than `ZTHRESH*noise` are flagged (flag value = 2048) and the estimated zeroth read signal is passed to the `NLINCORR` step, which accounts for that signal when applying linearity corrections and saturation checking on the zeroth-read subtracted images. Pixels with signal below `ZTHRESH*noise` are ignored.
- The `NLINCOR` file has an extension with saturation values for each pixel which is referenced here. Pixels which are saturated in the zeroth or first reads are flagged in the DQ and the number of found saturated pixels are reported.

The `ZSIGCORR` step estimates the source signal in the science zero read by subtracting the super zero read from the science zero read instead of calculating an estimated signal based on the first read and zero read + estimated exposure time between them (this was the case prior to Mar-2011). This way the difference in readout time for subarrays is not an issue, and also dark current subtraction is no longer necessary for the signal estimate (the `DARKFILE` is no longer used by this step).

Note that this technique will not work well for pixels covered by targets that are so bright that the signal is already beginning to saturate in either the zeroth or first readouts, because then it is difficult to accurately estimate the zeroth-read signal. `ZSIGCORR` therefore checks for saturation in the zeroth and first read images and flags the saturated pixels with a 256 flag in the DQ extension of corresponding `ima` imset (0-th or 1-st).

Pixels that are determined to have detectable signal in the zeroth read are flagged in the DQ arrays of the first imset of the output `ima` file with a data quality value of 2048; in this case this flag appears also in the final `flt` file. The `NLINFILE` is chosen based on the values of the `DETECTOR` and `USEAFTER` keywords, while the `DARKFILES` are selected based on the values of the `DETECTOR`, `CCDAMP`, `CCDGAIN`, `SAMP_SEQ`, `SUBTYPE` and `USEAFTER` keywords.

### 3.3.3 Bias Correction

- Header Switch: BLEVCORR
- Reference Files: OSCNTAB

The BLEVCORR step uses the reference pixels located around the perimeter of the IR detector to track and remove changes in the bias level that occur during an exposure. For each raw readout, the average signal level of the reference pixels is computed, subtracted from the image, and recorded in the MEANBLEV keyword in the SCI header (a resistant mean algorithm is used to compute such average).

The reference pixels located at the ends of each image row are used in this computation. Reference pixels are also located along the bottom and top of the detector, but have been found to be less reliable and are not used. There are 5 reference pixels at either end of each row, but the outermost one is ignored on each side, for a total of 8 being used per row.

As with the UVIS overscan correction, the boundaries of the reference pixel regions that are used in the computation are defined in the OSCNTAB reference table, in the BIASSECT\* columns. The BIASSECTA[1, 2] values indicate the starting and ending column numbers for the reference pixels on the left edge of the image, and the BIASSECTB[1, 2] give the values for the right side of the image.

The reference pixel regions are maintained throughout the remainder of processing, but are usually ignored or skipped over in the actual application of calibration algorithms. They are left in place in the calibrated data stored in the ima file at the end of processing, but are trimmed from the flt image file.

The reference file for bias level correction, OSCNTAB, is selected based on the value of the DETECTOR keyword only.

### 3.3.4 IR Zero-read Image Subtraction

- Header Switch: ZOFFCORR
- Reference Files: None

The ZOFFCORR step subtracts the zeroth read from all readouts in the exposure, including the zeroth read itself, resulting in a zero-read image that is exactly zero in the remainder of processing. The zeroth-read image is propagated through the remaining processing steps and included in the output products, so that a complete history of error estimates and data quality (DQ) flags is preserved.




---

*Note: In interpreting the IR Intermediate MultiAccum (ima) file, it is important to remember the file does not represent differences in adjacent reads, but always the difference between a given readout and the zero read. The signal rate recorded in each SCI extension of the ima file represents the average flux between that particular readout and the zero read.*

---

### 3.3.5 Error Array Initialization

- Header Switch: NOISCORR (not listed explicitly in image header, see text)
- Reference Files: CCDTAB

This step computes an estimate of the errors associated with the raw science data based on a noise model for the detector. The NOISCORR keyword is not user-accessible and always set to PERFORM. Currently the noise model is a simple combination of detector read noise (RN) and Poisson noise in the signal, such that:

$$\sigma_{IR} = \frac{\sqrt{RN^2 + counts * gain}}{gain}$$

where the read noise is in units of electrons, gain is the analog-to-digital conversion gain factor (in electrons DN<sup>-1</sup>) and counts is the signal in a science image pixel in units of DN. The detector read noise and gain are read from the CCDTAB reference file and use separate values for the particular amplifier quadrant with which each pixel is associated.

Throughout the remaining calibration steps the ERR image is processed in lock-step with the science (SCI) image, getting updated as appropriate. Errors are propagated through combination in quadrature. The ERR array for the final calibrated flt image is populated by the CRCORR step, based on the calculated uncertainty of the count rate fit to the MultiAccum samples (see [Section 3.3.13](#) for details).

The CCDTAB reference file used in this step is selected based on the value of the DETECTOR keyword only.

### 3.3.6 Detector Non-linearity Correction

- Header Switch: NLINCORR
- Reference Files: NLINFILE

In this step, the integrated counts in the science images are corrected for the non-linear response of the detectors, flagging pixels that undergo saturation (as



defined in the saturation extension of the `NLINFIL` reference image.) The observed response of the detector can be represented by two regimes:

- At low and intermediate signal levels the detector response deviates from the incident flux in a way that is correctable using the following expression

$$F_c = (1 + c_1 + c_2 \times F + c_3 \times F^2 + c_4 \times F^3) \times F$$

where  $c_1$ ,  $c_2$ ,  $c_3$ , and  $c_4$  are the correction coefficients,  $F$  is the uncorrected flux in DN and  $F_c$  is the corrected flux. The current form of the correction uses a third-order polynomial, but the algorithm can handle an arbitrary number of coefficients. The number of coefficients and error terms are given by the values of the `NCOEFF` and `NERR` keywords in the header of the `NLINFIL`.

- At high signal levels, as saturation sets in, the response becomes highly non-linear and is not correctable to a scientifically useful degree.

The signal in the zero read is temporarily added back to the zeroth read image of the science data before the linearity correction is applied and before the saturation is judged. Once the correction has been applied the signal is once again removed. This only occurs if the `ZSIGCORR` step is set to `PERFORM`. Saturation values for each pixel are stored in the `NODE` extension of the `NLINFIL`. After each group is corrected, the routine also sets saturation flags in the next group for those pixels that are flagged as saturated in the current group. This is necessary because the SCI image value of saturated pixels will sometimes start to go back down in the subsequent reads after saturation occurs, which means they could go unflagged by normal checking techniques. The `SAMP` and `TIME` arrays are not modified during this step. The `NLINFIL` reference file is selected based on the value of the `DETECTOR` keyword only.

### 3.3.7 Dark Current Subtraction

- Header Switch: `DARKCORR`
- Reference Files: `DARKFILE`

The `DARKCORR` step subtracts the detector dark current from the science data. The reference file listed under the `DARKFILE` header keyword is used to subtract the dark current from each sample. The `DARKFILE` reference file must have the same values for the `DETECTOR`, `CCDAMP`, `CCDGAIN`, `SAMP_SEQ`, and `SUBTYPE` keywords as the science image. Due to potential non-linearities in some of the signal components, such as reset-related effects in the first one or two reads of an exposure, the dark current subtraction is not applied by simply scaling a generic reference dark image by the exposure time and then subtracting it. Instead, a library of dark current images is maintained that includes darks taken in each of the available predefined `MULTIACCUM` sample sequences, as well as the available sub-array readout modes. The dark reference file is subtracted read-by-read from the stack of science image readouts so that there is an exact match in the timings and other characteristics of the dark image and the science image. The subtraction does not include the reference

pixels. The `ERR` and `DQ` arrays from the reference dark file are combined with the `SCI` and `DQ` arrays from the science image, but the `SAMP` and `TIME` arrays are unchanged. The mean of the dark image is saved to the `MEANDARK` keyword in the output science image header.

### 3.3.8 Photometry Keywords

- Header Switch: `PHOTCORR`
- Reference Files: `IMPHTTAB`

The `PHOTCORR` step updates the image header with keywords that allow the user to convert their data from counts rates to absolute fluxes, and perform calibrated photometry. The step is performed using tables of precomputed values stored in the `IMPHTTAB` file. The appropriate entry in `IMPHTTAB` is selected according to the observing mode, whose value stored the image header keyword `PHOTMODE`. The updated keywords are:

- `PHOTFLAM`: the inverse sensitivity in units of  $\text{erg cm}^{-2} \text{A}^{-1} \text{electron}^{-1}$
- `PHOTFNU`: the inverse sensitivity in units of  $\text{Jy sec}^{-1} \text{electron}^{-1}$
- `PHOTZPT`: the `STMAG` zero point
- `PHOTPLAM`: the bandpass pivot wavelength in  $\text{\AA}$
- `PHOTBW`: the bandpass RMS width in  $\text{\AA}$

### 3.3.9 Conversion To Signal Rate

- Header Switch: `UNITCORR`
- Reference Files: `None`

This step converts the science data from a time-integrated signal to a signal rate by dividing the `SCI` and `ERR` arrays for reach readout by the `TIME` array. No reference file is needed. The `BUNIT` keyword in the output data header reflects the appropriate data units. This step is skipped if the `BUNIT` value is already `COUNTS/S`. The flat fielding process (performed if `FLATCORR` is set to `PERFORM`), further changes the `BUNIT` by multiplying the image by the gain, therefore the final `BUNIT` value depends on the value of both `UNITCORR` and `FLATCORR`, as illustrated in [Table 3.4](#).

**Table 3.4: Possible values of BUNIT after calibrating IR data with calwf3.**

UNITCORR	FLATCORR	BUNIT AFTER CALIBRATION
OMIT	OMIT	COUNTS
OMIT	COMPLETE	ELECTRONS
COMPLETE	OMIT	COUNTS/S
COMPLETE	COMPLETE	ELECTRONS/S

### 3.3.10 Up-the-ramp Fitting and Cosmic Ray Identification

- Header Switch: CRCORR
- Reference Files: CCREJTAB

CRCORR combines the data from all readouts into a single image and, in the process, identifies and flags pixels suspected of containing cosmic-ray (CR) hits. The method is extensively described in [Fixsen et al. \(2000\)](#).

The data from all readouts are analyzed pixel-by-pixel, iteratively computing a linear fit to the accumulating counts-versus-exposure time relation. Samples flagged as bad in the DQ arrays, such as when saturation occurs midway through the exposure, are rejected from the fitting process. CR hits are identified by searching for outliers from the fit results. The rejection threshold is set by the value in the CRSIGMAS column of the Cosmic-Ray Rejection parameters reference table CCREJTAB, and has a default value of 4. When a CR hit is detected, a linear fit is then performed independently for the sets of readouts before and after the hit; if a CR hit is identified to have occurred during a sample, the value measured for that sample is included in the ‘after’ ramp segment. Those fitting results are then again checked for outliers. This process is iterated until no new CR are detected.

Pixel samples identified as containing a CR hit are flagged in the DQ arrays of the intermediate MultiAccum (ima) file, with DATAREJECT DQ value of 8192.

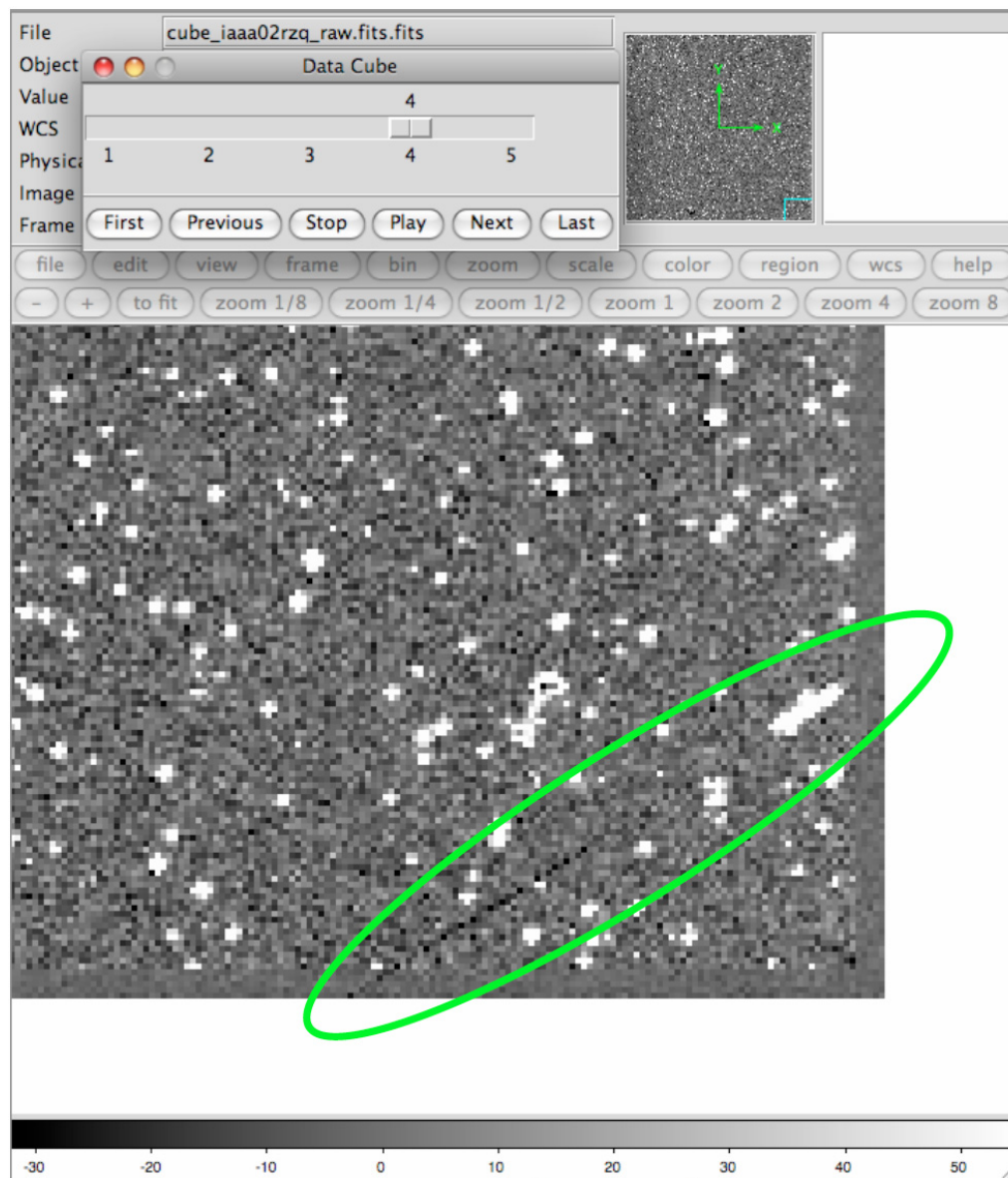
The DATAREJECT DQ flag is also set for all samples following the hit. Therefore, users looking at the ima file are made aware that the absolute value of the pixel is wrong after the first hit. However, this flagging smears the location of any hits possibly occurring after the first one.

Negative SPIKES in the accumulated counts vs. time relation have been observed in WFC3 data. They appear as sudden “drops” in the accumulated counts vs. time plots for individual pixels. (see e.g. Figure 1 in [WFC3 ISR 2010-13](#)).

These “negative CR hits” are also identified in the CRCORR step, and flagged with the SPIKE DQ flag, value = 1024. Appendix B of [WFC3 ISR 2009-40](#) gives a possible explanation for a sub-class of such events: they are normal cosmic rays that traverse the detector but instead of hitting the photo-sensitive HgCdTe pixel bulk, they hit other parts of the pixel (e.g. the electronics) that are sensitive to the charged particles. These events are clearly identified as CRs as a physical trail is visible in the raw images, a trail that goes from negative (when the CR goes through the electronics) to undetectable (where they go through layers that are not affected by the CR) to positive (when they release charge in the active HgCdTe region of the pixel), see

Figure 3.4. Other negative spikes are sometimes observed in isolated pixels and are attributed to “burst noise” (also called popcorn noise or random telegraph signal).

**Figure 3.4: A negative cosmic ray trail associated with a positive one in a single read of a raw image.**



The CR and SPIKES DQ flags are only present in the ima file and do not get carried over into flt products which combine data from all readouts.

Once all outliers have been identified, the slopes of each segment of non-flagged samples are computed via a linear fit to the counts vs. time data. This fit includes optimal weighting, with individual data points uncertainties including contributions from the read noise and the Poisson noise for the source and the dark current. The linear fit reports the best fitting slope and its uncertainty. The final count rate value for

a pixel (and its uncertainty) is determined by computing the weighted mean (and its uncertainty) of the individual samples slopes. The result of this operation is stored in the output flt file, where the SCI array contains the final slope computed for each pixel, the ERR array contains the estimated uncertainty in the slope, the SAMP array contains the total number of non-flagged samples used to compute the slope, and the TIME array contains the total exposure time of those samples.

Pixels for which there are no unflagged samples, e.g., permanently hot or cold pixels, still get a slope computed, which is recorded in the SCI array of the output flt file, but they will also have their DQ flags recorded in the DQ array of the flt file. Users should therefore be careful to always check the flt file DQ arrays to help determine whether a given SCI image value is trustworthy for subsequent analysis.

The basic rule of thumb is that in order for a DQ value to propagate into the *flt*, it needs to be present in all the reads of the *ima*. The 8192 flag does not get propagated because it shows where during the ramp the cosmic ray appeared. Nominally, when looking at the flt file, **calwf3** has already accounted for the effects of the cosmic ray. If a user really needs the information about those cosmic rays, the *ima* files are available and contain the complete record of when and where exactly each cosmic ray hit the detector.

A similar propagation scheme occurs for the saturation flag (DQ = 256). If, e.g., a pixel is saturated in the last two reads of a ramp, then those two reads are flagged with 256 in the *ima* file, and **calwf3** ignores them during line-fitting. The DQ value put into the flt file is 0 because **calwf3** has already dealt with the saturation and the effects are not in the flt. If saturation occurs in the first read of a ramp, the SCI extension of the flt file for that pixel contains an estimate of the flux equal to the value in the input zeroth read image, but the DQ extension of the flt does not get a 256 value added to it. If the zeroth read is also saturated, the flt file still contains the same flux estimate as in the first-read saturation case, but in this case the DQ flag 256 gets carried over to the output flt DQ extension.

For pixels where **calwf3** finds 4 or more CRs up the ramp, it flags the pixel with the UNSTABLE flag value = 32, which does propagate to the flt. In that case, the thinking is that four large signal jumps for a given pixel in a single ramp are a warning sign about the behavior of that pixel, and its measurements should not be trusted. DQ values from any sample are carried through to the flt file if a pixel has no good samples.

**Note:** *With the release of calwf3v3.3, the standard HST Data Processing changed the way IR SCAN data is processed: the value of CRCORR is set to OMIT. calwf3 performs up-the-ramp fitting during the CRCORR step, which for scan data does not produce a useful result. Setting CRCORR=OMIT stops the ramp fit from happening and instead produces an flt output image which contains the first-minus-last read result. Note that since the SCAN flt output image is not a fit up-the-ramp, the output image units will not be a rate but instead be in counts (if UNITCORR=OMIT) or electrons (if FLATCORR=COMPLETE).*

### 3.3.11 Flat-field Correction

- Header Switch: FLATCORR
- Reference Files: PFLTFIELD, LFLTFIELD, DFLTFIELD

The FLATCORR step corrects for pixel-to-pixel and large-scale sensitivity variations across the detector by dividing the science images by one or more flat-field images. A combined flat is created within **calwf3** using up to three flat-field reference files: the pixel-to-pixel flat (c), the low-order flat (LFLTFIELD), and the delta flat (DFLTFIELD). FLATCORR also multiplies the science data by the detector gain, using the mean gain from all the amplifiers. Therefore the calibrated data will be in units of electrons per second (or electrons if UNITCORR = OMIT).

The PFLTFIELD is a pixel-to-pixel flat-field correction file containing the small-scale flat-field variations. The PFLTFIELD is always used in the calibration pipeline, while the other two flats are optional. The LFLTFIELD is a low-order flat that corrects for any large-scale sensitivity variations across the detector. This file can be stored as a binned image, which is then expanded when being applied by **calwf3**. Finally, the DFLTFIELD is a delta-flat containing any needed changes to the small-scale PFLTFIELD. If the LFLTFIELD and DFLTFIELD are not specified in the SCI header, only the PFLTFIELD is used for the flat-field correction. If two or more reference files are specified, they are read in and multiplied together to form a combined flat-field correction image.

The flat-field correction is applied to all readouts of the calibrated IR MultiAccum stack, as well as the single image produced by the CRCORR function.

All flat-field reference images are selected based on the DETECTOR, CCDAMP, and FILTER used for the observation. A sub-array science image uses the same reference file(s) as a full-size image; **calwf3** extracts the appropriate region from the reference file(s) and applies it to the sub-array input image.

**Note:** *All WFC3 observations, not just dithered images, are processed with Astrodrizzle to correct for geometric distortion and pixel area effects. Alternatively, the Pixel Area Map file needs to be used to extract correct point-source photometry directly from flt files. See Section 3.2.10 on UVIS Flat-Field Correction for a discussion of distortion effects on photometry.*

### 3.3.12 Image Statistics Calculation

- Header Switch: None
- Reference Files: None

This step computes several useful image statistics using the “good pixels”, i.e. those with DQ value equal to 0, and updates several keywords in the image header. This operation is performed for every readout in the calibrated MultiAccum stack, as well as the final (CRCORR-produced) calibrated image. The updated keywords are: the minimum, mean, and maximum values (GOODMIN, GOODMEAN, GOODMAX, respectively), as well as the minimum, mean, and maximum signal-to-noise ratio (the ratio of the SCI and ERR pixel values) which are SNRMIN, SNRMEAN, SNRMAX, respectively. The number of good pixels, NGOODPIX, is also recorded. All these

quantities are updated in the SCI image headers. The minimum, mean, and maximum statistics are also computed for the ERR arrays.

### 3.3.13 Cosmic-ray rejection

- Header Switch: RPTCORR
- Reference Files: CCREJTAB

Associations with more than one member, which have been associated using REPEAT-OBS, are combined using **wf3rej** (see [Section 3.4.5](#) for more details). CR-SPLIT is not used for the IR channel. The task uses the same statistical detection algorithm developed for ACS (**acsrej**), STIS (**ocrrj**) and WFPC2(**crrej**), providing a well-tested and robust procedure. For all associations (including dithered observations), the DRZ products will be created by **Astrodrizzle**, which performs both cosmic ray detection (in addition to **wf3rej**, for REPEAT-OBS observations) and corrects for geometric distortion.

---

## 3.4 Pipeline Tasks

The following section contains information regarding the 5 high-level tasks that are called by the main program **calwf3**, namely **wf3cte**, **wf3ccd**, **wf32d**, **wf3ir**, **wf3rej**. These tasks can be called individually by the users from either the command line or within a python interpreter. They generally are “umbrella” tasks that can perform multiple data processing steps. However the user can control the processing flow (and limit it to individual steps) by properly setting the header keyword switches, as detailed in [Sections 3.2](#) (UVIS) and [3.3](#) (IR).

### 3.4.1 wf3cte

This routine is used to correct for Charge Transfer Efficiency (CTE) losses that cause electrons that are generated on the UVIS channel to be trapped by detector defects during readout. More details on the CTE phenomenon are given in [Chapter 6](#), see also the [WFC3 CTE webpage](#).

The PCTETAB reference file contains extensions of calibration images and tables of parameters used during the CTE correction stage. The header of this file also contains parameters for the CTE correction algorithm. These parameters, as well as others defaults used by **wf3cte** to correct the data are stored in the output image headers. Users who wish to use other settings for the CTE correction algorithm can adjust the pertinent keywords in their dataset header and **calwf3** will give them preference, see [WFC ISR 2016-02](#) for more information.

**wf3cte** performs the CTE correction on raw data files. If the calibration step keyword `PCTECORR` is set to `PERFORM` then the CTE correction will be applied to the dataset. Some caveats for its use:

- CTE corrections can *ONLY* be performed on raw data which has not been calibrated in any way.
- Data which have `BLEVCORR`, `BIASCORR` or `DARKCORR` set to `COMPLETE` will be rejected.
- The CTE correction step is implemented only for `FULL FRAME` images in **calwf3** v3.3, but v3.4 also corrects for CTE for the subarray apertures indicated in [Table 3.5](#) (the **calwf3** version used to process any data is stored in the header keyword "CAL\_VER"). The primary distinction is that these apertures have physical overscan pixels included which are used to calculate a secondary bias subtraction for the image before the CTE is measured; a future version of **calwf3** may enable CTE corrections for the remaining subarrays which don't have physical overscan pixels, but is still being validated by the WFC3 science team.

**Table 3.5:** Sub-array modes for which CTE correction is enabled in **calwf3** version 3.4. For sub-arrays not listed here, a [workaround](#) is available.

UVIS1-2K2A-SUB
UVIS1-2K2B-SUB
UVIS2-2K2C-SUB
UVIS2-2K2D-SUB
UVIS2-C1K1C-SUB
UVIS2-C512C-SUB
UVIS2-C512D-SUB
UVIS1-C512A-SUB
UVIS1-C512B-SUB
UVIS1-2K4-SUB
UVIS-QUAD-SUB
UVIS2-2K4-SUB

Calling the **wf3cte** executable produces a FITS file with the extension "\_rac" appended. This contains only the CTE corrected data, no other calibrations have been performed.

### Running wf3cte from a python terminal

In Python without TEAL:

```
from wfc3tools import wf3cte
wf3cte(filename)
```



In Python with TEAL:

```
from stsci.tools import teal
from wfc3tools import wf3cte
teal.teal('wf3cte')
```

### Displaying output from wf3cte in a Jupyter Notebook

When calling **wf3cte** from a Jupyter notebook, informational text output from the underlying **wf3cte.e** program will be passed through `print` as the calibration runs by default, and show up in the user's cell. This behavior can be customized by passing your own function as the `log_func` keyword argument to **wf3cte**. As output is read from the underlying program, the **wf3cte** Python wrapper will call `log_func` with the contents of each line (`print` is an obvious choice for a log function, but this also provides a way to connect **wf3cte** to the Python logging system by passing the `logging.debug` function or similar).

If `log_func=None` is passed, informational text output from the underlying program will be ignored, but the program's exit code will still be checked for successful completion.

### Input Parameters for the Python interface

```
input: str
    Name of input files
    · a single filename (iaa012wdq_raw.fits)
    · a Python list of filenames
    · a partial filename with wildcards (*raw.fits)
    · filename of an ASN table (*asn.fits)
    · an at-file (@input)
-1: value, optional
    as in minus one, this will make sure only 1
    processor/thread is used during processing,
    otherwise all available are used.
-v: verbose: bool, optional
    Print verbose time stamps?
```

## Command Line Options for the **wf3cte** executable

```
wf3cte.e input [-options]
```

Where the options include:

```
-v: verbose
-l: turn off multiprocessing
```

## Basic Steps In The CTE Correction

- The reference bias image named in the `BIACFILE` header keyword is subtracted from the data
- Parameters from the CTE parameter table, referenced in the `PCTETAB` header keyword, are read and stored
- The data are reformatted: each quadrant is rotated such that the readout amp is located at the lower left of the array. The reoriented four quadrants are then arranged into a single  $8412 \times 2070$  image (including the overscan pixels) with amps CDAB in that order. In this format, the pixels are all parallel-shifted down, then serial-shifted to the left
- An additional bias correction is performed using the residual bias level measured for each amplifier from the steadiest pixels in the horizontal overscan, this value is then subtracted from all the pixels in each respective amp
- The image is multiplied by the gain
- The bias subtracted image still contains contribution from the read-noise. The read-noise “electrons”, however are generated at readout and are not affected by CTE. Therefore, the bias subtracted image is separated at this stage into two components: one that is consistent with being pure read-noise and another that is a smooth version of the astronomical scene.
- The CTE reconstruction algorithm then operates on the "smooth" version of the scene, determining which pre-read-out charge distribution could be CTE-trailed to result in the "smooth" scene. The difference between these two images is an estimate of how CTE likely redistributed charge in the exposure. We add this difference to the original raw, uncorrected, uncalibrated image.
- The corrected image is now ready to continue through the rest of the pipeline. When the `DARKCORR` header keyword is set to `PERFORM`, the CTE corrected image will be dark-subtracted using the dark reference file referred to in the `DRKCFILE` header keyword.
- In the case of subarray image, the same steps are performed as above after the image has been placed into the correct full-frame reference position since the correction is dependent on the distance of the pixels away from the read-out amplifier.

### The PCTETAB and Algorithm Parameters

The following are new primary header keywords which will be updated in the data headers during the **wf3cte** step. They are also specified in the PCTETAB reference file.

KEYWORD	DESCRIPTION
CTE_NAME	name of cte algorithm [string]
CTE_VER	version number of cte algorithm [string]
CTEDATE0	date of wfc3/uvis installation in HST, in modified Julian days (MJD)
CTEDATE1	reference date of CTE model pinning, in modified Julian days (MJD)
PCTETLEN	max length of CTE trail
PCTERNOI	read-noise amplitude for clipping
PCTENFOR	number of iterations used in CTE forward modeling
PCTENPAR	number of iterations used in the parallel transfer
PCTENSMD	read-noise mitigation algorithm
PCTETRSH	over-subtraction threshold
PCTEFRAC	CTE scaling frac calculated from expstart and used in the algorithm
PCTERNOI	the read-noise clipping level to use
FIXROCR	make allowance for readout cosmic rays

The PCTETAB reference file has 4 extensions, two tables and two images:

Filename: zcv2057mi_cte.fits					
No.	Name	Type	Cards	Dimensions	Format
0	PRIMARY	PrimaryHDU	21	()	
1	QPROF	BinTableHDU	16	999R x 4C	['i', 'j', 'e', '20A']
2	SCLBYCOL	BinTableHDU	20	8412R x 6C	['i', 'e', 'e', 'e', 'e', '20A']
3	RPROF	ImageHDU	12	(999, 100)	float32
4	CPROF	ImageHDU	12	(999, 100)	float32

The first extension lists the charge-trap levels, the columns are respectively the trap number, the charge-packet size it applies to (in electrons), and the size of the trap (also in electrons).

The second extension contains the CTE scalings as a function of column number. There are 5 columns, each with 8412 elements. The first column contains the integer column number in the amp readout-aligned large array. The other columns contain the CTE scaling appropriate for that column at the 512th, 1024th, 1536th and 2048th rows respectively.

The third extension contains the differential CTE trail profile as a function of charge level in the form of an image

The fourth extension contains the cumulative CTE trail profile as a function of charge level, also in the form of an image.

### Output Files

If the user is running the separate **wf3cte.e** step a `_rac.fits` file will be produced. This is the same as a `_raw.fits` file except the CTE correction has been applied to the data.

If the `PCTECORR` step is set to `PERFORM`:

- when the `_raw.fits` file enters **calwf3**, then no intermediate `_rac.fits` file will be saved, unless you specify the `-s` flag, which instructs **calwf3.e** to save all intermediate files.
- the **calwf3** pipeline will produce both CTE calibrated product and non-CTE calibrated products. The CTE products have a 'c' at the end of their extension name, such as `_blc`, `_rac`, `_crc`, `_flc`, and the non-CTE calibrated products contain the familiar : `_blv`, `_crj`, `_flt`.

Note: The CTE correction step uses all available CPUs (while the rest of the calibration steps do not).

### 3.4.2 wf3ccd

This routine performs the initial processing steps for all the WFC3 UVIS channel data. These steps are:

- `DQICORR` - initializing the data quality array
- `ATODCORR` - perform the a-to-d conversion correction
- `BLEVCORR` - subtract the bias level from the overscan region
- `BIASCORR` - subtract the bias image
- `FLSHCORR` - subtract the post-flash image

**wf3ccd** first subtracts the bias and trims the overscan regions from the image. If an associated set of UVIS `CR-SPLIT` or `REPEAT-OBS` images is being processed, all of the overscan-trimmed images are sent through **wf3rej** to be combined and receive cosmic-ray rejection. The resulting combined image then receives final calibration with **wf32d**, which includes dark subtraction and flat fielding. If there are multiple sets of `CR-SPLIT` or `REPEAT-OBS` images in an association, each set goes through the cycle of **wf3ccd**, **wf3rej** and **wf32d** processing.

Only those steps with a switch value of `PERFORM` in the input files will be executed, after which the switch will be set to `COMPLETE` in the corresponding output files.

### Running wf3ccd from a python terminal

In Python without TEAL:

```
from wfc3tools import wf3ccd
wf3ccd(filename)
```

In Python with TEAL:

```
from stsci.tools import teal
from wfc3tools import wf3ccd
teal.teal('wf3ccd')
```

### Displaying output from wf3ccd in a Jupyter Notebook

When calling **wf3ccd** from a Jupyter notebook, informational text output from the underlying **wf3ccd.e** program will be passed through `print` as the calibration runs by default, and show up in the user's cell. This behavior can be customized by passing your own function as the `log_func` keyword argument to **wf3ccd**. As output is read from the underlying program, the **wf3ccd** Python wrapper will call `log_func` with the contents of each line. (`print` is an obvious choice for a log function, but this also provides a way to connect **wf3ccd** to the Python logging system by passing the `logging.debug` function or similar.)

If `log_func=None` is passed, informational text output from the underlying program will be ignored, but the program's exit code will still be checked for successful completion.

## Input Parameters for the Python interface

```

input: str
    Name of input files
    · a single filename (iaa012wdq_raw.fits)
    · a Python list of filenames
    · a partial filename with wildcards(*raw.fits)
    · filename of an ASN table (*asn.fits)
    · an at-file (@input)
output: str
    Name of the output FITS file.
dqicorr: str, "PERFORM/OMIT", optional
    Update the dq array from bad pixel table
atodcorr: str, "PERFORM/OMIT", optional
    Analog to digital correction
blevcorr: str, "PERFORM/OMIT", optional
    Subtract bias from overscan regions
biascorr: str, "PERFORM/OMIT", optional
    Subtract bias image
flashcorr: str, "PERFORM/OMIT", optional
    Subtract post-flash image
verbose: bool, optional
    Print verbose time stamps?
quiet: bool, optional
    Print messages only to trailer file?

```

## Command Line Options for the wf3ccd executable

```
wf32ccd.e input output [-options]
```

input may be a single filename

Where the options include:

```

-v: verbose
-f: print time stamps
-dqi: udapte the DQ array
-atod: perform gain correction
-blev: subtract bias from overscan
-bias: perform bias correction
-flash: remove post-flash image

```

### 3.4.3 wf32d

This routine performs the remaining series of tasks in the UVIS pipeline. The **wf32d** primary functions include:

- DARKCORR: dark current subtraction
- FLATCORR: flat-fielding
- PHOTCORR: photometric keyword calculations
- FLUXCORR: photometric normalization of the UVIS1 and UVIS2 chips

Only those steps with a switch value of **PERFORM** in the input files will be executed, after which the switch will be set to **COMPLETE** in the corresponding output files.

#### Examples

In Python without TEAL:

```
from wfc3tools import wf32d
wf32d(filename)
```

In Python with TEAL:

```
from stsci.tools import teal
from wfc3tools import wf32d
teal.teal('wf32d')
```

#### Displaying output from wf32d in a Jupyter Notebook

When calling **wf32d** from a Jupyter notebook, informational text output from the underlying **wf32d.e** program will be passed through `print` as the calibration runs by default, and show up in the user's cell. This behavior can be customized by passing your own function as the `log_func` keyword argument to **wf32d**. As output is read from the underlying program, the **wf32d** Python wrapper will call `log_func` with the contents of each line. (`print` is an obvious choice for a log function, but this also provides a way to connect **wf32d** to the Python logging system by passing the `logging.debug` function or similar.)

## Parameters

```

input: str
    Name of input files
    · a single filename (iaa012wdq_raw.fits)
    · a Python list of filenames
    · a partial filename with wildcards (*raw.fits)
    · filename of an ASN table (*asn.fits)
    · an at-file (@input)

output: str
    Name of the output FITS file.
dqicorr: str, "PERFORM/OMIT", optional
    Update the dq array from bad pixel table
darkcorr: str, "PERFORM/OMIT", optional
    Subtract the dark image
flatcorr: str, "PERFORM/OMIT", optional
    Multiply by the flatfield image
shadcorr: str, "PERFORM/OMIT", optional
    Correct for shutter shading (CCD)
photcorr: str, "PERFORM/OMIT", optional
    Update photometry keywords in the header
fluxcorr; str, "PERFORM/OMIT", optional
    Perform chip photometry normalization
verbose: bool, optional
    Print verbose time stamps?
quiet: bool, optional
    Print messages only to trailer file?

```

## Command Line Options for the wf32d executable

```
wf32d.e input output [-options]
```

input may be a single filename

Where the options include:

```

-v: verbose
-f: print time stamps
-d: debug
-dark: perform dark subtraction
-dqi: update the DQ array
-flat: perform flat correction
-shad: perform shading correction
-phot: perform phot correction

```



### 3.4.4 wf3ir

This routine contains all the instrumental calibration steps for WFC3 IR channel images. The steps are:

- DQICORR - initialize the data quality array
- ZSIGCORR - estimate the amount of signal in the zeroth-read
- BLEVCORR - subtract the bias level from the reference pixels
- ZOFFCORR - subtract the zeroth read image
- NLINCORR - correct for detector non-linear response
- DARKCORR - subtract the dark current image
- PHOTCORR - compute the photometric keyword values
- UNITCORR - convert to units of count rate
- CRCORR - fit accumulating signal and identify the cr hits
- FLATCORR - divide by the flat-field images and apply gain conversion

The output images include the calibrated image (flt file) and the intermediate multi-accumulated ramp image (ima file).

Only those steps with a switch value of `PERFORM` in the input files will be executed, after which the switch will be set to `COMPLETE` in the corresponding output files.

#### Running wf3ir from a python terminal

In Python without TEAL:

```
from wfc3tools import wf3ir
wf3ir(filename)
```

In Python with TEAL:

```
from stsci.tools import teal
from wfc3tools import wf3ir
teal.teal('wf3ir')
```

#### Displaying output from wf3ir in a Jupyter Notebook

When calling **wf3ir** from a Jupyter notebook, informational text output from the underlying **wf3ir.e** program will be passed through `print` as the calibration runs by default, and show up in the user's cell. This behavior can be customized by passing your own function as the `log_func` keyword argument to **wf3ir**. As output is read from the underlying program, the **wf3ir** Python wrapper will call `log_func` with the contents of each line. (`print` is an obvious choice for a log function, but this also provides a way to connect **wf3ir** to the Python logging system by passing the `logging.debug` function or similar.)

## Input Parameters for the Python interface

```

input: str
    Name of input files
    · a single filename (iaa012wdq_raw.fits)
    · a Python list of filenames
    · a partial filename with wildcards (\*raw.fits)
    · filename of an ASN table (\*asn.fits)
    · an at-file (@input)
output: str
    Name of the output FITS file.
verbose: bool, optional
    Print verbose time stamps?
quiet: bool, optional
    Print messages only to trailer file?

```

## Command Line Options for the wf3ir executable

```
wf32ir.e input output [-options]
```

input may be a single filename

Where the options include:

```

-v: verbose
-f: print time stamps

```

### 3.4.5 wf3rej

**wf3rej**, the cosmic-ray rejection and image combination task in **calwf3**, combines CR-SPLIT or REPEAT-OBS exposures into a single image, first detecting and then replacing flagged pixels. The task uses the same statistical detection algorithm developed for ACS (acsrej), STIS (ocrrej), and WFPC2 data (crrej), providing a well-tested and robust procedure.

First, **wf3rej** temporarily removes the sky background from each input image (if requested via the SKYSUB parameter in the CRREJTAB), usually computed using the mode of each image. Sky subtraction is performed before any statistical checks are made for cosmic rays. Next, **wf3rej** constructs an initial comparison image from each sky-subtracted exposure. This comparison image can either be a median- or minimum-value sky-subtracted image constructed from all the input images, and it represents the ‘initial guess’ of a cosmic-ray free image. The comparison image serves as the basis for determining the statistical deviation of each pixel within the input images.

A detection threshold is then calculated for each pixel based on the comparison image:

$$\tau_n = \sigma^2 \times (noise + value/gain + (scale \times value)^2) / T_n^2$$

where:

- $\sigma$  is the sigma value used as the detection limit (CRSIGMAS),
- *noise* is the readnoise in DN squared and gain is the e-/DN of the amplifier used to read the pixel,
- *scale* is the scale factor for the noise model,
- $T_n$  is the exposure time for the input image, and
- *value* is the pixel value (in DN) from the median or minimum combined comparison image.

The actual detection criterion for a cosmic ray is determined as:

$$\Delta = ((pix_n - sky_n)/T_n - median)^2$$

where:

- $pixel_n$  is the pixel value from input image  $n$ ,
- $sky_n$  is the sky background of image  $n$ , and
- *median* is the median or minimum pixel value from the comparison image.

If  $\Delta > \tau_n$  the pixel is flagged as a cosmic ray in the input image's DQ array and is ignored when images are summed together. Surrounding pixels within some expansion radius (CRRADIUS) are marked as 'SPILL' pixels and are given less stringent detection thresholds.

When all input images have been processed, the values of the non-rejected pixels are summed over all input images. Each pixel in the summed output array is then scaled by the total exposure time:

$$pixout(x, y) = T \cdot \frac{\sum_n (pix_n(x, y) - sky_n) m_n(x, y)}{\sum_n T_n m_n(x, y)} + \sum_n sky_n$$

where:

- $T_n$  is the exposure time for image  $n$ ,
- $m_n(x, y)$  is the mask value (0 for rejected pixels, 1 for good data) for the  $n$ -th image at pixel  $(x, y)$ ,
- $T$  is the total exposure time (regardless of whether all input images were used for that particular pixel). This corresponds to the value recorded in the header keywords `TEXPTIME` and `EXPTIME`.

The following keywords are also derived from the variables in this equation:

- `TEXPTIME` = `EXPTIME` =  $T$
- `SKYSUM` =  $\sum_n sky_n$
- `REJ_RATE` =  $(\sum_n T_n m_n(x, y) / T)$  averaged over all pixels
- `NCOMBINE` =  $n$

The remaining keywords `EXPSTART`, `EXPEND` are updated based on the values corresponding to the first and last input images, respectively.

In summary, the cosmic ray rejection task sums all non-rejected pixel values, computes the true exposure time for that pixel, and scales the sum to correspond to the total exposure time. The final scaled, cleaned pixel is written to the comparison image to be used for the next iteration. This process is then repeated with increasingly stringent detection thresholds, as specified by `CRSIGMAS`.

### Cosmic Ray Rejection Table

**wf3rej** uses the Cosmic Ray Rejection parameter table (`CRREJTAB`) to determine the number of iterations for cosmic-ray rejection, the sigma levels to use for each iteration, and the spill radius to use during detection. This allows the rejection process to be tuned to each detector and observation, with suitable defaults being applied during pipeline processing. Observers may fine-tune the cosmic-ray rejection parameters when manually reprocessing data with **wf3rej** by editing the `CRREJTAB`.

The `CRREJTAB` reference file contains the basic parameters necessary for performing cosmic-ray rejection. The column names and default values for the `CRREJTAB` are given in [Table 3.6](#). The appropriate row is selected based on the chip being processed (`CCDCHIP`), the number of images into which the exposure was split (`CR-SPLIT`), and the exposure time of each `CR-SPLIT` image (`MEANEXP`). If an exact match is not found for the exposure time, the table row with the closest value is used. If the `CR-SPLIT` value of the input images exceeds the values in the table, the table row with the largest `CR-SPLIT` value will be used. The sky fitting algorithm is controlled by the parameter `SKYSUB`, which can have values of ‘mode’, ‘mean’ or ‘none’. The ‘initial guess’ image is created using the median or minimum value of the input exposures, as specified by the value of `INITGUES`.

Cosmic-ray detection requires the specification of a threshold above which a pixel value is considered a cosmic ray. This threshold was defined above and uses the sigma rejection thresholds. These sigmas correspond to the `CRSIGMAS` column values in the `CRREJTAB` file. `SCALENSE` is a multiplicative term (in percent) for the noise model and is given as `scale` in the threshold equation above. This term can be useful when the pointing of the telescope has changed by a small fraction of a pixel between images. Under such circumstances, the undersampling of the image by the detector will cause stars to be mistakenly rejected as cosmic rays if a scale noise term is not included. This is a crude but effective step taken to satisfy the maxim of ‘do no harm’. However, for cases in which there have been no image-to-image offsets or the image is locally well-sampled, this will unduly bias against rejecting cosmic rays.

Pixels within a given radius, `CRRADIUS`, of a cosmic ray will also be treated as cosmic rays. A less stringent rejection threshold, `CRTHRESH`, can be used for detecting pixels adjacent to a cosmic ray. As for `CRSIGMAS`, `CRTHRESH` is also given as a sigma value. If `CRTHRESH` is exceeded, pixels within the defined radius of the cosmic ray will also be flagged. All pixels determined to be affected by a cosmic ray will have their DQ values set to 8192, as described in [Table 3.6](#).

**Table 3.6: Columns in cosmic-ray rejection parameter table.**

Column Name	Default Value	Contents
CRSPLIT	-	Number of exposures into which observation was split
CCDCHIP	-	Chip to which this conversion applies
MEANEXP	-	Average exposure time (sec) for each image
SCALENSE	30.0	Multiplicative term (in percent) for the noise model
INITGUES	minimum	Method for computing initial-guess image (minimum, median)
SKYSUB	mode	Sky fitting algorithm (mode, none)
CRSIGMAS	6.5, 5.5, 4.5	Rejection thresholds (sigma)
CRRADIUS	2.1	Radius (in pixels) for propagating cosmic ray
CRTHRESH	0.5555	Propagation factor
BADINPDQ	39	Data quality file bits to reject
CRMASK	yes	Flag CR-rejected pixels in input files?

### Running wf3rej from a python terminal

In Python without TEAL:

```
from wfc3tools import wf3rej
wf3rej(filename)
```

In Python with TEAL:

```
from stsci.tools import teal
from wfc3tools import wf3rej
teal.teal('wf3rej')
```

### Displaying output from wf3rej in a Jupyter Notebook

When calling **wf3rej** from a Jupyter notebook, informational text output from the underlying **wf3rej** program will be passed through `print` as the calibration runs by default, and show up in the user's cell. This behavior can be customized by passing your own function as the `log_func` keyword argument to **wf3rej**. As output is read from the underlying program, the **wf3rej** Python wrapper will call `log_func` with the contents of each line. (`print` is an obvious choice for a log function, but this also provides a way to connect **wf3rej** to the Python logging system by passing the `logging.debug` function or similar.)

## Input Parameters for the Python interface

```

input : str, Name of input files
    · a single filename (iaa012wdq_raw.fits)
    · a Python list of filenames
    · a partial filename with wildcards (\*raw.fits)
    · filename of an ASN table (\*asn.fits)
    · an at-file (@input)
output: string
    Name of the output FITS file.
crrehtab: string
    reference file name
scalense: string
    scale factor applied to noise
initgues: string
    intial value estimate scheme (min|med)
skysub: string
    how to compute the sky (none|mode|mean)
crsigmas: string
    rejection levels in each iteration
crradius: float
    cosmic ray expansion radius in pixels
crthresh: float
    rejection propagation threshold
badinpdq: int
    data quality flag bits to reject
crmask: bool
    flag CR in input DQ images?
shadcorr: bool
    perform shading shutter correction?
verbose: bool, optional
    Print verbose time stamps?

```

## Command Line Options for the wf3rej executable

```

wf3rej.e input output [-options]

```

Input can be a single file

Where the options include:

```

t: print the timestamps
v: verbose
shadcorr: perform shading shutter correction?
crmask: flag CR in input DQ images?
table <filename>: the crreftab filename
scale <number>: scale factor for noise
init <med|min>: initial value estimate scheme
sky <none|median|mode>: how to compute sky
sigmas: rejection levels for each iteration
radius <number>: CR expansion radius
thresh <number> : rejection propagation threshold
pdq <number>: data quality flag bits to reject

```

---

## 3.5 Manual Recalibration of WFC3 Data

### 3.5.1 Requirements for Manual Recalibration

#### Retrieving Software and Input Data Files

If observers decide to recalibrate their WFC3 data on their own, the following must be available on their system:

- Software currently being used by HST Data Processing (distributed in the Astroconda package and containing the **calwf3** executables and **Astrodrizzle**)
- Reference files obtained from the HST Data Archive
- Uncalibrated (raw) data files from the HST Data Archive
- Any association tables that describe observation sets.

Uncalibrated data and calibration reference files can be obtained from the [HST Data Archive](#).

If updated reference files are required for local reprocessing, they can be obtained using the interface to CRDS, described in [Section 3.1.4](#).

#### Setting up ‘iref’

Before any recalibration can be done, the user’s local directory containing the calibration reference files must be defined for the software tasks. For WFC3, this directory is referred to as ‘iref’. The raw image headers already contain the appropriate keywords that list the reference file names that were assigned during

STScI pipeline processing. The user must simply define the location of the ‘iref’ directory in the Unix environment:

```
setenv iref /mydisk/myiref/
```

If done from the command line, this setup must be done in the same window in which python will be started. Setting ‘iref’ from within python will not work, even though subsequently typing ‘show iref’ would suggest it might. For convenience, this setup command can be added to your .setenv file, so that the iref environment variable will always be defined. The ‘iref’ environment variable is required whether you are reprocessing through python or from your OS command line.

### Selecting Calibration Switches

The MAST HST Data Processing uses the most up-to-date calibration reference files by default. In order to use non-default reference files, manual recalibration is required. The calibration reference file keywords will need to be updated manually in the raw data files with the desired file names before running **calwf3**. In addition, the user can choose to change which calibration steps are performed by **calwf3** by resetting the values of the calibration switch keywords. These keywords are listed in [Table 3.7](#) along with their default values as used in the STScI pipeline. To change the values of any of the keyword switches, use a FITS keyword editor, such as the python package `astropy.io.fits`:

```
from astropy.io import fits

fits.setval('myfile_raw.fits', keyword= 'DARKCORR', value= 'OMIT', ext=0)
```



**Table 3.7: Calibration switch and default settings.**

SWITCH	DESCRIPTION	Criteria
PCTECORR	Perform CTE correction (UVIS)	DEFAULT = 'PERFORM' cte-corrected branch) / OMIT (non-cte-cor- rected branch)
DQICORR	Data Quality Array Initialization	DEFAULT = 'PERFORM'
ATODCORR	Analog-to-Digital Correction	DEFAULT = 'OMIT'
ZSIGCORR	Zero-read Signal Correction (IR)	DEFAULT = 'PERFORM'
BLEVCORR	CCD Overscan Region Subtraction (UVIS) or Reference Pixel Bias Correction (IR)	DEFAULT = 'PERFORM'
BIASCORR	Bias Image Subtraction (UVIS)	DEFAULT = 'PERFORM'
FLSHCORR	Post-flash Image Subtraction (UVIS)	If FLASHLVL > 0 then 'PERFORM' else 'OMIT'
FLUXCORR	Correct chips to be on the same zero point (UVIS)	DEFAULT = 'PERFORM'
CRCORR	UVIS Cosmic Ray Rejection:	If CRSPLIT or NRPTEXP > 1 then 'PERFORM', else 'OMIT'
	IR Cosmic Ray Rejection:	DEFAULT = 'PERFORM' (for scan observations this is however set to 'OMIT')
ZOFFCORR	Zero-read Image Subtraction (IR)	DEFAULT = 'PERFORM'
NLINCORR	Non-linearity Correction (IR)	DEFAULT = 'PERFORM'
DARKCORR	Dark Image Subtraction	DEFAULT = 'PERFORM'
FLATCORR	Flat-Field Correction	DEFAULT = 'PERFORM'
SHADCORR	Shutter Shading Correction (UVIS)	DEFAULT = 'OMIT'
UNITCORR	Units Conversion (IR)	DEFAULT = 'PERFORM'
PHOTCORR	Photometric Processing	DEFAULT = 'PERFORM'
RPTCORR	Repeat-Obs Processing (IR)	If NRPTEXP > 1 then 'PER- FORM', else 'OMIT'
EXPSCORR	Full calibration of individual exposures in an association	DEFAULT = 'PERFORM'
DRIZCORR	Drizzle Processing	DEFAULT = 'PERFORM'

### Set Up to Run the PHOTCORR Step

**calwf3** does not alter the units of the pixels in the image when calculating photometric information. Instead it calculates and writes the inverse sensitivity conversion factors (PHOTFLAM and PHOTFNU) and the ST magnitude scale zero point (PHOTZPT) into header keywords in the calibrated data files. Refer to

subsections on PHOTCORR in [Section 3.2.12](#) (UVIS) and [Section 3.2.8](#) (IR) for more information.

### Speed of Pipeline Processing

Reprocessing WFC3 UVIS and IR datasets can stress some computing platforms because of the potentially large data volume and CPU-intensive calculations. Great care has been taken to minimize the memory requirements of the pipeline software.

Line-by-line I/O used during UVIS processing is particularly useful when more than one image is operated on at a time, such as during flat-field application or combining images. Unfortunately, this places an extra burden on the I/O capabilities of the computer. **calwf3** requires up to 130MB of memory to process a full-frame UVIS image and up to 250MB for an IR exposure containing a full set of 16 non-destructive reads. **Astrodrizzle** requires up to 400MB. Geometric correction or dither-combining using **Astrodrizzle** will take extra time, because these are performed separately. WFC3 observers should keep these requirements in mind when securing computing resources for data processing.

## 3.5.2 calwf3 Examples

This section presents several examples of **calwf3** reprocessing. The boxes show commands and output to the screen. The following examples indicate commands that are typed into python. Pure python commands may still be used in a **PyRAF** session.

### Example 1: Reprocessing a Single Exposure

The following example uses hypothetical UVIS observations of a stellar cluster, observed with the F814W filter. The exposures are CR-SPLIT into two exposures of 20 seconds each. The association table for this observation is i8bt07020\_asn.fits. In Python, typing `fits.getdata('i8bt07020_asn.fits',1)` reveals the rootnames of the individual exposures: i8bt07oyq and i8bt07ozq.

For the purposes of this first example, assume that the observer desires to reprocess only one of these exposures. This example illustrates the steps required to reprocess a single exposure after changing the bias reference file from the default value to a file specified by the user.

1. We assume here that the user has followed the instructions in the section See “Setting up ‘iref’” at the beginning of [Section 3.5.1](#). We also assume that calibration reference files were obtained as part of the HDA request, and are stored in the local ‘iref’ directory (i.e., ‘/mydisk/myiref/’). In this example, the directory ‘/mydisk/’ contains the pipeline data.
2. To see what bias reference file is currently in use, use `astropy.io.fits.getval()` in Python.

```
from astropy.io import fits
fits.getval('i8bt07oyq_raw.fits', 'BIASFILE', 0)
```

3. Next, edit the primary image header of the raw file to reflect the name of the new bias file.

```
fits.setval('i8bt07oyq_raw.fits',
'BIASFILE',value='iref$new_bias_filename.fits')
```

4. Within the directory containing the pipeline products ('/mydisk/'), create the subdirectory 'recal'. Copy the raw file to this subdirectory, and 'cd' to it.
5. Finally, load the package and run **calwf3** on the single raw exposure.

```
from wfc3tools import calwf3
calwf3('ibt07oyq_raw.fits')
```

The product will be a single calibrated image with the '\_flt' file name suffix.

### Example 2: Reprocessing Multiple Exposures within an Association

This example uses the same data from Example 1 and illustrates the steps required to reprocess a WFC3 association after changing the bias reference file from the default value to a file specified by the user. The steps required are similar to the previous example, with a few modifications.

1. First, look at the contents of the association (asn) table. You will get a FITS\_rec.

```
fits.getdata('ibt07020_asn.fits',1)

FITS_rec([('I8BT07OYQ', 'EXP-CRJ', 1), ('I8BT07OZQ',
'EXP-CRJ', 1), ('I8BT07021', 'PROD-CRJ', 1)],
dtype=(numpy.record, [('MEMNAME', 'S14'), ('MEMTYPE',
'S14'), ('MEMPRSNT', 'i1')]))
```

2. To see what bias reference file is currently in use, use fits.getval( ).

```
fits.getval('i8bt07oyq_raw.fits', 'BIASFILE',0)
```

3. Edit the primary image header of all the raw images to reflect the name of the new bias file.

```
for raw in glob.glob('i8bt07*raw.fits'):
    fits.setval(raw, 'BIASFILE', value = 'iref$mybias.fits', ext=0)
```




---

*Note: If this command is executed in the same directory in which you have run the previous example, then one of the `flt` files will already exist and `calwf3` will not overwrite existing images. Either delete the existing `flt` file, move it to a separate directory, or rename it.*

---

4. Within the directory containing the pipeline products (`/mydisk/`), create the subdirectory `'recal'`. Copy the raw file to this subdirectory, and `'cd'` to it.
5. Finally, load the package and run **calwf3** on the single raw exposure.

```
from wfc3tools import calwf3
calwf3('ibt07020_asn.fits')
```

The products will be two separate calibrated `flt` images (`i8bt07oyq_flt.fits`, `i8bt07oyq_flt.fits`) and a single CR-combined `crj` image (`i8bt07021_crj.fits`).

### Example 3: Reprocessing Images taken as part of a Dither Pattern

When using IR images that are part of a 2-point line dither pattern the steps required to reprocess images are the same as in Example 2, but the format of the association and the data products are different. If you wish to use images that are part of a dither pattern that uses non-default dark reference files then replace step 3 from above with this step:

1. Edit the primary image header of all the raw files to reflect the name of the new dark reference file.

```
for raw in glob.glob('i8e654*raw.fits'):
    fits.setval(raw, 'DARKFILE', value = 'iref$mydark.fits', ext=0)
```

The output products from this run of **calwf3** will be two separate calibrated datasets, consisting of `ima` and `flt` files for each of the input images. In subsequent processing **Astrodrizzle** can be used to combine the two `flt` files into a single `drz` image (`i8e654010_drz.fits`).

# WFC3 Images: Distortion Correction and AstroDrizzle

In this chapter . . .

4.1 WFC3 Geometric Distortion / 88

4.2 Distortion Corrections and Image Combination / 92

4.3 References / 94

## 4.1 WFC3 Geometric Distortion

WFC3 images exhibit significant geometric distortion, similar to that seen in ACS images. The required folding of the light paths in both channels to fit within the instrument's optical-bench envelope results in substantial tilts of the focal surfaces with respect to the chief rays. The WFC3 UVIS detector is tilted at  $\sim 21$  degrees producing a rhomboidal elongation of  $\sim 7\%$ . The IR detector has a  $\sim 24$  degree tilt about its x-axis, creating a rectangular elongation of  $\sim 10\%$ . The orientations of the WFC3 detector edges for both detectors are at approximately 45 degrees with respect to the V2 and V3 coordinate axes of the telescope. [Figure 2.2 of the \*WFC3 Instrument Handbook\*](#) shows the WFC3 apertures in the telescope's V2, V3 reference frame.

The first on-orbit measurements of the geometric distortion for the WFC3 detectors were made in 2009 during SMOV (Servicing Mission Observatory Verification). Astrometric fields in 47 Tuc (NGC 104) and the LMC were observed with multiple offsets in programs 11444 (UVIS, filter F606W) and 11445 (IR, filter F160W).

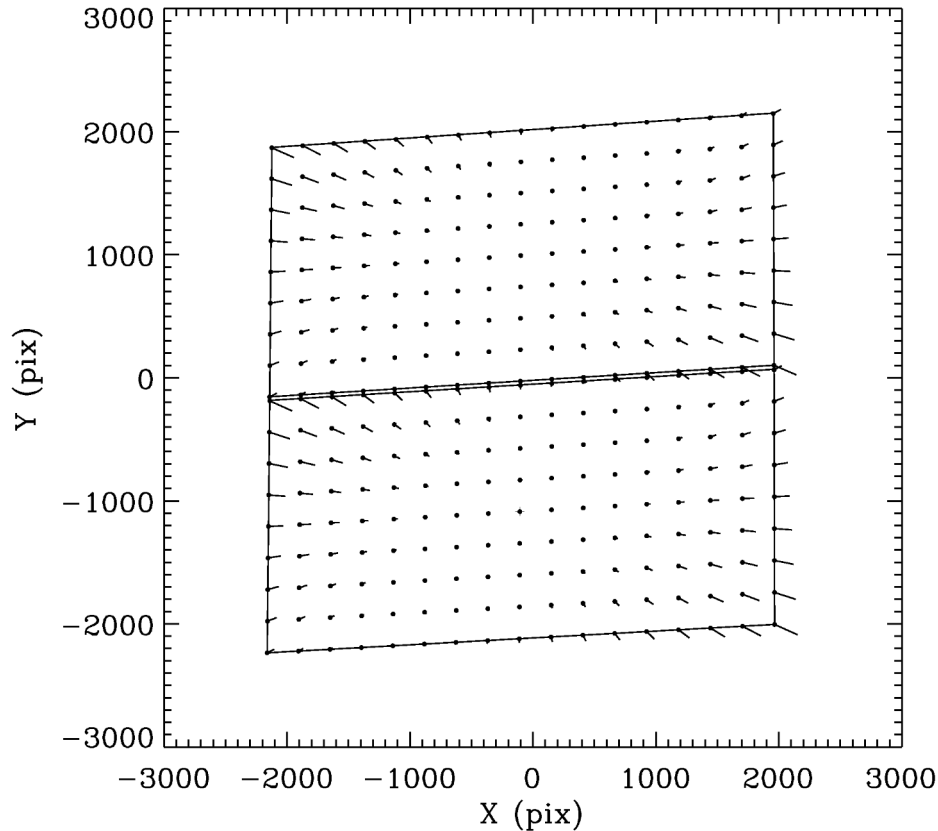
The derived WFC3 geometric distortion, as described in [WFC3 ISR 2009-33](#) and [WFC3 ISR 2009-34](#), and updated in [WFC3 ISR 2012-07](#), is presented as a fourth-order polynomial model and is accurate to a precision level of better than 0.1

pixel in the UVIS and IR or 4 mas and 10 mas, respectively. In Cycles 18, 19, 20, the globular cluster Omega Centauri was observed through 14 UVIS and 5 IR filters (WFC3 Calibration Programs 11911, 11928, 12353 and 13100). Therefore, for each of the 14 calibrated UVIS and 5 calibrated IR filters, unique polynomial coefficients of the geometric distortion ( [WFC3 ISR 2012-07](#)), in the form of Instrument Distortion Coefficient Tables (IDCTABS), are used to correct for distortion in MAST drizzled data products. These reference files are also available to users who wish to reprocess their data with the **DrizzlePac/AstroDrizzle** software.

For the UVIS CCDs, on top of this large-scale geometric distortion, there is a micro-distortion, which consists of fine-scale systematics in the residuals from the best-fit polynomial solutions. These systematic residuals typically extend to  $\sim 0.15$  pixel and vary in amplitude depending on the location within a CCD chip. Such residuals cannot be removed by a polynomial model. These fine-scale and low-amplitude distortions are the result of the manufacturing process. That is, the lithographic mask pattern used during the chip manufacture is imprinted on the detector. The correction for the lithographic pattern imprint is implemented in **DrizzlePac/AstroDrizzle** as a 2-D bilinear interpolation (D2IMFILE, Detector to Image distortion correction reference file) which is applied prior to the large-scale distortion (polynomial model) correction (IDCTAB) ([WFC3 ISR 2013-14](#)). The look-up table is incorporated by **AstroDrizzle** in the pipeline, using the filename specified in the D2IMFILE keyword in the primary image header. AstroDrizzle attaches new fits extensions to the calibrated image of type 'D2IMARR' (four extensions total, two for each chip in each X and Y axis). See [Table 2.4](#) for details on these additional image header extensions.

In addition to the pixel-grid irregularities there are fine-scale non-polynomial filter-dependent distortions that have been calibrated for a subset of 15 UVIS filters (see [Table 2.4](#)). These are specified in the NPOLFILE keyword in the primary image header and attached to the image as FITS extensions (four extensions, two for each CCD chip and each X and Y axis), [WFC3 ISR 2014-12](#). Each element of the  $64 \times 32$  table is bi-linearly interpolated pixel-by-pixel in UVIS images by **AstroDrizzle**.

**Figure 4.1: Non-linear components (vectors magnified by 10) of the geometric distortion on the WFC3-UVIS detector.**



#### 4.1.1 The UVIS Channel

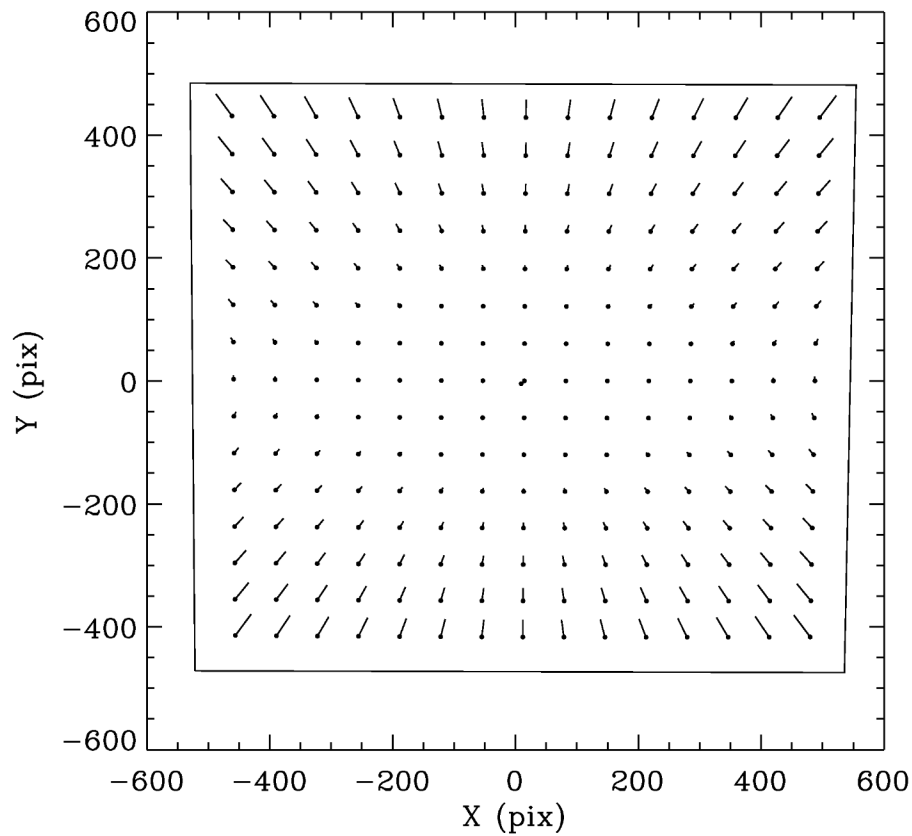
Figure 4.1 illustrates the shape of the UVIS channel field of view as projected onto the sky. As noted above, its rhomboidal shape is due primarily to the tilt of the CCD around its detector diagonal with respect to the chief ray. The angle between the x- and y-axes is  $\sim 86.1$  degrees. The field diagonals are tilted slightly from the V2- and V3-axes (see Figure 1.2). There is a  $\sim 1.2''$  gap between the two CCD chips. The dots in the diagram indicate where points in the image would be located without non-linear distortion, and the vectors, scaled up by a factor of 10, indicate the actual locations of the points on the sky, including the non-linear distortion components. The corner displacements are about 140 pixels, corresponding to  $5.5''$ . The principal effect is the diagonal variation of scale. At the center of UVIS1 (CCD CHIP1, top), the scale in the x-direction is  $0.0396''/\text{pixel}$ , and  $0.0393''/\text{pixel}$  in the y-direction. For UVIS2 (CCD CHIP2, bottom), these scales are  $0.0398''/\text{pixel}$ , and  $0.0398''/\text{pixel}$ , respectively. UVIS1 forms a slightly distorted rectangle  $162'' \times 81''$  in size, while UVIS2 subtends  $163'' \times 82''$ . In the presence of distortion, it is not possible to flat field the image in such a way as to preserve both surface brightness and flux. The convention that has been adopted in the pipeline preserves surface brightness, therefore a correction is necessary if the goal is to measure accurate fluxes via point-source photometry. See

[Section 9.1.11](#) and [WFC3 ISR 2010-08](#) for a discussion on the effects of the pixel area map on photometry.

### 4.1.2 The IR Channel

The IR detector field of view is nominally concentric with the UVIS field, but it subtends a smaller area on the sky,  $138'' \times 123''$ . The detector tilt is about the x-axis, so the projected aperture shape is nearly a rectangle, with the angle between the x- and y-axes on the sky nearly 90 degrees as shown by the outline in [Figure 4.2](#). At field center, the x- and y-scales are 0.135 and 0.121"/pixel, respectively. A vector plot of the deviation from linearity is also shown in [Figure 4.2](#), where the deviations have been magnified by a factor of 10 for illustrative purposes. The largest deviation is  $\sim 10$  pixels, corresponding to about  $1.4''$ .

**Figure 4.2: Non-linear components (vectors magnified by 10) of the geometric distortion on the WFC3-IR detector.**





## 4.2 Distortion Corrections and Image Combination

Because the WFC3 focal plane is tilted with respect to the incoming beam, the projected pixel area on the sky varies across the field of view in calibrated (flt/flc.fits) images. As a result, pixels in different regions of the detector collect a different amount of light simply due to their projected area on the sky. Observations of a constant surface brightness object would therefore have count rates per pixel that vary over the detector, even if every pixel had the same sensitivity.

In order to produce images that appear uniform for uniform illumination, the WFC3 flat fields include the effect of the variable pixel area across the field (see [Section 5.4](#)). As a consequence of dividing by the flat field, two stars of equal brightness in an flt/flc.fits image falling on different portions of the detector would not have the same total counts. To correct for this effect, the calibrated ‘flt/flc.fits’ images may be multiplied by the effective pixel area map available at [http://www.stsci.edu/hst/wfc3/pam/pixel\\_area\\_maps](http://www.stsci.edu/hst/wfc3/pam/pixel_area_maps) (see [WFC3 ISR 2010-08](#)). For the UVIS channel, this represents a 7% effect across a diagonal of the mosaicked image. For the IR channel, the area of the pixels varies by 8% from the bottom to the top of the image.

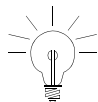
Alternatively, this effect is accounted for in the pipeline by drizzling, where the geometric distortion solution is used to correct all pixels to equal area on the sky in ‘drz/drc.fits’ data products. Because drizzling conserves flux, users should recover the aperture photometry from drz/drc images and from flt/flc images multiplied by the pixel area map.

### 4.2.1 AstroDrizzle in the Pipeline

WFC3 data obtained from MAST are corrected for geometric distortion with **AstroDrizzle**, which replaced MultiDrizzle in the OPUS pipeline for WFC3 data on June 7, 2012. During pipeline processing, calibrated data that belong to an association (e.g. as defined by the user in APT via a standard dither pattern, a REPEAT-OBS, or CR-SPLIT pair, see [Table 2.2](#)) are corrected for distortion and drizzle-combined with cosmic-ray rejection. If the associated images are dithered, they are aligned using the World Coordinate System (WCS) information in their headers before being combined. If there is no association table, each single-exposure WFC3 image is drizzled to correct for geometric distortion. Additional WFC3-specific rules define that images obtained with the same filter within a given visit are associated and thus combined.

**AstroDrizzle** uses the MDRIZTAB reference table to define a default set of parameter values that work well for most use cases. Each detector has its own MDRIZTAB, and each row provides the parameter settings specific to the number of input images per association. **AstroDrizzle** relies on the Image Distortion Correction Table (IDCTAB), the Detector to Image Distortion Correction (D2IMFILE, UVIS only), and the Non-polynomial Filter-Dependent Distortion (NPOLFILE) reference files for a description of the WFC3 distortions. Additional reference files to correct for

filter-dependent residuals (NPOLFILE) are added once on-orbit measurements are made.




---

*Users may obtain the latest IDCTAB, D2IMFILE, NPOLFILE and MDRIZTAB reference files from the following page:*  
<http://www.stsci.edu/hst/observatory/cdb/SIfileInfo/WFC3/reftable-queryindex>

---

Information about the geometric distortion is extracted from these reference files and stored as Simple Image Polynomial (SIP) header keywords and as additional FITS extensions in the \*\_flt.fits/flc.fits images. Please refer to Table 2.4 or to Section 3.2.3 in the [DrizzlePac Handbook](#) for details.

The steps performed by **AstroDrizzle** include the following:

- Correct the geometric distortion
- Align images using the header World Coordinate System
- Perform cosmic-ray rejection using the \*\_flt/flc.fits files as input (Note: IR flt data are already corrected for cosmic rays, but the drizzling process does identify further detector artifacts and rejects them during the combination process.)
- Convert the UVIS data from units of electrons to electrons per second (IR data are already in e-/s)
- Combine associated (e.g. dithered) observations into a single product

In general, pipeline drizzled products retrieved from MAST are recommended to be used as “quick-look” products. Reprocessing through AstroDrizzle is highly recommended to achieve the most scientifically accurate data products. Four main areas for improvement may include: (1) image alignment, (2) sky subtraction, (3) cosmic ray rejection, and (4) final image resolution.

### 4.2.2 Manual AstroDrizzle Reprocessing

Drizzled images combined in the pipeline were produced using a default set of parameters that are suitable for the widest range of scientific applications. These defaults, however, may not produce the optimum science data quality for many programs, and those images will require post-pipeline processing. Additionally, MAST creates drizzled products only for images taken in a single visit, so multiple visits can be drizzled together only by reprocessing.

While single visit data with small dithers (like the 4-point dither box) are usually aligned to better than 0.1 pixel, the drizzled products are created using the native detector plate scale, and with a drop size or PIXFRAC of 1.0. In these cases, the

resolution of the drizzled products can be improved by fine-tuning the final sampling by experimenting with the scale and pixfrac parameters.

Single-visit data with larger dithers (for example, to create mosaics) may have residual shifts of a few tenths of a pixel or more and residual rotations of a few thousandths of a degree. When combining data from different visits, tweaks to the image alignment are usually necessary since different sets of guide-star pairs may have been used. Offsets of the same target at different rolls are typically  $\sim 0.3$  to  $0.5''$ . See [Appendix B of the DrizzlePac Handbook](#) for more information.

Poor alignment can lead to improper cosmic-ray rejection, and inadvertent flagging of some astronomical sources as cosmic rays, compromising the photometric accuracy of the final data products. Additionally, a poor estimate of the sky background, for example in images where a bright target fills the frame, may also affect the accuracy of cosmic-ray rejection, and in turn, of the resulting photometry.

### 4.2.3 AstroDrizzle Documentation

**AstroDrizzle** is available as part of the **DrizzlePac** software, which contains all the tools for manually reprocessing (aligning and combining) calibrated HST data. This software may be obtained from the [DrizzlePac](#) webpage.

This page also provides useful resources such as the [DrizzlePac Handbook](#), a 'Quick Start Guide' to drizzling, a set of worked examples, and some basic video tutorials.

---

## 4.3 References

- V. Kozhurina-Platais, et al., 2009, *ISR 2009-34: WFC3 SMOV Proposal 11445 - IR Geometric Distortion Calibration*. <http://www.stsci.edu/hst/wfc3/documents/ISRs/WFC3-2009-34.pdf>
- V. Kozhurina-Platais, et al. 2009, *ISR 2009-33: WFC3 SMOV Proposal 11444 - UVIS Geometric Distortion Calibration*. <http://www.stsci.edu/hst/wfc3/documents/ISRs/WFC3-2009-33.pdf>
- V. Kozhurina-Platais, M. Dulude, T. Dahlen, C. Cox, 2012, *WFC3-ISR-2012-07: WFC3/UVIS and IR Multi-Wavelength Geometric Distortion*. <http://www.stsci.edu/hst/wfc3/documents/ISRs/WFC3-2010-08.pdf>
- V. Kozhurina-Platais, D. Hammer, N. Dencheva, & W. Hack, WFC3 ISR 2013-14, *Astrometric Correction for WFC3/UVIS Lithographic-Mask Pattern*. <http://www.stsci.edu/hst/wfc3/documents/ISRs/WFC3-2013-14.pdf>
- V. Kozhurina-Platais *ISR 2014-12: Astrometric Correction for WFC3/UVIS Filter-Dependent Component of Distortion*. <http://www.stsci.edu/hst/wfc3/documents/ISRs/WFC3-2014-12.pdf>
- S. Gonzaga, et al., 2012 *The DrizzlePac Handbook*. [http://documents.stsci.edu/hst/HST\\_overview/documents/DrizzlePac/DrizzlePac.cover.html](http://documents.stsci.edu/hst/HST_overview/documents/DrizzlePac/DrizzlePac.cover.html)
- L. Dressel, 2017. *Wide Field Camera 3 Instrument Handbook*, Version 9.0 (Baltimore: STScI)
- J. S. Kalirai, Cox, C., Dressel, L., et al., [WFC3 ISR 2010-08 Pixel Area Maps](#)

# WFC3-UVIS Sources of Error

## In this chapter . . .

5.1 Gain and Read Noise / 95
5.2 Bias Subtraction / 96
5.3 Dark Current and Hot Pixels / 97
5.4 UVIS Flat Fields / 101
5.5 Image Anomalies / 109
5.6 Generic Detector and Camera Properties / 112
5.7 UVIS Photometry Errors / 122
5.8 References: / 122

## 5.1 Gain and Read Noise

### 5.1.1 Gain

Photoelectrons that accumulate in a CCD pixel are read out (as voltage) and converted to data numbers (DN), often called Analog-to-Digital Units (ADUs), by the analog-to-digital converter (ADC). The ADC output is a 16-bit number, capable of producing a maximum of 65,535 DN for each pixel. A straightforward scheme in which one DN corresponds to one electron would make it impossible to measure signals larger than 65,535 electrons. The conversion gain, defined as the number of electrons per DN, provides a way of changing the dynamic range of electrons that can be measured. Although it is possible to operate the WFC3 CCD detector at gains of 1, 1.5, 2, and 4 e-/DN, only a gain of 1.5 e-/DN is supported. This gain permits sampling of the entire dynamic range of the detectors, with negligible impact on the readout noise. The gains for the WFC3 CCDs, routinely measured every year, have been stable to within 1-2% since launch in May 2009 ([WFC3 ISR 2013-02](#), [WFC3 ISR 2015-05](#)).

and [WFC3 ISR 2016-13](#)). The current values are summarized in [Table 5.1](#). The gains were measured in flat-field images via the standard mean-variance technique: the inverse slope of the mean signal level plotted versus the variance yields the gain.

**Table 5.1: WFC3/UVIS Gains (measurement errors are:  $\sim 0.01$  e-/DN)**

CCD Chip	Amp	Gain (e-/DN)
1	A	1.57
1	B	1.57
2	C	1.58
2	D	1.58

### 5.1.2 Read Noise

The average read noise level measured in the bias frame science area pixels at the default gain setting ( $1.5\text{e-/DN}$ ) are summarized in [Table 5.2](#). Scatter in the measurements based on data acquired between June 2009 and July 2015 is less than 1%, depending on the amplifier (WFC3 ISRs [2017-17](#), [2015-13](#), [2009-26](#))

**Table 5.2: WFC3/UVIS readout noise (electrons) and uncertainty for unbinned and binned modes.**

Mode	Amplifier A			Amplifier B			Amplifier C			Amplifier D		
Binning	1x1	2x2	3x3	1x1	2x2	3x3	1x1	2x2	3x3	1x1	2x2	3x3
Mean	2.97	3.11	3.22	3.03	3.15	3.26	2.95	2.99	3.09	3.06	3.29	3.38
Uncertainty	0.01	0.02	0.04	0.01	0.01	<0.01	0.00	<0.01	0.01	0.01	0.02	<0.01

An analysis of the statistical behavior of the WFC3 ADCs shows some tendency for the least significant bit to be slightly biased at the readout speed adopted by the WFC3 electronics (see [WFC3-ISR 2005-27](#)). This minor effect should not degrade the photometric and noise characteristics of the WFC3/UVIS images.

## 5.2 Bias Subtraction

### 5.2.1 Bias Calibration

Bias reference frames are acquired frequently for scientific calibration purposes and for monitoring the detector performance. Multiple bias frames are stacked into a

reference superbias image, removing the cosmic rays accumulated during the readout time enhancing the signal-to-noise ratio of the final results. **calwf3** performs the bias correction in two steps (see [Section 3.2.5](#) and [Section 3.2.6](#)). The first consists in subtracting a global bias level, measured from the overscan regions, which provide a measure of the instrument bias level at the time when the images are taken. The location of the overscan regions in a raw image varies, depending upon the type of readout that is performed. This overscan-based bias level is subtracted from the raw image through the `BLEVCORR` step in the WFC3 calibration pipeline. In the second step, residual two-dimensional bias structure is removed via the superbias reference file correction applied via the `BIASCORR` step.

### 5.2.2 Bias Correction for WFC3 Subarrays

When science data are obtained in subarray format, the requisite dark and flat-field corrections are obtained from the full-frame calibration files, extracted from the appropriate subregion. The superbias correction is also extracted from full-frame 4-amp readout superbias files (if the subarray resides entirely within a single detector quadrant). Tests have shown that this does not degrade the quality of the dark, flat-field or bias corrections as compared to full-frame data. For subarrays that span detector quadrants, special superbias files must be constructed from individual bias frames read out through the same amplifier as the subarray. For example, a single-chip readout (the largest possible subarray) read out through amp A must be calibrated with a superbias constructed from single-chip bias frames read out through amp A; similarly, science data read out through amp B must be calibrated with a superbias constructed from bias frames read out through amp B.

---

## 5.3 Dark Current and Hot Pixels

### 5.3.1 Dark Current

Superdark reference files are generated on a daily basis, with typically between 10 - 18 dark images (acquired over 4-5 days) in each superdark. The individual darks are recalibrated with the latest superbias file and most recent **calwf3** software version, stacked to remove cosmic rays and converted from DN to e-/sec. Any pixels with values  $> 54$  e-/hr are considered hot; their values are left unchanged in the science extension and flagged with a value of 16 in the DQ extension which is propagated into the final science image `*_flt.fits` DQ extensions. In this way, observers can decide whether to ignore hot pixels (for instructions on how to control which bit masks are used during drizzling, please consult the [HST DrizzlePac Handbook](#)) or to allow the dark subtraction to stand. Because the mean dark current in the WFC3 CCDs is so low ( $\sim 8$  e-/hr/pixel in late-2017) it is very difficult to achieve, with only 10-18 dark images, a useful signal-to-noise for pixels that have normal levels of dark current. Subtracting

these uncertain values from science images during **calwf3** processing would introduce noise into the calibrated images; therefore all good (non-hot) pixels in the SCI extensions of superdark reference images are set to an anneal-cycle-averaged value (i.e. each good pixel in the superdark reference image is set to the average value of that pixel over all individual darks in an anneal cycle, of order 100, see [WFC3 ISR 2016-08](#)) in the chip. Users can verify whether the darkfile most appropriate to their observations has been installed for pipeline use in several different ways:

- re-retrieving the images from the MAST, which automatically updates the headers and recalibrates the data
- by checking the CRDS ([Calibration Reference Data System](#)).
- using [Starview](#) to obtain a list of best reference files

Using an old superdark reference file can produce a poor dark correction: either leaving too many hot pixels uncorrected and unflagged, or creating many negative "holes" caused by the correction of hot pixels which were not actually hot in the science data (i.e., if the detectors were warmed to anneal hot pixels in the interim).

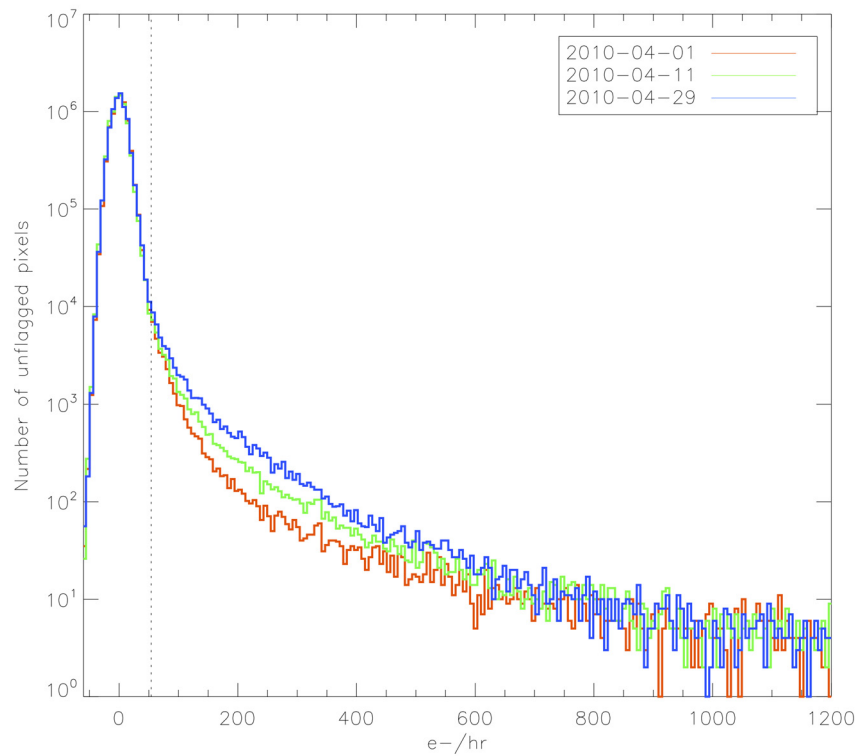
### 5.3.2 Hot Pixels

Two types of bad pixels are routinely monitored using on-orbit WFC3 data: hot pixels and dead pixels. Hot pixels, i.e., those pixels with a higher than normal dark current, are identified in dark frames using a threshold of 0.015 e-/sec (54 e-/hr). The cutoff was chosen based on the tail of the dark histogram in early on-orbit data (see [Figure 5.1](#)) as well as visual examination of the dark frames. The number of hot pixels increases over time due to on-orbit radiation damage; periodic anneal procedures, where the UVIS detector is warmed to ~20C, successfully fix a small percentage of the hot pixels. Hot pixel locations and levels are provided in the UVIS superdark reference files which are subtracted from science data, though dithering can mitigate their effect as well.

Dead pixels, specifically dead columns, are identified through visual inspection of both individual and stacks of internal frames. Bad pixel locations are propagated into the bad pixel mask (header keyword BPIXTAB and the file name \*\_bpx.fits) that is applied by **calwf3** in the standard data reduction pipeline. Currently there are ~8000 dead pixels in chip 1 (amps A and B) and ~16000 in chip 2 (amps C and D).



**Figure 5.1: Histograms of three dark images (hot pixel threshold of 0.015 e-/sec marked with vertical dotted line).**



### Trending

We have chosen a limit of 0.015 e-/s/pixel (54 e-/hr) as a threshold above which we consider a pixel to be "hot" based on the tail of the histogram as well as a visual examination of 900-s dark frames taken during Cycle 17. Figure 5.1 shows a histogram of CR-free pixels from 900-s darks taken at three different times after the April 2010 anneal procedure: immediately following the procedure (red line), about 10 days later (green line) and about 18 days later (blue line). The increase in hot pixels due to on-orbit radiation damage is apparent; the anneal procedures have been found to fix a fraction of the hot pixels which accumulate over time. The hot pixel cutoff is shown with a vertical line at 54 e-/hr; at this threshold, the growth rate for WFC3 hot pixels is ~1000 pixel/day (see [WFC3 ISR 2016-08](#) for more information on darks and hot pixels).

Figure 5.2 shows the number of hot pixels as a function of time since the installation of WFC3 on HST. The monthly anneal intervals are represented by the alternating grey and white regions while the red vertical lines represent the Science Instrument Command and Data Handling Unit (SIC & DH) lockups, when (prior to Oct 2009, WFC3 SIC&DH lockups warmed the chips i.e. essentially another anneal).

Since Nov 8, 2012 (green vertical line), the UVIS darks have been post-flashed, i.e., a background of 12 e-/pixel is applied to each image. Post-flashing preserves faint signal in pixels far from the amps that otherwise would have been undetectable due to

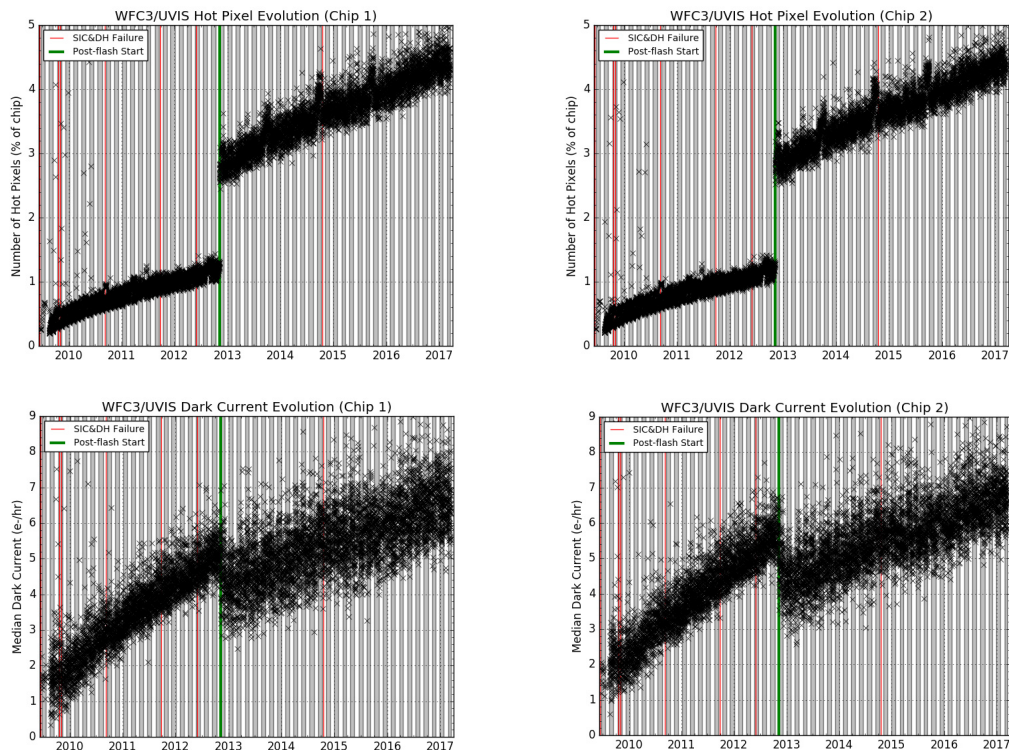


CTE losses. The result is a jump in the number of \*detected\* hot pixels. In addition, the suppression of CTE trails by the post-flash also causes a commensurate reduction in the overall measured dark current. CTE trails are also removed by the pixel-based algorithms. Dark current and hot pixel plots are updated, as resources allow, on the [WFC3 Performance Monitoring webpage](#).

The WFC3 CCD detectors degrade over time due to exposure to the space environment. This damage manifests itself in the darks as an increase in the number of individual hot pixels as well as in an overall higher dark current (CTE losses, another manifestation of damage, is discussed in [Chapter 6](#)). Based on a fit to non post-flashed dark frames taken since launch, the median dark current (excluding hot pixels) is increasing by  $\sim 0.5$  e-/hr/pixel/year and is currently at  $\sim 8$  e-/hr/pixel ([Figure 5.2](#)). The number of permanent hot pixels, i.e., pixels that the anneals are unable to fix, is growing by about 35/chip/day, or 0.05-0.1% per month.

**Figure 5.2: Percentage of UVIS hot pixels ( $>0.015$  e-/s) versus time**

**At top: Percent of UVIS hot pixels ( $>0.015$  e-/s) versus time for Chip 1 (top left) and Chip 2 (right). At bottom: median UVIS dark current as a function of time. The green vertical line (Nov 8, 2012) marks the start of post-flash for UVIS dark frames (see text). Monthly anneal intervals are marked by the grey and white regions. The red vertical lines mark SIC & DH failures. (The published plots were updated on March 20th 2017.)**



## 5.4 UVIS Flat Fields

The UVIS flat fields provide a spatial map of the total instrument response and represent the combined throughput of multiple components along the optical path. The flats include both a high spatial frequency component that accounts for variations in the pixel-to-pixel response (P-flat) and a low spatial frequency component (L-flat) that corrects for large-scale modulations across the detector, and as such are often referred to as LP-Flats.

The flats in use from WFC3's commissioning in 2009 (`t*_pfl.fits`) were derived from ground test data ([WFC3 ISR 2008-46](#)). These flats were found to contain a large internal window reflection affecting ~45% of the detector field of view at a level of 1-2%. A simplified geometric model was used to remove this feature from the ground flats ([WFC3 ISR 2011-16](#)). Corrections for additional low frequency components, due to differences between the ground and in-flight optical paths, were computed from on-orbit photometry of bright stars in Omega Centauri dithered across the detector ([WFC3 ISR 2013-10](#)). In-flight solutions (`v*_pfl.fits`) were delivered on December 14, 2011 for the 42 full-frame filters (excluding the QUAD filters which currently still use the ground flats). Flats for  $2 \times 2$  and  $3 \times 3$  binned modes (`w*_pfl.fits`) were delivered on August 29, 2012 (WFC3 TIR 2012-04).

To support the new chip-dependent photometric calibration, a new set of flat fields (`z*_pfl.fits`) were delivered on February 23, 2016 ([WFC3 ISR 2017-07](#)). These include revised L-flat corrections based on CTE-corrected Omega Centauri photometry, and a new temperature-dependent correction for the UV filters. The photometric repeatability of white dwarf standards stepped across the field of view is now better than 1% r.m.s. and 3% peak-to-peak over the full wavelength range of the detector ([WFC3 ISR 2016-04](#) and [WFC3 ISR 2016-05](#)).

### 5.4.1 Ground Flats

In the spring of 2008, flat fields for the UVIS channel were produced at the Goddard Space Flight Center during the third and final thermal vacuum campaign (TV3) using the CASTLE Optical Stimulus (OS). CASTLE, which stands for Calibration Stimulus from Leftover Equipment, is an HST simulator capable of delivering OTA-like, external, monochromatic point source and broadband full field illumination. Flats were acquired in only the standard CCD readout configuration of four amplifiers (ABCD), gain=1.5 and binning= $1 \times 1$ . Flat fields with the OS Xenon and Halogen lamps were taken with the detector at its nominal operating temperature of -82C. Flats for the ultraviolet (UV) filters were acquired at a warmer detector temperature (-49C) using the deuterium lamp to achieve higher count rates.

With a total signal of at least 75,000 electrons, the UVIS flat fields achieve an r.m.s. error better than 0.4% per pixel. The ground flats were normalized by the median value in a  $100 \times 100$  pixel region in UVIS1 amplifier A, coordinates [1032:1133,328:429]. This region was selected to avoid the small dark rings ("droplets") that are spread across the UVIS field of view. The droplets are likely

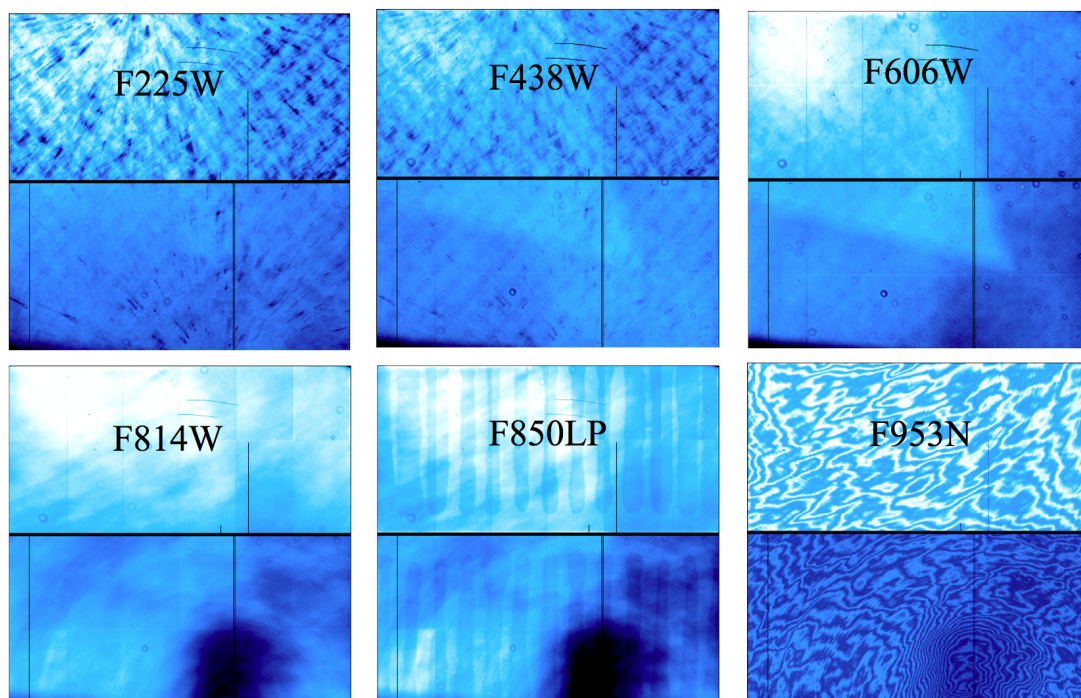
mineral residue on the outer window of the flight detector caused by a condensation event that occurred before TV3 ([WFC3 ISR 2008-10](#)). About one-third of these droplets moved in a coherent way during launch ([WFC3 ISR 2009-27](#)).

Unlike the ACS/WFC detector, the two UVIS chips were not cut from the same silicon wafer and should be considered as two independent detectors. For the 42 full-frame filters, the UVIS2 flats were divided by the UVIS1 normalization value in order to preserve the overall sensitivity difference between chips. In this way, calibrated flat-fielded (\*\_flt.fits) or drizzled (\*\_drz.fits) data products only required the use of a single zeropoint value for each filter. For the QUAD filters, on the other hand, each quadrant was normalized using a  $100 \times 100$  pixel box in the corresponding amplifier, and therefore each carries its own unique zeropoint.

Because of geometric distortion, the area of the sky seen by a given pixel is not constant; therefore, observations of a uniform surface brightness object will have count rates per pixel that vary over the detector, even if every pixel has the same sensitivity. In order to produce images that appear uniform for uniform illumination, the flat fields include the effect of the variable pixel area across the field. A consequence of dividing by these flat fields is that two stars of equal brightness falling on different portions of the detector will not have the same total counts in a calibrated (\*\_flt.fits) image. To correct for this effect, point source photometry extracted from flat-fielded images should be multiplied by the effective pixel area map (see [Section 9.1.11](#)). Alternatively, this correction is accounted for in the pipeline by AstroDrizzle (see [Section 4.2](#)), where the distortion reference files are used to correct all pixels to equal area on the sky for drizzled (\*\_drz.fits) data products.

A subsample of ground test UVIS flat fields are shown in [Figure 5.3](#). A complete set may be found in the ‘UVIS CASTLE Photometric Filter Flat-Field Atlas’ ([WFC3 ISR 2008-46](#)). On-orbit corrections to the flat fields are described in the next two sections.

**Figure 5.3: A subset of flat fields obtained during ground testing, where dark regions correspond to lower response pixels. Notable features include a cross-hatch pattern at wavelengths less than 500 nm due to structure in the detection layer, a large diffuse spot in UVIS2 for wavelengths greater than ~600nm due to variations in the detector thickness, vertical striping in the long pass filters which see through the detector to glue adhesive on the other side of the CCD, and fringing in narrow band filters at wavelengths greater than ~600nm.**



### 5.4.2 On-orbit Corrections

Due to differences in the optical path, flat fields acquired in-flight were expected to differ from those obtained during ground testing, since neither the laboratory flat-field illumination nor the on-orbit internal lamp flats provides an accurate simulation of the OTA. Corrections to the spatial response were characterized by observing dense star clusters with multiple telescope orientations and large dithered steps across the detector ([WFC3 ISR 2009-06](#)). Placing the same stars over different portions of the detector and measuring relative changes in brightness, local variations in the response (L-flats) were computed.

Initial on-orbit data confirmed that the ground flats did not fully correct low- and mid-frequency structure, and SMOV calibration program 11452 (UVIS Flat-Field Uniformity) showed differences of ~1.5 to 4.5% in a subset of 6 filters based on observations of two galactic globular clusters (see ([WFC3 ISR 2009-19](#))). Supplemental observations were obtained in Cycles 17 and 18 (programs 11911 & 12339) in a key set of 10 broadband filters used most frequently by observers: F225W, F275W, F336W, F390W, F438W, F555W, F606W, F775W, F814W, F850LP.



The same mathematical algorithm for deriving ACS in-flight corrections ([ACS ISR 2003-10](#)) was used to characterize the accuracy of the UVIS ground flats. Aperture photometry was performed on the cluster data with a radius of 0.2'' (5 pixels) to minimize uncertainties due to crowding. Then, a spatially variable aperture correction to 0.4'' (10 pixels) was applied to each image to account for variations in the PSF with detector position and telescope focus, including temporal effects such as breathing and long term focus drifts ([WFC3 ISR 2013-11](#)). Because of spatial and temporal variability in the UVIS encircled energy, the aperture corrections for radii smaller than 0.4'' (10 pixels) are most accurate when computed directly from bright stars in each image.

The first set of L-flat corrections showed evidence of an extended wedge shaped artifact in the ground flats (see [Figure 5.3](#) where the wedge is most prominent in the F606W flat). This same feature was noticed in on-orbit flats obtained by observing the dark side of the Earth during periods of full moon illumination (programs 11914 and 12709). This extended feature, dubbed the UVIS 'flare', is a result of the tilted UVIS focal plane, where light is reflected multiple times between the detector and the two chamber windows. When a point source is positioned in the lower right quadrant of the UVIS detector, out of focus reflections between the CCD and the two windows appear along a diagonal from the source towards the upper left (see [Section 5.5.1](#)). When the detector is illuminated by a uniform surface brightness source, the summation of defocused ellipses creates the wedge shaped 'flare' apparent in both the ground flats and the on-orbit Earth flats. The L-flat residuals showed a negative imprint of the flare, implying that it is not a true feature of the L-flat, but instead an internal reflection in the ground flat which is imprinted on the Omega Centauri images during the flat fielding process.

A geometric model ([WFC3 ISR 2011-16](#)) was used to predict the shape and extent of the flare and the relative strength of the four internal reflections with respect to the primary source (see [Figure 5.4](#)). The absolute strength of the flare as a function of wavelength was estimated from the preliminary L-flat solutions, and this was used to scale and divide the model from the ground flats. L-flats were then recomputed from cluster photometry recalibrated with flare-free ground flats. Sensitivity residuals for the 10 broadband filters are shown in [Figure 5.5](#), represented as a chessboard grid of basis functions of order  $2^n$ , where the 4<sup>th</sup> and 5<sup>th</sup> order solutions result in a  $16 \times 16$  and  $32 \times 32$  pixelated version of the UVIS detector (with each grid pixel representing an independent solution). With the exception of the two bluest UV flats, which were obtained with the detector running warmer than usual during ground testing, the sensitivity residuals show a general wavelength dependence, where the required correction deviates from unity more at longer wavelengths compared to shorter ones.

**Figure 5.4: Geometric model of the UVIS flare as a set of 4 internal reflections for a source that uniformly illuminates the detector.**

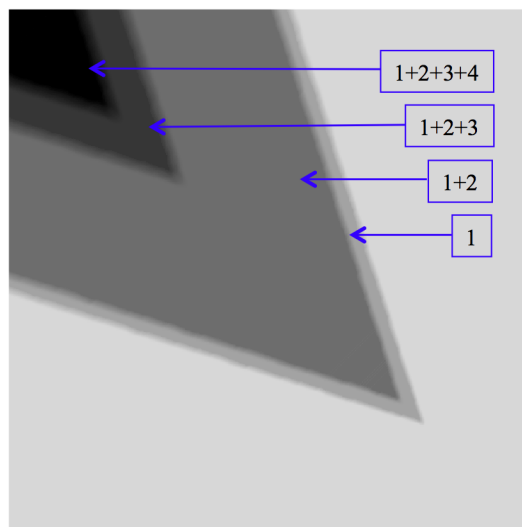


**Figure 5.5: Low frequency corrections to the flare-corrected ground flats for 10 filters. Blue indicates regions of the detector where the flats overcorrect the data, making the photometry too faint. The solutions are presented as a  $32 \times 32$  grid, such that one grid pixel corresponds to  $128 \times 128$  detector pixels. The exceptions are F225W, F275W, and F850LP for which  $16 \times 16$  grid solutions were used, and one grid pixel corresponds to  $256 \times 256$  detector pixels.**

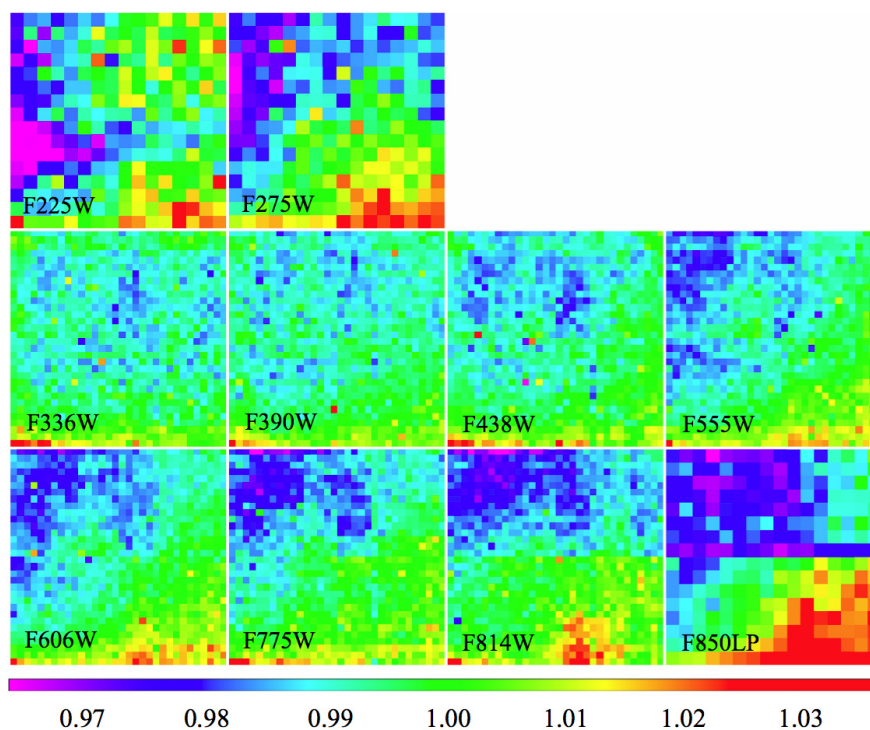
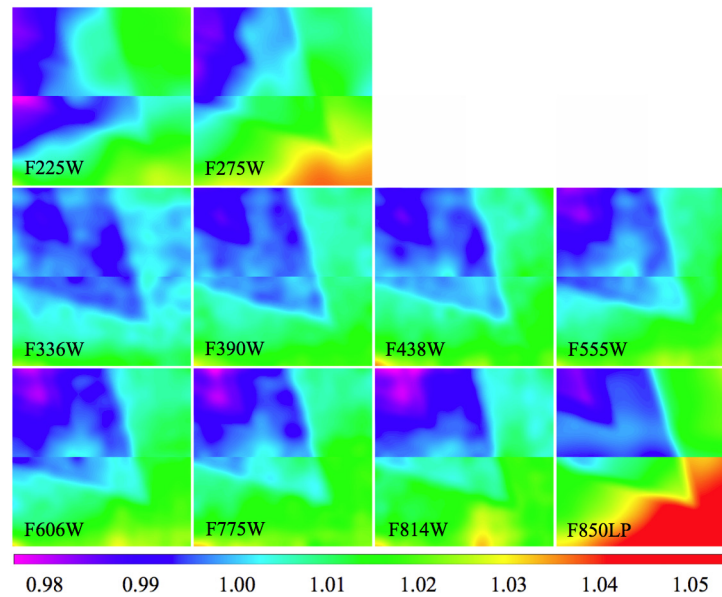


**Figure 5.6: Ratio of the 2011 pipeline flats to the 2009 ground flats. Blue indicates that the ground flats overcorrect the data, making sources too faint. The residuals include contributions from both the flare and the stellar L-flat.**



Rather than carry a separate set of L-flat reference files, revised LP-flats were created by multiplying the ground P-flats (flare removed) with smoothed versions of the pixelated L-flat. [Figure 5.6](#) shows the ratio of the improved 2011 pipeline flats with respect to their 2009 solutions for the 10 broadband filters with on-orbit calibration data. The 2011 solutions differ by 0.6 to 1.8% rms, with a maximum change of ~2.8 to 5.5%, depending on filter ([WFC3 ISR 2013-10](#)).

For the remaining 32 full-frame filters, flat-field corrections (including both the flare and the stellar L-flat) were computed via interpolation based on the filter pivot wavelength, using the weighted average of the residual flat for the two filters nearest in wavelength. The wavelength dependence of both the flare and the L-flat in [Figures 5.5](#) and [5.6](#) suggests that interpolation is a valid approximation for filters with no available on-orbit cluster data.

To quantify the accuracy of the new flat fields, white dwarf standards were stepped across the detector field of view to measure their photometric repeatability. For filters with pivot wavelength greater than 300nm, photometry in a 10-pixel aperture was repeatable to better than 0.7% rms and 2.7% peak-to-peak. The flux residuals showed a weak correlation with position (e.g. the number of y-transfers), suggesting that some of the spatial variation was due to CTE losses during readout at a level of 0.5-1.0%. For UV filters, the photometric residuals from stepped data calibrated with the 2011 flats were 1.8% rms and 6.7% peak-to-peak ([WFC3 ISR 2015-18](#)).

The 2011 in-flight flats corrected for sensitivity offsets between the two chips using dithered stellar photometry, but the average cluster population is significantly redder than the stepped white dwarfs used to derive the zeropoints. When dividing the cluster stars into separate populations by their intrinsic color, differential photometry of sources dithered between the chips showed offsets in the measured count rate that

correlated with the source's intrinsic color. For the UV filters, this offset was as large as 5% in F225W for blue versus red populations, though red leaks ([Section 6.5.2 of the \*WFC3 Instrument Handbook\*](#)) limit the accuracy of this prediction at the 1-2% level.

### 5.4.3 Chip-Dependent Flats

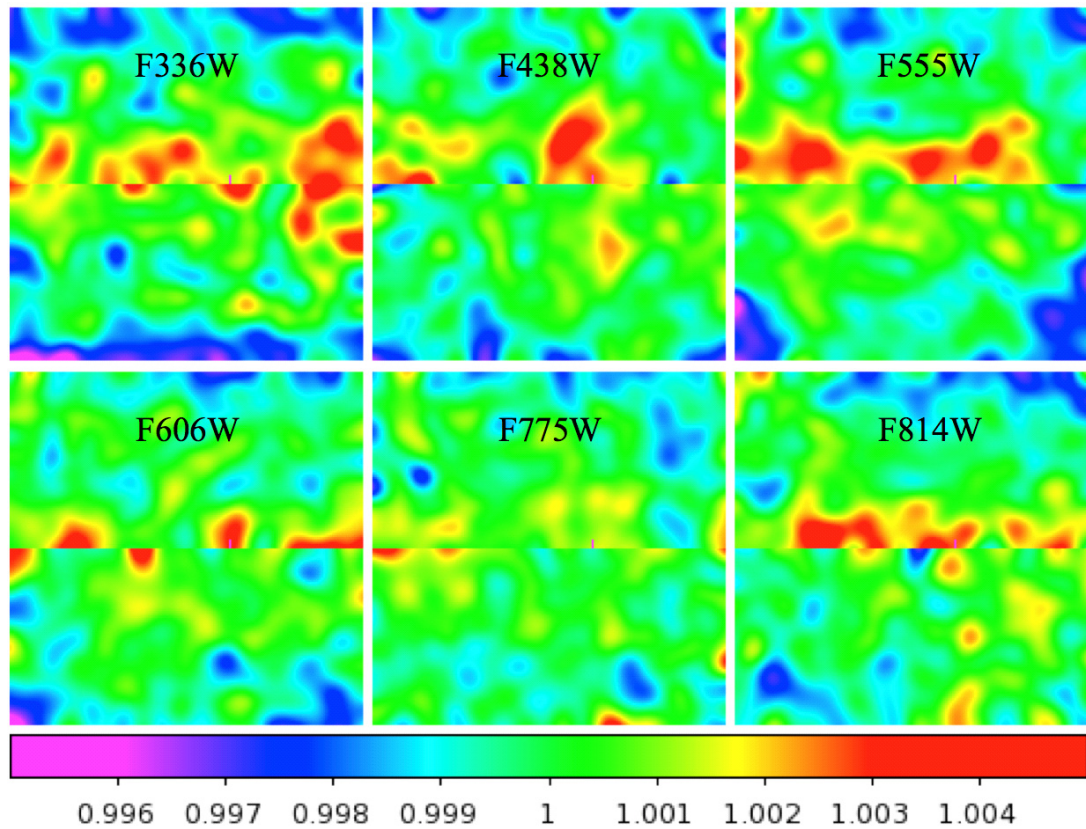
The quantum efficiencies of the two UVIS chips differ at wavelengths shorter than about 400 nm (see [Section 5.4.1 of the \*WFC3 Instrument Handbook\*](#)). Motivated by this, a chip-dependent approach to the photometric calibration was adopted in February 2016 to better track any changes with time as the two detectors age. Prior to this date, sensitivity offsets between chips were derived from stars in Omega Centauri dithered between UVIS1 and UVIS2, as described in [Section 5.4.2](#), and these were corrected by **calwf3** as part of the flat fielding step (FLATCORR). Photometric keywords such as PHOTFLAM, the inverse sensitivity, were then populated in the image header via the PHOTCORR photometry switch, where a single value of PHOTFLAM applied to both UVIS1 and UVIS2.

In the chip-dependent approach, the L-flats were computed from CTE-corrected star cluster data using stars dithered over a single chip only. The LP-flats were then normalized by the median value of each chip. To ensure that count rate photometry in calibrated data remains continuous across the two chips, **calwf3** (version 3.3+) makes use of a new calibration switch (FLUXCORR), which multiplies the UVIS2 science extension by the sensitivity ratio (PHTRATIO) of the two chips (see [Section 9.1](#) and [WFC3 ISR 2014-16](#) for details). This ratio is empirically derived from photometry of white dwarf standards measured for UVIS1 and UVIS2 separately as part of the UVIS photometric calibration program ([WFC3 ISR 2016-03](#)).

For the majority of filters, the improvement in the chip-dependent flats is small and is primarily attributed to correcting for CTE losses in the star cluster data used to determine the L-flat. [Figure 5.7](#) shows the ratio of the CTE-corrected L-flat to the 2011 L-flat for six broadband filters, where the total correction from the center to edge of each chip is on average 0.6%.



**Figure 5.7: Ratio of the 2016 to 2011 L-flat, showing the change after applying CTE-corrections to the Omega Centauri calibration data. The color bar spans a range of 1%.**

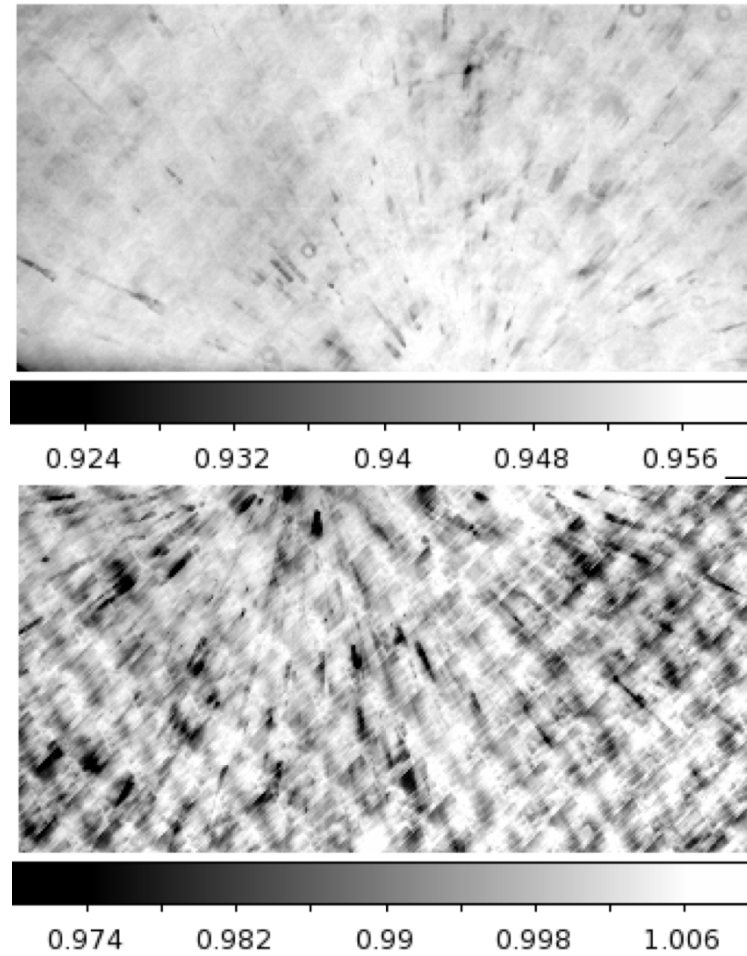


Flats for the four bluest UVIS filters (F218W, F225W, F275W, F280N) include an additional correction to the spatial response with temperature. Due to ground equipment limitations, these flats were obtained at a warmer detector temperature ( $-49^{\circ}\text{C}$ ) during ground testing and have now been corrected with in-flight data (obtained at  $-82^{\circ}\text{C}$ ). White dwarf standard stars stepped across the two chips showed flux residuals which correlate with a crosshatch pattern in the UV flat fields at spatial scales of  $\sim 50 - 100$  pixels. These data were used to derive a linear correction model which improves the spatial repeatability from  $\sim 7\%$  to  $\sim 3\%$  peak-to-peak (WFC3 ISR 2016-05). Figure 5.8 shows the ratio of the 2016 to 2011 flats for F275W, where the crosshatch correction is more pronounced for UVIS1.

The UVIS chip-dependent calibration is intended to produce uniform count rates across the two chips for sources similar in color to the white dwarf standards. As discussed in Section 5.4.2, count rate offsets of several percent are found in the UV for red versus blue stars, but these appear to impact only the photometric zeropoints and not the flat fields themselves. Monochromatic flats obtained during ground testing with an optical stimulus at wavelengths 310, 530, 750, and 1250 nm showed no evidence of spatial residuals in the flat ratio with wavelength. For the most accurate UV photometry, users may wish to ‘back out’ the UVIS2 scaling performed by **calwf3** and apply separate zeropoints to each detector (WFC3 ISR 2017-07). For targets with multiple populations observed in the UV, corrections to the photometric zeropoints as

a function of spectral type may be derived using pysynphot (see [Section 9.1](#) for details).

**Figure 5.8: Flat ratio 2016/2011 flats for F275W, with the color bar for each chip spanning a total range of 4%, but offset by 5% to account for the chip sensitivity offset. The new UV flats correct for mid-frequency residuals in a crosshatch pattern that are a result of the colder in-flight operating temperature.**



## 5.5 Image Anomalies

Some UVIS images may contain features that are not direct images of astronomical sources. The causes of these features include multiple reflections between optical surfaces (detector, filters, and windows) of light from the astronomical scene, scattered light from bright sources outside the detector FOV, light from the bright Earth that is scattered in the OTA, and electronic cross talk between readout amplifiers. In general, these artifacts are not calibrated and cannot be removed by the WFC3 pipeline.

Examples of the different kinds of image anomalies can be found on the [WFC3 website](#).

### 5.5.1 Ghosts

Ghosts appear as images of the pupil formed from the light of a bright target in, or near, the UVIS detector FOV. The target light is scattered twice (or more) by optical surfaces forming one (or more) out of focus images. The separation of the ghost from the source depends upon the separation of the scattering surfaces and the angle of scattering. Filter ghosts are formed by scattering of the near-normal source light at the surfaces of a filter and, as such, are found close to, or overlapping, the source image. Further details concerning these ghosts may be found in [WFC3 ISR 2007-09](#).

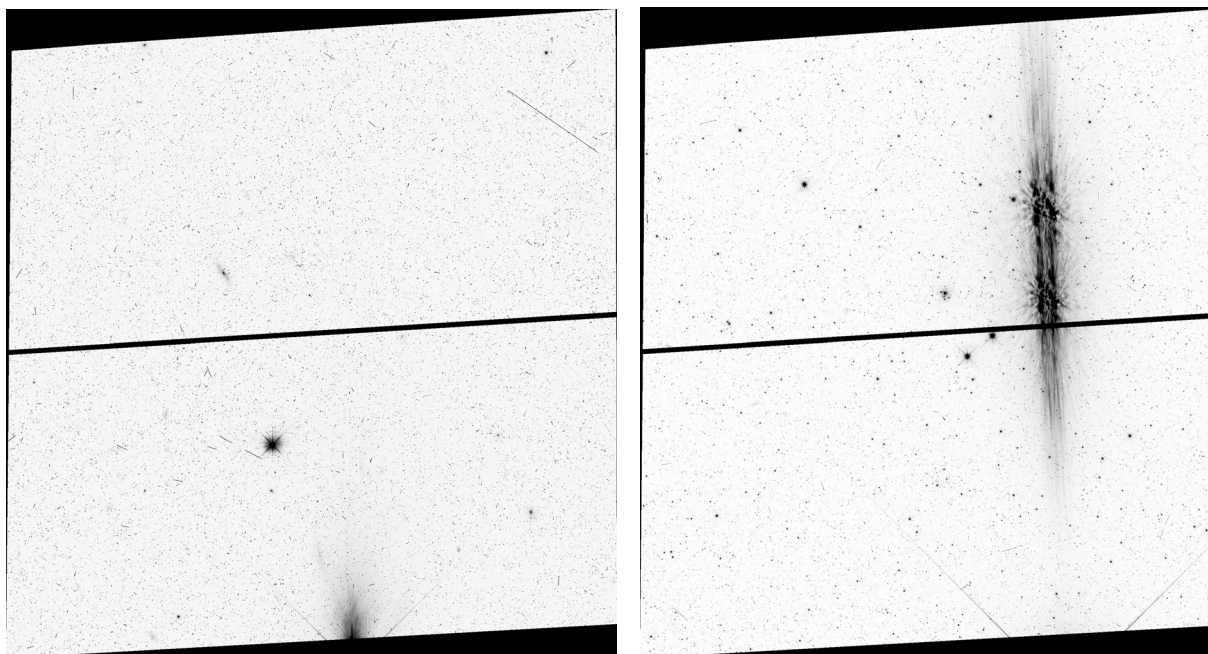
Scattering between the UVIS CCD and either the detector, or dewar window forms so-called ‘optical’ ghosts. These ghosts are separated by ~80" from their source generally in pairs (a "figure eight"). Further details may be found in [WFC3 ISR 2001-17](#), [WFC3 ISR 2004-04](#), [WFC3 ISR 2007-21](#) and [WFC3 ISR 2011-16](#).

### 5.5.2 Dragon’s Breath and Scattered Light

Bright sources immediately outside the image frame on WFC3/UVIS can create (mostly minor) light anomalies in the form of spurious signal redirected into the field of view and affecting the image (see [Figure 5.9](#)). Dragon’s Breath (when the light originates from the edge) or Scattered Light (when the light is somewhat displaced from the edge) affect about 12% of a subset of images recently surveyed. It occurs when a bright source lies within the 20" area outside of the image frame, and peaks when the neighboring source has a V band magnitude around 11.9 or 14.6 ([WFC3 ISR 2017-02](#)). The source of scattering along the optical path is not completely understood. Most cases of Dragon’s Breath and Scattered Light are minor and will not adversely affect a science image.

**Figure 5.9: Dragon’s Breath and Scattered Light on WFC3/UVIS**

Examples of Dragon’s Breath and Scattered Light on WFC3/UVIS. Left: Dragon’s Breath spills into the image frame from the bottom of the image. Right: Scattered light projects into the center of the image from a source directly underneath. (These examples are shown because they obviously visually demonstrate the effect, but most cases of Dragon’s Breath are much less dramatic both in number of affected pixels and flux from the effect.) For an interactive catalog of Dragon’s Breath affected images see: [http://www.stsci.edu/hst/wfc3/ins\\_performance/anomalies/bokeh\\_dragon.html](http://www.stsci.edu/hst/wfc3/ins_performance/anomalies/bokeh_dragon.html)



### 5.5.3 Cross Talk

Whenever two or more quadrants are read out simultaneously, there is a chance of generating electronic crosstalk (Janesick 2001). Both channels in WFC3 do exhibit some crosstalk (CT) though the level is very low. In the UVIS detectors, point sources and extended targets generate low-level mirror images in the quadrant adjoining the target quadrant, i.e., amps A+B and amps C+D are coupled. In the IR channel, the CT is also a low-level mirror image although in this case, the coupled amps are 1+2 (upper left and lower left, when image is displayed with  $x=1, y=1$  at lower left) and 3+4 (upper right and lower right). In both channels, the CT appears as a negative image; thus, these electronically induced features are unlikely to be confused with e.g. optical ghosts.

Figure 5.10 shows a UVIS image with CT (from WFC3 ISR 2009-03). The UVIS crosstalk is linear, negative, and appears at the level of  $\sim 10^{-4}$  to  $10^{-5}$  of the source. Specifically, in full-frame, unbinned UVIS readouts, the CT level is  $\sim 2 \times 10^{-4}$  of the source when the target is in quadrants A or C and about  $8 \times 10^{-5}$  when the target is in quadrants B or D (WFC3 ISR 2009-03).

Crosstalk in the UVIS channel only occurs in the chip containing the target, it does not cross between chips. To within the errors, the CT due to hot pixels and cosmic rays is the same as for point or extended sources. Dithering of observations can help mitigate the low-level effects of CT: the mirror image nature of the CT moves the



features in a direction opposite to the target motion, i.e., they will appear to be transients and thus be removed during the drizzling procedure.

A standalone IDL procedure is available for correcting UVIS data for crosstalk, effectively restoring pixels to a mean, which is well within 1 sigma of the mean of surrounding pixels. The code is described in [WFC3 ISR 2012-02](#) and can be downloaded at:

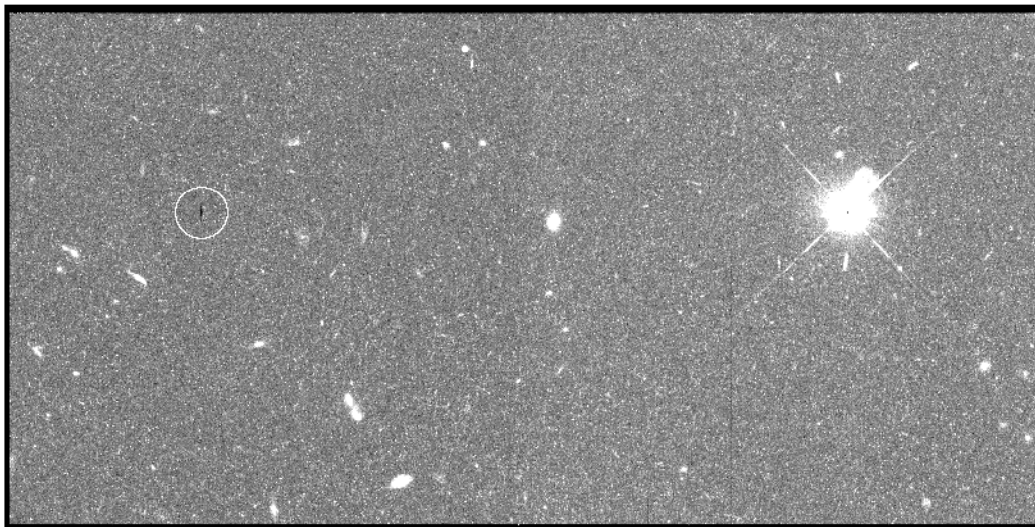
<http://www.stsci.edu/hst/wfc3/tools/crosstalk>.

A standalone python procedure is also now available for correcting UVIS data for crosstalk. The code as well as a description of its use is available at:

[http://www.stsci.edu/hst/wfc3/ins\\_performance/anomalies/python\\_crosstalk\\_correction.zip](http://www.stsci.edu/hst/wfc3/ins_performance/anomalies/python_crosstalk_correction.zip)

**Figure 5.10: UVIS Crosstalk.**

UVIS crosstalk (shown with a hard stretch to emphasize the CT). The slightly saturated star is in the B quadrant at right; the resulting mirror image CT (circled) is in the A quadrant at left. The partial dark column below and to the left of the PSF is a bad column.



## 5.6 Generic Detector and Camera Properties

### 5.6.1 Full Well Depth

Conceptually, full well depths can be derived by analyzing images of a rich starfield taken at two significantly different exposure times, identifying bright but still unsaturated stars in the short exposure image, calculating which stars will saturate in the longer exposure and then simply recording the peak value reached for each star in electrons (using a gain that samples the full well depth, of course). In practice, it is also necessary to correct for a ~10% "piling up" effect of higher values being reached

at significant levels of over-saturation relative to the value at which saturation and bleeding to neighboring pixels in the column begins (see [WFC3 ISR 2010-10](#)).

Since the full well depth varies over the CCDs, it is desirable to observe a rich star field with a gain that samples the full well depth (e.g. the default WFC3 UVIS gain), and for which a large number of stars saturate. Calibration and GO programs have serendipitously supplied the requisite data of rich fields observed at two different exposure times.

There is a real and significant large-scale variation of the full well depth on the UVIS CCDs. The variation over the UVIS CCDs is from about 63,000 e- to 72,000 e- with a typical value of about 68,000 e-. There is a significant offset between the two CCDs, as visible in Figure 5 of [WFC3 ISR 2010-10](#).

### 5.6.2 Linearity at Low to Moderate Intensity

Linearity at low and moderate exposure levels is measured by comparing back-to-back exposures of NGC 1850. [Figure 5.11](#) shows the response of UVIS2, where aperture sums for stars with flux greater than about 2,000 e- in a short exposure (central pixel would be at greater than about 350 e-) show apparently perfect linear response when compared to the counts in the same aperture in an exposure 50 times as long. However, below a level of 2,000 e- the ratio of long to short exposure counts deviates from a linear response. At total aperture flux of about 200 e- in the short exposure, the total flux values are ~ 5% lower than expected based on scaling from the corresponding long exposure.

[Figure 5.12](#) shows data from both UVIS CCDs for stars yielding short exposure aperture sums of 500 to 2000 e-. A clear signature appears that is consistent with perfect linearity for stars near the readout amplifiers, with linearly growing losses in the short relative to long exposure with distance from the amplifiers. This is consistent with losses induced by finite charge transfer efficiency in successive parallel shifts in clocking the charge packets off the CCDs.

The WFC3 team constantly monitors the extent to which CTE losses influence faint object photometry. Results from the past and ongoing calibration programs are summarized in [Chapter 6](#).

**Figure 5.11: Loss of linearity at low and moderate intensity due to finite Charge Transfer Efficiency.**

The upper panel shows the counts in  $r = 3$  pixel apertures for several thousand stars in back-to-back 500s and 10s exposures plotted against each other. To better illustrate small differences, the lower panel shows the same data after binning and plotting as the ratio of long to short, which in this case would result in values of 50.0 for perfect linearity.

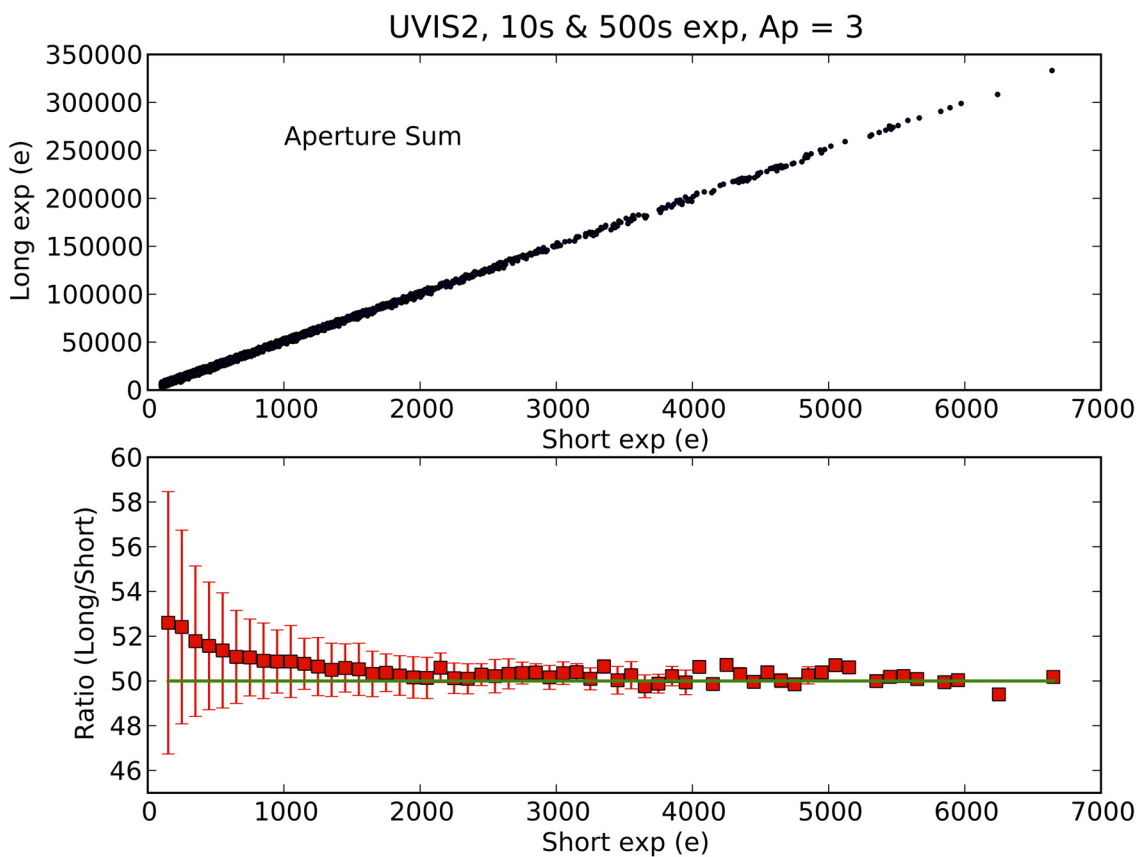
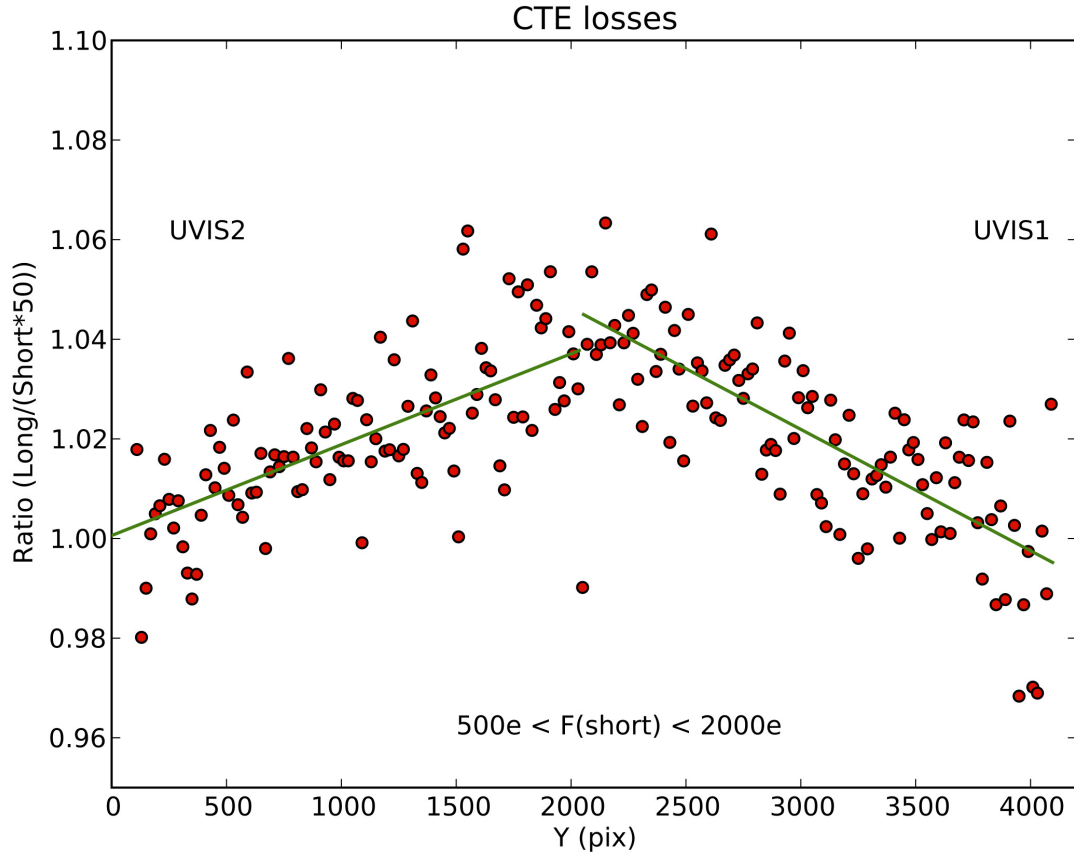


**Figure 5.12: CTE Losses For Short Exposure Image for UVIS1 and UVIS2**

Ratio of fluxes in short and long exposures as a function of Y position. This shows the data from the previous figure for UVIS2, plus similar data for UVIS1 plotted against y-position in the concatenated detector space. Y-values near 2050 correspond to the maximum distance from the readout amplifiers, and hence the most parallel shifts inducing CTE losses.



### 5.6.3 Linearity Beyond Saturation

The response of the WFC3 UVIS CCDs remains linear not only up to, but well beyond, the point of saturation. [WFC3 ISR 2010-10](#) shows the well behaved response of WFC3: electrons are clearly conserved after saturation -- in some locations with the need for a minor calibration, as provided in the ISR, in other regions no correction is needed. This result is similar to that of the STIS CCD ([Gilliland et al. 1999](#)) the WFPC2 camera ([Gilliland, 1994](#)) and ACS ([ACS ISR 2004-01](#)). It is possible to easily perform photometry on point sources that remain isolated simply by summing over all of the pixels into which the charge has bled.

To characterize the accuracy of point source photometry for sources in which one or more pixels have exceeded the physical full well depth we used a dataset consisting of multiple exposures taken back-to-back on a moderate-to-rich star field with a broad range of exposure times resulting in both unsaturated and saturated data for many stars.

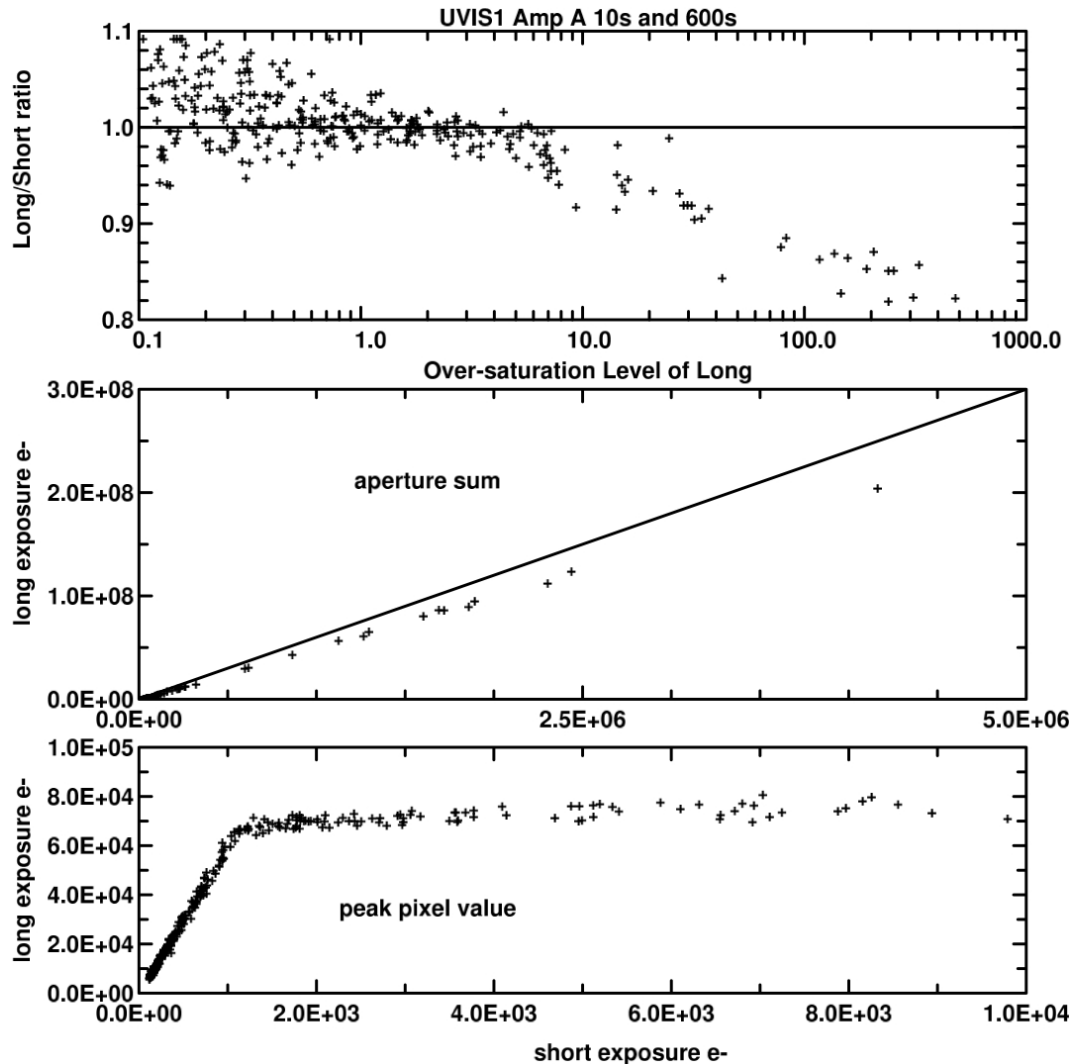


Results for Amp A are summarized in Figure 5.13 and Figure 5.14. Over a range of nearly 7 magnitudes beyond saturation, photometry remains linear to  $\sim 1\%$  after a simple correction (taken from WFC3 ISR 2010-10). For Amp C the response is sufficiently linear beyond saturation that no correction is required.

These results are based on the use of FLT images. The flux conservation ensured by AstroDrizzle leads to equally good results for linearity beyond saturation when comparing long and short \*\_drz.fits images.

**Figure 5.13: Linearity Analysis for Amp A**

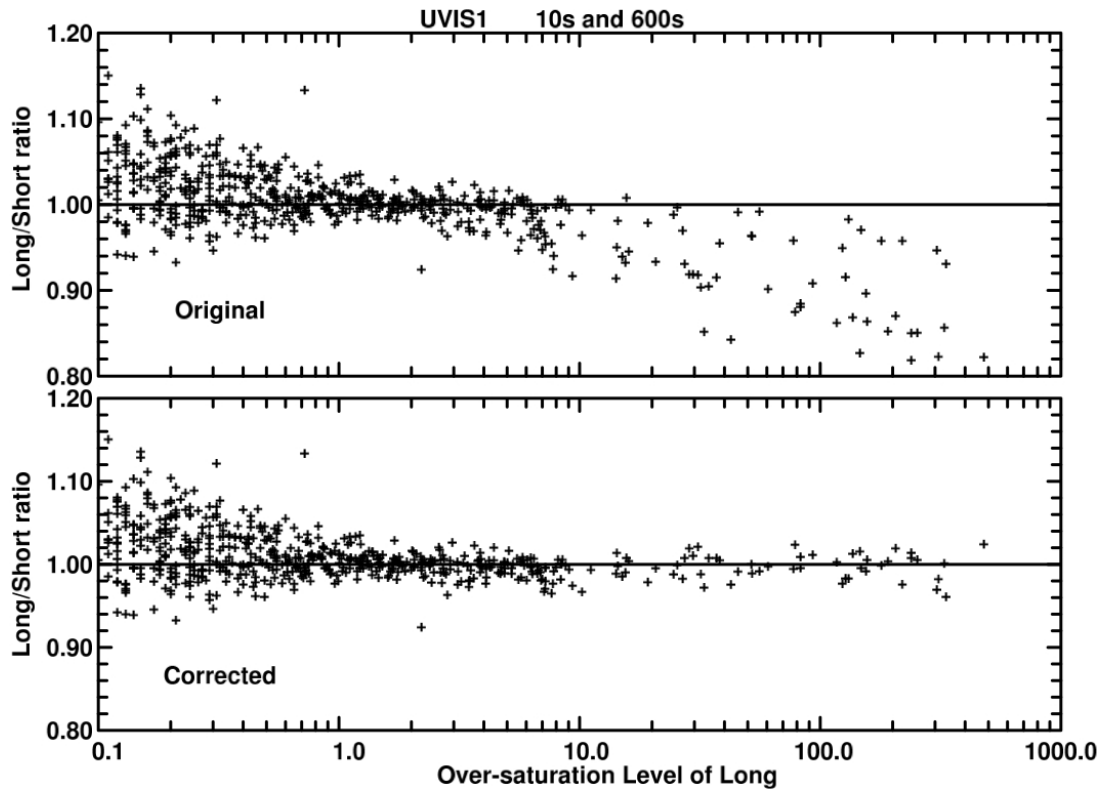
Analysis of linearity beyond saturation for Amp A on UVIS1. The upper panel shows the ratio of counts in the long exposure divided by the counts in the short exposure multiplied by the relative exposure time; linearity would thus result in a value of unity. The x-axis shows the multiplicative degree by which a star is over-saturated in the long exposure. The middle panel shows the long exposure aperture sums versus short exposure aperture sums. The lower panel shows the peak data value in the long exposure relative to the short exposure value. The response is linear up to the value of 68,000 e<sup>-</sup> (y-axis) where the long exposure encounters saturation. Amp A data show significant deviations from a linear response for over-saturations near and beyond 10.



Analysis of linearity beyond saturation for Amp A on UVIS1. The upper panel shows the ratio of counts in the long exposure divided by the counts in the short exposure multiplied by the relative exposure time; linearity would thus result in a value of unity. The x-axis shows the multiplicative degree by which a star is over-saturated in the long exposure. The middle panel shows the long exposure aperture sums versus short exposure aperture sums. The lower panel shows the peak data value in the long exposure relative to the short exposure value. The response is linear up to the value of 68,000 e<sup>-</sup> (y-axis) where the long exposure encounters saturation. Amp A data show significant deviations from a linear response for over-saturations near and beyond 10.

**Figure 5.14: Long vs. Short Exposure Ratios of Linearity**

Top panel shows the count rate ratio between long and short exposures for both amplifier quadrants of UVIS1 (Amps A and B) vs. the oversaturation level in the long exposure. Bottom panel shows the same data but after applying the corrections as described in [WFC3 ISR 2010-10](#). At high levels of saturation, the Long to Short count ratios are restored to unity and the scatter is much reduced.



### 5.6.4 Shutter Stability

The WFC3-UVIS shutter is a circular, rotating blade divided into two open and two closed quadrants (See [Section 2.3.3 of the WFC3 Instrument Handbook](#) for details). Operationally, the shutter mechanism has two distinct modes, based on commanded exposure times. At the shortest commanded exposure time of 0.5 seconds, the shutter motion is continuous during the exposure, rotating from the closed position through the open position and on to the next closed position. For commanded exposure times of 0.7 seconds and longer (0.6 seconds is not allowed),

the shutter rotates into the open position, stops and waits for an appropriate amount of time, and then rotates to the closed position.

For short exposure times, detector position-dependent exposure time (shutter shading), A versus B blade shutter dependence, stability, and timing accuracy were assessed using data taken during SMOV. For a full discussion of the analysis of shutter behavior from on-orbit data see [WFC3 ISR 2009-25](#) and [WFC3 ISR 2015-12](#). No systematic difference in shutter behavior (exposure time, repeatability, etc.) is found when comparing the A and B blades of the shutter. Even at the shortest exposures, the measured shutter shading does not exceed  $\sim 0.2\%$  across the detector. The small magnitude of this effect means that no correction for shutter shading is necessary in `calwf3`.

The stability of shutter timing is a bit more problematic. Results are based on Eleven pairs of back-to-back exposures at each commanded exposure time were analyzed. For exposure times of 1.0 seconds or shorter, the rms variation in exposure time for a series of images is 1% or greater, implying possible difficulty in achieving 1% photometric accuracy. For a commanded exposure time of 0.5 seconds, the rms variation is 1.9%. For commanded exposure times of 0.7 and 0.8 seconds, the true exposure times vary by 1.5% and 1.4% respectively. At an exposure time of 1.0 second, the rms variation falls to 1.0%.

While the rms variations were all less than 2%, we observed individual exposures at each commanded exposure time that deviated by larger amounts. For the 0.5, 0.7, 0.8 and 1.0-second exposures, we found individual exposures with measured errors of 4.0%, 4.0%, 3.0%, and 2.0% respectively. This implies that exposures of 1.0 seconds or shorter may experience timing fluctuations that could compromise a goal of 1 or even 2.0% accuracy. This conclusion regarding shutter stability is not regarded as robust, but is most consistent with a simple and conservative interpretation of the test data.

Finally, our investigation of measured versus commanded exposure times indicated that for exposures commanded to be 0.5 seconds, the shutter was actually open for 0.48 seconds. Similarly, for exposures commanded to be 0.7 seconds, the measured exposure time was in fact 0.695 seconds. For these exposure times, the EXPTIME header keyword value is updated in the science image headers to reflect the actual (as opposed to commanded) exposure times.

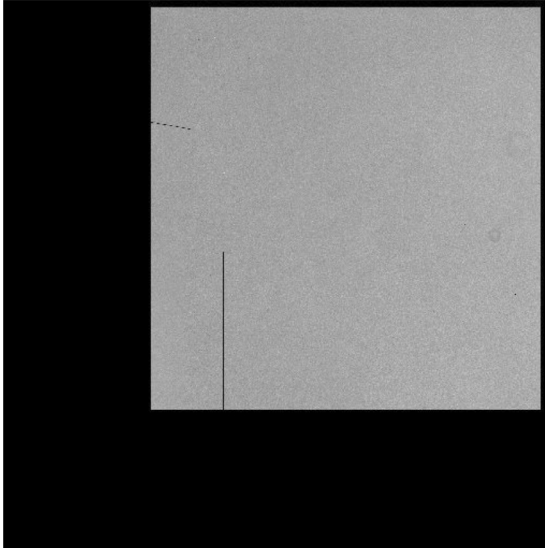
### 5.6.5 Fringing

At wavelengths longer than about 650 nm, silicon becomes transparent enough that multiple internal reflections in the UVIS detector can create patterns of constructive and destructive interference, or fringing. Fringing produces wood-grain patterns in response to narrow-band illumination at long wavelengths, see [Figure 5.15](#).

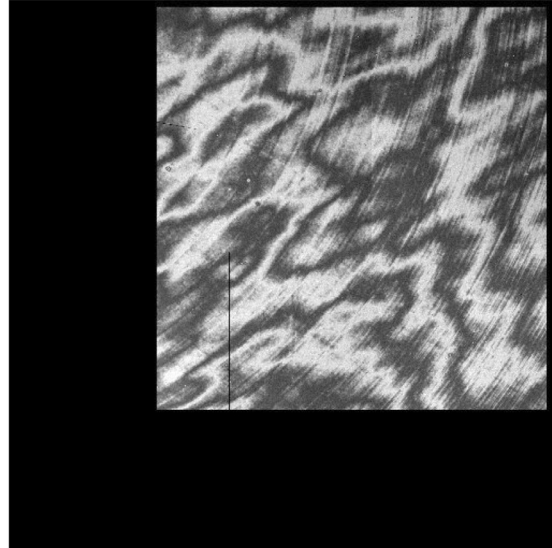
**Figure 5.15: Fringe Flats**

Quadrant B of two ground flat fields: one affected by fringing (right) and one not affected (left). Black region of the FQ906N flat is masked to avoid areas affected by the quad filter edges; the same region of F673N is masked for consistency.

F673N flat field (quadrant B)



FQ906N flat field (quadrant B)



The amplitude and phase of the fringes is a strong function of the silicon detector layer thickness and the spectral energy distribution of the illumination. Fringe amplitude--the contrast between constructive and destructive interference--is greatest at the longest wavelengths (where the high transparency allows more internal reflections) and for the narrowest spectral energy distributions. For broad SEDs, interference is averaged over phase, so that the amplitude of the fringing is reduced. Thus fringing is significant for UVIS imaging data only if narrow-band red filters are used, or if sources with red line emission are observed.

Flat fields from ground tests (see [WFC3 ISR 2008-46](#)) have been used to estimate the magnitude of fringing effects, for a continuum light source, in the narrow-band red filters (see [Table 5.3](#) and [WFC3 ISR-2010-04](#)). Each column lists a different metric of fringe amplitude, for a control filter (F606W) and for the filters in which fringing effects could be detected in the flat-field data. These metrics can best be understood by examining the histograms ([Figure 5.16](#)) of the flat fields shown in [Figure 5.15](#).

Table 5.3: Metrics of fringe amplitude based on ground flat fields

Filter	Distance Between Histogram Peaks	Manual Peak-to- Trough	Quadrant	RMS Deviation	Full Width At 20% Maximum
	percent	percent		percent	percent
F606W			B	1.0	3.0
F606W			C	1.2	3.3
F606W			D	1.2	3.3
F656N		2.2 +/-1.2	A	1.4	4.9
F656N		1.7 +/- 1.1	B	1.3	4.5
F656N		1.7 +/- 1.2	C	1.6	5.1
F656N		3.2 +/- 1.3	D	1.5	5.1
F658N			A	1.3	4.4
F658N			B	1.2	3.9
F658N			C	1.4	4.4
F658N		0.9 +/- 1.1	D	1.3	3.7
F673N			A	0.9	3.1
F673N			B	1.0	3.2
F673N			C	1.3	3.6
F673N		0.5 +/- 1.1	D	1.4	4.2
F953N	17.8	19.8 +/- 1.7	A	7.6	23.7
F953N	17.3	20.8 +/- 1.8	B	7.8	24.0
F953N	14.9	17.8 +/- 1.7	C	7.1	23.5
F953N	15.0	11.5 +/- 1.6	D	6.7	22.9
FQ672N		4.6 +/- 1.3	D	2.0	7.0
FQ674N		2.4 +/- 1.3	B	2.1	7.4
FQ727N		2.3 +/- 1.1	D	1.6	5.3
FQ750N		1.2 +/- 1.1	B	1.3	4.5
FQ889N	7.8	10.0 +/- 1.3	A	3.8	13.5
FQ906N	12.5	12.2 +/- 1.4	B	5.4	18.2
FQ924N	6.9	10.1 +/- 1.4	C	4.4	16.5
FQ937N	9.4	14.2 +/- 1.4	D	5.0	18.4

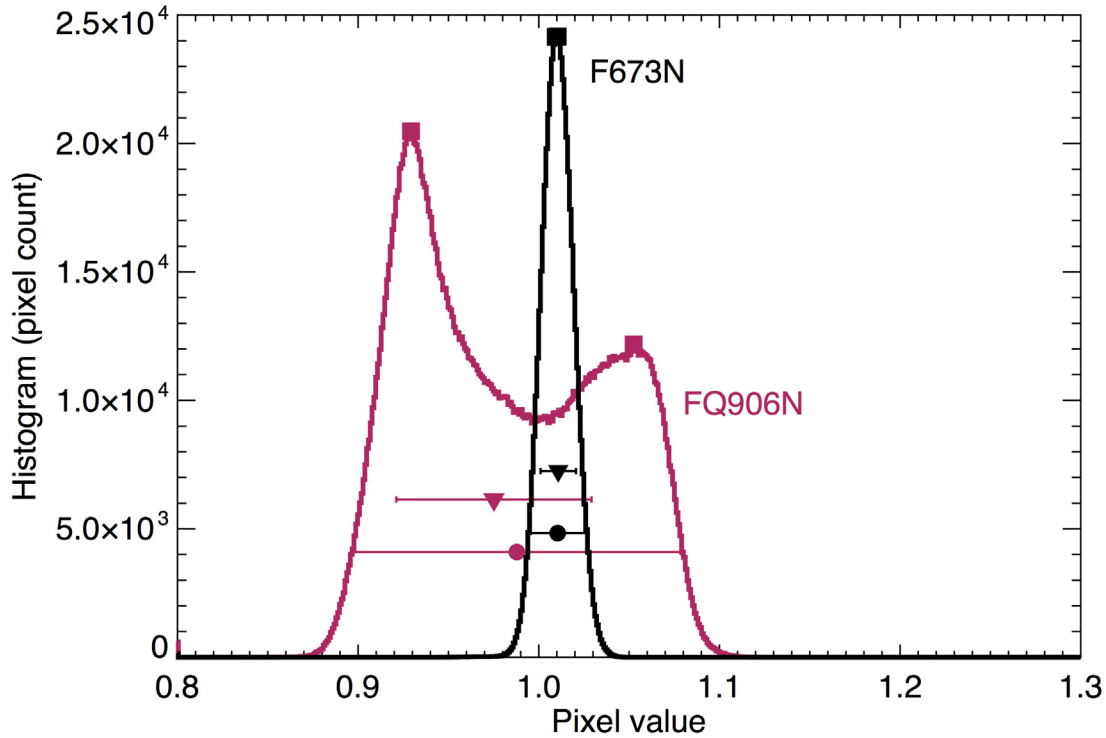
Values are given in units of percentage of the normalized flat-field signal level. Each metric is described in the text and graphically represented in [Figure 5.16](#)

The fifth data column in the table is simply the root mean square deviation from the mean of the sample, and is indicated by triangles with horizontal error bars in the histograms. Filters/quadrants with rms deviations greater than corresponding values for the control filter (F606W) may be influenced by fringing. The last column is full width at 20% maximum, rather than full width at 50% maximum, because this metric is more effective for bimodal pixel brightness distributions in filters with strong fringing, such as FQ906N (pictured). The second data column gives the separation between histogram peaks, which can be detected in flat-field data for only the five

reddest of the twelve filters affected by fringing. Squares in Figure 5.15 mark the histogram peaks. Adjacent fringes were also manually sampled, and the results reported in the second data column.

**Figure 5.16: Histograms of the two flat-field samples shown in Figure 5.15.**

Symbols correspond to fringe amplitude metrics listed in Table 5.3: rms deviation (triangles with error bars), full width at 20% maximum (circles with error bars), and bimodal histogram peaks (squares).



For estimating photometric uncertainties in data taken with these filters, it may be useful to consider how much the rms deviation in the flat fields departs from that of the control filter F606W. For exposure time calculations of targets affected by fringing, the full width at 20% maximum or the distance between histogram peaks may be the most useful metric. To understand how small dithers might affect photometry of targets that happen to fall on adjacent positive and negative fringes, the manually determined amplitude might be most appropriate. For sources with SEDs very similar to the calibration lamp, application of the pipeline flat fields should considerably reduce the effect of fringing on the data.

## 5.7 UVIS Photometry Errors

The estimated errors for the chip-dependent inverse sensitivity for the WFC3 UVIS channel computed from observation of the three white dwarf standards are: Error in the mean: 1.3% (statistical) and Absolute error: 1.3% (systematic, uncertainties in the white dwarf models used as absolute standards). The signal to noise ratio, per observation, for the standard stars is such that the Poisson error is  $\sim 0.2\%$  or less for the wide band filters. For those users who need precise photometry, a complete error analysis would include Poisson noise of the science target as well the additional sources of photometric error of flat fielding (see Section 5.4), spatial repeatability ( $\sim 0.5\%$ , but see Section 5.4.2), temporal variation (see Section 9.1), readnoise (Section 5.1.2), uncertainty in the encircled energy ( $\sim 0.5\%$  at the infinite aperture - Hartig priv. comm.), charge transfer efficiency corrections (CTE, see Chapter 6) and processing error (see Newberry, 1991 and Newberry, 1999).

## 5.8 References:

- S. Baggett, WFC3 ISR 2009-03: *WFC3 TV3 Testing: UVIS-1 Crosstalk*.  
<http://www.stsci.edu/hst/wfc3/documents/ISRs/WFC3-2009-03.pdf>
- S. Baggett, E. Sabbi, P. McCullough, WFC3 ISR 2009-27: *WFC3 SMOV Proposal 11422/ 11529: UVIS SOFA and Lamp Checks*.  
<http://www.stsci.edu/hst/wfc3/documents/ISRs/WFC3-2009-27.pdf>
- T. M. Brown & Olivia Lupie, WFC3 ISR 2004-04, *Filter Ghosts in the WFC3 UVIS Channel*.  
<http://www.stsci.edu/hst/wfc3/documents/ISRs/WFC3-2004-04.pdf>
- T. Brown, WFC3 ISR 2007-09: *UVIS Channel Filter Ghosts after Filter Replacement*,  
<http://www.stsci.edu/hst/wfc3/documents/ISRs/WFC3-2007-09.pdf>
- T. Brown, WFC3 ISR 2007-21, *WFC3 TV2 Testing: UVIS Channel Glint*.  
<http://www.stsci.edu/hst/wfc3/documents/ISRs/WFC3-2007-21.pdf>
- T. Brown, G. Hartig, S. Baggett, WFC3 ISR 2008-10: *WFC3 TV3 Testing: UVIS Window Contamination*. <http://www.stsci.edu/hst/wfc3/documents/ISRs/WFC3-2008-10>
- R. L. Gilliland, 1994, ApJ, 435, L63-66. <http://adsabs.harvard.edu/abs/1994ApJ...435L.63G>
- R.L. Gilliland et al., 1999, PASP, 111 1009-1020. <http://www.jstor.org/stable/10.1086/316407>
- R. L. Gilliland, *ACS CCD Gains, Full Well Depths, and Linearity up to and Beyond Saturation*.  
<http://www.stsci.edu/hst/acs/documents/isrs/isr0401.pdf>
- R. Gilliland, A. Rajan and S. Deustua, WFC3 ISR 2010-10: *WFC3 UVIS Full Well Depths, and Linearity Near and Beyond Saturation*.  
<http://www.stsci.edu/hst/wfc3/documents/ISRs/WFC3-2010-10.pdf>
- H. Gunning, C. Pavlovsky, S. Baggett, WFC3 ISR 2013-02, *WFC3 Cycle 19 Proposal 12690:UVIS Gain*. <http://www.stsci.edu/hst/wfc3/documents/ISRs/WFC3-2013-02.pdf>



- H. Gunning, WFC3 ISR 2015-05, *WFC3 Cycle 21 Proposal 13561: UVIS Gain*,  
<http://www.stsci.edu/hst/wfc3/documents/ISRs/WFC3-2015-05.pdf>
- B. Hilbert, WFC3 ISR 2009-25: *UVIS Channel Shutter Shading*.  
<http://www.stsci.edu/hst/wfc3/documents/ISRs/WFC3-2009-05.pdf>
- J. Janesick, 2001, *Scientific charge-coupled devices*, SPIE Optical Engineering Press, (Bellingham, WA)
- H. Khandrika and S. Baggett, WFC3 ISR 2015-13, *WFC3 UVIS Read Noise*,  
<http://www.stsci.edu/hst/wfc3/documents/ISRs/WFC3-2015-13.pdf>
- J. Mack, E. Sabbi, & T. Dahlen, WFC3 ISR 2013-10: *In-flight Corrections to the WFC3 UVIS Flat Fields*. <http://www.stsci.edu/hst/wfc3/documents/ISRs/WFC3-2013-10.pdf>
- P. McCullough, WFC3 ISR 2011-16, *Geometric model of UVIS window ghosts in WFC3*.  
<http://www.stsci.edu/hst/wfc3/documents/ISRs/WFC3-2011-16.pdf>
- M. V. Newberry, 1991 *Signal-to-Noise Consideration For Sky-subtracted CCD Data*, PASP 103, 122,.  
<http://adsabs.harvard.edu/full/1991PASP..103..122N>
- M. V. Newberry, 1999, *Increasing Precision and Accuracy in Photometric Measurements in Precision CCD Photometry*, ASP Conference Series, Vol. 189, Edited by Eric R. Craine, David L. Crawford, and Roy A. Tucker. ISBN: 1-58381-015-3 (1999), p.74  
<http://adsabs.harvard.edu/full/1999ASPC..189...74N>
- M. Robberto & B. Hilbert, WFC3 ISR 2005-27, *The Behaviour of the WFC3 UVIS and IR Analog-to-Digital Converters*. <http://www.stsci.edu/hst/wfc3/documents/ISRs/WFC3-2005-27.pdf>
- E. Sabbi, M. Dulude, A.R. Martel, S. Baggett, H. Bushouse, WFC3 ISR 2008-46: *WFC3 Ground P-flats*. <http://www.stsci.edu/hst/wfc3/documents/ISRs/WFC3-2008-46.pdf>
- K. Sahu, C.M. Gosmeyer, S. Baggett, WFC3 ISR 2015-12, *WFC3/UVIS Shutter Characterization*.  
<http://www.stsci.edu/hst/wfc3/documents/ISRs/WFC3-2015-12.pdf>
- M. Stiavelli, J. Sullivan, And C. Hanley WFC3 ISR 2001-17: *Modeling the Impact of Ghosts in WFC3/UVIS*. <http://www.stsci.edu/hst/wfc3/documents/ISRs/WFC3-2001-17.pdf>
- A. Suchkov & Sylvia Baggett, WFC3 ISR 2012-02, *WFC3/UVIS Crosstalk and Crosstalk Correction*.  
<http://www.stsci.edu/hst/wfc3/documents/ISRs/WFC3-2012-02.pdf>
- M.H. Wong, WFC3 TIR 2010-01, *WFC3/UVIS Fringing: Ground test data and analysis codes*. Available by request from [help@stsci.edu](mailto:help@stsci.edu).
- M. Wong, WFC3 ISR 2010-04: *Amplitude of fringing in WFC3/UVIS narrowband red filters*.  
<http://www.stsci.edu/hst/wfc3/documents/ISRs/WFC3-2010-04.pdf>



# Charge Transfer Efficiency (CTE) in WFC3/UVIS

In this chapter . . .

6.1 Overview / 124
6.2 CTE Losses And Background / 125
6.3 The Nature Of CTE Losses / 126
6.4 The Pixel-Based Model / 128
6.5 Empirical Corrections / 130
6.6 Dealing With CTE Losses In WFC3/UVIS Images / 131
6.7 Sink Pixels / 132
6.8 References / 135

---

## 6.1 Overview

WFC3/UVIS was installed on board the HST in May of 2009. At the end of cycle 24, in the summer of 2017, the instrument has completed its eight year of operation in the harsh radiation environment of low-Earth orbit. There are three main consequences of radiation damage: an increase in the number of hot/warm pixels, an increase in dark current, and an increase in the number of charge traps, which lead to CTE (charge-transfer efficiency losses) and sink pixels. Some of the hot pixels can be annealed away, by warming the detector to ~20C during the monthly anneal procedures (e.g., Figure 6 in [WFC3 ISR 2016-08](#)) but there is a gradual build-up of permanent hot pixels over time. There is no indication that annealing reduces CTE losses.

This chapter describes the various aspects of CTE losses in the WFC3/UVIS detector. The first section provides a general overview and compares CTE losses in WFC3/UVIS to those in ACS/WFC. The next section discusses the nature of WFC3/UVIS losses in more detail, focusing on how the mini-channel makes it possible to minimize CTE losses. [Section 6.4](#) describes the pixel-based model in more detail, in terms of how it was constructed and how the pixel-based-reconstruction procedure can be run. [Section 6.5](#) gives a brief overview of the empirical formula-based correction for point sources. The final section discusses how best to deal with CTE losses in WFC3/UVIS images in terms of prevention, mitigation, and correction.

---

## 6.2 CTE Losses And Background

ACS/WFC, installed in HST in March 2002, has been in space about 7 years longer than WFC3, yet in some ways the CTE losses in WFC3/UVIS have become more severe than those in ACS/WFC. CTE losses became apparent for WFC3/UVIS even before it had been on orbit for a year. In fact, CTE losses for even moderately bright targets were 2-3 times greater than expected CTE losses based on ACS performance in its first years on-orbit ([ACS ISR 2009-01](#)). However, the faster degradation seen by UVIS 2009/2010 was also occurring on ACS as well ([Massey, 2010, MNRAS 409L, 109](#)). As discussed in the [CTE White paper](#), one contributing factor was likely the solar minimum:

1) the strength and extent of the South Atlantic Anomaly, where most of the CTE traps are thought to be formed, is known to be anti-correlated with solar activity (e.g. [Casadio et al. 2010](#)) and

2) the installation of WFC3 on HST coincided with solar minimum while the installation of ACS occurred during a period of higher solar activity.

An additional factor in the WFC3/UVIS CTE behavior is the low image background. WFC3/UVIS images tend to have much lower backgrounds than ACS images for several reasons. First, WFC3/UVIS was designed to be sensitive to low S/N objects, with low readnoise ( $\sim 3$  e-/pixel) and low dark current ( $\sim 8$  e-/pixel/hr in 2017 and increasing by  $\sim 1$  e-/hr/year). The dark current of ACS is about 50-55 e-/hour. Second, the WFC3/UVIS pixels are 40% smaller than the ACS/WFC pixels, and as such they intercept correspondingly fewer sky photons, again keeping the background low. Finally, images obtained with the WFC3/UVIS complement of UV and narrow-band filters often have extremely low sky backgrounds. For all these reasons, even deep UVIS science exposures frequently have backgrounds of less than 5 electrons, whereas similar ACS/WFC science exposures almost never have backgrounds less than 25 electrons. (For a summary of WFC3/UVIS backgrounds see, [WFC3 ISR 2012-12](#) and for ACS, [ACS ISR 2012-04](#).)

## 6.3 The Nature Of CTE Losses

CTE losses arise during the readout process, as the charge packet for each pixel is transferred pixel-by-pixel down the detector, in parallel, to the serial register. As the packet moves through the silicon of the detector, it often encounters imperfections (traps) in the lattice that have been caused by radiation damage. These traps can temporarily detain individual electrons. Once an electron is trapped, it becomes separated from its original charge packet. The electron is often released some time later during the readout and finds itself in an upstream pixel. For this reason, CTE takes charge away from downstream pixels and deposits it into upstream pixels; visually, the effect results in “trails” of charge that extend out from sources in the direction opposite the readout amplifier. Charge packets that have more electrons tend to occupy a physically larger volume within the pixel. As such, larger packets provide larger cross-sections to traps as the packets are shuffled through the silicon lattice. For the WFC3/UVIS model we discuss below in [Section 6.4](#), a cloud with ten electrons, for example, will see about 3 times more traps than a cloud with only 1 electron. It is worth noting, however that even though losses increase in an absolute sense when we have more electrons in a cloud, the per-electron fractional losses go down with increasing packet size.

**Figure 6.1: Effect of Electron Traps**

(Left) The dark line shows the cumulative number of traps in each column as a function of the size of the electron packet. The dotted line shows the extrapolation of the power law from the bright end. (Right) The derivative of the curve on the left. This shows the marginal number of traps seen by the Nth electron. The dip between 12 and 30 electrons shows the “sweet spot” background level, where the charge transfer is maximized at low background levels.

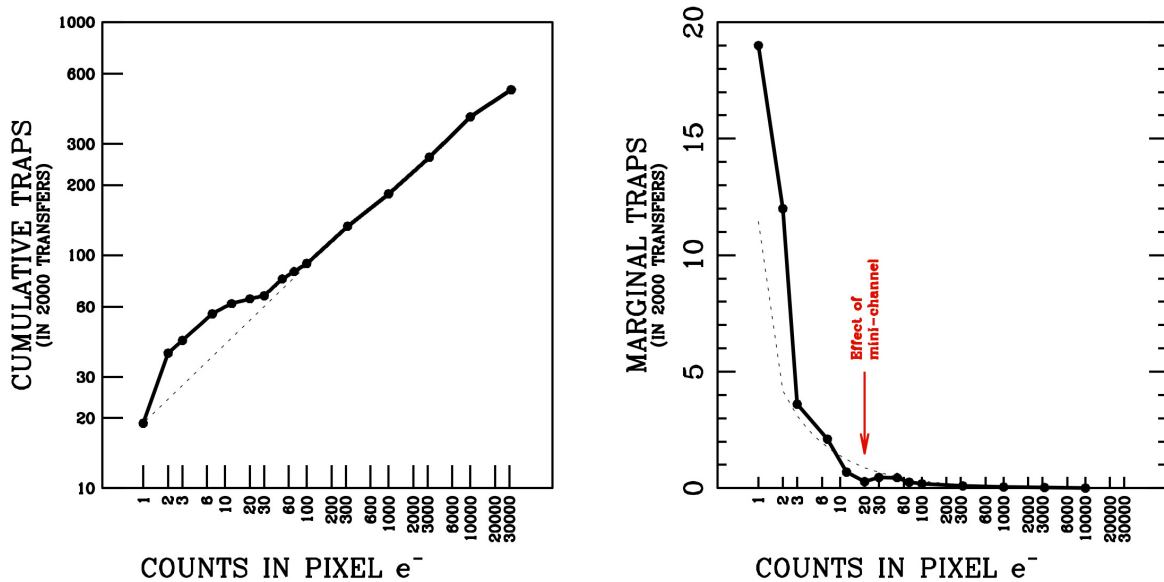


Figure 6.1 shows the model constructed by [Anderson et al. \(2012\)](#) (see the document on the [CTE-Tools webpage](#) and [Section 6.4](#) below). The model was based on the analysis of dark exposures taken in August 2012, and specifically on the analysis of the blurring experienced by hot and warm pixels. On the left, we show the cumulative number of traps as a function of packet size. We see that a charge packet that contains just one electron will encounter 20 traps on its 2000-pixel journey to the serial register, if there is no background. Clearly we should not expect such an electron to survive the journey. A charge packet with ten electrons will encounter 60 traps and is also not likely to be detected. A packet with 100 electrons will lose 90, and something should therefore be detected at the readout register.

Of course an isolated packet that starts with 100 electrons will not maintain that size all the way down, so in practice it will see fewer traps than this. Packets with 1000 electrons will lose only about 200 electrons, so 80% of them will survive to the register. Packets with 10,000 electrons on an image with no background will lose only about 4% of their electrons.

The behavior of this curve provides strong evidence for the presence of a "supplemental buried channel" or a "mini-channel". The channel, a key design feature in the WFC3 chips, was constructed to confine small packets to a narrow channel within the silicon in order to minimize their exposure to charge traps. The first few electrons in this channel would inevitably see a large number of traps, but subsequent electrons would find themselves relatively shielded from losses, as traps have been partially filled by preceding electrons. The fact that the observed trend in [Figure 6.1](#) is steeper than average on the left but flattens out in the middle is attributed to the mini-channel.

In the right panel of [Figure 6.1](#) we show the marginal number of traps, i.e. the number of traps that would be seen by the Nth electron in a charge packet. The first electron will encounter almost 20 traps on its path to the readout register. As such it has a  $10^{-12}$  chance of making the journey without being delayed. The second electron will see 12 traps, the third 4, and the tenth less than 1.

Note that this curve cannot predict the original number of electrons from the observed number, since as a charge packet gets shuffled down the detector, it loses electrons and therefore its electron-loss-rate changes in a very non-linear way. It is also the case that downstream packets can "prefill" traps, such that upstream packets can be shuffled down the chip with fewer losses. This can also cause asymmetries in source shapes. This is why a forward-modeling routine is required to reconstruct the pixel distribution. The fact that the marginal losses drop sharply as the charge packet gets larger means that if we have a small level of background in an image, then many of the traps will be kept filled by the background and will not therefore affect the science photons. The curve shows that if we have a background of zero in an image, then a marginal electron will see twenty traps, but if the background is 10, it will likely see less than one trap. If the background is around 12, in fact, we find that a marginal science electron has about an 80% chance of making it to the readout register (as of August 2012). This corresponds to the dip in the marginal distribution, which is related to the flattening in the cumulative distribution, and which is likely a consequence of the mini-channel.

Finally, we note that the delta-function charge packets that we have been considering in our study of warm pixels in dark exposures are not typical of science sources. Even unresolved objects on UVIS have a point-spread-function shape (PSF), which means that the central pixel has 20% of the light and the immediately adjacent pixels receive about 10% of the light. As such the outer pixels of sources will fill some traps that the sources' inner pixels will not have to experience. This increases the overall transfer efficiency of real-world sources over the delta functions we have access to in the darks.

---

## 6.4 The Pixel-Based Model

The previous section made reference to the pixel-based model of CTE losses. The WFC3/UVIS model is based on the empirical model that was constructed by [Anderson & Bedin \(2010\)](#), which itself was inspired by the model in [Massey et al. \(2010\)](#) for ACS/WFC.

The basic model assumes that each column contains a number of charge traps distributed evenly among its pixels from  $j=1$  to  $j=2048$ . Charge packets for pixels at the top of the chip will see all of the traps, those in the middle at  $j=1024$  will see half of them, and those at  $j\sim 200$  will experience a tenth of them. Each trap will grab and hold a particular electron in a charge packet (the first, the second, the hundredth, etc). The model also has a release profile for each trap. Typically, there is a 20% chance the electron will be released into the first upstream pixel, a 10% chance it will be released into the second upstream pixel, etc. We find for WFC3/UVIS that essentially all trapped electrons are released after 60 transfers. The two sets of parameters for the model are therefore: the distribution of traps as a function of electron-packet size and the release-probability distribution for trapped electrons.

The readout process is simulated by going up through each column from  $j=1$  (close to the readout amplifier) to  $j=2015$  and determining (1) which electrons will be trapped during the journey down the detector to the serial register and (2) when these trapped electrons will be released. Even though this is a stochastic process in reality, the model treats it as deterministic. The end result is that the observed distribution of pixel values gets blurred somewhat in the upstream direction relative to the original distribution, leading to the characteristic CTE trails seen behind sources in CTE-affected UVIS images.

In order to determine optimal parameters for the model, we examined the blurring experienced by hot and warm pixels in a variety of dark exposures taken in August 2012 with both short (100s) and long (900s) exposure times, and with various post-flash background levels (from zero up to 60 electrons). In practice, the model was constrained by first solving for the pre-readout distribution of warm pixels from scaling down the long-dark exposures, then fitting a trailed model to the actual trailed short-dark observations. The variety of background levels provided additional constraints. The first set of parameters (the distribution of traps as a function of charge-cloud size) is shown in [Figure 6.1](#).

In order to use the model on science images, we must invert this procedure: we must determine what original image - when pushed through the readout algorithm-

generates the observed distribution. This is formally a non-linear deconvolution process.

There are several challenges to a pixel-based reconstruction. One challenge is that the observed images represent not just the charge that arrived at the readout, but they represent this charge *plus* a contribution from the readnoise (3.1-3.2 electrons for UVIS). The other challenge is that the model assumes an even distribution of traps throughout the detector, even though in actuality this distribution is stochastic: each column will naturally have a slightly different number of traps and even the distribution of traps within each column will not be perfectly uniform.

The readnoise introduces a serious complication. An empty image will be readout to have a variance of about 3.2 electrons in each pixel due to readnoise. If the original image on the detector had a pixel-to-pixel variation of 3.2 electrons on a background of near zero, then the charge-transfer process would blur the image out so much that the image that reached the amplifier would have a variance of less than 0.5 electron. The CTE reconstruction algorithm determines what the original image would have to be in order to be read out as the observed image. If we include readnoise in this observed target image, then the original image would have to start with an extremely large amount of pixel-to-pixel variation (perhaps 15 electrons of noise) for it to end up with 3.2 electrons noise after the blurring readout process. We would have to increase the noise by a factor of five to arrive at the image that was read out. This clearly will not produce a realistic reconstruction, so we need to find some way to mitigate this "readnoise amplification".

We address this issue by taking the observed image (which has had readnoise added to it) and determining the smoothest possible image that is consistent with the image, modulo readnoise. We choose the smoothest possible image, since the smoother the image, the less the readout algorithm will redistribute charge. While this may not give us the *true* counts that arrived at the readout register, it should provide us with the most conservative possible CTE correction. The pixel-based reconstruction algorithm then operates on this "smooth" image, and the redistribution of flux is applied to the observed image (which still has the readnoise in it).

The other challenge to a pixel-based reconstruction is that the model assumes that each pixel has the same number of fractional traps, even though in reality the traps are quantized: most pixels have no traps, while some may have several. The WFC3/UVIS team has examined overscan and charge-injection data in an effort to construct a rough model of the specific trap distribution within each column, but since charge injection is possible at only a very high level (15,000 electrons per pixel), it is very difficult to explore the lower-level charge traps, which are the most relevant to science images. So, until we can find a better way to pin down the location of traps, the simplistic uniform trap-density model will have to suffice.

Previously, the pixel-based CTE correction was a standalone FORTRAN program available for download from the [CTE-tools](#) web page. However, the pixel-based CTE correction is now part of the automated calibration pipeline for all UVIS full-frame images (**calwf3** version 3.3 and later) and most<sup>1</sup> UVIS subarray images (**calwf3** version 3.4 and later). Controlled via a new header calibration switch (PCTECORR = PERFORM), and associated calibration table (PCTETAB) and CTE-corrected



reference files (e.g. DRKCFILE), **calwf3** will by default produce two sets of products: the standard non-CTE-corrected (e.g. \*\_raw.fits, \*\_flt.fits, \*\_drz.fits) files as well as the new CTE-corrected results (\*\_flc.fits, \*\_drc.fits). Observers can use the \*\_flc.fits and \*\_drc.fits data products in the same way as \*\_flt.fits and \*\_drz.fits files.

In general, the pixel-based correction should be good to about 25%. The correction can enable recovery of a significant fraction of faint sources (WFC3 ISR 2016-17). However, in low-signal/low-background situations where the losses can become greater than 50%, it can be hard to trust any reconstruction procedure.

To help evaluate the efficacy of the CTE-correction, the CTE monitor analysis has been performed with and without the correction (WFC3 ISR 2017-09, and WFC3 ISR 2016-17). Those results show that as of 2017, for images with the recommended minimum 12 e-/pixel background, flux losses are 5-15%, depending on source brightness. With CTE-correction, those losses are effectively 0 or sometimes over-corrected by a few percent. For images with less than the recommended background, the CTE correction is able to reduce flux losses from ~50% down to ~15% for faint sources, from ~15% to <~5% for intermediate-brightness sources, and from ~5% down to 0 for the brightest sources (e.g., Fig 8 and Fig 10 in WFC3 ISR 2017-09 and Fig 4 in WFC3 ISR 2016-17).



Online

---

*The WFC3 CTE webpage is at:*

[http://www.stsci.edu/hst/wfc3/ins\\_performance/CTE/](http://www.stsci.edu/hst/wfc3/ins_performance/CTE/)

---

## 6.5 Empirical Corrections

Empirical corrections provide an alternate way to correct for CTE losses of observations of point sources or estimate future CTE loss levels. Noeske et al., (WFC3 ISR 2012-09) studied star clusters NGC6791 and 47 Tuc and examined how the measured fluxes of stars varied when particular stars were placed close to and far from the readout register. They documented the losses experienced by point sources as a function of (1) the electron flux of the point source, (2) the detector Y position of the source, (3) the background level, and (4) the date of the observation.

These corrections are provided in the form of polynomials and can be used to estimate how many electrons were originally present in the aperture before the readout process. The conclusions in this ISR and in the more recent follow-up studies (WFC3 ISR 2017-09, and WFC3 ISR 2016-17) mirror the conclusions from the pixel-based-model study: namely, that even a small amount of background (2-3

---

1. For observers utilizing unsupported subarrays (UVIS2-M1K1C-SUB and UVIS2-M512C-SUB), there is a workaround available that uses the standalone FORTRAN CTE-correction code (STAN Issue 18)

electrons) can have a significantly ameliorative effect on charge-transfer efficiency, and backgrounds of 10-30 e- can reduce CTE losses to the perturbation level (less than 20% losses for all stars).

The most recent empirical corrections are described in [WFC3 ISR 2017-09](#), which also provides an analysis of the long term behavior of the UVIS CTE using observations of star clusters.

---

## 6.6 Dealing With CTE Losses In WFC3/UVIS Images

There are many ways of dealing with imperfect charge-transfer efficiency in WFC3/UVIS images. The White Paper by [MacKenty and Smith \(2012\)](#), provides a detailed discussion of the many issues and trade-offs. Here, we give an overview of their conclusions.

The best way to deal with CTE losses is by minimizing them in the first place. Neither the reconstruction algorithm nor the empirical correction is perfect, so minimizing the need for these corrections is the best way to combat CTE losses. This can be done in several ways. The easiest method is to place the source close to the readout register, thereby minimizing the number of readout transfers during which CTE losses occur. This is, of course, possible only for fields-of-interest that are relatively small.

Another way to minimize CTE losses is to ensure that the background has at least 12 electrons per pixel. This puts the marginal electrons into the "sweet spot" of the mini-channel (see the right half of [Figure 6.1](#)), so that a maximum fraction of them will survive the parallel-transfer process (about 80% as of Aug 2012). Users can consult the graphs found in [WFC3 ISR 2012-12](#) to predict the number of electrons they might expect in a typical background pixel for empty fields observed through various filters for a given exposure time. The [WFC3/UVIS imaging exposure time calculator](#) provides an estimate of the predicted total background and will provide a warning if it falls below the recommendation. In images where the predicted background is less than 12 electrons, using the POST-FLASH option is recommended to add enough electrons to increase the background counts up to this level. Note that exceeding 12 electrons has **not** been shown to improve the charge-transfer efficiency,



but it **does** increase the noise in each pixel. Therefore, it is best to use the minimum POST-FLASH necessary.




---

**NOTE:** *The post-flash levels in APT and the ETC represent the average across the FOV. The PF illumination pattern varies by  $\sim \pm 20\%$  across the FOV, brightest in B/D quadrants and falling off towards A&C corners, see:*

*[http://www.stsci.edu/hst/wfc3/ins\\_performance/CTE/postflashA.jpg](http://www.stsci.edu/hst/wfc3/ins_performance/CTE/postflashA.jpg). As a consequence, observers desiring a specific e/pixel level across the entire FOV will want to increase the requested levels by  $\sim 20\%$ .*

---

For exposures that were treated with POST-FLASH to raise the background level for CTE loss mitigation, the background noise is naturally increased and the signal to noise ratio of the science targets correspondingly lowered. While long exposures should always be broken up into dithered sub-exposures to improve PSF sampling and remove detector artifacts and cosmic rays, exposures requiring POST-FLASH should be broken into fewer, longer sub-exposures if possible. This way, the POST-FLASH induced signal to noise reduction will be alleviated as the science source signal increases linearly with exposure time, while the background noise is kept constant at approximately 12 electrons per pixel through a suitable choice of added POST-FLASH background. Once CTE losses have been minimized in a data set, it will still likely be important to correct the observations for whatever losses have occurred, or at the very least obtain an estimate of how the readout process may have degraded the original image. One can use either the pixel-based correction for general scenes of point and extended sources (Section 6.4) or the empirical formula correction (see Section 6.5) for point sources.

---

## 6.7 Sink Pixels

With the advent of post-flashing in 2012, a new type of image defect was identified, see [WFC3 ISR 2014-04](#) for the discovery and [WFC3 ISR 2014-19](#) for a more thorough analysis. Such defects are caused by pixels that contain a modest number of charge traps (typically 20–100  $e^-$ ). When read out, these sink pixels do not correctly report the number of electrons that were generated in them by photons. Sink pixels simply have lower counts than adjacent “normal” pixels (see Figure 4 of [WFC3 ISR 2014-22](#)). This phenomenon is distinct from normal pixel-to-pixel sensitivity variations, in that photons that interact with sink pixels do generate electrons, but some of these electrons do not shuffle out of the pixel during the readout process, and are thus not recorded with that pixel. Investigations suggest that sink pixels are created by cosmic ray events ([WFC3 ISR 2014-19](#), [WFC3 ISR 2014-22](#)); thus it appears that

most of the sink pixels may be a consequence of on-orbit radiation damage. Only a very small population of sink pixels were found in data taken before launch ([WFC3 ISR 2014-19](#), [WFC3 ISR 2014-22](#)). At present, no sink pixel has been found to heal or be recovered.

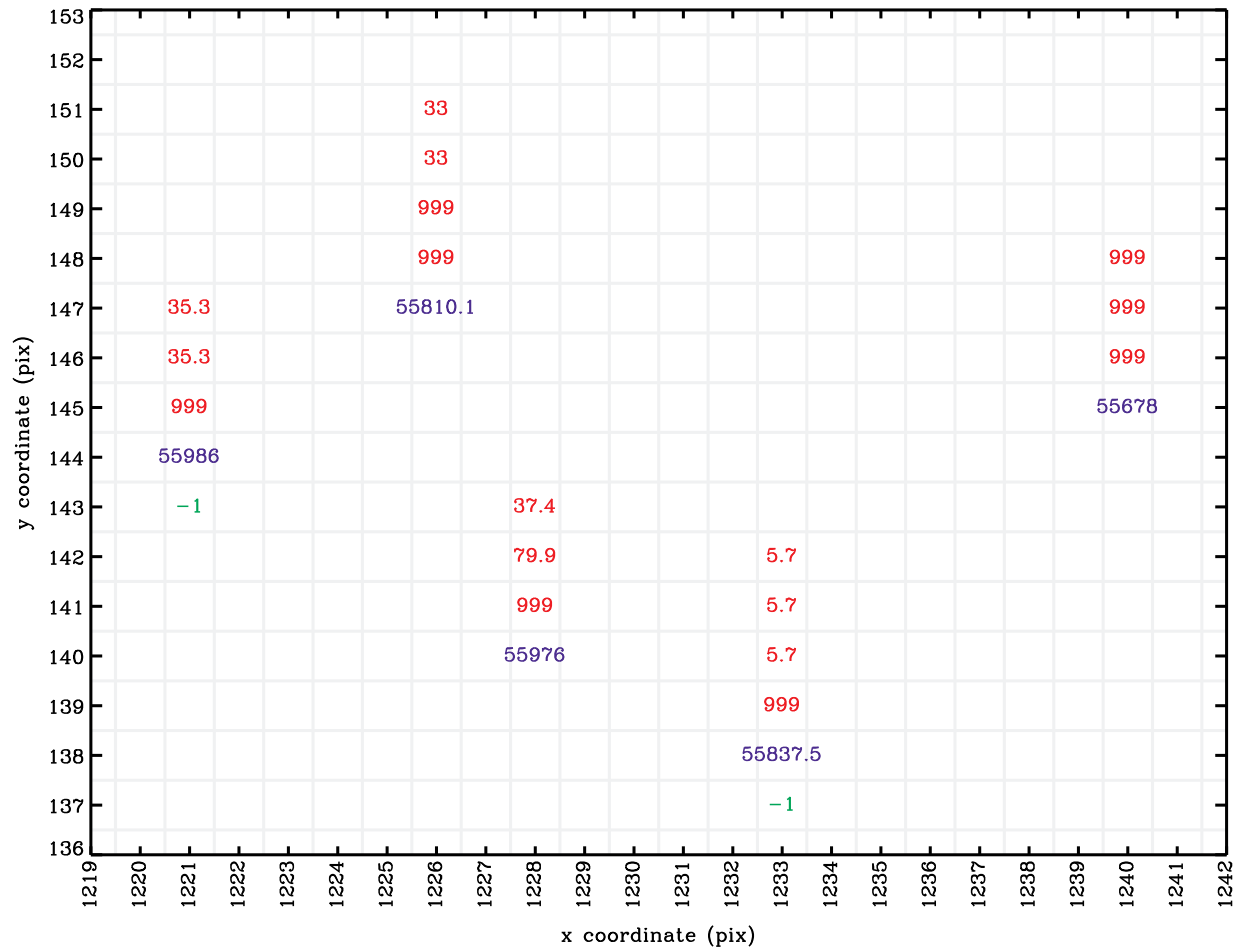
The impact of sink pixels on the background level depends on their locations in an image. For images with high backgrounds ( $\sim 85 \text{ e}^-$ ) and for sink pixels near the readout register, the sink pixels have little effect on upstream pixels in the same column. However, for lower backgrounds or for pixels far from the readout register, the interplay between CTE losses and sink pixels can extend the sink pixel profile to more than 10 pixels. A single sink pixel can affect both downstream pixels and several upstream pixels, depending on the background (see Figure 3 of [WFC3 ISR 2014-19](#)). So although sink pixels are rare ( $\sim 0.05\%$  of the detector), in low-background imaging they can corrupt as much as  $\sim 0.5\%$  of the detector.

Since the behavior of the sink pixels is scene-dependent, the WFC3 team has decided to take a conservative approach to flag all pixels in a given image that are likely to be affected. The impact of a sink pixel on the scene depends on the local scene itself. If a source lands on a sink pixel (or even on the streak of a sink pixel), then the electrons in the source will limit the trail behind the sink in the same way that more background would. In order to calibrate the impact of background on each sink pixel, 41,762 sink pixels were identified as producing streaks that affect  $\sim 6 \times 10^5$  pixels ([WFC3 ISR 2014-22](#)). From this map a new reference is generated: a SNKCFILE that contains the modified-Julian date (MJD) of the appearance of the sink pixel on orbit, as well as information on whether the downstream adjacent pixels are affected by the sink pixel, and on how far upstream the sink pixel trails extend (see [Figure 6.2](#)).

The current **calwf3** (version 3.3+) uses the SNKCFILE to populate the data quality array of a science image with 1024 for flagged pixels. More details on the flagging process are given in [Section 3.2.7](#), as well as in [WFC3 ISR 2014-22](#). Note that the sink pixels flagging is performed regardless of CTE-correction i.e. both flt and flc will have sink pixel flagged.

Figure 6.2: Schematic of the SNKCFILE sink-pixel reference file.

The figure is reproduced from [WFC3 ISR 2016-06](#) and adapted from [WFC3 ISR 2014-22](#). The figure shows the sink (blue), enhanced downstream (green), and low upstream (red) pixels. Empty pixels have zero and are not impacted by sink pixels. The sink pixel (blue) value refers to the MJD of the appearance of the sink pixel. The red values tell the pipeline when to flag each upstream pixel, based on the value in the sink pixel. If the sink pixel value is less than the listed number, the upstream pixel gets flagged. If the downstream pixel is -1 in the SNKCFILE, then it is always flagged as impacted.



---

## 6.8 References

- J. Anderson, & L. Bedin, *An Empirical Pixel-Based Correction for Imperfect CTE. I. HST's Advanced Camera for Survey*, 2010, PASP 122 1035. <http://www.jstor.org/stable/10.1086/656399>
- J. Anderson, *et al* 2012, *The Efficacy of Post-Flashing for Mitigating CTE-Losses in WFC3/UVIS Images*.  
[http://www.stsci.edu/hst/wfc3/ins\\_performance/CTE/ANDERSON\\_UVIS\\_POSTFLASH\\_EFFICACY.pdf](http://www.stsci.edu/hst/wfc3/ins_performance/CTE/ANDERSON_UVIS_POSTFLASH_EFFICACY.pdf)
- S. Baggett, and J. Anderson, 2012, WFC3-ISR-2012-12, *WFC3/UVIS Sky Backgrounds*  
[http://www.stsci.edu/hst/wfc3/documents/ISRs/WFC3-2012-12\\_v1\\_0.pdf](http://www.stsci.edu/hst/wfc3/documents/ISRs/WFC3-2012-12_v1_0.pdf)
- S. Baggett, C. Gosmeyer, and K. Noeske, *WFC3/UVIS Charge Transfer Efficiency 2009 -2015*  
<http://www.stsci.edu/hst/wfc3/documents/ISRs/WFC3-2015-03.pdf>
- M. Bourque, M., S. Baggett, 2016, ISR 2016-08: *WFC3/UVIS Dark Calibration: Monitoring Results and Improvements to Dark Reference Files*  
<http://www.stsci.edu/hst/wfc3/documents/ISRs/WFC3-2016-08.pdf>
- J. Mackenty, & L. Smith, 2012, *CTE White Paper*.  
[http://www.stsci.edu/hst/wfc3/ins\\_performance/CTE/CTE\\_White\\_Paper.pdf](http://www.stsci.edu/hst/wfc3/ins_performance/CTE/CTE_White_Paper.pdf)
- Massey *et al.*, 2010, *Pixel-based correction for Charge Transfer Inefficiency in the Hubble Space Telescope Advanced Camera for Surveys*, MNRAS 401 371.  
<http://mnras.oxfordjournals.org/content/401/1/371>
- K. Noeske, *et al.*, 2012, WFC3 ISR 2012-09, *WFC3 UVIS Charge Transfer Efficiency October 2009 to October 2011*. <http://www.stsci.edu/hst/wfc3/documents/ISRs/WFC3-2012-09.pdf>
- Sokol, J. Anderson, L. Smith, 2012 ACS-ISR-2012-04, *Assessing ACS/WFC Sky Backgrounds*.  
<http://www.stsci.edu/hst/acs/documents/isrs/isr1204.pdf>

# WFC3/IR Sources of Error

**In this chapter . . .**

7.1 WFC3/IR Error Source Overview / 136
7.2 Gain / 137
7.3 WFC3/IR Bias Correction / 137
7.4 WFC3 Dark Current and Banding / 138
7.5 Blobs / 142
7.6 Detector Nonlinearity Issues / 144
7.7 Count Rate Non-Linearity / 146
7.8 IR Flat Fields / 147
7.9 Pixel Defects and Bad Imaging Regions / 151
7.10 Time Variable Background Contamination / 155
7.11 IR Photometry Errors / 158
7.12 References / 158

---

## 7.1 WFC3/IR Error Source Overview

In comparison to the previous IR detectors flown on the Hubble Space Telescope, the WFC3/IR detector data is subject to far fewer problems thereby simplifying the tasks of data reduction and analysis. We present and discuss the known error sources to allow careful data processing which will yield improved results. Each is identified, its impact on the data is illustrated, and, if available, possible processing solutions are presented.

## 7.2 Gain

Gain, a fundamental scaling parameter of the IR detector, relates the registered number of analog-to-digital units (ADUs) or equivalently, data numbers (DNs), to the number of accumulated photoelectrons. Like the UVIS channel, the Analog to Digital Converter (ADC) outputs a 16-bit number, allowing output signal values ranging from 0 to 65535 (i.e.  $2^{16} - 1$ ) for each pixel.

The WFC3 IR detector has a nominal gain setting of 2.5 e-/DN in order to provide complete sampling of the full-well of the IR detector ( $\sim 80,000$  electrons, which is  $\sim 32,000$  DN at the nominal gain). Due to slight hardware differences, effective gain values in each quadrant of the detector deviate slightly from the nominal gain. Twice yearly, the effective gain is measured via the mean-variance technique on pairs of internal flat fields: the mean signal level is plotted against the variance in signal, and the gain is the inverse of the slope. See [WFC3 ISR 2015-14](#) for more information on this method and the status of the IR gain from 2010-2015. [Table 7.1](#) summarizes the current values of the effective gain measured in each quadrant of the IR detector. The WFC3 group will continue to monitor the effective gain of the detector twice yearly to evaluate its stability over time.

**Table 7.1: Gain measurements for each quadrant in e-/DN, averaged over all epochs of observations. Quadrants 1, 2, 3, and 4 are the 512 x 512 pixel detector quadrants that are read out independently from the outer corner.**

Quadrant.	Gain	Error
1	2.252	0.054
2	2.203	0.039
3	2.188	0.036
4	2.265	0.053

## 7.3 WFC3/IR Bias Correction

At the beginning of each MULTIACCUM observation, when the detector is reset, a net DC bias with a value of order 11,000 DN is introduced. For details, see [Section 7.7.2 of the WFC3 Instrument Handbook](#). The overall bias level is somewhat different within each readout quadrant. In addition, there is a fixed pattern signal representing the inherent pixel-to-pixel reset levels. In standard MULTIACCUM processing a two-step process is used to remove these signals.

First, reference pixels are used to remove any changes in the overall bias level that may occur during the exposure. The 5 columns of reference pixels on the left and right sides of the IR detector are insensitive to illumination and are used to measure the bias

level of the detector at the time of each readout. During **calwf3** processing, the mean measured signal of the reference pixels in each read is calculated and subtracted from all of the science pixels on the detector for that read. This method has the advantage of removing any bias drifts with time. [WFC3 ISR 2002-06](#) details the method of reference pixel bias subtraction, while [WFC3 ISR 2012-05](#) shows reference pixel behavior, and compares various methods of subtracting the reference pixel signal. A long-term drift in the raw pixel values of the reference pixels and the zeroth read signals has been observed over the course of on-orbit observations (see Figures 5 and 6 of [WFC3 ISR 2017-04](#)) but has had no adverse effect on the final calibration. The reference pixel level subtraction is performed in the BLEVCORR step of **calwf3**.

Next, pixel-to-pixel and quadrant-to-quadrant differences in reset levels are removed by subtracting the zeroth readout of the exposure from all subsequent readouts. This is performed in the ZOFFCORR step of **calwf3**. The IR bias signal is therefore not a component of any of the calibration reference files, because it is removed using data contained in the science exposure itself.

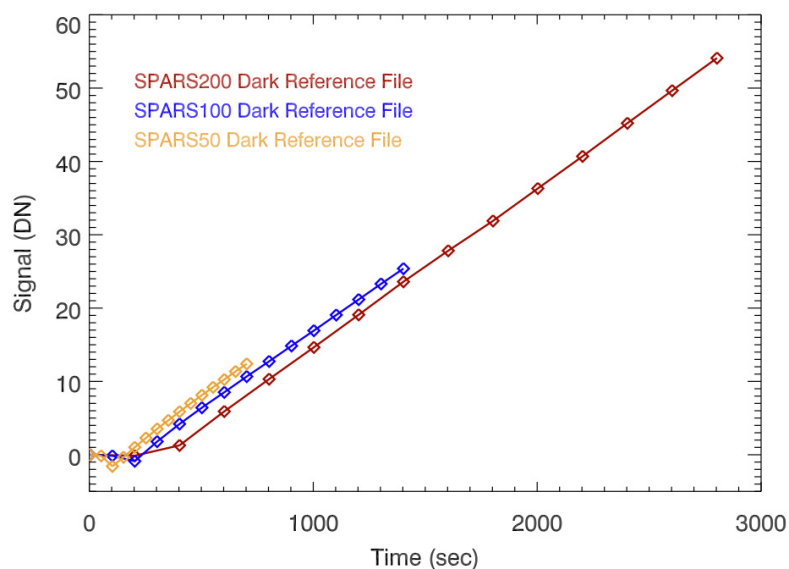
---

## 7.4 WFC3 Dark Current and Banding

### 7.4.1 Dark Current Subtraction

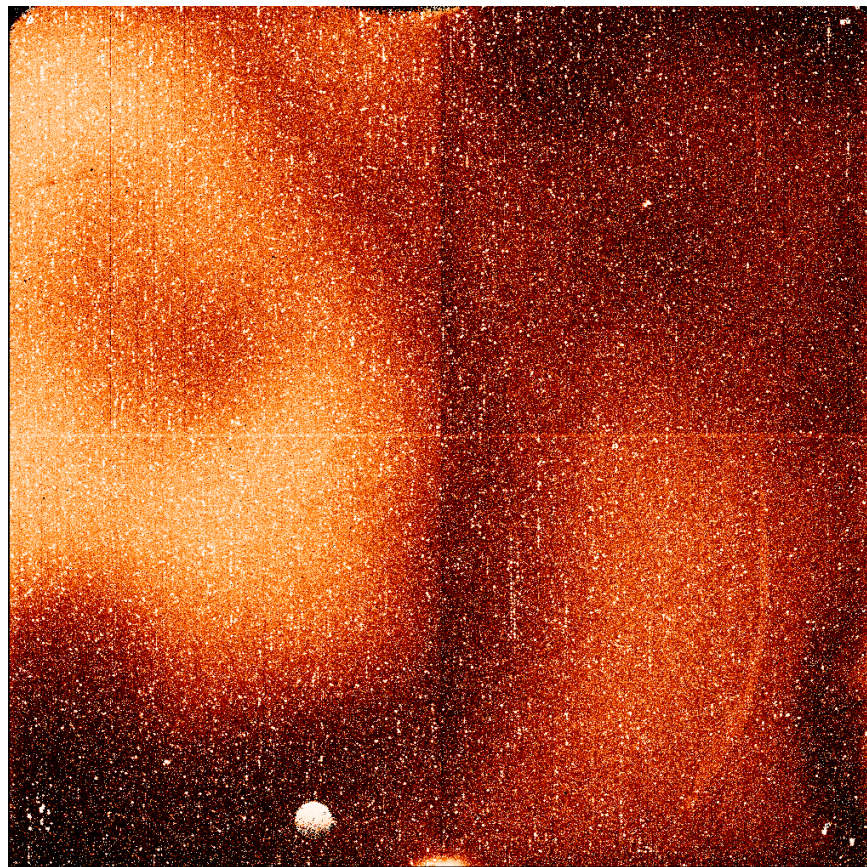
The dark current in the IR detector is the signal measured when no illumination source is present. In an ideal detector, this signal would grow linearly with integration time. In practice, the dark current behavior of the IR detector is dependent upon the timing pattern used to collect each observation and is not constant for the duration of a given MULTIACCUM ramp. In certain situations, the measured dark current can even be negative. [Figure 7.1](#) shows a plot of the mean measured dark current signal versus time for three different timing patterns. Note that the three curves are not superimposed one another, nor do they show a straight line for the entire duration of the ramps. Details are presented in [WFC3 ISR 2009-21](#). For these reasons, there is a separate MULTIACCUM dark current reference file for each sample sequence and mode (full-frame, subarray) combination. During pipeline processing, **calwf3** subtracts the appropriate dark current ramp read-by-read from the science observation.

The behavior of the IR darks has been analyzed in on-orbit data spanning Sep 2009 - June 2016. Although the darks possess a similar signal pattern across the detector, the median dark rates vary by as much as  $\sim 0.03$  e-/s ([WFC3 ISR 2017-04](#)). The distribution of these median values has a triangular shape with a mean and standard deviation of  $0.049 \pm 0.007$  e-/s. There is no apparent systematic long-term trend in the dark signal ([WFC3 ISR 2017-04](#)).

**Figure 7.1: Dark Current Signal vs Time.**

The dark current calibration files are created from a stack of dark up-the-ramp datasets which are taken on a regular basis throughout each observing cycle. For each sample sequence, the dark current calibration file is created by calculating the robust (outlier rejected) mean signal for each pixel in each read. Calculated uncertainties in the dark current calibration signals (in the error arrays of these files) are propagated into the error arrays of the calibrated science observations at the time of the dark current subtraction by **calwf3**. [Figure 7.2](#) illustrates the large-scale dark current structure, showing the measured signal rate in a high signal-to-noise dark current calibration ramp. In general, the upper left quadrant of the detector has the highest dark current, while the upper right has the lowest.



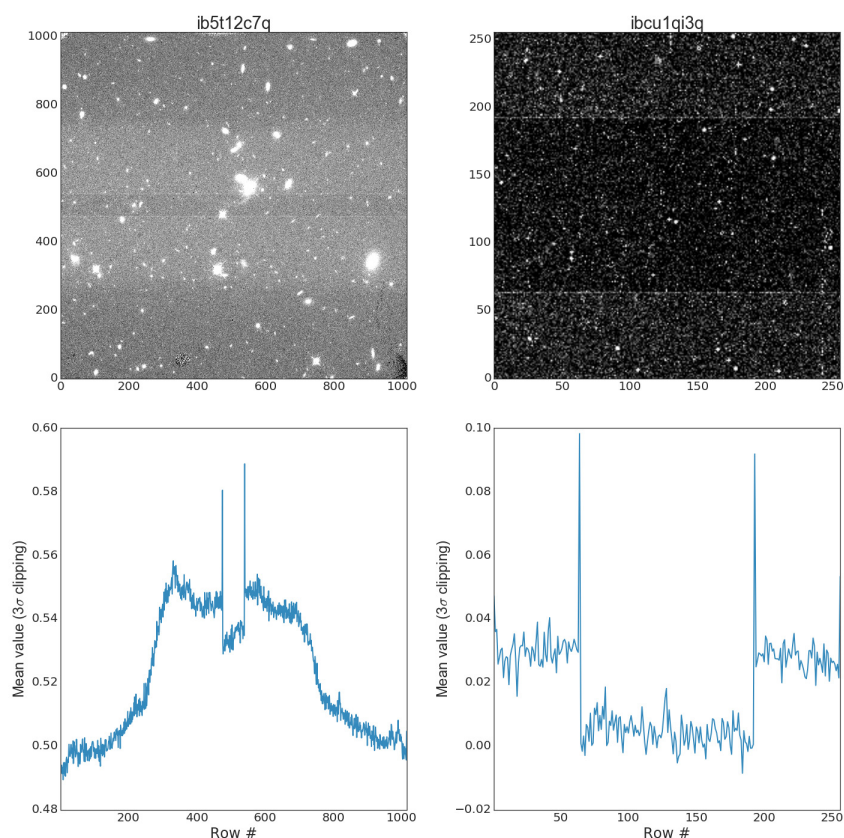
**Figure 7.2: Dark Current Image.**

### 7.4.2 Banding

Banding occurs when an IR observation (or observations) in a smaller readout format immediately precedes one in a larger subarray or a full-frame. Banded images exhibit a rectangular region containing pixels whose brightness levels are offset by typically  $\pm 3$ -5 DN from values in the rest of the image. The band is centered vertically in the larger (second) image, extending all the way across the image horizontally, and has a height equal to the height of the smaller (first) subarray observation. This is illustrated in [Figure 7.3](#) (top panels). The banded region is outlined on top and bottom by single rows of pixels with even brighter levels. The bottom panels of [Figure 7.3](#) show the respective vertical brightness profiles. For more information, please refer to [WFC3 ISR 2011-04](#) and the last paragraph of Section 7.4.4 of the *WFC3 Instrument Handbook*.

**Figure 7.3: Examples of banded images.**

**Top Left:** 64-pixel-high band in a SPARS50 full-frame science image. **Top Right:** 128-pixel-high band in a SPARS10  $256 \times 256$  subarray dark calibration image. **Bottom panels:** 3-sigma clipped robust mean along the x-axis of the two images in the top panels. Note the central banded regions and the two higher spikes from the rows that bound them.



## Mitigation

### *Observation Planning*

Banding can be prevented by avoiding mixed aperture sizes within the same orbit. If a variety of aperture sizes are required, observations should be sequenced from largest to smallest aperture sizes.

### *Dealing with Banded Observations*

Some early dark calibration files exhibited banding, so banding may have been imprinted during the calibration process. Observations retrieved from the archive are automatically reprocessed with the latest calibration files (which are now band-free), so simply re-retrieving one's observations from MAST may solve the problem.

If recalibration does not solve the problem, banded observations may still be scientifically viable. For brighter point sources, the effects of the low-level banding may not be significant and/or may be subtracted as sky. For fainter point sources or

extended targets that straddle two or more bands, banded observations may still be scientifically salvageable if one can perform independent sky subtraction in each of the band regions.

## 7.5 Blobs

Small blemishes called “blobs” appear in all WFC3/IR images ([Figure 7.4](#) and [Figure 7.5](#)). They are most noticeable in observations with high background or in observations of large, extended objects. Regions of lower sensitivity, by as much as 15% in a few cases but often much less than that, the blobs are caused by particulates on the surface of the mirror mounted upon the Channel Select Mechanism (CSM). A number of reports describe the blobs and their effects on IR data (WFC3 ISRs [2010-06](#), [2012-15](#), [2014-21](#), [2015-06](#), [2017-16](#)).

IR blobs were first observed shortly after WFC3 was installed on HST. The blobs have been increasing in number monotonically in time; no blob, once it appears, has disappeared. Hence, they have been increasing in number monotonically with time. The rate of appearance was higher in the first year after launch (2009) than it was later. [WFC3 ISR 2014-21](#) describes the time-dependent flag used by `calwf3` to mark pixels associated with the blobs (see also the discussion later in this Section).

Once a specific blob appears, it remains unchanged in size, cross section, or position relative to other blobs. However, due to slight non-repeatability in positioning of the CSM mechanism, the pattern of blobs on the IR detector can shift slightly from one image to the next by up to  $\sim 1$  pixel.

Because the CSM mirror is near to the telescope’s Cassegrain focus, and because the flat CSM mirror is slightly tilted with respect to the focal plane, the blobs’ radii systematically increase from the detector’s upper right corner (where they are nearly in focus, with radii less than  $\sim 4$  pixels) to the lower left corner (where they have radii of  $\sim 13$  pixels). Given their number and sizes, as of 2017, the blobs affect less than 2% of all pixels. An up-to-date list of blobs (i.e., new blobs since 2014) is maintained in [WFC3 ISR 2014-21](#) Table 4.

Each blob has a unique absorption cross section. Pixels associated with the “worst” blobs are flagged using the DQ=512 bit and stored in the DQ extension of the pipeline calibrated FLT file. Appropriate dithering can permit cleaning of blobs from combined images, as described in [WFC3 ISR 2010-09](#). An alternative method of correcting for blobs using a [blob flat field](#) is described in [WFC3 ISR 2014-21](#); its effectiveness for stellar photometry is presented in [WFC3 ISR 2015-06](#).

We note for completeness that because the CSM mirror is moved out of the beam in order for light to enter the UVIS channel, no blobs occur in UVIS images. However, UVIS images do contain “droplets” (cf. [Section 5.4.1](#)).

**Figure 7.4: IR Flat and Blobs.** Left: IR flatfield. The black spots are the blobs. Right: the IR Blob Mask in 2016.

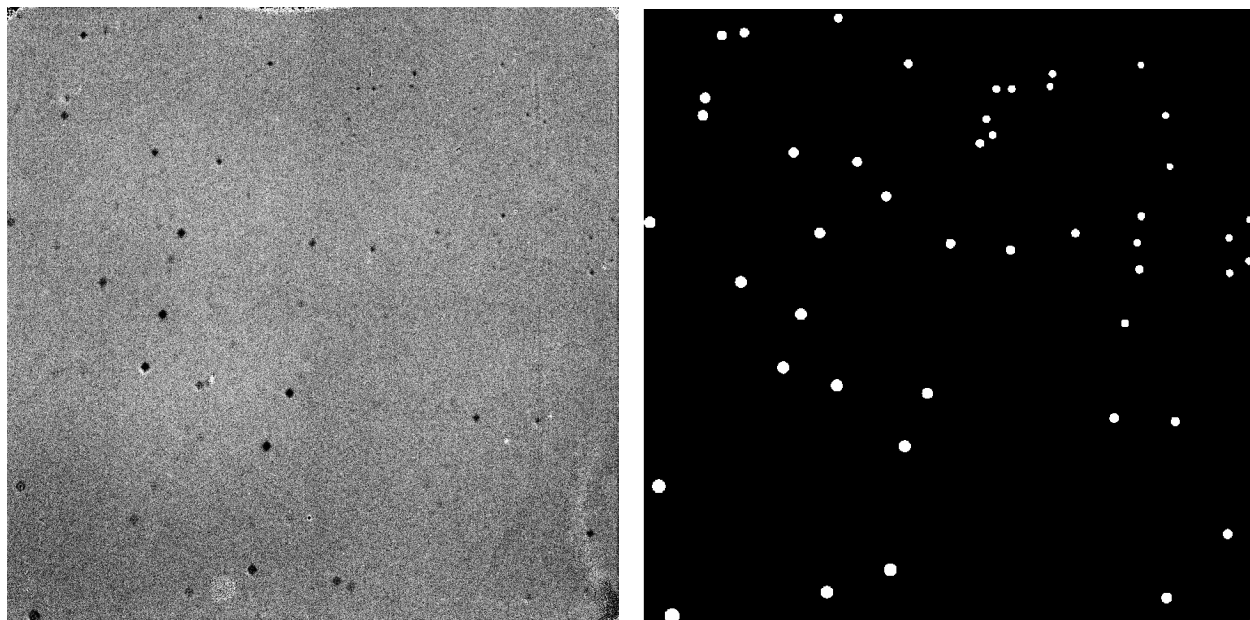
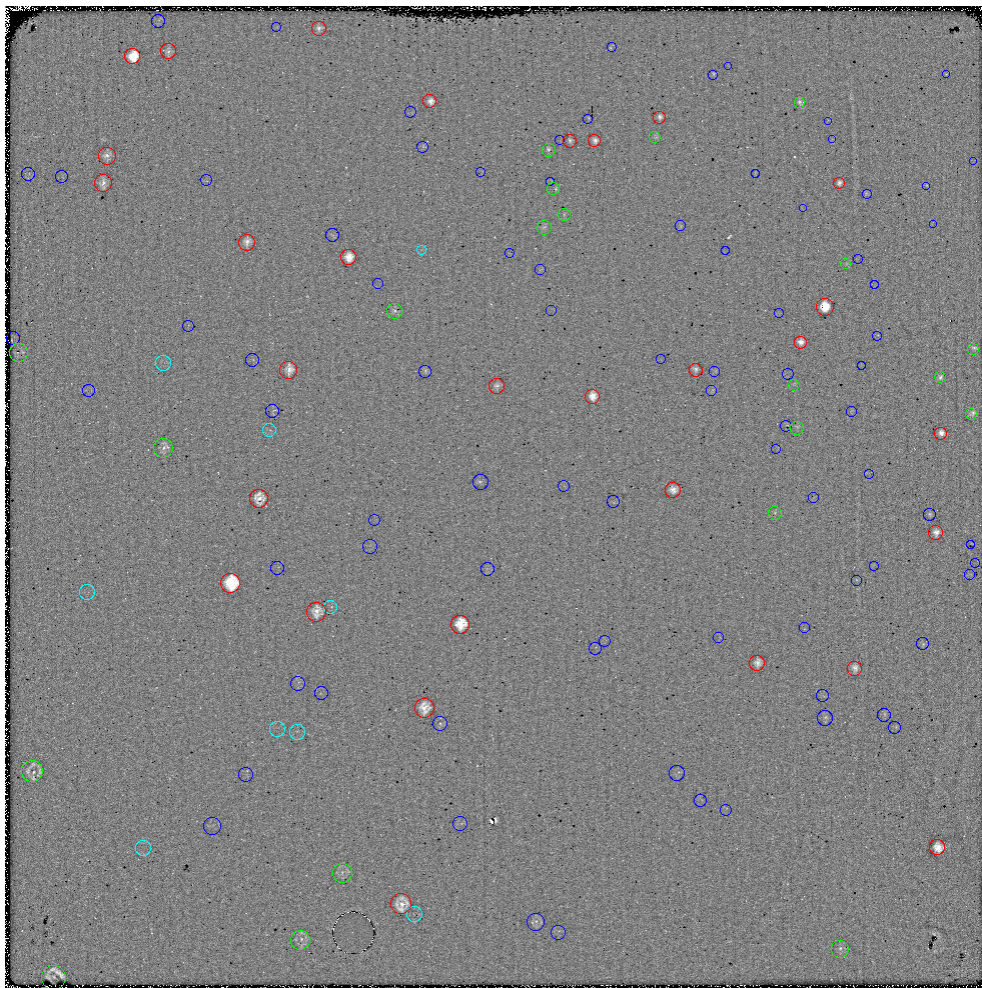




Figure 7.5: Blobs on the WFC3 IR detector as of Jan 2018 ([WFC3 ISR 2014-21](#)).

A dark earth flat image ratio with blobs known through January 2018 highlighted. The blobs are color-coded by strength (total counts in a circular aperture encircling each blob) from weak to strong: cyan, blue, green, red. Only the green and red blobs are flagged in the IR DQ array. [WFC3 ISR 2014-21](#) illustrates the method for finding the original list of blobs. These were found using a mixture of automated and visual methods. Since then all the new blobs have been visually identified by the WFC3 team.



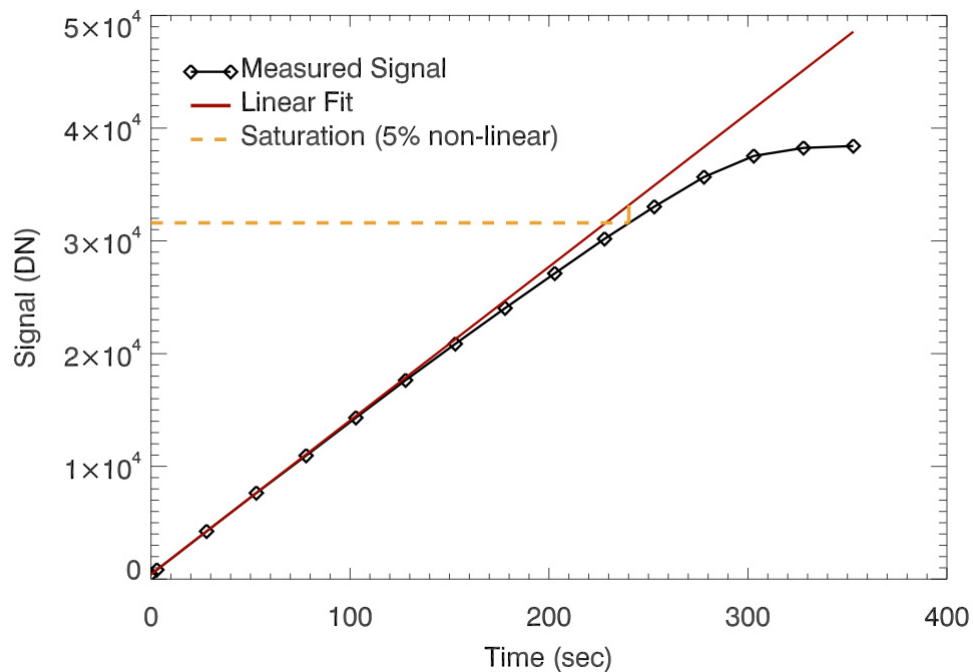
## 7.6 Detector Nonlinearity Issues

### 7.6.1 Nonlinearity Calibrations

HgCdTe detectors, such as that in the WFC3/IR channel, are inherently non-linear in their response to incident photons. [Figure 7.6](#) shows the measured signal up the ramp for a single pixel during a flat-field ramp. The black diamonds show that the

measured signal is clearly non-linear as the signal increases. The red line is a linear fit to reads at low signal levels, extended out to the end of the ramp. The difference between these two lines (normalized by the measured signal values) represents the amount of non-linearity in the measured signal. By measuring this difference for each pixel using a set of flat-field ramps, the non-linearity behavior of each pixel is characterized, and a correction produced. This correction takes the form of a 3rd order polynomial, as seen in the equation below, that relates the measured and idealized signal and is applied by **calwf3** in the NLINCORR step of the processing. Further details can be found in [WFC3 ISR 2008-39](#). The non-linearity correction in **calwf3** currently uses quadrant-averaged polynomials derived from ground testing data.

**Figure 7.6: Measured non-linear response of an IR pixel.**



### 7.6.2 Non-Zero Zeroth Read Correction for Bright Sources

As described in [Section 7.3](#), the first non-destructive readout after the detector reset provides the reference bias level for each pixel in a WFC3/IR science image. This image is referred to as the ‘zeroth readout’ or ‘zeroth read’. Due to the timing patterns in use, this read is collected at a finite time after the detector reset. Because the IR channel has no shutter, when a bright source is present in the field, a non-negligible amount of charge may accumulate on the detector between the time of the detector reset and the zeroth read. This implies that after the subtraction of the zeroth read from all subsequent reads in a ramp, the pixels at the location of the bright source will be under-reporting the amount of signal they were subjected to during the

ramp. While this has no effect on the **calwf3** calculation of the signal rate, it can lead to errors in the non-linearity correction step, since this correction is based on the absolute signal level.

In order to correct for this situation, the **ZSIGCORR** step in **calwf3** (very similar to that in the **calnica** software for NICMOS) computes an estimate of the number of counts for each pixel in the zeroth readout of a **MULTIACCUM** ramp, based on the count rate measured between the first two reads. This information is then used in the non-linearity correction (**NLINCORR**) step to estimate the absolute signal in each pixel and apply the appropriate linearity correction and saturation checks for that signal level.

---

## 7.7 Count Rate Non-Linearity

Previous HgCdTe detectors on HST have suffered from a count-rate dependent non-linearity, motivating a search for a similar effect on the WFC3/IR detector. An initial measurement of this effect was made by comparing the photometry of star clusters observed over a wide dynamic range and at overlapping wavelengths in WFC3/IR and NICMOS and/or ACS-WFC (see [WFC3 ISR 2010-07](#)). Utilizing a color term to account for differences in the observed bandpasses, statistically-significant non-linearity was detected in WFC3/IR photometry in the same direction but a few times smaller than that observed in NICMOS. Based on 235 stars in 47 Tuc observed with WFC3/IR in F110W and F160W and in similar bandpasses in NICMOS Camera 2, the non-linearity of WFC3/IR is measured at  $0.011 \pm 0.0023$  and  $0.010 \pm 0.0025$  mag per dex<sup>1</sup>, respectively, over a range of 10 magnitudes (4 dex). An independent measurement utilizing 1390 stars in NGC 3603 observed with ACS/WFC F850LP and WFC3/IR F098M yields a very similar result,  $0.010 \pm 0.0033$  mag/dex. The consistency of this measurement from two different comparison detectors of different technology suggests this result is robust. An additional analysis of the WFC3 IR count rate non linearity was carried out using observations of 24 brights stars that were also acquired by 2MASS( [WFC3 ISR 2011-15](#)). This work found that the count rate non linearity of the IR detector is less than 0.01 mag per dex, consistent with the earlier findings.

The impact of the count-rate non-linearity is that photometry of faint (i.e., sky dominated) sources calibrated with the published WFC3/IR zeropoints (derived from bright standard stars) will appear  $0.04 \pm 0.01$  mag too faint.

---

1. One dex is a factor of 10. Thus 1 mag per dex means a difference of 1 magnitude per factor of 10 in brightness.

## 7.8 IR Flat Fields

As for the UVIS channel (see [Section 5.4](#)), the IR channel flat-field reference files consist of two components. A high signal-to-noise component created from ground test data for pixel-to-pixel variations in the QE (P-flat). A second low frequency component (L-flat) derived from on-orbit observations accounts for differences between the ground based and on-orbit optical paths.

### 7.8.1 Ground Flats (P-flats)

During spring 2008, flat-field images for the IR channel were produced in the laboratory (see [WFC3 ISR 2008-28](#)) during the third and last thermal vacuum campaign (TV3) using the CASTLE Optical Stimulus (OS) system. The CASTLE is an HST simulator designed to deliver an OTA-like external beam to WFC3. It can provide either point-source or flat-field illumination in either monochromatic or broadband mode. Flat fields with the OS tungsten lamp were taken with the detector at its nominal operating temperature.

During TV3, CASTLE flat fields were acquired using the SPARS10 sample sequence, with varying numbers of readouts (samples) per exposure, chosen to obtain a signal of about 60,000 electrons per pixel in the final read. Four up-the-ramp exposures were taken per filter, providing a mean signal-to-noise ratio of  $\sim 500$ , yielding corrections down to a level of 0.2%.

### 7.8.2 On-orbit Test of the Ground Flats

To test the large-scale uniformity of the IR channel detector response as provided by the TV3 ground-based flat fields, in-flight observations of the globular cluster Omega Centauri using multiple pointing dithered patterns were taken during SMOV4 (program 11453). By placing the same group of stars over different portions of the detector and measuring relative changes in brightness, low frequency spatial variations in the response of the detector were measured. Average photometric errors of  $\pm 1.5\%$  were found in the original IR ground-based flat fields (see [WFC3 ISR 2009-39](#)), due to differences between the CASTLE and in flight optical paths. To further investigate low frequency residuals in in-flight sensitivity, additional observations of Omega Centauri were obtained during HST Cycles 17 and 18 at multiple dither positions and with different roll angles (programs 11928 and 12340). By observing the same stars at different locations of the detector and measuring relative differences in brightness, local variations in response were computed. The same methodology and software developed for the ACS L-flats( [ACS ISR 03-10](#)) was used for this work. For application to **WFC3**, the IR detector was divided into  $16 \times 16$  grid and a unique solution was calculated for each grid point, representing the deviations from unity. Low frequency L-flats were derived for the F098M, F110W, F125W, F139M, and F160W filters. Results show the L-flat variations have an rms of

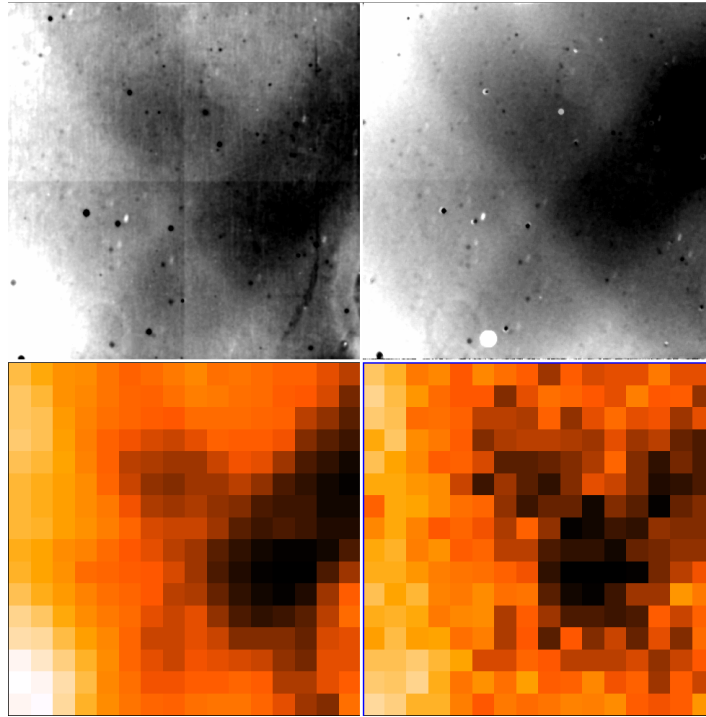


~1.1% with a peak-to-peak of  $\pm 2.5\%$ . While these results strongly suggest that ground based flat fields need to be corrected for residual low frequency structure, the signal-to-noise in the L-flat solutions was not sufficient to derive high quality corrections over the whole detector. Instead, deep images with small number of sources were used to derive the L-flat solutions.

### 7.8.3 On-orbit L-flats from Sky Observations.

L-flat corrections to the ground based IR flat-field images were calculated by combining calibration and GO IR data taken between September 2009 and December 2010. Details of this procedure are given in [WFC3 ISR 2011-11](#). In short, all observations taken with the F098M, F105W, F110W, F125W, F140W, and F160W filters with an exposure time in excess of 300s were flat fielded using the ground based flat field and then combined filter per filter after masking out objects. This resulted in a high quality sky image for the F160W filter, and somewhat noisier sky images for F098M and F125W. There were insufficient input images to derive sky images with adequate signal-to-noise in the remaining three filters (F105W, F110W, F140W). Comparing the resulting sky image between filters showed no clear indication of any color dependence of the low frequency structures. Therefore a final gray sky image was constructed using all available data (about 2000 datasets). Top left panel of [Figure 7.7](#) shows the gray sky image. As can be seen in the figure, there are significant low frequency structures due to differences between the CASTLE and inflight optical paths.

**Figure 7.7:** Top left: gray IR sky image. Top right: Earth flat taken in the F105W filter. Bottom left: 16 x 16 binned image of the gray IR sky image. Bottom right: Stellar L-flat from aperture photometry of Omega Centauri (F160W).



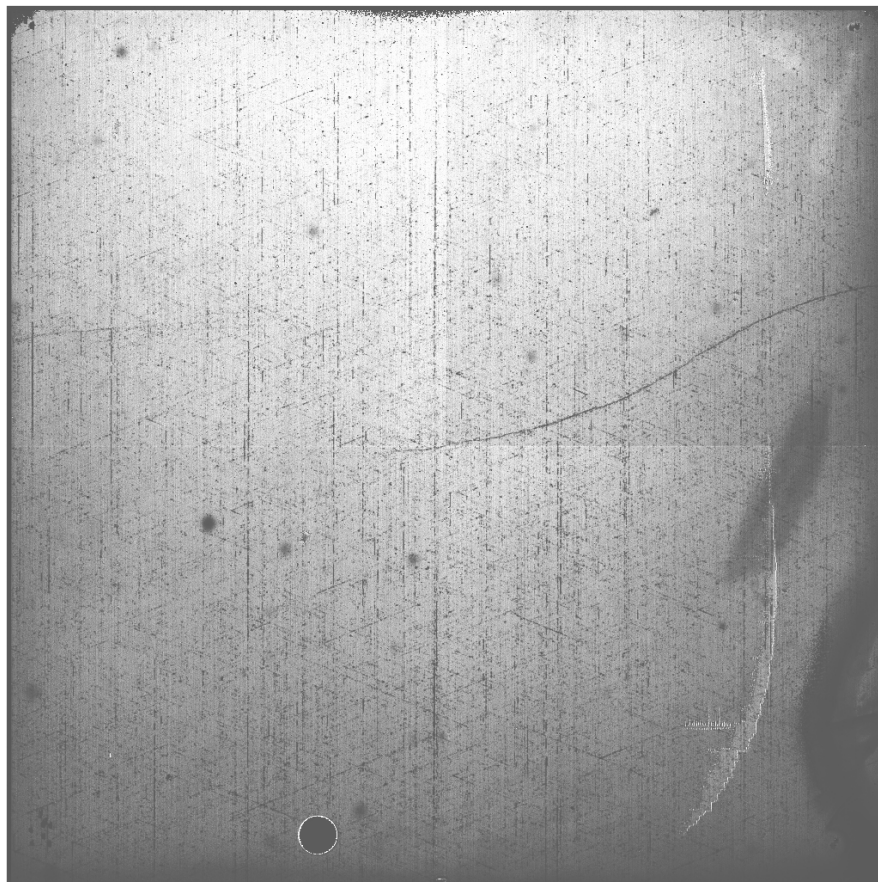
Images showing the difference between CASTLE and in-flight illumination patterns were also derived from observations of the moonlit Earth limb (program 11917). An image in the F105W filter, after having been flat fielded using the ground based flat-field image, is shown in the top right panel of [Figure 7.7](#). Both the shape and the amplitude of the low-frequency structures are very similar to the image derived from sky observations. To compare the sky image with results obtained from Omega Centauri, we bin the sky image to a  $16 \times 16$  grid, the same resolution used for the L-flat derived from the star cluster observations. The bottom left panel of [Figure 7.7](#) shows the binned sky image, while the bottom right panel shows the L-flat in the F160W filter derived from stellar observation. The same low frequency structures are present in both images, i.e. the results are consistent. The lower signal-to-noise in the stellar derived L-flat is apparent in the image.

#### 7.8.4 Pipeline Flats

The current IR pipeline flat-field images were constructed by combining the ground based high frequency P-flats with the gray sky image (discussed in the previous section). Before combining images, the noise was removed from the gray sky image using Fourier filtering. This was done mainly to remove outlier pixels. The gray sky image therefore represents an L-flat correcting for low and mid-frequency structure. Each flat-field image was normalized to 1.0 over the image section [101:900,101:900], which excludes areas of the detector known to contain anomalies

such as the "Death Star" and the "Wagon Wheel" (see Section 7.9.2). Figure 7.8 shows an example of a pipeline flat field (F160W).

**Figure 7.8: Pipeline flat-field image in the F160W filter.**



The photometric accuracy using the pipeline flat fields is better than 0.5% (peak to peak variation of -1.5 to +1.6%) if avoiding the outermost 128 pixels of the edge of the detector. Within the “Wagon-Wheel” region and the edge of the detector, photometric accuracy is reduced to about 0.8% (peak to peak variation of -2.0 to +1.9%).

The calibration files based on combining the CASTLE ground flat fields and the gray on-orbit L-flat were ingested into the HST Data Archive on Dec 2010. Observers with WFC3 IR data retrieved from the archive prior to that date can re-request their data in order to have them processed using the latest flat-field calibration files.

Online

---

*Additional discussion and the latest information about IR flat fields can be found on the WFC3 website*  
[http://www.stsci.edu/hst/wfc3/analysis/ir\\_flats](http://www.stsci.edu/hst/wfc3/analysis/ir_flats)

---

Because of geometric distortion effects, the area of the sky seen by a given pixel is not constant; therefore, observations of a constant surface brightness object will have count rates per pixel that vary over the detector, even if every pixel has the same sensitivity. In order to produce images that appear uniform for uniform illumination, the observed flat fields include the effect of the variable pixel area across the field. A consequence of dividing by these flat fields is that two stars of equal brightness do not have the same total counts after the flat fielding step. Thus, point source photometry extracted from a flat-fielded image (flt) must be multiplied by the effective [pixel area map](#). This correction is accounted for in pipeline processing by **AstroDrizzle**, which uses the geometric distortion solution to correct all pixels to equal areas. In the drizzled images (drz), photometry is correct for both point and extended sources.

---

## 7.9 Pixel Defects and Bad Imaging Regions

### 7.9.1 Bad Pixels

Various on-orbit calibration programs have been used to identify bad pixels and regions on the IR detector. All pixels found anomalous enough to potentially impact data analysis results are flagged and listed in the current bad pixel table reference file. While these pixels are listed in the bad pixel table and propagated into the data quality (DQ) arrays of the observer's ima and flt files produced by **calwf3**, the flagged science pixels will still have **calwf3**-calculated signals and signal rates in the science (SCI) arrays. It is therefore important for observers to pay attention to the DQ arrays in their data, and use them to identify which pixels to ignore in any post-**calwf3** data reduction and analysis (such as **AstroDrizzle**).



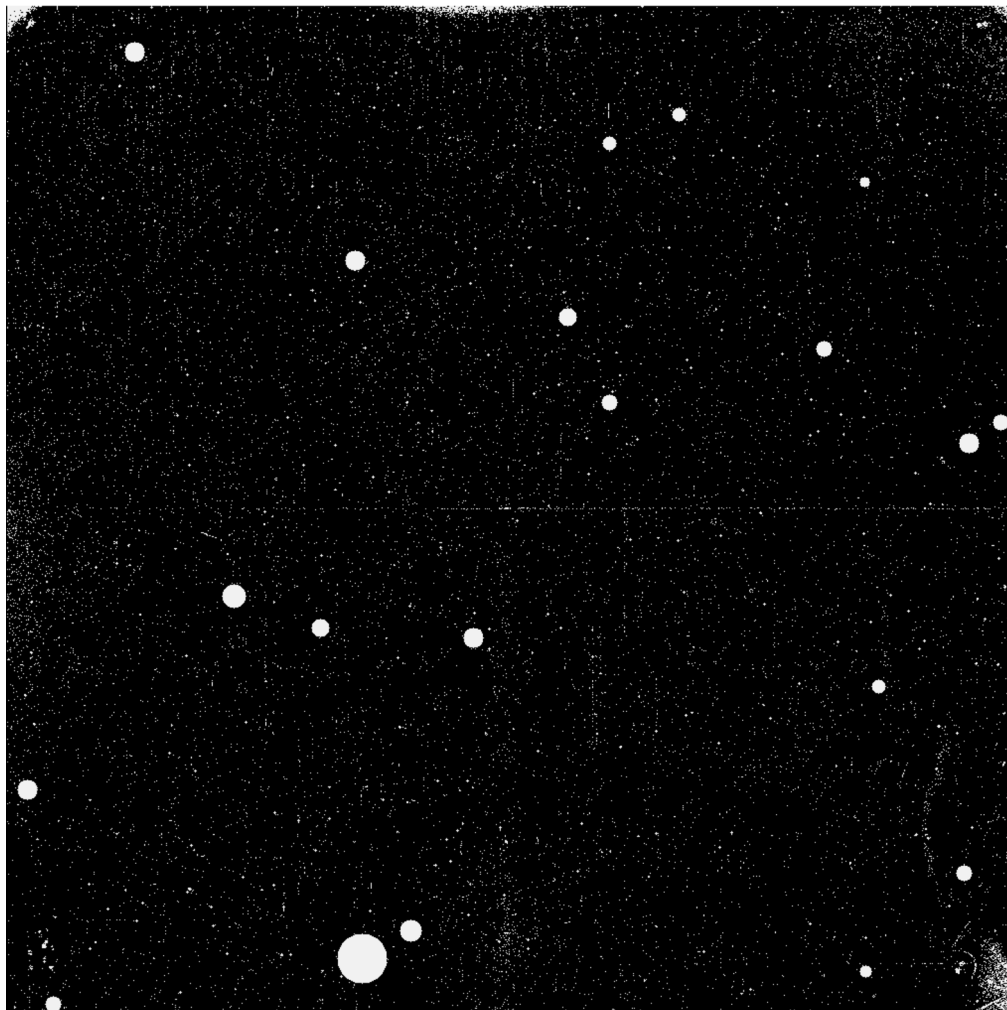

---

*It is the responsibility of the observer to determine which types of bad pixels are acceptable and which are to be avoided during data analysis. Use the DQ arrays for this purpose.*

---

During **calwf3** processing, the bad pixel table is imprinted onto the data quality (DQ) array associated with each ramp. Using the pixel values in the DQ array, observers can tailor the types of bad pixels used in their analysis. The current default for IR channel data is for **Astrodrizzle** to ignore (treat as bad) all pixels with any flag except 512 and 64. The 512 flag is used to identify pixels affected by blobs, while the 64 flag is currently not attached to any type of bad pixel and not used. Observers can change the `driz_sep_bits` parameter within **Astrodrizzle** to modify this default and adjust which types of bad pixels to use or ignore.

Figure 7.9: Example of an IR Bad Pixel Mask. White pixels are flagged in the bad pixel mask.



### 7.9.2 Off-nominal Detector Regions

As noted in [Section 5.7.7 of the \*WFC3 Instrument Handbook\*](#), there are several coherent features on the IR detector composed of poorly performing pixels. The “Death Star”, the large circular feature at the left bottom edge of the detector, is a collection of pixels which have extremely low QE and exhibit unstable behavior. The unbonded pixels in the upper left and right corners and along the top edge of the detector are unresponsive to illumination. These pixels have all been flagged as dead in the bad pixel mask and should be avoided during analysis. In the lower right corner of the detector is the feature known as the “Wagon Wheel”. This is a collection of pixels with quantum efficiencies 25% to 50% below normal. This does not mean that these pixels cannot be used during data analysis, but sources in this region will have a lower signal-to-noise ratio than they would elsewhere on the detector. This fact will be



captured in the error arrays of **calwf3** calibrated data. A more detailed description of these detector regions is given in [WFC3 ISR 2008-28](#).

### 7.9.3 Dead Pixels

These are pixels with a very low quantum efficiency which measure little or no signal when illuminated. In addition to the dead pixels found through the analysis of on-orbit data, we also manually marked the pixels comprising the “Death Star” as dead. In total, about 3300 pixels are flagged as dead (0.3% of the detector’s light-sensitive pixels), marked with a 4 in the bad pixel table (see [WFC3 ISR 2010-13](#) for details). Other than those pixels within the “Death Star”, dead pixels are scattered randomly across the detector. We recommend that observers ignore any pixel marked as dead.

### 7.9.4 Bad Zeroth Read Pixels

These are pixels which exhibit anomalous signals in the zeroth read of a data ramp, usually due to being shorted or unbonded (see [WFC3 ISR 2003-06](#)). This implies that many of the bad zeroth read pixels are also flagged as dead. By flagging bad zeroth read pixels in the bad pixel table, we are taking a conservative approach to bad pixel behavior. Historically, pixels with a off-nominal signal in the zeroth read displayed other non-nominal behaviors. Based on this experience, we felt it safer to flag these pixels. As with all flavors of bad pixels, observers should determine whether or not using these pixels will have a significant impact on their analysis.

In total, there are about 5000 pixels (~0.5% of the science pixels) flagged as bad in the zeroth read. These pixels are largely concentrated in the areas of the “Death Star”, the upper corners, and along the quadrant boundaries of the detector.

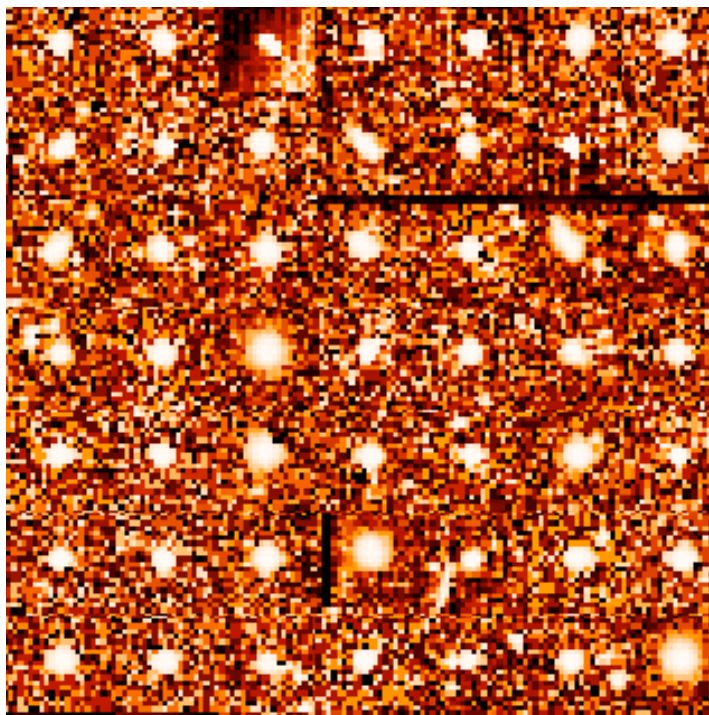
### 7.9.5 Unstable Pixels

These pixels display an inconsistent measurement of signal in a set of nominally identical ramps. Unstable pixels are characterized more thoroughly in [WFC3 ISR 2010-13](#) and [WFC3 ISR 2012-11](#). Unstable pixels observed on the WFC3/IR detector display a wide range of behaviors: some unstable pixels appear stable and repeatable in almost all ramps, but will measure appreciably different signal values in only one or two ramps. Other unstable pixels display signal values that vary wildly from ramp to ramp in all observations of a data set. Pixels flagged by these searches are all flagged with a value of 32 in the final bad pixel mask. There are a total of 16,500 unstable pixels (1.6% of all science pixels) on the IR detector. Due to the unpredictable behavior of these pixels, we recommend against including them in data analysis.

### 7.9.6 Snowballs

Curious but relatively innocuous anomalies which occasionally appear in IR observations are "snowballs". These sources have an extended, fuzzy appearance in the data. Snowballs are transient, extended sources that appear in IR channel data at rates of roughly 1.2 snowballs per hour of exposure time. The snowballs are suspected to be caused by natural radioactivity within the detector itself. Specifically, alpha particles emitted by thorium and/or uranium at  $\sim 1$  ppm concentration in the detector can explain the observed characteristics of the snowballs ([WFC3 ISR 2009-44](#)). Similar to the manner in which cosmic rays appear, the entire flux of a snowball is deposited into the detector's pixels instantaneously. A typical snowball affects about 10 pixels, depositing between 200,000 and 500,000 electrons, and saturating 2-5 pixels. [Figure 7.10](#) shows a  $7 \times 7$  mosaic of snowballs gathered from ground testing and on orbit data. With their behavior mimicking that of cosmic ray impacts, **calwf3** is able to remove snowballs from WFC3/IR data during standard pipeline processing. That, combined with low rate of occurrence, implies that snowballs should have a minimal impact on science observations. Further details on snowballs can be found in [WFC3 ISR 2009-43](#) (initial snowball characterization) and in [WFC3-2015-01](#) (longterm characterization). In 6200 hours of exposure time (over 5 years of operation) 7400 unique snowball events were detected on the IR array. No trend in occurrence is seen.

**Figure 7.10: A mosaic of snowballs generated using ground and on-orbit data.**

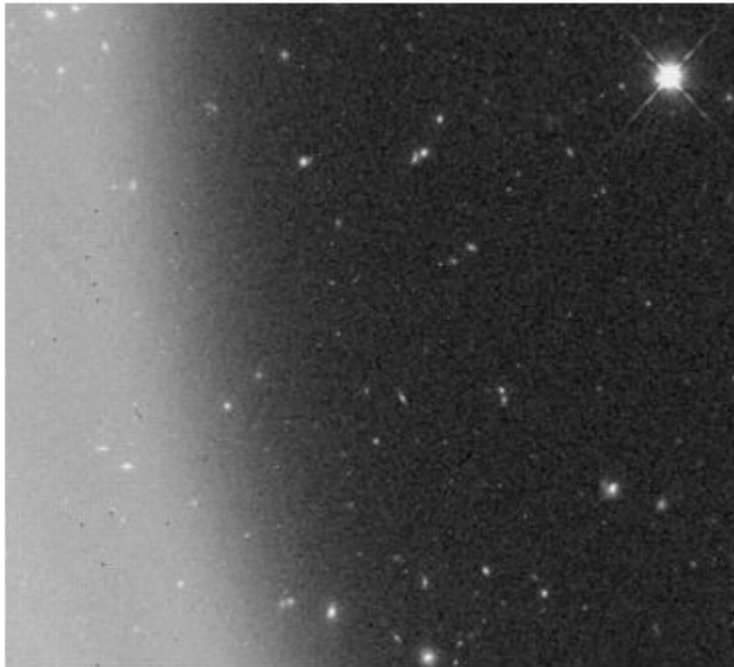


## 7.10 Time Variable Background Contamination

### 7.10.1 Scattered Earthlight

For certain HST orientations, the WFC3/IR detector can be subject to elevated and/or irregular background levels. Observations made when HST is pointing near the bright Earth limb can result in the leftmost  $\sim 200$  columns of the detector being subjected to background levels up to twice as bright as that on the rest of the chip. This is due to scattered Earth light. [Figure 7.11](#) shows an example of this behavior. The overall shape of this high background region is very similar from one affected image to another, but the brightness of the scattered light varies as the HST pointing approaches or recedes from the bright Earth limb. Details on the nature of this effect in IR darks can be found in [WFC3 ISR 2009-21](#). This effect can often be present for observations made when the limb angle, which is the angle between HST's pointing direction and the nearest limb of the bright Earth, is less than  $\sim 30$  degrees.

**Figure 7.11: IR Image affected by scattered earth-shine.**



### 7.10.2 Metastable Helium 1.083 $\mu\text{m}$ Emission Line

An additional source of background contamination is caused by the He line at  $1.083 \mu\text{m}$ . Filters whose bandpasses contain this He line are F105W, F110W and the G102 grism. The emission line originates from metastable helium in the Earth's upper atmosphere which, when present, can increase the IR background by up to factors of 6



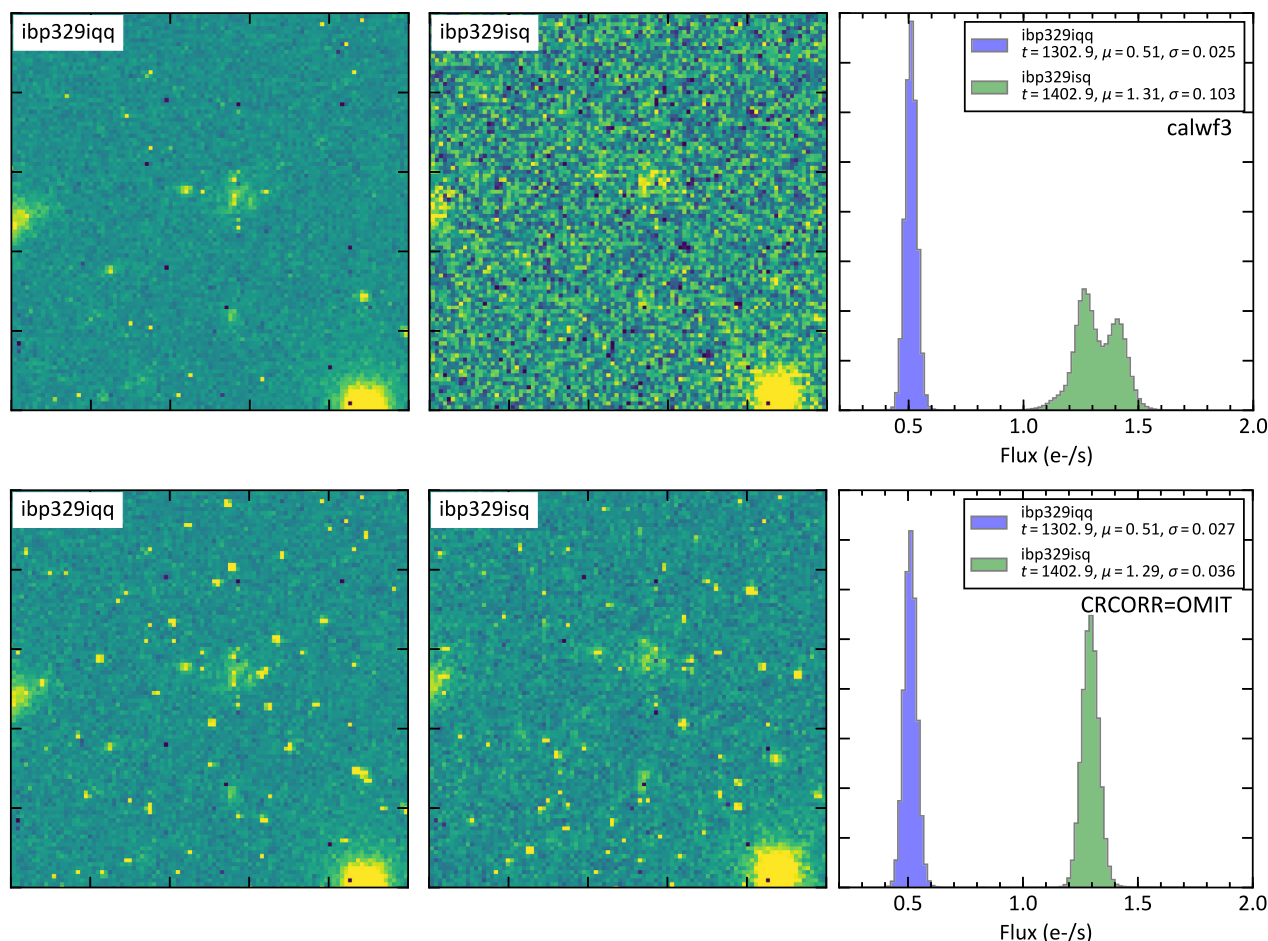
above the nominal zodiacal background. This spatially diffuse source affects portions of HST orbits where both the telescope and the atmosphere are illuminated by sunlight. [WFC3 ISR 2014-03](#) describes this effect more fully while [WFC3 ISR 2016-16](#) provides mitigation strategies (summarized in the next section).

### 7.10.3 Time-variable IR Background Mitigation Strategies

Strong time variation in the background can corrupt the **wf3ir** cosmic-ray identification algorithm (CRCORR, [Section 3.3.9](#)), which assumes that a given pixel sees a constant count rate from the combination of sources and diffuse background (i.e., the "ramps" are linear). Strong time variation in the background can trip the CR thresholds, with most or all of the image identified as a CR at a given read. Furthermore, since the background variation is fairly smooth from read to read any algorithm that tries to iteratively identify clean reads before and after a CR hit will likely fail.

The primary impact of the strong background variations is to increase noise as it reduces the available exposure time in the final flt products (e.g. only one or two reads out of 15 are used to form the flt). Furthermore, the distribution of background pixel values frequently shows multi-modal non-Gaussian shapes as different parts of the image trip and confuse the CR algorithm in different ways ([Figure 7.12](#)).

**Figure 7.12: Comparison of a pair of back-to-back F105W exposures where the first exposure (left) showed a constant zodiacal light background and the Helium line background increased rapidly over the duration of the second exposure (center column). The pixel distribution of the second exposure is poorly behaved (right): the noise is not simply higher due to the elevated background level but it also shows a bimodal non-Gaussian structure. Exposures such as these should either be discarded or reprocessed, for example, with strategies outlined in [WFC3 ISR 2016-16](#). The bottom panels show the same images and pixel distributions for images which have been reprocessed via `wf3ir` using `CRCORR=OMIT`. The noise properties of the products are better behaved but the cosmic rays must now be identified by other means.**



[WFC3 ISR 2016-16](#) provides more detail on how to identify exposures affected by these time-variable backgrounds as well as suggestions for reprocessing the affected exposures. The most straightforward strategy is to simply treat the WFC3/IR detector like a standard CCD and take the final read as the measure of the total flux accumulated during the exposure. This strategy is insensitive to any background variations during the exposure, but requires the user to then identify CRs by other means, for example, comparing dithered exposures with **AstroDrizzle**. [WFC3 ISR 2016-16](#) also provides a hybrid algorithm for removing the time variation of the background while still performing the CR identification within the **wf3ir** pipeline.

## 7.11 IR Photometry Errors

The estimated errors for the inverse sensitivity of the WFC3 IR channel computed from observations of the white dwarf standards plus a G-type star are  $\sim 2\%$  (statistical) 2-3% absolute (systematic, uncertainties in the models used as absolute standards). The signal to noise ratio, per observation, for the standard stars is such that the formal Poisson error is  $\sim 0.2\%$  for the wide band filters. For users who need precise photometry, a complete error analysis would include Poisson noise of the science target as well as the additional sources of photometric error of flat fields, spatial repeatability ( $\sim 1\%$  peak to peak), temporal repeatability (1% peak to peak), readnoise, uncertainty in the encircled energy ( $\sim 0.5\%$  at the infinite aperture - Hartig personal communication), uncertainty in the gain (section 7.1), and processing errors (sky subtraction, dark subtraction, correction for persistence). We do not yet understand why the photometric repeatability for the IR detector is so poor, this is under active investigation at the current time.

## 7.12 References

- H. Bushouse, *WFC3 IR Ground P-Flats*, WFC3 ISR 2008-28,  
<http://www.stsci.edu/hst/wfc3/documents/ISRs/WFC3-ISR-2008-28.pdf>
- T. Dahlen, L. Dressel, and J. Kalirai, *Dithering strategies for WFC3*, WFC3 ISR 2010-09  
<http://www.stsci.edu/hst/wfc3/documents/ISRs/WFC3-ISR-2010-09.pdf>
- M. J. Durbin, M. Bourque, S. Baggett, IR “Snowballs”: Long-Term Characterization, WFC3 ISR 2015-01, <http://www.stsci.edu/hst/wfc3/documents/ISRs/WFC3-ISR-2015-01.pdf>
- M. J. Durbin, and P. R. McCullough, *The Impact of Blobs on WFC3/IR Stellar Photometry*, WFC3 ISR 2015-06., <http://www.stsci.edu/hst/wfc3/documents/ISRs/WFC3-ISR-2015-06.pdf>
- M. Giavalisco, K. Sahu, R. Bohlin "New Estimates of the Sky Background for the HST Exposure Time Calculator", WFC3 ISR 2002-12  
<http://www.stsci.edu/hst/wfc3/documents/ISRs/2002/WFC3-2002-12.pdf>
- B. Hilbert, S. Baggett, M. Robberto. *Masking Technique on WFC3-IR Images*, WFC3 ISR 2003-06,  
<http://www.stsci.edu/hst/wfc3/documents/ISRs/WFC3-ISR-2003-06.pdf>
- B. Hilbert, *WFC3 TV3 Testing: IR Channel Nonlinearity Correction*, WFC3 ISR 2008-39,  
<http://www.stsci.edu/hst/wfc3/documents/ISRs/WFC3-ISR-2008-39.pdf>
- B. Hilbert, & P. McCullough, *WFC3 SMOV Results: IR Channel Dark Current, Readnoise, and Background Signal*, WFC3 ISR 2009-21.  
<http://www.stsci.edu/hst/wfc3/documents/ISRs/WFC3-ISR-2009-21.pdf>
- B. Hilbert, V. Kozhurina-Platais, and E. Sabbi, *WFC3 SMOV Program 11453: IR Flat Field Uniformity*, WFC3 ISR 2009-39  
<http://www.stsci.edu/hst/wfc3/documents/ISRs/WFC3-ISR-2009-39.pdf>

- B. Hilbert, *Snowballs in the WFC3-IR Channel: Characterization*, WFC3 ISR 2009-43, <http://www.stsci.edu/hst/wfc3/documents/ISRs/WFC3-ISR-2009-43.pdf>
- B. Hilbert & H. Bushouse, *WFC3/IR Bad Pixel Table: Update Using Cycle 17 Data*, WFC3 ISR 2010-13, <http://www.stsci.edu/hst/wfc3/documents/ISRs/WFC3-ISR-2010-13.pdf>
- B. Hilbert, *WFC3/IR Reference Pixel Characterization #1: Comparison of Bias Subtraction Methods*, WFC3 ISR 2012-05, <http://www.stsci.edu/hst/wfc3/documents/ISRs/WFC3-ISR-2012-05.pdf>
- B. Hilbert, and L. Petro, *WFC3/IR Dark Current Stability*, WFC3 ISR 2012-11, <http://www.stsci.edu/hst/wfc3/documents/ISRs/WFC3-ISR-2012-11.pdf>
- P. R. McCullough, J. Mack, M. Dulude, and B. Hilbert, *Infrared Blobs: Time-dependent Flags*, WFC3 ISR 2014-21, <http://www.stsci.edu/hst/wfc3/documents/ISRs/WFC3-ISR-2014-21.pdf>
- N. Pirzkal, A. Viana, A. Rajan, *The WFC3 IR "Blobs"*, WFC3 ISR 2010-06, <http://www.stsci.edu/hst/wfc3/documents/ISRs/WFC3-ISR-2010-06.pdf>
- M. Robberto, C. Hanley, I. Dashevsky, *The reference pixels on the WFC3 IR detectors*, WFC3 ISR 2002-06, <http://www.stsci.edu/hst/wfc3/documents/ISRs/WFC3-ISR-2002-06.pdf>

# Persistence in WFC3/IR

In this chapter...

8.1 Image Persistence / 160
8.2 Evaluating the Amount of Persistence in Science Images / 163
8.3 Mitigating the Effects of Persistence / 166
8.4 References / 169

## 8.1 Image Persistence

Image persistence is a phenomenon commonly observed in HgCdTe IR detectors. It is an afterglow of earlier images that in the case of the WFC3 IR detector is present when pixels are exposed to fluence<sup>1</sup> levels greater than about 40,000 electrons. In cases where portions of the detector are heavily saturated in the initial image, the afterglow can be detectable at levels comparable to the background for several hours.

A very obvious example of persistence is shown in [Figure 8.1](#). The image shows a high galactic latitude field; the observation was taken to search for the optical counterpart to a  $\gamma$ -ray burst. However two visits from separate IR programs had preceded the observation of this field. The afterglow of the bright sources in these dithered observations is clearly visible as 5 point line patterns in [Figure 8.1](#).

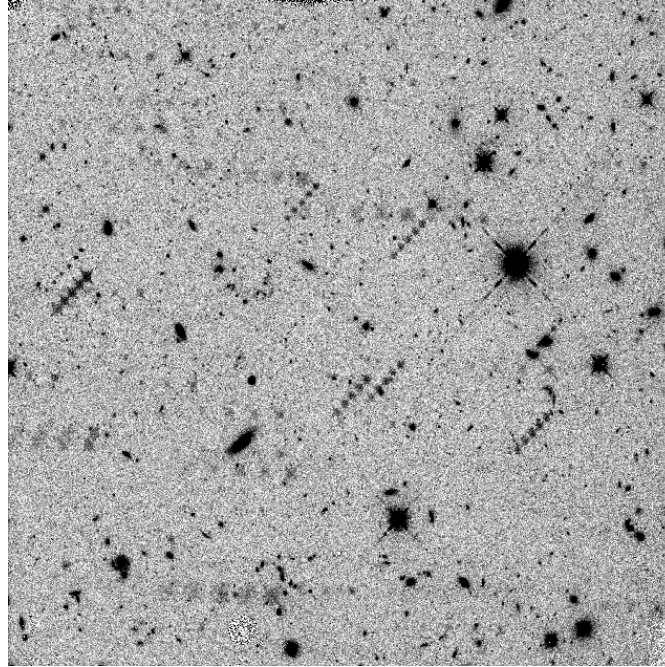
---

1. Fluence here is expressed in electrons. We use this nomenclature, however, with some “abuse-of-notation” regardless of whether or not the pixel full-well capacity is reached. Therefore when values larger than the typical  $\sim 80,000$   $e^-$  full-well capacity for the WFC3/IR channel are reported throughout this Chapter, their meaning is not that of “detected” electrons, but rather that of “electrons that would have been detected for an infinite full-well capacity”. This number is basically proportional to the impinging photon flux multiplied by the exposure time.”



**Figure 8.1: Persistence in an IR image.**

Example of an IR image, ia21h2e9q, in which persistence due to earlier visits is very obvious. The amplitude of the persistence for the brightest pixels in the diagonal trails of stars is about 0.1 electrons/sec. The image is plotted on a linear scale from 0.7 to 0.9 electrons/sec.



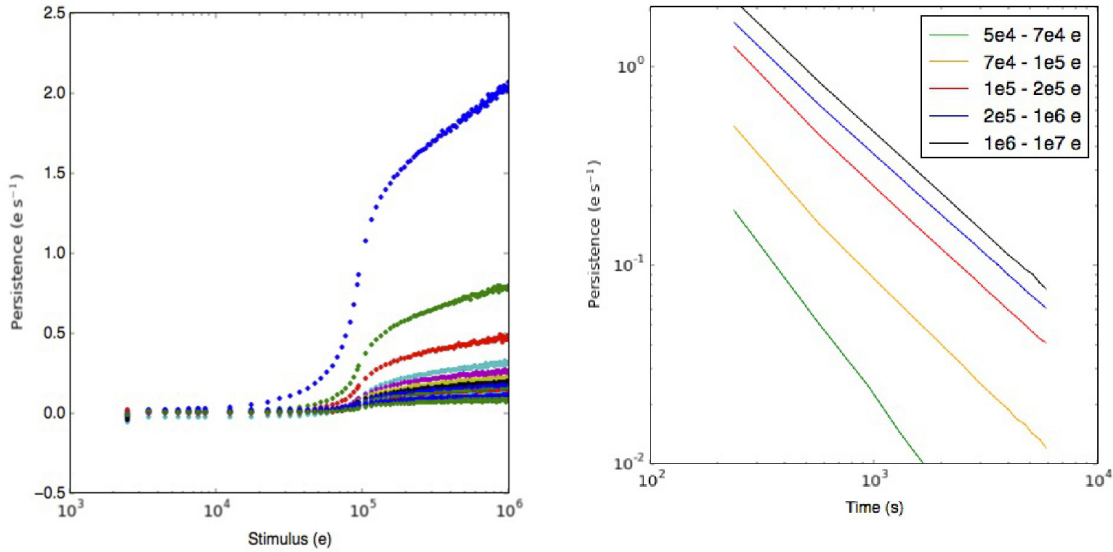
The pixels in the WFC3 IR array and other HgCdTe IR detectors are operated as reversed biased diodes. Resets increase the reverse bias. Electron-hole pairs created when light falls on the detector reduce the bias. Persistence is understood to arise from imperfections, traps, within the detector pixels that are exposed to free charge as the bias is reduced. The number of traps exposed is determined by the amount of charge accumulated in the diode. A small percentage of order, 1% of the free charge ([WFC3 ISR 2013-07](#)) is captured by the traps and released later, creating the afterimages known as persistence. Resets prevent more charge from being trapped, because they remove free charge from the location of the imperfections, but do not affect the charge that has already been trapped. A detailed theory of persistence has been presented by Smith et al., ([2008a](#), [2008b](#) and [WFC3 ISR 2013-07](#)).

Different HgCdTe IR detectors have different persistence characteristics. In WFC3, a pixel exposed to an effective fluence level of  $10^5$  electrons produces a signal of about 0.3 e-/sec 1000 s after the exposure. The signal decays with time as a power law with a slope of about -1. Thus at 10,000 s, the flux will be about 0.03 e-/sec, compared to the dark current of 0.048 e-/sec (median). As shown in the left panel of [Figure 8.2](#), the amount of persistence in the WFC3 IR detector depends strongly on the fluence of the earlier exposure. This shape of the curve reflects the density of traps in different regions of the pixels (and the fact that once the detector is saturated the voltage levels within the diodes do not change much with increasing fluence). The right panel of [Figure 8.2](#) shows the power law decay of the persistence at different fluence levels.

**Figure 8.2: Persistence as a function of stimulus and time.**

**Left.** Persistence as a function of stimulus in a series of dark frames after an observation of the globular cluster Omega Cen. Each color represents one dark image, hence the color sequence indicates a time sequence in the darks series (blue is the first dark, green the second, and so on).

**Right.** The persistence decay as a function of time. Each color represents the persistence decay-with time for pixels grouped by different fluence values in the stimulus exposure (Long et al 2012)..



A further complexity of persistence modeling is due to the fact that persistence actually depends not just on the total fluence, but on the complete exposure history. The traps have finite trapping times (see [WFC3 ISR 2013-06](#), [WFC3 ISR 2013-07](#)). A short exposure of a source that results in a fluence of 10<sup>5</sup> electrons produces less persistence than a longer exposure of a fainter source that reaches the same fluence level, because in this second case the traps have more time to capture free electrons before the diode gets reset. While tracking the complete history of each WFC3/IR pixel is a huge task, to a good level of approximation it is possible to model persistence only as a function of total fluence and total exposure time in the stimulus image. This model, which is currently used by the WFC3 team to predict persistence and derive the persistence products (see [Section 8.2](#)) is thoroughly described in [WFC3 ISR 2015-15](#), and is parametrized as:

$$P(t) = A \left( \frac{t}{1000} \right)^{-\gamma}$$

where  $t$  is the time since the end of the stimulus exposure, in seconds, and  $A$  and  $\gamma$  are function of both exposure time and fluence level in the stimulus exposure. We refer to this model as the “A- $\gamma$ ” model.

Additionally, clear evidence of spatial variation in persistence across the IR detector has been measured. One quadrant (upper left) has a higher persistence amplitude than the other three. The shapes of the power law exponents also appear to

differ between quadrants. Using a correction flat provides a factor of two reduction in the peak to peak uncertainties. This flat is incorporated into the persistence prediction software and available from MAST (Version 3.0.1 of the persistence software). A full description is in [WFC3 ISR 2015-16](#).

Persistence of the magnitude (and importance) seen in [Figure 8.1](#) is rare. This is in part because contact scientists check phase II submissions to identify programs that are likely to cause large amounts of persistence and mission planners inhibit WFC3 IR observations for 2 orbits after such observations. However, this process is only intended to identify the worst cases of persistence and the process is not error free. A large proportion of the exposures taken with WFC3 have some saturated pixels and all of these pixels have the potential to generate persistence in the next observation in the schedule. Inhibiting IR observations after all exposures that could generate persistence would make it impossible to schedule the large numbers of IR observations that are carried out with HST, and in most cases, small amounts of persistence do not affect the science quality of the data, as long as observers and data analyzers take time to examine their IR images for persistence.

---

## 8.2 Evaluating the Amount of Persistence in Science Images

As described above, persistence in an image depends on images that have been obtained previously. However, when an observer retrieves his/her data, the observations that came before will most likely be proprietary and inaccessible to the observer. To address this difficulty, the WFC3 team has developed a set of prototype software that estimates the persistence in an observer's image. Although not currently part of the standard calibration pipeline, the WFC3 team runs these persistence estimation tools on all WFC3 IR images. The tools produce an html file summarizing the amount of persistence in the image as well a several FITS files that can be used in downstream analysis of the HST data.

The output products, which consist of a combination of html files and a number of FITS files, can be retrieved by observers through MAST using a special screen located at:

<http://archive.stsci.edu/prepds/persist/search.php>.

The query screen is shown in [Figure 8.3](#).



Figure 8.3: MAST search screen used to retrieve information about persistence.

Normally, these output data products are available a few weeks after an IR observation has taken place.

There are two types of persistence that generally affect data analysis differently. We define *external* persistence as persistence that is generated by an earlier visit, and *internal* persistence as persistence generated within the same visit as the image in question. External persistence is not within the control of the observer, and can appear anywhere in an IR image. Internal persistence is usually less important, since at least in the case of small dithers, it affects regions of the detector which are in the wings of the point spread function of bright sources. The results of a query from the persistence query screen for Visit H of program ID 11189 are shown in Figure 8.4. The columns EXT1, EXT2 and EXT3 indicate that 0.3%, 1.89% and 6.83% of the pixels were predicted to have external persistence exceeding 0.1, 0.03, and 0.01 e-/sec. The columns labeled TOT1, TOT2, and TOT3 provide the percentages for the sum of external and internal persistence. If all of the estimates of persistence for a dataset in

the results screen, particularly those having to do with external persistence, are zero then one should not need to investigate further.

Observers should check for persistence as part of their evaluation of the science data quality of their observations. Observers should do so early enough that they have an opportunity to submit a [Hubble Observation Problem Report](#) (HOPR) if the data are so compromised by the existence of external persistence in their images that the science they proposed cannot be carried out. Data analyzers should also check to determine whether they need to take persistence into account in analysis.

If the summary estimates in the results screen indicate there is persistence, then more information about the amount of persistence and its location in the images can be obtained by clicking on the links associated with data set column in the results screen. (If the data are still proprietary, you will be asked for your MAST login name and password at this point). This will bring up a page that contains additional text as well as a number of images showing where persistence is predicted. There are also various *thumbnail images*, showing how well the persistence is removed by the model in selected areas of an image. The utility of these thumbnails varies, depending upon the crowding of the image with *real* sources. An algorithm is used to try to select regions of the image which have the largest amounts of persistence but which are not very crowded, so that it is easy to establish the sky level and automatically generate thumbnails. But this algorithm is not very sophisticated, and in many cases, all of the regions with significant persistence lie in regions of the image that contain brighter *\*real\** objects. Nevertheless, inspecting the images is recommended, and should help one to determine, qualitatively, whether persistence is likely to affect the science one is attempting to carry out.

**Figure 8.4: Results of MAST persistence query.**

Dataset	Asn ID	Proposal ID	Visit	Aper	Target	RA (J2000)	Dec (J2000)	Exp Time	Filter	PI Last Name	Release Date	Status	EXT1	EXT2	EXT3	TOT1	TOT2	TOT3
<a href="#">ia21h2e9q</a>	IA21H2010	11189	<a href="#">H2</a>	IR	GRB090423	09 55 32.674	+18 09 01.32	1302.900	F160W	Tanvir	2011-01-26 07:18:02	Complete_2.0	0.040	1.220	5.020	0.040	1.240	4.970
<a href="#">ia21h2e9q</a>	IA21H2010	11189	<a href="#">H2</a>	IR	GRB090423	09 55 32.632	+18 09 01.53	1302.900	F160W	Tanvir	2011-01-26 07:18:02	Complete_2.0	0.010	0.860	4.850	0.020	0.920	4.810
<a href="#">ia21h2ecq</a>	IA21H2010	11189	<a href="#">H2</a>	IR	GRB090423	09 55 32.634	+18 09 01.28	1302.900	F160W	Tanvir	2011-01-26 07:18:02	Complete_2.0	0.000	0.340	3.250	0.000	0.360	3.240
<a href="#">ia21h2edq</a>	IA21H2010	11189	<a href="#">H2</a>	IR	GRB090423	09 55 32.592	+18 09 01.49	1302.900	F160W	Tanvir	2011-01-26 07:18:02	Complete_2.0	0.000	0.220	3.140	0.010	0.260	3.140
<a href="#">ia21h2efq</a>	IA21H2010	11189	<a href="#">H2</a>	IR	GRB090423	09 55 32.639	+18 09 01.63	1302.900	F160W	Tanvir	2011-01-26 07:18:02	Complete_2.0	0.000	0.080	1.840	0.000	0.100	1.840
<a href="#">ia21h2egq</a>	IA21H2010	11189	<a href="#">H2</a>	IR	GRB090423	09 55 32.597	+18 09 01.85	1302.900	F160W	Tanvir	2011-01-26 07:18:02	Complete_2.0	0.000	0.050	1.710	0.010	0.080	1.720
<a href="#">ia21h2eiq</a>	IA21H2010	11189	<a href="#">H2</a>	IR	GRB090423	09 55 32.679	+18 09 01.67	1302.900	F160W	Tanvir	2011-01-26 07:18:02	Complete_2.0	0.000	0.010	0.610	0.000	0.030	0.630
<a href="#">ia21h2ejq</a>	IA21H2010	11189	<a href="#">H2</a>	IR	GRB090423	09 55 32.637	+18 09 01.89	1302.900	F160W	Tanvir	2011-01-26 07:18:02	Complete_2.0	0.000	0.000	0.440	0.010	0.030	0.460
<a href="#">ia21h2elq</a>	IA21H2020	11189	<a href="#">H2</a>	IR	GRB090423	09 55 32.674	+18 09 01.32	1302.900	F160W	Tanvir	2011-01-26 07:18:02	Complete_2.0	0.000	0.000	0.230	0.000	0.020	0.260
<a href="#">ia21h2enq</a>	IA21H2020	11189	<a href="#">H2</a>	IR	GRB090423	09 55 32.632	+18 09 01.53	1302.900	F160W	Tanvir	2011-01-26 07:18:02	Complete_2.0	0.000	0.000	0.000	0.000	0.010	0.030
Dataset	Asn ID	Proposal ID	Visit	Aper	Target	RA (J2000)	Dec (J2000)	Exp Time	Filter	PI Last Name	Release Date	Status	EXT1	EXT2	EXT3	TOT1	TOT2	TOT3

The software applied to all WFC3/IR images also produces several FITS files, as summarized in [Table 8.1](#), for each flt file in a dataset. The \*\_extper.fits and \*\_persist.fits files contain predictions of the external and total persistence in a dataset. The \*\_flt\_cor.fits file is an flt file with the total persistence subtracted. These files can be retrieved from MAST as a tar.gz file by clicking one of the Visit links; each Visit must be retrieved separately. In situations where there is some persistence predicted in a science image, displaying these persistence product FITS files along with original data in DS9 or some other image display is ultimately the best way to determine whether persistence needs to be taken into account in down-stream analysis of the data.

**Table 8.1: Files Associated with Persistence Correction**

Generic Filename	Contents
_extper.fits	Prediction of external persistence
_persist.fits	Prediction of total persistence
_flt_cor.fits	flt file with persistence model subtracted

## 8.3 Mitigating the Effects of Persistence

Two possible ways to mitigate persistence are to 1) exclude the affected pixels from the analysis, or 2) subtract the persistence signal from the data and use the modified data in the analysis.

Simple procedures can be used to mark compromised pixels and modify the data quality extensions of the flt files. Typically one would use the persist.fits products to define an acceptable level of persistence, say 0.01 e-/sec, based upon a visual inspection of the data and the corresponding persistence images. This level can be used to flag all pixels in the persist.fits image that have larger predicted persistence. The choice of level would be based on the science objective and the fraction of pixels impacted. For example, if the DQ extension of the flt.fits image is defined as im1 and the persist.fits product as im2, the following python code could be used:

```
tol = 0.01
Boolean_mask = im2 >= tol
im1[Boolean_mask] += 1024
```

The 1024 value is a currently unused data quality flag for the IR detector.

This method is typically very good at flagging persistence from previous observations in staring mode. However, the “A-gamma” model predictions show some discrepancy from the observed amount of persistence for images taken shortly before the image of interest (short-term persistence). While the model is still being improved, the user should be aware that the estimated internal persistence may differ from what is observed. In a similar fashion, when persistence is from prior *scanned* observations, the model significantly underestimates the level of persistence observed in the data. The “A-gamma” model relies on fluence estimates from the flt images of prior observations. Therefore, it implicitly assumes that the estimated flux in the flt reflects the actual impinging flux on the pixels. The CRCORR step of **calwf3** works by fitting a line to the accumulating charge between reads, but for scan-mode observations, the flux is only accumulating in a very short interval, thus the pipeline is unable to report the true flux (See also [Section 10.2](#) on IR scanned observations). This is true not only for the scans but also for other moving targets that end up in WFC3/IR observations,

like asteroid trails in external observations ([WFC3 ISR 2017-18](#)) or bright cities or even ships that are imaged during the observations of the dark-earth IR flats taken by the WFC3 team to calibrate the IR blobs, see [Section 7.5](#). Persistence in these cases is very poorly estimated.

However, for both internal persistence and for persistence from moving targets, the “A-gamma” model does still predict the location of persistence on the detector very well. The actual predicted values could be off, however, by orders of magnitude. Therefore, the user is advised to tune the tolerance level to account for these possible mismatches.

Once the pixels are flagged, down-stream analysis proceeds as it normally would, assuming the tools that are used take data quality flags into account. Persistence is a property of the pixel: as long as the observer who planned the original observations created a set of dithered images, using this procedure to flag bad-persistence pixels should not significantly impact the science.

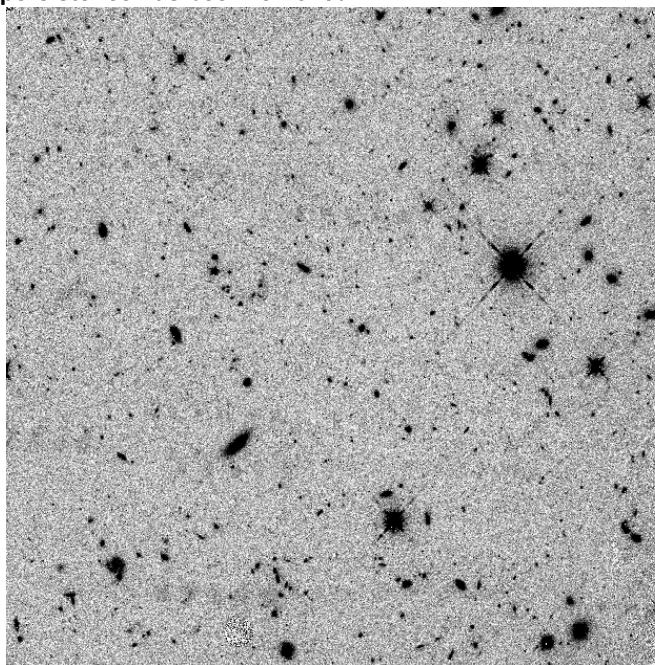
As an example, using **AstroDrizzle** to exclude those flagged pixels would result in a combined image that is largely cleansed of the effects of persistence. In some cases, the threshold defined from inspection of the `flt.fits` may not be low enough to detect lower-level persistence, so the deeper, combined `drz.fits` images may be used to verify whether persistence was fully removed.

An alternative is to use the persistence-subtracted files in down-stream analysis. If one adopts this approach, one should carefully inspect the `_flt_cor.fits` corrected data products (produced by simply subtracting the `persist.fits` model directly from the `flt.fits` image) to evaluate how well persistence has been subtracted from the image. It is important to inspect all of the images in a particular science observation as the persistence signal will decline with time. Typically in situations in which there is persistence, about 90% of the persistence signature is removed by the model. Because there are variations in persistence which are still being studied, including spatial variations across the detector, the corrected data products can be either under- or over-subtracted, particularly in the case of internal persistence where the power law model is not optimal for estimating the short term decay.

The persistence-subtracted image of our example is shown in [Figure 8.5](#). The image is much cleaner, especially at the center of the image where the  $\gamma$ -ray burst had occurred. However, a careful inspection shows some residual signatures of the persistence, particularly due to the set of early images that produced the *horizontally-stepped faint features* in the original image. Sometimes one can do better by scaling the persistence model and producing one's own persistence-subtracted image. It is also, of course, possible to combine these approaches as well, flagging the worst pixels in the persistence-corrected images, and then using **AstroDrizzle** to produce a combined image.

**Figure 8.5: Image with Persistence subtracted.**

Same as the image shown in [Figure 8.1](#) but with persistence subtracted. Much, but not all of the persistence has been removed.



At some point, we expect to release the tools we have for general use. In the meantime, if persistence remains a significant problem in the analysis of your images in spite of the approaches suggested above, please contact the help desk ([help@stsci.edu](mailto:help@stsci.edu)). It is possible that by changing some of the parameters in the model, we can provide better estimates of the persistence in an `flt` file, particularly in situations where several earlier visits have affected a science image.

In all cases in dealing with persistence, as is true of most problems associated with data analysis, first assess the severity of the problem and then choose a method of handling the issue that is consistent with the science being carried out. Users concerned about the effects of persistence on their data should check for updates on the [WFC3 web pages](#), [WFC3 Persistence pages](#) in the periodically released [STANs](#), as well as the [Instrument Science Reports](#).



## 8.4 References

- Bergeron, L. E. and Dickinson, M. E. 2003, *Removal of Cosmic Ray persistence from Science Data using the Post-SAA Darks*, [NICMOS ISR 2003-010](#)
- Dahlen, T., 2013, *WFC3/IR Internal Flat Fields*, [WFC3 ISR 2013-04](#)
- Hilbert, B. and Petro, L., 2012, *WFC3/IR Dark Current Stability*, [WFC3 ISR 2012-11](#).
- Hilbert, B., 2012, *WFC3/IR Reference Pixel Characterization #1: Comparison of Bias Subtraction Methods*, [WFC3 ISR 2012-05](#).
- Hilbert, B and McCullough, P., 2010, *WFC3 SMOV Results: IR Channel Dark Current, Readnoise, and Background Signal*, [WFC3 ISR 2009-21](#).
- Long, K., S. Baggett, S.M., MacKenty, J.W., and Riess, A.G., 2012, *Characterizing persistence in the IR detector within the Wide Field Camera 3 instrument on the Hubble Space Telescope*, [Proceedings of the SPIE, 8442, 84421W-9](#)
- Long, K. S., Baggett, S. M., and MacKenty, J. W. 2013a, *Characterizing Persistence in the WFC3 IR Channel: Finite Trapping Times*, [WFC3 ISR 2013-06](#)
- Long, K. S., Baggett, S. M., and MacKenty, J. W. 2013b, *Characterizing Persistence in the WFC3 IR Channel: Observations of Omega Cen*, [WFC3 ISR 2013-07](#)
- Long, K. S. 2013, *Characterizing Persistence in the WFC3 IR Channel: A revised model*, [WFC3 ISR 2013-08](#)
- Long, L.S, Baggett S.M., and MacKenty, J.W., *Persistence in the WFC3 IR Detector: Spatial Variations*, [WFC3 ISR 2015-16](#)
- Robberto, M., C. Hanley, and I. Dashevsky, 2002, *The reference pixels on the WFC3 IR detectors*, [WFC3 ISR 2002-06](#).
- Smith, R.M., Zavodny, M., Rahmer, G. and Bonati, M., 2008a, *A theory for image persistence in HgCdTe photodiodes*, [Proceedings of the SPIE, 7021, 70210J-1](#)
- Smith, R. M., Zavodny, M., Rahmer, G., Bonati, M., 2008b, *Calibration of image persistence in HgCdTe photodiodes*, [Proceedings of the SPIE, 7021, 70210K-1](#)
- Sunnquist, B., Mack, J., Khandrika, H., *Asteroids in the WFC3/IR Frontier Fields Images*, [WFC3 ISR 2017-18](#)
- Thatte, D., Dahlen, T. et al., 2009, [NICMOS Data Handbook](#), version 8.0, pg 1.

# WFC3 Data Analysis

In this chapter . . .

9.1 Photometry / 170
9.2 Astrometry / 196
9.3 Spectroscopy / 199
9.4 STSDAS and STSCI_PYTHON Software / 209
9.5 Specific Tools for the Analysis of WFC3 / 211
9.6 References / 214

## 9.1 Photometry

### 9.1.1 Photometric Systems

The WFC3 filters naturally define their own photometric system and users are encouraged to refer their photometric results to this native system. The natural instrumental magnitude of an object observed in a WFC3 filter is instrumental mag =  $-2.5 \log(\text{count rate})$ , where the count rate is in units of electrons per second (e-/sec). WFC3 supports the STMAG, ABMAG and VEGAMAG photometric systems and provides zero points for these, in addition to the filter-dependent instrument sensitivity, which converts the measured count rate (e-/sec) to a mean flux density  $F_\lambda$  in units of  $\text{erg cm}^{-2} \text{s}^{-1} \text{\AA}^{-1}$  and  $F_\nu$  in units of  $\text{erg cm}^{-2} \text{s}^{-1} \text{Hz}^{-1}$ .

The STMAG and ABMAG systems define an equivalent flux density for a source, corresponding to the flux density of a source of predefined spectral shape that would produce the observed count rate, and convert this equivalent flux to a magnitude. The conversion is chosen so that the magnitude in V corresponds roughly to that in the Johnson system.

In the STMAG system, the flux density is expressed per unit wavelength, and the reference spectrum is flat in  $F_\lambda$ . An object with  $F_\lambda = 3.63 \times 10^{-9} \text{ erg cm}^{-2} \text{s}^{-1} \text{\AA}^{-1}$  will have STMAG=0 in every filter, where the STMAG zero point is 21.10.

- $\text{STMAG} = -2.5 \log F_\lambda - 21.10$

In the ABMAG system, the flux density is expressed per unit frequency, and the reference spectrum is flat in  $F_\nu$ . An object with  $F_\nu = 3.63 \times 10^{-20} \text{ erg cm}^{-2} \text{ s}^{-1} \text{ Hz}^{-1}$  will have magnitude ABMAG=0 in every filter, where the ABMAG zero point is 48.6.

- $\text{ABMAG} = -2.5 \log F_\nu - 48.6$

The relationship between ABMAG and STMAG is:

- $\text{ABMAG} = \text{STMAG} - 5 \log (\text{PHOTPLAM}) + 18.692$

where  $F_\nu$  is expressed in  $\text{erg cm}^{-2} \text{ s}^{-1} \text{ Hz}^{-1}$ ,  $F_\lambda$  in  $\text{erg cm}^{-2} \text{ s}^{-1} \text{ \AA}^{-1}$ , and PHOTPLAM is the bandpass pivot wavelength in angstroms.

Formally, the HST VEGAMAG system is defined by the absolute spectral energy distribution of Vega, such that Vega has VEGAMAG=0 at all wavelengths. Thus, the VEGAMAG magnitude of an object with flux  $F$  is

$$m_{\text{vega}} = -2.5 \log_{10} (F_{\text{object}}/F_{\text{vega}})$$

where  $F_{\text{vega}}$  is the CALSPEC observed flux density of Vega. For the equations that define the average flux, see [Bohlin 2014](#). In the Johnson-Cousins magnitude system, the average value of six A0V stars sets the zero point values so that  $U-B=0$  and  $B-V=0$  ([Johnson & Morgan, 1953](#)) and by extension  $V-R=0$  and  $V-I=0$  ([Cousins 1974](#)). In this system Vega has the following magnitudes:  $U=0.03$ ,  $B=0.03$ ,  $V=0.03$ ,  $R=0.07$ ,  $I=0.10$ ,  $J=-0.18$ ,  $H=-0.03$ ,  $K=0.13$ . The VEGAMAG system is convenient for many observers because of its long heritage; however, the ABMAG system is popular with large imaging surveys.

A detailed discussion of these three photometric systems within the context of HST observations is provided in [Sirianni et al., 2005](#) as well as [WFC3 ISR 2009-31](#). Further information on the VEGAMAG system is also provided in [Bohlin & Gilliland \(2004\)](#), the ABMAG system in [Oke \(1964\)](#) and the STMAG system in [Koorneef et al., 1986](#). Although convenient, transformation to these (as well as other) photometric systems always has a limited precision and is dependent on the color range, surface gravity, and metallicity of the source stars considered (see [Sirianni et al., 2005](#), for a nice discussion).

### 9.1.2 Photometric Zero Points

The photometric zero point of a telescope/instrument/filter combination is a convenient way to characterize the overall sensitivity of the system. By most definitions, the zero point represents the magnitude of a star-like object that produces one count per second within a given aperture (see [Maiz Apellaniz 2007](#)). For WFC3, this throughput measures the performance within a given bandpass taking into account the HST Optical Telescope Assembly (OTA), pick-off mirror, mirror reflectivity, filter throughput, transmission of the outer and inner window, and the quantum efficiency (QE) of the detector. For HST instruments such as WFC3, the zero points depend on the absolute flux calibration of HST white dwarf model atmosphere spectra, and therefore they will change whenever that calibration is improved.



The photometric zero point can be determined using several techniques. In **pysynphot** a user can renormalize a spectrum to 1 count/sec in the appropriate WFC3 bandpass and output the zero point in the selected magnitude system (assuming that updated throughput tables are included in the local **pysynphot** installation). This is described in the **pysynphot** examples, [Section 9.1.10](#). Similarly, the most updated STMAG and ABMAG zero points for WFC3 data can be computed using photometric keywords in the SCI extension(s) of the image header. Specifically, the keyword PHOTFLAM is the inverse sensitivity and represents the flux density ( $\text{erg}/\text{cm}^2/\text{sec}/\text{\AA}$ ) of a star that produces a response of one electron per second in this bandpass. The header keyword PHOTPLAM is the pivot wavelength of the filter. The header keywords PHOTFLAM and PHOTPLAM relate to the STMAG and ABMAG zero points through the formulae:

$$\text{STMAG\_ZPT} = -2.5 \text{ Log (PHOTFLAM)} - \text{PHOTZPT} = -2.5 \text{ Log (PHOTFLAM)} - 21.10$$

$$\text{ABMAG\_ZPT} = -2.5 \text{ Log (PHOTFLAM)} - 21.10 - 5 \text{ Log (PHOTPLAM)} + 18.692$$

### 9.1.3 UVIS Chip-Dependent Calibration

The UVIS imaging channel consists of two separate e2v (now Teledyne e2v) CCDs mounted side by side. The two detectors (chips) have different quantum efficiencies at wavelengths  $< 3500 \text{ \AA}$  where UVIS2 is up to  $\sim 30\%$  more sensitive than UVIS1. At longer wavelengths, the response of two detectors is similar to within 0.5%. Motivated by the different quantum efficiencies, evidence that the CCDs are aging differently, and the desire to improve the accuracy and precision of the photometry, the UVIS photometric calibration is now determined for each chip independently. New flat fields have been computed for all full-frame filters (excluding the QUAD filters and the grism), with low-frequency corrections for the in-flight sensitivity computed separately for each chip ([WFC3 ISR 2016-04](#), [WFC3 ISR 2016-05](#)). The 2016 reference files are now normalized to the median value of each chip, removing any correction for sensitivity offsets between chips from the flats (see [Section 5.4.3](#)). Instead, the chip sensitivity ratio is computed from calibration observations of white-dwarf standards measured on each chip in order to correct for any offsets in the quantum efficiency as a function of wavelength.

On February 23, 2016, the WFC3 calibration pipeline was modified to support the chip-dependent calibration (**calwf3** version 3.3 and greater, note: the version used to reduce a specific image is recorded in the CAL\_VER header keyword). Two new header keywords PHTFLAM1 and PHTFLAM2 are populated with the inverse sensitivity values for UVIS1 and UVIS2, respectively. The PHOTFLAM keyword is populated with the value of PHTFLAM1 for backward compatibility with user software. A new keyword switch FLUXCORR (see [Sections 3.2.13](#) and [3.4.3](#)) scales UVIS2 to match UVIS1 by multiplying the UVIS2 science array by the inverse sensitivity ratio,  $\text{PHTRATIO} = \text{PHTFLAM2}/\text{PHTFLAM1}$ . After applying PHTRATIO, a point source should produce approximately the same number of electrons on UVIS1 and UVIS2 in calibrated (flt, flc) images corrected for distortion

using the pixel area map (see [Section 9.1.11](#)), such that a single value of PHOTFLAM may be used for the full frame image. Subarray data obtained with UVIS2 are also scaled by the PHTRATIO. This ensures that objects have the same signal regardless of the chip on which they were observed.




---

*While the new solutions represent a significant change in the calibration software and reference files, this change should be transparent to the majority users who will still only need to keep track of a single set of inverse sensitivities values (PHOTFLAM) for both chips. For UV photometry, where bandpass differences between the two chips are significant, a flowchart for determining which photometric keywords to use is provided in [Section 9.1.7](#).*

---

The original 2009 photometric calibration was based on the average of two white dwarf standards GD153 and GRW + 70d5824 ([WFC3 ISR 2009-31](#)) and used a smooth polynomial fit to correct for the increased on-orbit sensitivity with wavelength. By 2012, a larger cumulative set of calibration observations made it possible to replace the polynomial fits with more accurate filter-dependent corrections. These revised solutions were based on the average of three white dwarfs (GD153, GD71, G191B2B) plus the G-type star P330E. These were not documented in a formal ISR, but were posted to the WFC3 photometry web page and populated in the image headers. In 2016, the inverse sensitivity values were recomputed using only calibration observations of the three white dwarfs, obtained over a time period of six years and measured at multiple positions on the detector. ***The 2016 inverse sensitivity values are systematically ~3% smaller than the prior set of solutions across the full wavelength range of the UVIS detector*** and are a result of improvements in the photometric reduction. More detail on the improved reduction is available in [WFC3 ISR 2016-01](#), [ISR 2016-03](#) and [ISR 2017-14](#). [Figures 9.1](#) shows the ratio of the inverse sensitivity values from 2016 to 2012 as a function of the filter pivot wavelength, where the mean ratio for both chips is ~0.97.

The systematic change in the new chip-dependent calibration brings the UVIS photometric system closer to ACS/WFC. This is illustrated in [Figures 9.2](#), which plots the difference in magnitude (WFC3/UVIS - ACS/WFC) in the STMAG system for observations of NGC104 obtained in the F814W filter from programs 11452 and 10737 for WFC3 and ACS, respectively. With the prior (2012) UVIS calibration, relative photometry between the two detectors measured in a large 0.5" aperture radius (the standard for ACS photometry) shows a mean offset of 0.036 mag. This offset is reduced to 0.001 mag with the improved 2016 calibration.

Figure 9.1: Inverse sensitivity ratio (2016/2012) for UVIS1 in blue and UVIS2 in red (reproduced from ISR 2016-03, Figure 10). The dashed and dot-dashed lines mark the average ratio for each chip at a value  $\sim 0.97$ .

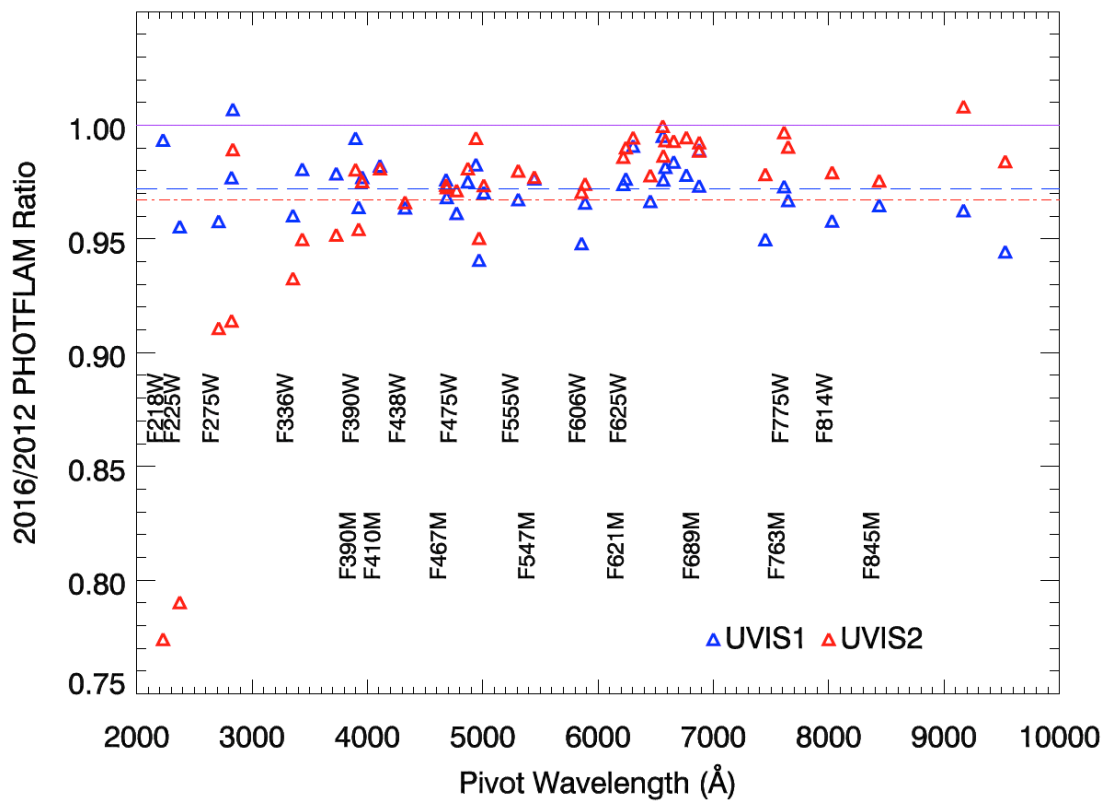
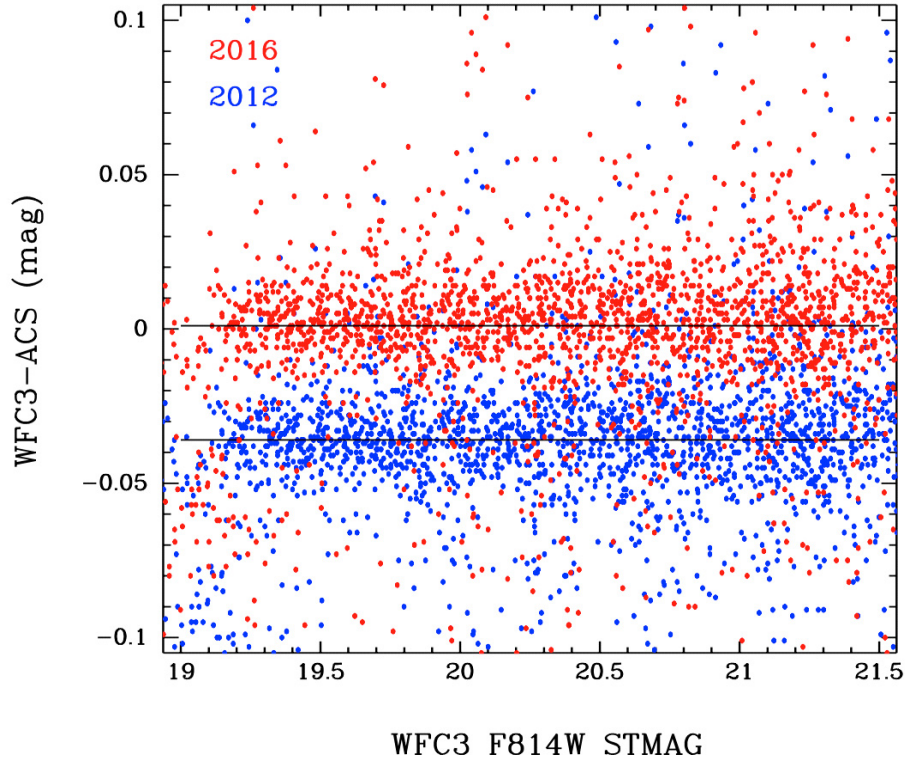


**Figure 9.2: Relative photometry (WFC3/UVIS - ACS/WFC) of NGC 104 in the F814W filter measured in the standard ACS 0.5" aperture radius. The blue points show an offset of  $\sim 0.036$  magnitude between the two systems when using with the 2012 UVIS photometric calibration. This offset is reduced to  $\sim 0.001$  magnitudes with the new 2016 UVIS chip-dependent calibration (red points). The  $\sim 3\%$  systematic offset in the new PHOTFLAM (inverse sensitivity) values shown in [Figures 9.1](#) brings the WFC3/UVIS photometric system closer to ACS/WFC.**



The WFC3/UVIS photometric keyword values have historically been reported in the image header for the infinite aperture, with accompanying encircled energy tables to correct photometry performed at smaller apertures. For convenience, two sets of zero point tables have been provided to users, corresponding to both the infinite and the 10 pixel aperture ([WFC3 ISR 2009-31](#)). In the 2016 release, two sets of tables were again computed, but the values populated in the image header changed convention to correspond to a 10 pixel aperture. This resulted in PHOTFLAM values which were  $\sim 10\%$  larger than the 2012 values due primarily to the change in aperture. Based on feedback from the WFC3 user community and for consistency with other HST instruments, the chip-dependent inverse sensitivity values in the image header reverted back to the ‘infinite’ aperture as of June 15, 2017 (**calfw3** version 3.4.1 onwards), which is defined at a radius of 6" (151 pixels). The revised 2017 photometric calibration is described in [WFC3 ISR 2017-14](#) and is based on better polynomial fits to the wavelength-dependent components of the throughput response and improved models for the three white dwarf standards. Current estimates of the photometric uncertainties are  $\sim 1.5\%$  for broadband filters,  $\sim 2\text{--}3\%$  for medium band,

and 5-10% for narrow band filters. Further discussion of the photometric errors is provided in [Section 5.7](#).

The chip-dependent calibration is implemented via a revised image photometry reference table (IMPHTTAB) which now contains two new extensions corresponding to the inverse sensitivity of each chip, PHTFLAM1 and PHTFLAM2 (see [Section 3.2.12](#)) for the infinite aperture. The 2017 solutions are concordant with the current synthetic photometry tables available in the calibration reference data system (CRDS), and these are described in detail in [WFC3 ISR 2016-07](#). A history of critical IMPHTTAB reference file deliveries and corresponding versions of the **calwf3** software is provided in [Table 9.3](#) of [Section 9.1.7](#). Due to the change in aperture convention, the 2017 keyword values are now ~10% smaller than the 2016 values. Comparing the inverse sensitivity values at the same aperture, the 2017 values differ from 2016 by ~0.5% on average. The 2017 VEGAMAG zero points, on the other hand, changed by up to 0.1 mag in the UV compared to 2016, when they were calculated using the CALSPEC model for Vega. These are now calculated using Vega's most recent CALSPEC STIS spectrum which differs by up to 10% at wavelengths shorter than 3000 Å. The latest calibration is described in [WFC3 ISR 2017-14](#) and on the WFC3 main [photometry webpage](#), which provides a link to the new [UVIS](#) tables for both the infinite and the 10 pixel aperture.

### 9.1.4 UV Photometry

One motivation of the chip-dependent calibration was to quantify and correct for bandpass differences, i.e. the response functions, between the two detectors in the UV. Even when two systems (telescope + UVIS1 or UVIS2) use the same filter, the effective bandpasses can be dissimilar ([WFC3 ISR 2017-07](#)).

Calibrated WFC3 data products (\*flt.fits, \*flc.fits) are combined in the pipeline using AstroDrizzle to create distortion-free data products (\*drz.fits, \*drc.fits) with the two CCD chips drizzled to the same output frame. AstroDrizzle assumes the images are in units of counts or count rate and not in the flux units used for photometry. This means that the same (hot WD) star must have the same count rate on both chips for the drizzle software to properly combine dithered data in which the sources cross the chip boundary. Because of the different effective bandpasses in the UV, the measured count ratio between chips for the hot white dwarf standards does not equal the PHTRATIO value provided in the 2016 IMPHTTAB (z\*imp.fits) for several filters (see below). For example, the ratio of count rates between the two CCDs is about 2% higher in F225W filter than the ratio of the computed inverse sensitivity values ([WFC3 ISR 2017-07](#)).

On November 21, 2016, the team delivered a revised IMPHTTAB, which scales the PHTFLAM1 values by a factor reflecting the empirical count rate ratio of the calibration standards. *These modified values of PHTFLAM1 are provided for the four UV filters (F218W, F225W, F275W and F200LP), such that the PHTRATIO values in the image headers match the observed count rate ratios for the white dwarfs. In these cases, the PHOTFLAM values should be used for photometry, and not the PHTFLAM1 values which have been modified to normalize the count rate ratio.* For

many applications, the difference for the two detectors is small compared to the photometric errors, so using a single PHOTFLAM value for the entire array is reasonable.

For programs which require precise UV photometry, users are advised to treat the two chips as separate detectors and use the chip-dependent keyword values. For UVIS1, this means simply multiplying the measured count rate by PHOTFLAM. For UVIS2, the science array has already been scaled by PHTRATIO, so flux calibration may be achieved by dividing the measured count rate by PHTRATIO and then multiplying by PHTFLAM2, as reported in the image header. (Equivalently, this may be achieved simply by multiplying by PHTFLAM1.) Photometry may be computed directly from the calibrated data products (\*flt.fits, \*flc.fits) multiplied by the pixel area map to account for geometric distortion. Alternately, users can correct for variations in the pixel area by drizzling each chip separately prior to performing photometry. This makes it easier to keep track of which inverse sensitivity value to use with which detector pixels, and this can be especially important for observations obtained at different orientations or with large dithers. More detail on UV photometry recommendations is provided in [WFC3 ISR 2017-07](#).




---

*A flowchart for determining which photometric keywords to use for various calibration goals is provided in [Figure 9.3](#) of [Section 9.1.7](#).*

---

For targets with multiple color populations, the UV count rate ratio across the two chips depends on the color of the source. Tests that separate the stars in Omega-Centauri into groups by color show that relative photometry of the same stars placed on different chips have a constant offset for sources redder than the white dwarf standards at the level of a few percent, and this offset increases linearly with spectral type ([WFC3 ISR 2015-18](#) and [WFC3 ISR 2016-05](#)). Further study of color terms for the UV filters is currently underway.

### 9.1.5 UVIS QUAD Filter Photometry

The QUAD filter calibration is unchanged from 2012 and still makes use of pre-flight flats that contain the UVIS flare (see [Figure 5.4](#)). *Full-frame observations using a QUAD filter always have the 'FILTER' keyword populated with the filter element that corresponds to quadrant A, regardless of which filter was requested in the Phase II submission. [Table 9.1](#) lists the four spectral elements associated with a single QUAD element, where the value of the filter keyword reported in the image header corresponds to amplifier A.* Users can instead query the value of the “ASN\_ID” keyword in their data to look for that association in MAST, where the database is populated with the correct ‘FILTER’ keyword. This discrepancy is due to different software systems creating the MAST database and populating the file header keywords. Observations with QUAD filters in subarray mode only cover a single



quadrant (spectral element) and hence always have the correct filter keyword reported in their headers.

To avoid problems with using PHOTFLAM values from the wrong quadrant, all observations using QUAD filters have the PHOTCORR and FLUXCORR switches set to OMIT, so the photometric keywords are not populated in the image header during **calwf3** processing. PHOTFLAM values thus have to be retrieved elsewhere, for example from Table 8 in [WFC3 ISR 2017-14](#) or from the [QUAD filter](#) tables available on the WFC3 photometry website.

**Table 9.1: The WFC3 UVIS channel contains five QUAD filters: each is a 2×2 mosaic of filter elements occupying a single filter slot, with each amplifier (quadrant) providing a different bandpass. Each image header FILTER keyword will be set to the amp A value for full-frame observations and set to the proper QUAD filter for subarray observations covering only one quadrant.**

Filter wheel	Slot	Amp A	Amp B	Amp C	Amp D
11	4	FQ508N	FQ674N	FQ575N	FQ672N
12	1	FQ437N	FQ378N	FQ232N	FQ243N
12	2	FQ387N	FQ492N	FQ422M	FQ436N
12	3	FQ889N	FQ937N	FQ906N	FQ924N
12	4	FQ619N	FQ750N	FQ634N	FQ727N

### 9.1.6 IR Photometric Calibration

For the IR detector, the original 2009 photometric calibration was based on the average of the HST standards GD153 and P330E, a hot white dwarf and G-type star. As for UVIS, a smooth polynomial fit was used to correct for the increased on-orbit sensitivity with wavelength ([WFC3 ISR 2009-30](#)). By 2012, a larger cumulative set of calibration data allowed for more accurate filter-dependent corrections to the sensitivity with wavelength. The revised solutions were based on the average of three white dwarfs (GD153, GD71, G191B2B) plus P330E. While these solutions were not documented in a formal ISR, they are available from the WFC3 photometry webpage. Independent calibrations from the four standards agree to within ~1% in most filters, and the inverse sensitivity per filter, PHOTFLAM, is set to the average of the measurements.

The IR calibration is unchanged from 2012, and current estimates of the photometric uncertainties are ~2% for broadband filters and 5-10% for narrow band filters. Further discussion of the photometric errors is provided in [Section 7.11](#). The IR photometry header keywords are populated by **calwf3** using the IMPHTTAB reference file, which is described in [Section 9.1.7](#).

The IR detector has a low-level count rate non-linearity at ~1% per dex over a range of 12 magnitudes (see [Section 7.7](#)). Since bright standard stars (11th magnitude) are used to calibrate the detector, this means that faint source photometry (at the sky count rate ~23rd magnitude) using the computed set of IR zero points will be systematically ~4.5% too faint ([WFC3 ISR 2010-07](#) and [2011-15](#)). Additional

calibration data has been obtained in Cycle 24 (programs 14868 and 14870) to further quantify and correct for this effect as a function of wavelength.

### 9.1.7 Image Photometry Reference Table

After December 2012, the HST calibration pipeline software (HSTCAL) no longer calls SYNPHOT to calculate the photometric keyword values on-the-fly. Instead it makes use of an image photometry lookup table, the IMPHTTAB, for each WFC3 channel which contains the values for PHOTFLAM (the inverse sensitivity), PHOTPLAM (the filter pivot wavelength), and PHOTBW (the filter bandwidth). The WFC3 data reduction pipeline **calwf3** v3.1.6 was implemented at this time to support the change. For more detail see:

<http://wfc3tools.readthedocs.io/en/stable/wfc3tools/history.html>.

The version of **calwf3** used to calibrate WFC3 data may be found in the image header keyword CAL\_VER. The current IMPHTTAB reference file for the IR channel is listed in [Table 9.2](#).

The UVIS chip-dependent calibration was implemented in **calwf3** v3.3. This required a new 5-extension IMPHTTAB reference file to carry additional keywords reflecting the inverse sensitivity for each CCD chip, PHTFLAM1 and PHTFLAM2. A history of this reference file is provided in [Table 9.3](#), which highlights the change in the standard aperture used to define the inverse sensitivity values written to the image header.




---

***NOTE: For observations spanning multiple epochs, users are advised to verify that the same IMPHTTAB reference file was used to process all data.***

---

If data from multiple-visits programs are retrieved from MAST at different times (e.g. after the execution of each visit), it may be possible to observe systematic differences due to changes in the reference files and/or software. In this case, users have two options: 1) re-retrieve all pertinent datasets for the given science program from [MAST](#) or 2) reprocess the RAW files offline with a self consistent version of **calwf3** and reference files. For manual reprocessing instructions, see the examples in the, [Section 3.5](#).



**Table 9.2: The IMPHTTAB reference file used to populate the IR photometry keywords in the image header.**

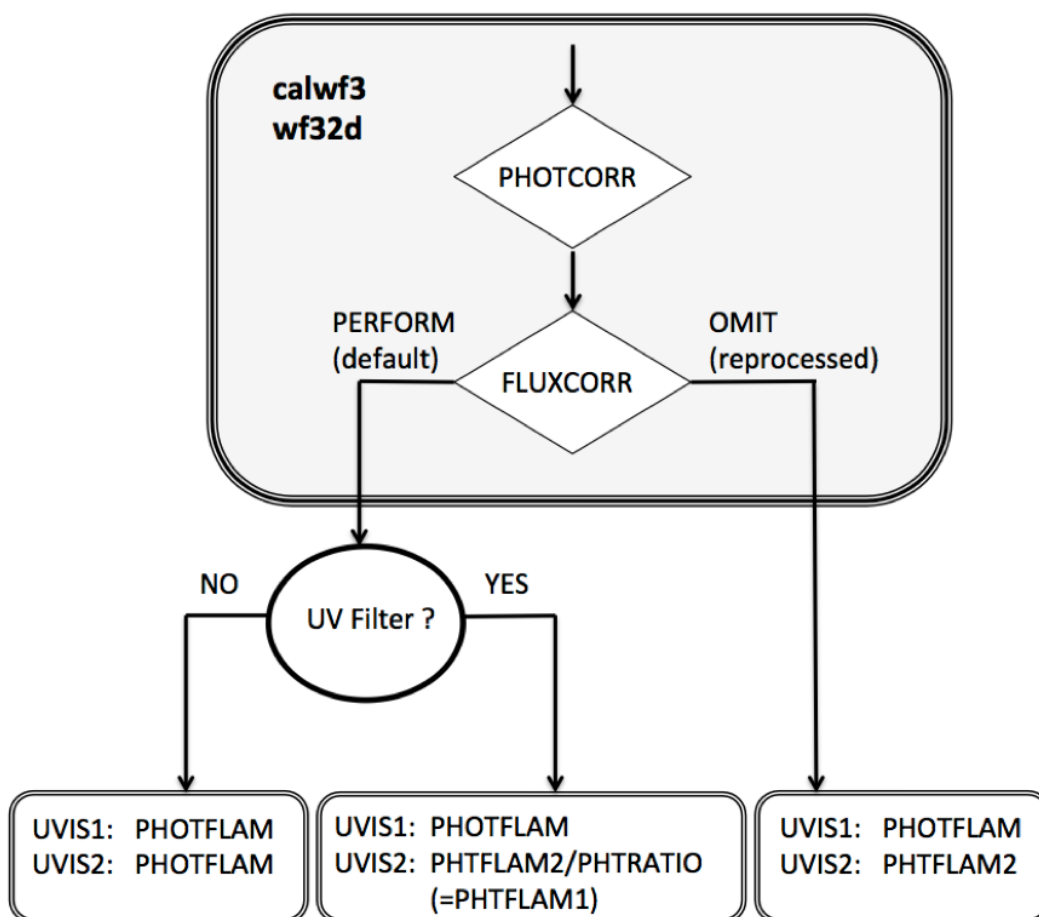
Activation Date	Reference File	Standard aperture	Description	Documentation
2012 Nov 19	wbj1825si_imp.fits	Infinite	First active IMPHTTAB, 3 extension FITS file, Used with <b>calwf3</b> v3.1; Based on data from 2009-2012, averaged for 3 WD's plus P330E	2012 Values on Web-site only

**Table 9.3: A history of the IMPHTTAB reference file used to populate the UVIS photometry keywords in the image header.**

Activation Date	Reference File	Standard aperture	Description	Documentation
2012 Dec 28	wbj1825si_imp.fits	Infinite	First active IMPHTTAB, 3 extension FITS file; Used with <b>calwf3</b> v3.1; 'Single Chip' solution; Based on data from 2009-2012, averaged for 3 WD's plus P330E	2012 Values on Web-site only
2013 Jul 03	x5h1320fi_imp.fits	Infinite	Based on 2012 solutions for 3 WD's and P330E; corrected by <1% to remove flat field normalization	2012 Values on Web-site only
2016 Feb 23	zcv2057li_imp.fits	10 pixel	Chip-dependent solution; 5 extension FITS file; Used with <b>calwf3</b> v3.3+; Master DRZ per filter for 3 WD's observed from 2009-2015; Change is ~4% from 2012.	ISR-2016-03
2016 Nov 21	0bi2206ti_imp.fits	10 pixel	Same as <b>zcv2057li_imp.fits</b> except equalizes UV count-rate across chips for blue sources. Change is 2% in F225W and 1% in F218W, F275W	ISR-2017-07
2017 Jun 15	1681905hi_imp.fits	Infinite	Better polynomial fits to data and updated models, matches synphot tables delivered April 2016; Used with <b>calwf3</b> v3.4.1; Change is ~0.5% from 2016 at the same standard aperture.	ISR-2017-14

Figure 9.3: Inverse sensitivity keywords to use for photometry

For UVIS data retrieved after June 15, 2017, this flowchart is useful for determining which set of inverse sensitivity keywords to use for photometry. The light gray box shows the final calwf3 processing steps in the wf32d module. The data products (\*flt.fits, \*flc.fits) obtained from MAST are created with FLUXCORR set to PERFORM in calwf3. For most filters, a single keyword (PHOTFLAM) may be used for both chips. For the UV filters F218W, F225W, F275W, F200LP, bandpass differences between the chips means that the count ratio may not be equal across the two chips. In order to combine the two chips to create the \*drz.fits, \*drc.fits data products, calwf3 multiplies the UVIS2 science array by PHTRATIO (the inverse sensitivity ratio) to equalize the count rate of the hot, blue white dwarf standards across the two chips. Hence, using a single PHOTFLAM value for both chips may lead to errors of up to 2% in these filters ([WFC3 ISR 2017-07](#)). To achieve higher photometric accuracy in these four UV filters, users are advised to treat the two chips as independent detectors. This is achieved either by using an alternate set of keywords (bottom center) or by setting FLUXCORR to OMIT, reprocessing the \*raw.fits data with calwf3, and using a third set of keywords (bottom right). Note that PHOTFLAM is always the correct value to use for UVIS1. For combining \*flt.fits, \*flc.fits products which span multiple epochs (orientations) with AstroDrizzle, the majority of users are advised to use the FLUXCORR-scaled data products and a single PHOTFLAM value for photometry.



### 9.1.8 Aperture Corrections

The response (inverse sensitivity) values for the two WFC3 channels are computed for an infinite aperture and for an aperture radius of 10 pixels. Initially the infinite aperture measurement was obtained by taking the counts (i.e., of a standard star) in a large 2" aperture and correcting to the infinite aperture using an encircled energy (EE) model (see [WFC3 ISR 2009-37](#) and [WFC3 ISR 2009-38](#)). Currently, the UVIS detector uses filter-based encircled energy curves for aperture corrections (see Tables 6,7 in [WFC3 ISR 2017-14](#)).

The infinite aperture response value can be scaled to the equivalent aperture-based response using the encircled energy fractions, which are wavelength specific. For example, the measured flux in the UVIS F606W filter within a 10 pixel aperture is ~91% of the total flux and within a 50 pixel (2.0") aperture is ~98% of the total flux. For the IR detector, the flux in F140W within an aperture radius of 3 pixels is ~84% of the total flux and ~97% within an aperture radius of 2.0".

**Pysynphot** may be used to scale the total counts from an infinite aperture to a specific radius using the ‘aper’ keyword as part of the observing mode. This is shown in Example 1 of [Section 9.1.10](#), eg. for the 10 pixel (0.3962") aperture on UVIS1:

```
bp = pysynphot.ObsBandpass('wfc3,uvis1,f814w,aper#0.3962')
```

In order to reduce errors due to background variations and to optimize the signal-to-noise, aperture photometry and PSF-fitting photometry are often performed by measuring the flux within a small radius around the center of the source. However, small aperture measurements need to be adjusted to a “total count rate” by applying an aperture correction (in magnitude units) or an encircled energy fraction (in flux units). For example, when making use of the 0.3962" set of zero point tables, users should determine the offset between their own ‘small aperture’ photometry and aperture photometry within a 10 pixel radius aperture. This can be done by measuring a few bright stars in an uncrowded region of the field of view and applying the offset to all photometric measurements. If such stars are not available, one can use the tabulated EE values (see the following paragraph). Alternately, one can use the new MAST PSF search tool to download PSFs extracted from WFC3 archival data for a similar detector position and focus as the observation of interest. Further information on the PSF search tool by selecting Collection WFC3 UVIS PSF at:

<https://mast.stsci.edu/portal/Mashup/Clients/Mast/Portal.html>.

Model encircled energies have been tabulated in [WFC3 ISR 2009-37](#) for IR and [WFC3 ISR 2009-38](#) for UVIS. New chip-dependent, filter-based EE fractions have been computed for the UVIS detector and spliced to the 2009 in-flight models at  $r=35$  pixels (~1.4"). These may be found in [WFC3 ISR 2017-14](#) for radii between 3 and 10 pixels and on the WFC3 photometry web pages for radii up to 50 pixels (~2.0"). The 2017 filter-dependent EE values agree with the 2009 models to ~1% for most filters. However users should be reminded that accurate aperture corrections are a function of time and position on the detector. Blind application of tabulated encircled energies should be avoided for small apertures (i.e.,  $r < 8$  pixels for UVIS,  $r < 3$  pixels for IR).

where the measured photometry (and the EE fraction) is strongly dependent on the telescope focus and orbital breathing (see [WFC3 ISR 2013-11](#)).

### 9.1.9 Color Corrections

In some cases it may be desirable to compare WFC3 photometric results with existing datasets in different photometric systems (e.g., WFPC2, ACS, SDSS, 2MASS, Johnson-Cousins). Since the WFC3 filters do not have exact counterparts in any other “standard” filter set, the accuracy of these transformations is limited. Moreover if the transformations are applied to objects whose spectral type (e.g., color, metallicity, surface gravity) do not match the spectral type of the calibration observation, serious systematic effects can be introduced.

Transformation coefficients for different spectral types and astronomical sources have been published in [WFC3 ISR 2014-16](#). The photometric transformation coefficients between Johnson-Cousins UBVI filters and WFC3-UVIS wide-band filters for a given object spectrum can also be found at <https://colortool.stsci.edu>. Users are encouraged to calculate their own transformation coefficients to specific photometric systems. Example 3 in [Section 9.1.10](#) shows how to use **pysynphot** to compute these photometric transformations.

As described in [Section 9.1.4](#), the UV filters show color terms of several percent such the count rate photometry of the same stars measured on different CCD chips shows offsets which vary with the color of the source.

### 9.1.10 Pysynphot Examples

The WFC3 synthetic throughput tables may be obtained from the Calibration Reference Data System (CRDS) at:

<http://www.stsci.edu/hst/observatory/crds/throughput.html>

New component tables supporting the UVIS chip-dependent photometric calibration are described in [WFC3 ISR 2016-07](#).

To run the following examples, the user should define the local path to throughput tables before starting python using one of the two commands below. For users not at STScI, replace `/grp/hst/cdb/` with your local directory containing the CRDS reference files.

```
> setenv PYSYN_CDBS/mydisk/myiref/          # if running from a
csh/tcsh terminal
> export PYSYN_CDBS="/mydisk/myiref/"      # if running in bash
```

**Example 1.** Compute the UVIS inverse sensitivity values (and the equivalent STMAG, ABMAG, and VEGAMAG values) for F814W on UVIS1 in a 10-pixel (0.3962”) aperture, assuming a flat spectrum. The python code below shows how to reproduce the values in Tables 4 and 5 of [WFC3 ISR 2017-04](#). The python code below

replaces the following pyraf synphot command for computing the pivot wavelength and inverse sensitivity in a bandpass:

```
# pyraf command bandpar wfc3,uvis1,f814w,aper#0.3962 photlist=pivwv,uresp
```

```
# pyraf equivalent
import pysynphot as S
import numpy as np
vega= S.FileSpectrum('/mydisk/myiref/alpha_lyr_stis_008.fits')
bp = S.ObsBandpass('wfc3,uvis1,f814w,aper#0.3962')
stmag = -21.1-2.5*np.log10(bp.unit_response())
abmag =
-21.1-2.5*np.log10(bp.unit_response())-5*np.log10(bp.pivot())+18.692
vegauvis = S.Observation(vega,bp)
vegamag= 2.5*np.log10(vegauvis.countrate())
print 'Obsmode=', bp
print 'PivotWave=', '{0:.2f}'.format(bp.pivot())
print 'Photflam=', '{0:.6g}'.format(bp.unit_response())
print 'STMAG=', '{0:.3f}'.format(stmag)
print 'ABMAG=', '{0:.3f}'.format(abmag)
print 'VEGAMAG=', '{0:.3f}'.format(vegamag)
```

### OUTPUT:

```
Obsmode= wfc3,uvis1,f814w,aper#0.3962
PivotWave= 8048.151
Photflam= 1.64279e-19
STMAG= 25.861
ABMAG= 25.025
VEGAMAG= 24.598
```

**Example 2.** Renormalize a 5,000 K blackbody for WFC3/IR in the F110W filter and output the zero point in the ABMAG system. The fourth line ‘spec.renorm’

renormalizes the blackbody spectrum to produce 1 count/sec in the Johnson V band. The python code below is the equivalent to the pyraf command:

```
# pyraf command calcphot wfc3,ir,f110w "rn(bb(5000),band(v),1,counts)" form=abmag
```

```
# pyraf equivalent
import pysynphot as S
import numpy as np
bp = S.ObsBandpass('wfc3,ir,f110w')
v_band = S.ObsBandpass('johnson,v')
spec = S.BlackBody(5000)
spec_renorm = spec.renorm(1,'counts',v_band)
obs = S.Observation(spec_renorm,bp)
print 'ABMAG=', '{0:.3f}'.format(obs.effstim('abmag')), 'for Obsmode=',bp
```

### OUTPUT:

```
ABMAG= 25.821 for Obsmode= wfc3,ir,f110w
```

**Example 3.** Find the color term for a 5000 K blackbody between the Cousins-I and WFC3/UVIS1 F814W bandpasses in the ABMAG system. (Since the Cousins-I bandpass does not have pre-defined binset, we use the binning from HST/WFC3 UVIS1 detector). The python code below is the equivalent to the pyraf command from Example 2 in [WFC3 ISR 2014-16](#):

```
# pyraf command calcphot 'band(i)-band(wfc3,uviss1,f814w)' spectrum='bb(5000)' form=abmag
```

```
# pyraf equivalent
import pysynphot as S
import numpy as np
bp = S.ObsBandpass('wfc3,uvis1,f814w')
i_band = S.ObsBandpass('i')
spec = S.BlackBody(5000)
obs_wfc3 = S.Observation(spec, bp)
obs_i = S.Observation(spec, i_band, binset=obs_wfc3.binwave)
color=obs_i.estimate('abmag') - obs_wfc3.estimate('abmag')
print 'ABMAG(i)-ABMAG(UVIS1,F814W)= ', '{0:.3f}'.format(color)
```

**OUTPUT:**

```
ABMAG(i)-ABMAG(UVIS1,F814W)= 0.007
```

**9.1.11 Pixel Area Maps**

The WFC3/UVIS CCDs and WFC3/IR detector contain pixels that vary in their area on the sky as a result of the geometric distortion. As a consequence of this, more light will fall on a larger pixel relative to a smaller pixel, leading to an overall gradient in an image of a smooth background. However, the flat-fielding process in the HST **calwf3** pipeline is designed to produce images that have a flat background (e.g., sky), thereby suppressing counts (hereafter taken to be in units of electrons) in larger pixels relative to smaller pixels. Hence, while surface photometry measurements will be correct, the measured total brightness of sources on flat images will vary depending on the position of the object, and the areas of the pixels at that location.

To achieve uniform aperture photometry over the detector, most users will measure counts on distortion free images. The geometric distortion can be corrected using **AstroDrizzle**. The output of this processing will be a drz or drc image, which has a flat sky and contains pixels that are uniform in area (i.e., through proper corrections of the distortion and related pixel area variations). Therefore, photometry of any source in a drz image will yield the same count rate (electrons per second) irrespective of the position of the source on the image. Photometry measured on an flat image therefore requires a field-dependent correction factor to:

- achieve uniformity in the measured count rate of an object across the field,
- match the output drizzled count rate.

This correction, in the form of an image, is called the Pixel Area Map (PAM), and comes from the derivatives of the geometric distortion polynomial. The size of the

PAM image is the same as the flt image and each pixel value is set to the normalized area of that pixel. By multiplying the flt images by the PAM, users will recover the same count rate on flt images and drz images, and the same zero point will apply to both data products:  $\text{drz\_flux} = \text{flt\_flux} \times \text{PAM}$ , where the flt image has been converted to counts per second.

A contour plot of relative pixel size across the UVIS image, normalized to the central pixel, is shown in [Figure 9.4](#). The ratio of maximum to minimum pixel area over the detector is 1.074.

The variation of pixel area across the IR channel to be used for correction of point-source photometry from distortion-corrected images is shown in [Figure 9.5](#). The maximum deviation from the central value is 4.1%.

A detailed description of the WFC3 UVIS and IR PAMs is provided in [WFC3 ISR 2010-08](#). This description also discusses a unique choice for normalizing the WFC3 PAMs that differs from previous instruments. This choice ensures that the PAMs do not artificially scale the flt flux by large amounts. Rather, the PAMs simply serve to provide a relative correction of the counts based on the size of pixels as compared to the size of a reference pixel near the center of the detectors (see detailed description in the ISR).

Online

---

*The PAMs along with a brief description, are available at [http://www.stsci.edu/hst/wfc3/pam/pixel\\_area\\_maps](http://www.stsci.edu/hst/wfc3/pam/pixel_area_maps)*

---



**Figure 9.4: Variation of the effective pixel area with position on the UVIS detector. Darker shading indicates pixels with smaller area. Contours are drawn at 1% increments.**

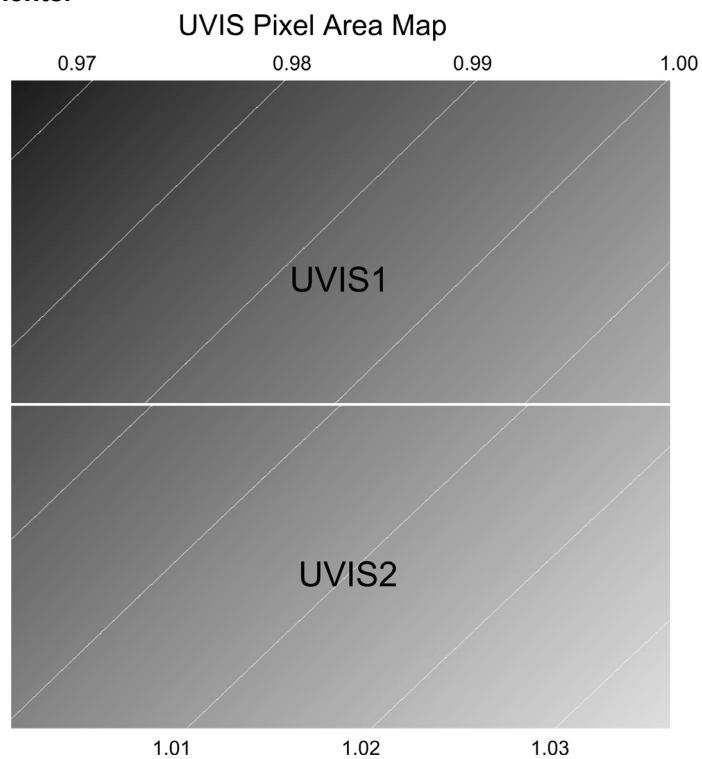
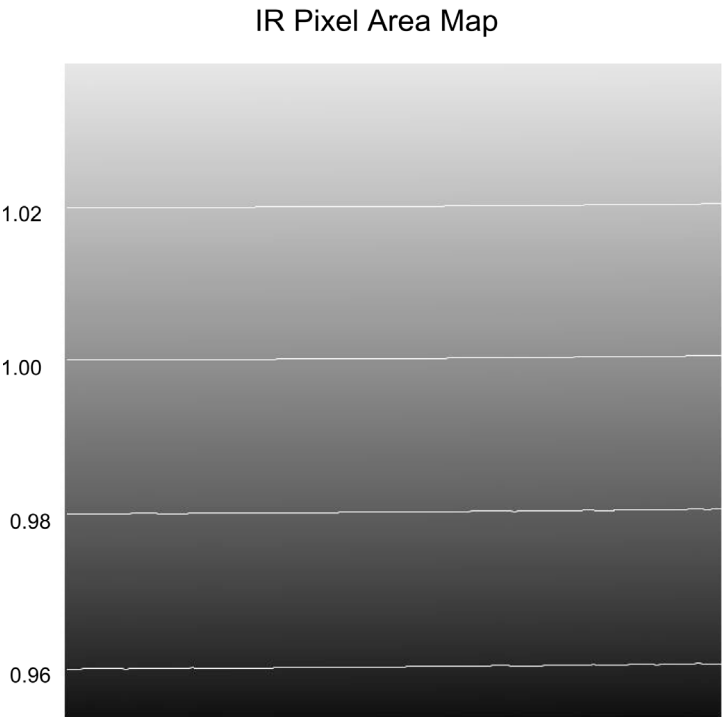


**Figure 9.5: Variation of the effective pixel area with position on the IR detector. Darker shading indicates pixels with smaller area. Contours are drawn at 2% increments.**



**PAM Concept Illustration**

To illustrate the concepts of extended source and point source photometry on flt and drz images we consider a simple idealized example of a 3x3 pixel section of the detector. We assume that the bias and dark corrections are zero and that the quantum efficiency is unity everywhere.

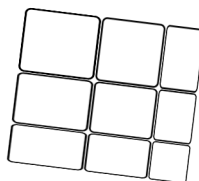
*Example #1 Constant Surface Brightness Object*

Let's suppose we are observing an extended object with a surface brightness of 2 e-/pixel in the undistorted case. With no geometric distortion the image is:

Actual Scene on the Sky	2	2	2
	2	2	2
	2	2	2

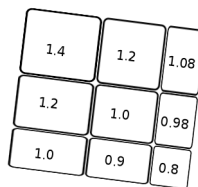
In reality WFC3 suffers from geometric distortion and as a consequence pixels are not square and the pixel area varies across the detector

Detector pixel layout on the sky



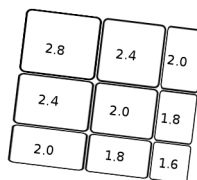
Let's suppose the pixel area map (PAM) is:

Detector pixel layout on the sky



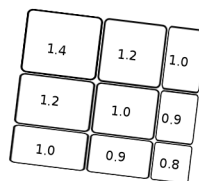
As a result in the raw data there is an apparent variation in surface brightness.

RAW image:



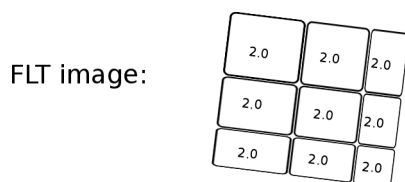
The geometrical area of each pixel is imprinted in the flat field as well as the photometric sensitivity. In this example, since we assumed that the quantum efficiency is unity everywhere, the flat field is just the equivalent of the PAM:

Flat field:

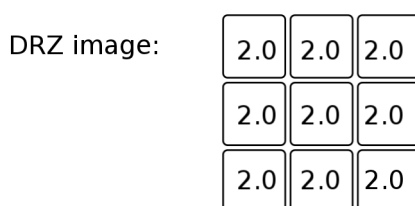


WFC3 flat fields are designed to level out a uniformly illuminated source and not to conserve total integrated counts, so after the flat-field correction the FLT image has

the correct surface brightness and can be used to perform surface photometry. However the image morphology is distorted.

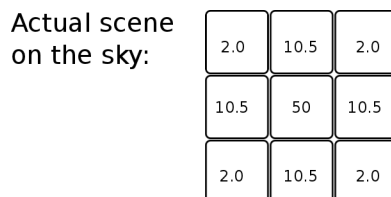


**AstroDrizzle** can be run on the FLT image. The result is that each pixel is free of geometric distortion and is photometrically accurate.



### *Example #2 Integrated photometry of a point source*

Now let's suppose we are observing a point source and that all the flux is included in the 3x3 grid. Let the counts distribution be:

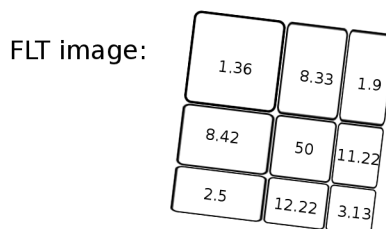


The total counts are 100. Due to the geometric distortion, the PSF as seen in the raw image is distorted. The total counts are conserved, but they are redistributed on the CCD.

After the flat-field correction, however, the total counts are no longer conserved:



In this example the counts now add up to 99.08, instead of 100.



In order to perform integrated photometry the pixel area variation need to be taken into account. this can be done by multiplying the FLT image by the PAM or by running **AstroDrizzle**.




---

*Users working on the FLT x PAM images need to compute new aperture corrections.*

---

Only by running AstroDrizzle can the geometric distortion be removed, but both approaches correctly recover the count total as 100. Users should be cautioned that this is just an idealized example. In reality the PSF of the star extends to a much bigger radius. If the user decides to work on the flat-fielded image after correcting by the pixel area map, they need to calculate a new aperture correction to the total flux of the star. The aperture corrections discussed in Section 7.2.2 are only for AstroDrizzle output images. In most cases the aperture correction for distorted images will be quite different from the same star measured in the drz image. This is particularly true for small radius apertures.

### 9.1.12 CTE

To date, all CCDs flown in the harsh radiation environment of HST suffer degradation of their charge transfer efficiency (CTE). The effect of CTE degradation is to reduce the apparent brightness of sources, requiring the application of photometric corrections to restore measured integrated counts to their *true* value.

On-orbit data taken with the WFC3 UVIS detector shows evidence for CTE degradation see [Section 6.3](#).

### 9.1.13 Red Leak

The design and manufacture of the UV filters was based on a careful balance of the achievable in- and out-of-band transmissions: in general, higher in-band transmission results in poorer suppression of out-of-band transmission, and vice versa. The WFC3 filters represent an attempt to achieve an optimum result, maximizing the in-band

transmission while keeping the out-of-band transmission as low as possible in order to minimize red leaks.

Table 9.4 below summarizes the red-leak levels for the WFC3 UV filters. The table lists the fraction of the total signal that is due to flux longward of 400 nm, as a function of effective temperature. This was calculated by convolving a blackbody of the given effective temperature (Teff) with the system throughput in the listed filter. As can be seen from the table, red leaks should not be an issue for observations of any objects taken with F275W or F336W. The other UV filters have some red leaks, whose importance depends on stellar temperature. The red leaks in F218W and F300X, for example, exceed ~1% for objects cooler than ~6000 K, while in F225W the red leak reaches ~1% for objects with even cooler temperatures. The most extreme red leaks arise from F218W and F225W observations of objects with effective temperature (Teff) of ~4000 K or cooler, necessitating appropriate corrections.

**Table 9.4: Fraction of flux longward of 400 nm as a function of effective temperature.**

Teff (K)	F218W	F225W	F275W	F300X	F336W
1000	1	1	1	1	1
2000	9.9E-01	9.9E-01	8.4E-01	5.5E-01	3.0E-02
3000	6.0E-01	2.7E-01	3.0E-02	8.9E-02	8.4E-04
4000	1.1E-01	1.8E-02	3.1E-03	3.3E-02	1.4E-04
5000	2.7E-02	3.2E-03	8.6E-04	1.7E-02	4.5E-05
6000	9.9E-03	1.0E-03	3.8E-04	1.0E-02	2.2E-05
7000	4.9E-03	4.6E-04	2.2E-04	7.3E-03	1.3E-05
8000	2.8E-03	2.5E-04	1.5E-04	5.5E-03	9.0E-06
9000	1.9E-03	1.6E-04	1.1E-04	4.4E-03	6.8E-06
10000	1.3E-03	1.1E-04	8.6E-05	3.7E-03	5.4E-06
11000	1.0E-03	8.6E-05	7.1E-05	3.2E-03	4.5E-06
12000	8.3E-04	6.9E-05	6.0E-05	2.8E-03	3.9E-06
13000	6.9E-04	5.7E-05	5.3E-05	2.6E-03	3.5E-06
14000	5.9E-04	4.8E-05	4.8E-05	2.3E-03	3.1E-06
15000	5.1E-04	4.2E-05	4.3E-05	2.2E-03	2.9E-06
20000	3.3E-04	2.6E-05	3.2E-05	1.7E-03	2.2E-06
30000	2.1E-04	1.7E-05	2.4E-05	1.3E-03	1.7E-06
40000	1.8E-04	1.4E-05	2.1E-05	1.2E-03	1.5E-06
50000	1.6E-04	1.3E-05	2.0E-05	1.1E-03	1.4E-06

### 9.1.14 UV Contamination

The UVIS detector is regularly monitored for contamination effects. These are related to volatile molecules that can progressively accumulate on either the detector itself or on other optical surfaces, and can cause a decline of sensitivity. When present, contamination is expected to manifest as a wavelength-dependent decline in the photometric throughput, strongest in the bluest filters. Historically, this monitoring has been done via observations of the spectrophotometric white dwarf standard GRW+70d5824 (GRW+70) in several key filters from 200 nm to 600 nm, with red filters acting as a control ([WFC3 ISR 2014-20](#)). Recently, several major updates have been made to the UVIS contamination monitoring program, including the transition to a second white dwarf standard star, GD153, in late-2015 ([WFC3 ISR 2017-15](#)), and additional monitoring data using scan-mode observations ([WFC3 ISR 2017-21](#)).

Presently, GD153 is observed every five weeks and GRW+70 is observed every three months. Flux within a ten-pixel aperture is measured for each image. Each measurement is then compared to a baseline flux value, defined as the median flux of the earliest observations in that subset of data. Drifts in throughput are characterized by the slope of a linear fit to the percent change in flux, with respect to the baseline value, versus time. One example of the flux monitoring data for GRW+70 is shown in [Figure 9.6](#) for the F606W filter in both UVIS1 and UVIS2 detectors.

[Figure 9.7](#) shows the cumulative flux losses in units of percent loss per year as function of wavelength, based on linear fits to GRW+70 photometric measurements in a subset of blue filters (F218W, F225W, F275W, F336W, F438W) and in two control filters (F606W and F814W). These are also reported in [Table 9.5](#) along with the estimated uncertainties.

A small, steady decline in count rate is found for most filters but no evidence of contamination. These declines range from 0.01% to 0.3% per year and are stronger in longer wavelength filters, the opposite of the signature for contamination. Similar temporal changes are found for both standards, and the long-term trends in throughput agree with previous trends derived in 2014. For F606W, this amounts to a total decline of ~2.4% over eight years from 2009-2017. Work is underway to derive time-dependent corrections to the inverse sensitivity (zero point) values reported in the image header via the image photometry table (IMPHTTAB) reference file.

**Table 9.5:** The percent loss in flux per year,  $\text{Flux}_{\text{amp}}$ , for the white dwarf standard GRW+70d5824 observed in the A and C amplifiers, where  $\text{Stddev}_{\text{amp}}$  is the estimated uncertainty.

Filter	$\text{Flux}_A$	$\text{Stddev}_A$	$\text{Flux}_C$	$\text{Stddev}_C$
F218W	-0.001	0.014	+0.017	0.020
F225W	+0.024	0.022	+0.021	0.020
F275W	-0.058	0.017	+0.026	0.023
F336W	-0.016	0.023	+0.008	0.027
F390M	-0.196	0.049	-0.006	0.048
F438W	-0.193	0.020	-0.179	0.032
F467M	-0.248	0.061	-0.120	0.050
F547M	-0.283	0.038	-0.141	0.038
F555W	-0.214	0.057	-0.175	0.043
F606W	-0.312	0.018	-0.249	0.021
F814W	-0.170	0.023	-0.110	0.022
F850LP	-0.173	0.124	-0.165	0.046
F218W	-0.001	0.014	+0.017	0.020

**Figure 9.6:** Flux loss (percent) for GRW+70d5824 in the F606W filter measured in UVIS1 and UVIS2 based on observations from 2009 to 2016. Observations marked with 'X' were data taken in amplifiers B and D and were not included in the linear fit due to the limited date range. The symbols 'm' and  $\sigma$  annotated on the plot represent the slope (percent loss per year) and the total scatter in the data over the full MJD date range. See Table 9.5 for losses in other UVIS filters.

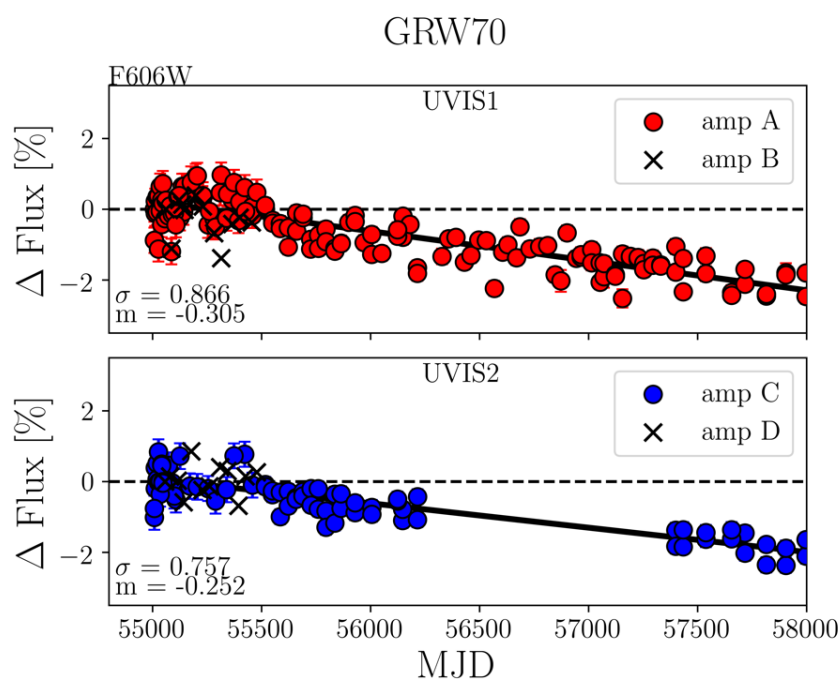
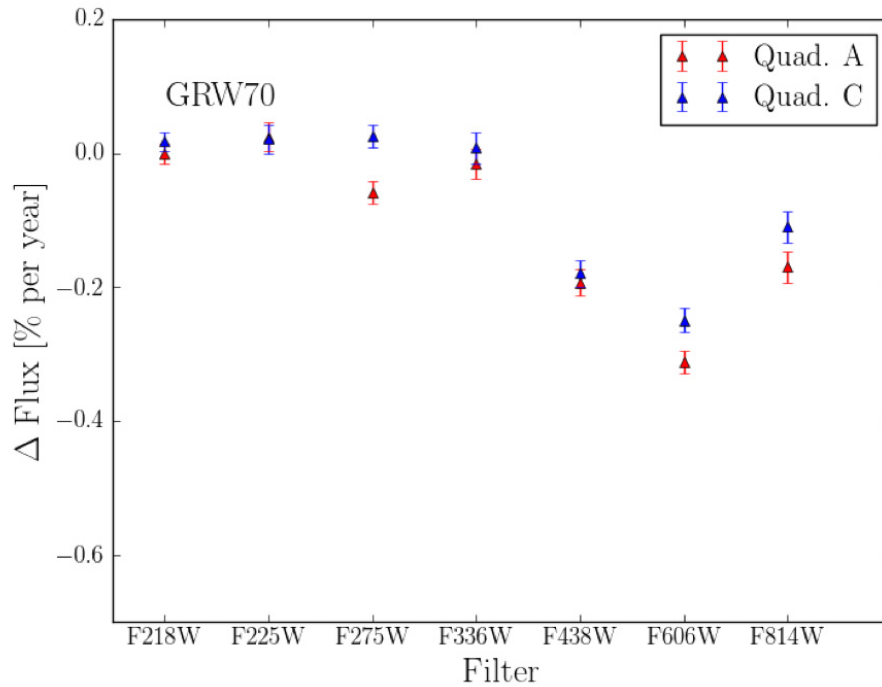




**Figure 9.7:** Flux loss (percent per year) as a function of wavelength based on linear fits to GRW+70d5824 photometric measurements in a subset of blue filters (F218W, F225W, F275W, F336W, F438W) and control filters (F606W and F814W) from observations between 2009 and 2016.



## 9.2 Astrometry

### 9.2.1 Coordinate Transformations

There are three coordinate systems applicable to WFC3 Images. First, there is the position of a pixel on the geometrically distorted flat-fielded images (FLT) after pipeline processing through **calwf3**. Second, there is the pixel position on the drizzled images (DRZ) created by **AstroDrizzle**, which corresponds to an undistorted pixel position on a tangent plane projection of the sky. Third, there is the corresponding world coordinate (RA, Dec) position on the sky.

There are utilities to transform between these coordinate systems that are built on the **WCSLIB**, a C library that implements the FITS standards for World Coordinate System (WCS) information. For transformations involving (FLT) images, the distortion information in the FITS header is used to correct for the very large effects of geometric distortion. **Drizzlepac** and **astropy WCS** are two commonly used **Python** interfaces to this library that implement these transformations.

For example, consider an object found at x,y pixel position (152,156) on UVIS chip 1 on an FLT image (test\_flt.fits). The position on the celestial sphere, and the corresponding pixel position on a distortion-corrected DRZ file (test\_drz.fits) can be found as follows.

*Example #1 Pixel position on FLT to sky position using astropy wcs.all\_pix2world*

```
>>>from astropy.io import fits
>>>from astropy.wcs import wcs
```

Create wcs object containing WCS keywords from header.

```
>>>flt_wcs = wcs.WCS(fits.open('test_flt.fits')[1].header, fits.open('test_flt.fits'))
```

Find RA and Dec corresponding to pixel position (152,156) on the FLT.

```
>>> pixcrd_flt = np.array([[152,156]])
>>> flt_skycoords = flt_wcs.all_pix2world(pixcrd_flt,1)
```

astropy.wcs.all\_pix2world does all three transformations in series (table lookup distortions, SIP, and core WCS) from pixel to world coordinates.

*Example #2 Pixel position on FLT to sky position using drizzlepac pixtosky*

```
>>> from drizzlepac import pixtosky
```

Find RA and Dec corresponding to pixel position (152,156) on the FLT.

```
>>> flt_skycoords =
pixtosky('test_flt.fits['sci',1]',152.0,156.0
```

The x,y pixel position in the DRZ frame corresponding to a coordinate in the FLT frame can also be found.

*Example #3 Pixel position in FLT frame to DRZ frame, astropy.wcs*

Continuing from the code in Example 1:

Also create wcs object from DRZ file

```
>>>drz_wcs = wcs.WCS(fits.open(test_drz)[1].header, fits.open(test_drz)[1])
```

Use all\_pix2world to convert the sky position (found in Ex 1.) into DRZ pixel position.

```
>>>drz_pix = drz_wcs.all_world2pix(flt_skycoords, 1)
```

*Example #4 Pixel position in FLT frame to DRZ frame, drizzlepac pixtopix*

```
>>> x_drz,y_drz = pixtopix.tran('test_flt.fits[sci,1]',
    'test_drz.fits[sci,1]', 'forward', 152.0,156.0)
```

## 9.2.2 Absolute and Relative Astrometry

The astrometric information in the header of a WFC3 image is derived, in part, from the measured and catalog positions of the particular guide stars used. As a result, the absolute astrometry attainable by using the image header world coordinate system is limited by two sources of error. First, the positions of guide stars are not known to better than about 200 mas. Second, the calibration of the FGS to the instrument aperture introduces a smaller, but significant error, approximately 15 mas. Although absolute astrometry cannot be done to high accuracy without additional knowledge, relative astrometry with WFC3 is possible to a much higher accuracy. In this case the limitations are primarily the accuracy with which the geometric distortion of the camera has been characterized. Typical accuracy of the distortion correction in the pipeline with the standard fourth order polynomial solutions is 0.1 pixels (4 mas for the UVIS and 10 mas for the IR).

## 9.2.3 Impact of Guide Star Failure

The guiding performance and pointing stability of HST are described in the HST Primer. The normal guiding mode uses two guide stars that are tracked by two of HST's Fine Guidance Sensors (FGSs). However, sometimes two suitable guide stars are not available and single-star guiding is used instead with the telescope roll controlled by the gyros. These observations will suffer from small drift rates. To determine the quality of tracking during these observations please review Chapter 6 of the [Introduction to the HST Data Handbooks](#). The gyros have a typical drift rate of 1.5 mas/sec. This causes a rotation of the target around the single guide star, which in turn introduces a small translational drift of the target on the detector. The exact size of the drift depends on the exact roll drift rate and distance from the single guide star to the target in the HST field of view. For WFC3, the roll about the guide star produces a translation of 7 mas (0.2 UVIS pixel, 0.05 IR pixel) in 1000 sec and 38 mas (1.0 UVIS pixel, 0.3 IR pixel) per orbit.

The Tweakshifts task may be used to measure and correct for such shifts between successive exposures. The drift over an orbital visibility period can be calculated from these numbers; the typical visibility period in an orbit (outside the Continuous Viewing Zone [CVZ]) is in the range 52-60 minutes, depending on target declination (see [Section 6.4](#) of the [HST Primer](#)). The drifts inherent to single-star guiding are not represented in the image header astrometric information, and have two important consequences:

- There will be a slight drift of the target on the detector within a given exposure. For the majority of observations and scientific applications this will not degrade the data (especially if the exposures are not very long). The drift is smaller than the FWHM of the point spread function (PSF). Also, the typical jitter of the telescope during an HST observation is 0.003-0.005", even when two guide stars are used.
- There will be small shifts between consecutive exposures. These shifts can build up between orbits in the same visit. This will affect the **AstroDrizzle** products from the pipeline, since these rely on the header astrometry, hence the structure of sources in the image will be degraded during the cosmic ray rejection routine. This can however be addressed during post-processing if the user first measures the shifts and then runs **AstroDrizzle** off-line, using the measured shifts.

Also, even when two guide stars are used, there is often a slow drift of the telescope up to 0.01"/orbit due to thermal effects. So, it is generally advisable to check the image shifts, and if necessary measure them to improve the alignment of exposures before running **AstroDrizzle** off-line to perform the cosmic ray rejection and image combination.

In summary, for most scientific applications, single-star guiding will not degrade the usefulness of WFC3 data, provided that the shifts are measured post-facto and **AstroDrizzle** is re-run offline using these shifts. However, we do not recommend single-star guiding for the following applications:

- Programs that require very accurate knowledge of the PSF such as astrometric programs
- Programs that rely critically on achieving a dithering pattern that is accurate on the sub-pixel scale. (However, note that even with two-star guiding this can often not be achieved).

Observers who are particularly concerned about the effect of pointing accuracy on the PSF can obtain quantitative insight using the TinyTim software package. While this does not have an option to simulate the effect of a linear drift, it can calculate the effect of jitter of a specified RMS value.

---

## 9.3 Spectroscopy

### 9.3.1 Using the WFC3 Grisms

WFC3 contains three grism elements: the G280 in the UVIS channel and the G102 and G141 in the IR channel. The grisms provide slitless spectra over the whole field of view of each channel. These spectroscopic modes have the well-known advantages and disadvantages of slitless spectroscopy. The chief advantage is large-area coverage,

which enables spectroscopic surveys. Among the disadvantages are overlap of spectra, high background from the integrated signal over the passband, and modulation of the resolving power by the sizes of dispersed objects.

In the UVIS channel, the G280 grism provides spectroscopy over a useful wavelength range of 200-400nm, at a dispersion of  $\sim 14 \text{ \AA}$  per pixel in the first order. The two grisms for the IR channel cover the wavelength ranges 800-1150nm (G102) and 1075-1700nm (G141). The dispersions are 24.5 and 46.5  $\text{\AA}$  per pixel, respectively. The primary aim of the reduction of WFC3 slitless spectra is to provide one-dimensional wavelength- and flux-calibrated spectra of all objects with detectable spectra. The reduction presents special problems because of the dependence of the wavelength zero point on the position of the object in the field, the blending of spectra in crowded fields, and the need for flat-field information over the whole available wavelength range. The **aXe** software package is designed for the automated extraction, calibration, visualization, and simulation of spectra from slitless spectroscopic instruments. It was originally developed by the Space Telescope - European Coordinating Facility (ST-ECF), a former department of the European Space Agency (ESA). As of January 1, 2011, STScI has taken responsibility for support and distribution of the software.



Online

---

*The aXe software and documentation can be downloaded from*  
<http://aXe-info.stsci.edu/>

*The aXe cookbook is available at* [http://www.stsci.edu/hst/wfc3/analysis/grism\\_obs/cookbook.html](http://www.stsci.edu/hst/wfc3/analysis/grism_obs/cookbook.html)

---

A slitless Spectroscopy Workshop was held at STScI in November, 2010, with a focus on using the **aXe** software. The webcast for this event can be found at:

<https://webcast.stsci.edu/webcast/searchresults.xhtml?searchtype=20&eventid=141&sortmode=1>

The normal method for taking WFC3 slitless spectra is to take a pair of images, one direct and one dispersed, of each target field, with no shift in position between the two. The direct image provides the reference position for the spectrum and thus sets the pixel coordinates of the wavelength zero point on the dispersed image.

The WFC3 UVIS and IR grisms have some unique properties that result in different types of issues associated with data for the two different channels. These are discussed in more detail below. There are, however, some common issues associated with all grism observations, which we highlight here.

### **Bright Stars**

The brightest objects produce spectra that can extend far across the detector. This is especially problematic for the UVIS G280 grism, where the relative throughput of the higher spectral orders is significant. These spectra provide a strong source of

contamination for fainter sources. In addition, the higher order spectra are increasingly out of focus and thus spread in the cross-dispersion direction. Bright stars also produce spatially extended spectra formed by the wings of the PSF.

### **Resolution and Object Size**

In slitless spectroscopy the object itself provides the ‘slit’. The WFC3 PSF has a high Strehl ratio over most of the accessible wavelength range of the gratings and therefore the degradation of point sources beyond the theoretical resolution is minimal. The spectral resolution for an extended object, however, will be degraded depending on the size and light distribution in the object and spectral features will be diluted.

### **Zeroth Order**

The grism 0th order is only detectable for brighter objects observed with the IR gratings because that order contains only a small fraction of the total flux. This faint feature is therefore easily mistaken for an emission line. The direct image can be used to determine the position of the 0th order for each source, which allows the 0th order feature in the dispersed images to be distinguished from emission lines. For the UVIS G280 grism, the 0th order has high throughput and is therefore more readily distinguished from emission features. The high throughput of the G280 0th order also means that it will often be saturated in long exposures, which leads to CCD charge bleeding and potential contamination of adjacent spectra.

### **Background**

The background in a single grism image pixel is the result of the transmission across the whole spectral range of the disperser and can therefore be high, depending on the spectrum of the background signal. The IR grism background includes not only signal from the sky, but also thermal emission from the telescope and WFC3 optics. The detected background in the IR gratings shows a distinct two-dimensional structure that is due to the overlapping of the background spectral orders. This background needs to be carefully removed before extracting the spectra of targets. The G280 grism, on the other hand, produces relatively low background compared to the IR gratings, because of the faintness of the sky in the near-UV and optical.

### **Crowding**

Because of the high sensitivities of the WFC3 gratings, observations of moderately crowded fields can produce many instances where spectra overlap. It is important to know if a given spectrum is contaminated by that of a neighbor. This can be determined by performing simulations of the grism image with software such as [aXesim](#) using a catalog of positions, brightnesses, and angular extents of sources in the field. The simulations can be used to choose a telescope roll angle which eliminates or minimizes contamination for specific sources of interest. Contamination can also be mitigated by obtaining grism observations of the same field at different telescope roll angles, which improves the chances of cleanly extracting the spectrum for a given target.

### Extra-field Objects

There will inevitably be cases where objects outside the field of view result in spectra getting dispersed into the field, resulting in contamination of sources within the field. This is more serious for the G280 where the spectra are long relative to the size of the detector. In such cases reliable wavelengths can not be determined for the extra-field object unless the 0th order is also present. Even then, the wavelength zero point will be relatively uncertain because the 0th order is somewhat dispersed and therefore difficult to localize. The extent of the out of field area has been determined for the G102 and G141 IR grisms. The effective field of view extends to pixel -189 on the left of the detector and +85 on the right. This is described in some details in [WFC3 ISR 2016-15](#).

### 9.3.2 Pipeline Calibration

The direct image of a direct-plus-grism image pair can be fully reduced by **calwf3**, including bias subtraction, dark subtraction, flat fielding, and computation of the photometric zero point in the header. In contrast to direct images, no single flat-field image can be correctly applied to grism images, because each pixel contains signal arising from different wavelengths. Flat fielding must therefore be applied during the extraction of spectra once the wavelength corresponding to each pixel is known from post-pipeline processing with **aXe**. With **aXe**, the user can apply flat-field corrections which are dependent on the wavelength falling on each pixel, as specified by the position of the direct image and the dispersion solution. So during **calwf3** processing the FLATCORR step is still performed, but the division is done using a special flat-field reference file that only contains information on the relative gain offsets between the different detector amplifier quadrants. This allows the FLATCORR step to still apply the gain correction (converting the data to units of electrons for UVIS or electrons per second for IR) and thus also corrects for offsets in gain between the various quadrants of the detectors.

The **calwf3** flt products should then be the starting point for all subsequent reduction of slitless data with **aXe** or other software. The units of the data in the SCI and ERR extensions of these files are electrons for UVIS and electrons per second for IR. The primary output of **aXe** is a file of extracted, flux calibrated spectra, provided as a FITS binary table with as many table extensions as there are extracted spectra.

### 9.3.3 Slitless Spectroscopy Data and Dithering

The common approach to dithering WFC3 imaging data, in order to improve the sampling of the PSF and to allow for the removal of bad pixels, applies equally well to slitless spectroscopy data. For long grism observations the data taking is typically broken into several sub-orbit dithered exposures.

The **AstroDrizzle** task, which is normally used to correct for the geometrical distortion of WFC3 and combine dithered exposures, is not generally applicable to grism observations. This is due to the fact that the spatial distortion correction would

only be applicable to the cross-dispersion direction of grism images. For similar reasons, the combining of dithered grism images before extracting spectra is not generally recommended. Every detector pixel has a different spectral response, which has not yet been corrected in the calibrated two-dimensional images (see [Section 9.3.2](#) on flat fielding). Combining dithered grism images before extraction will combine data from different pixels, making it difficult or impossible to reliably flat field and flux-calibrate the extracted spectra. Extracted spectra from dithered images can be properly combined into a final spectrum using the **aXedrizzle** task in the **aXe** package.

**AstroDrizzle** processing of dithered grism exposures can, however, be useful for simple visual assessment of spectra in a combined image and for the purpose of flagging cosmic-ray (CR) hits in the input flt images. When **AstroDrizzle** detects CR's in the input images it inserts flags to mark the affected pixels in the DQ arrays of the input flt files. The **aXe** spectral extraction can then be run on these updated flt images utilizing the DQ flags to reject bad pixels. This is very useful for rejecting the large number of CR hits that occur in long UVIS G280 exposures. It is not as necessary for IR grism images, because the IR flt files have already had CR's rejected by the **calwf3** up-the-ramp fitting process.

### 9.3.4 Spectroscopy with the WFC3 G280 Grism

The filters most often used for obtaining a direct image in tandem with the G280 grism are the F300X and F200LP. The direct image provides the reference position for the spectrum and thus sets the pixel coordinates of the wavelength zero point on the dispersed image. The G280 wavelength zero point is generally calibrated to an accuracy of about 1 pixel. It is not possible to use the 0th-order image of a source in a G280 exposure to establish the source position, because the 0th-order is somewhat dispersed.

Spectra produced by the G280 grism are oriented in WFC3 images with the positive spectral orders to the left (lower x-axis pixel index) of the 0th-order spot, with wavelength increasing to the left. Negative orders are located to the right, with wavelength increasing to the right. The +1st order extends to the left of the 0th order a distance of about 1/4 of the image width. The throughput of the +1st order of the G280 is only somewhat larger than that of higher orders and of the negative orders. This leads to heavy overlap of the orders at wavelengths greater than ~400nm. In addition, there is curvature of the spectra at the blue ends of the orders. The amplitude of the curvature is about 30 pixels in the detector y-axis. Due to the relatively significant throughput of the higher orders, the spectra of very bright objects may extend across nearly the entire field of view of the detector. See [WFC3 ISR 2009-01](#) for more details on the characteristics and calibration of the G280 grism.

As an example, [Figure 9.8](#) shows a G280 image of the Wolf-Rayet star WR-14, which is used as a wavelength calibrator. Superimposed on the dispersed image is a F300X image, which illustrates the relative location of the direct image of the source (circled in [Figure 9.8](#)). The full 4096-pixel x-axis extent of the detector is shown, which is completely filled by the positive and negative orders of this bright source.



**Figure 9.8:** Appearance of the G280 spectral orders on the detector. The circled source is the superimposed position of the F300X direct image. The 0th-order is the bright source in the center, with the positive and negative orders extending to the left and right, respectively. The image shows the full 4096-pixel extent of the detector in the x-axis.

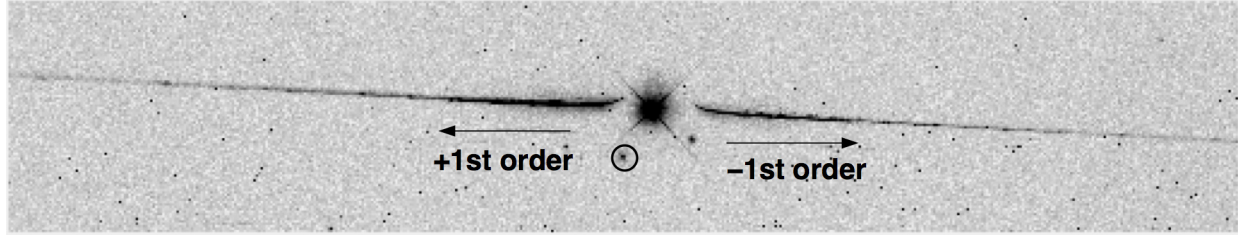
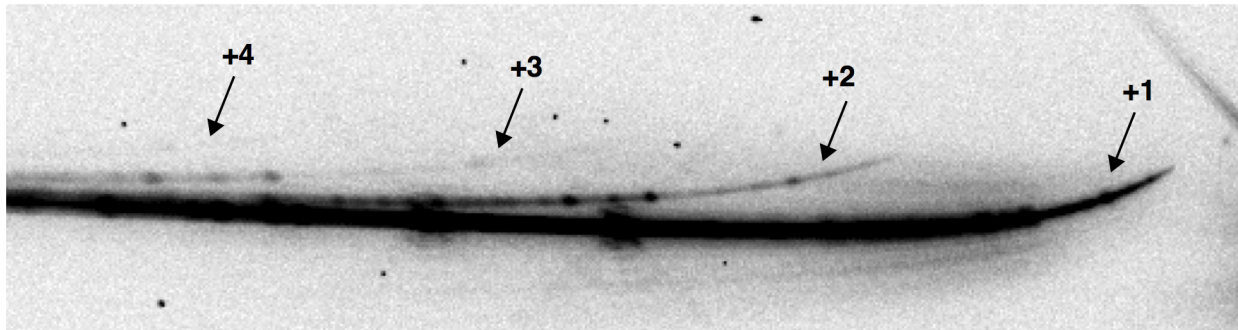


Figure 9.9 shows a zoomed view of the first several positive spectral orders of this source, where wavelength increases to the left. Notice how the blue end of each order curves upwards, and that at longer wavelengths (greater than  $\sim 400\text{nm}$ ) there is significant overlap of adjacent orders. Very bright sources produce spectra in which orders up to 6-8 can be detected. These spectra, which in principle can be analyzed (although dispersion solutions have been determined for only the first few orders), provide a strong source of contamination for the spectra from fainter objects. In addition, the higher order spectra are increasingly out of focus and thus spread in the cross-dispersion direction.

**Figure 9.9:** Zoomed view of the G280 positive spectral orders. Overlap between the +1 and +2 orders occurs for wavelengths greater than about  $400\text{nm}$ .



### 9.3.5 Spectroscopy with the WFC3 IR Grisms

The dispersion of the G102 grism is high enough that only the positive 1st and 2nd order spectra generally lie within the field of the detector. For the lower-dispersion G141 grism, the 0th, 1st, 2nd, and 3rd order spectra lie within the field for a source that has the 1st order roughly centered. The IR grisms have the majority ( $\sim 80\%$ ) of their throughput in the +1st order, resulting in only faint signals from the other orders. The trace of the observed spectra are well described by a first-order polynomial, however the direct-to-dispersed image offset is a function of the source position in the field. The tilt of the spectra relative to the image axes are small, being only  $0.5\text{-}0.7$  degrees. Typical filters used for obtaining companion direct images are the F098M

and F105W for the G102, and the F140W and F160W for the G141. Other medium- and narrow-band filters can be used when necessary to prevent saturation of very bright targets. The image centroids of sources at a given telescope pointing will depend on the filter used. These filter-dependent systematic variations, which are documented in [WFC3 ISR 2012-01](#), are generally at the sub-pixel level, but must be taken into account during the spectral extraction and reduction process, if the filter that is used to take the direct images is different from the filter in which the trace is calibrated. Version 4.32 of the G102 and G141 grism configuration files now include filter specific configuration files which include the direct filter wedge corrections.

The dispersion direction of the IR grisms is opposite to that of the G280, with the positive spectral orders appearing to the right of the 0th order and wavelength also increasing to the right. Examples of G102 and G141 observations of the flux calibration standard star GD153 are shown in [Figure 9.10](#) and [Figure 9.11](#) respectively.

**Figure 9.10: A G102 grism observation of the star GD-153. The location of the source in the accompanying direct image is shown superimposed. The entire x-axis extent of the detector is shown.**

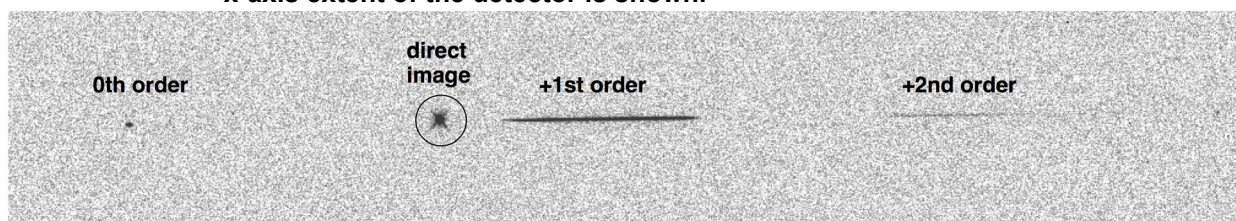
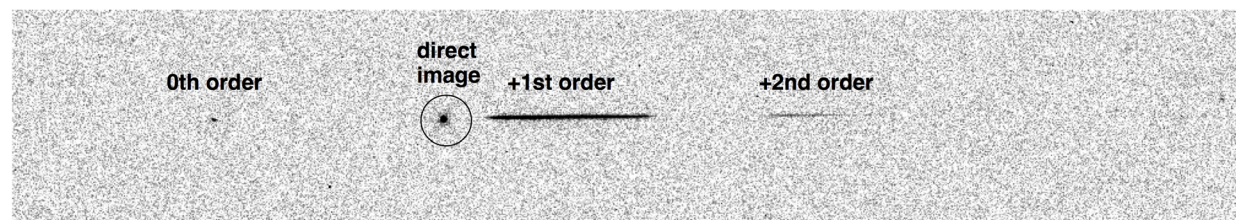


**Figure 9.11: A G141 grism observation of the star GD-153. The location of the source in the accompanying direct image is shown superimposed. The entire x-axis extent of the detector is shown.**



### 9.3.6 Extracting and Calibrating Slitless Spectra

The software package **aXe** provides a streamlined method for extracting spectra from WFC3 slitless spectroscopy data. **aXe** is distributed as part of the **Anaconda** package. More information can be found at <http://axe-info.stsci.edu/>

There is a detailed **aXe** manual and a cookbook specific to WFC3 grism data reduction, both of which are available from the **aXe** webpages, so only a brief outline of its use is presented here. Other software packages are also available and a current list can be obtained from:

[http://www.stsci.edu/hst/wfc3/analysis/grism\\_obs/wfc3-grism-resources.html](http://www.stsci.edu/hst/wfc3/analysis/grism_obs/wfc3-grism-resources.html).

### 9.3.7 Reducing WFC3 grism data

The basic steps involved in extracting spectra from grism images are:

- **Make a direct image source catalog.** This step consists of identifying and cataloging sources from a direct image in the field of the grism image. The source positions and sizes are used later to define extraction boxes and calculate wavelength solutions in the extraction step. The source information is often derived from an **AstroDrizzled** combination of direct images.
- **Prepare the grism images and remove sky background.** In this step a scaled master sky background image is subtracted from the grism images.
- **Project master source catalog positions to coordinate system of direct images.** If the source catalog was derived from dithered or drizzled direct images, then the catalog positions need to be transformed back to the coordinate system of each direct image.
- **Extract sets of pixels for each object spectrum.** The spectra of all objects in the transformed catalog are extracted from each grism image.
- **Combine all spectra of each object using aXedrizzle.** All 2-dimensional spectra for each object are combined and CR-rejected using drizzle techniques. The results are 2-d spectral images and 1-d tables.

The starting point is always a set of dispersed slitless images and the derived catalog of objects in the images. Information about the location of the spectra relative to the position of the direct image, the tilt of the spectra on the detector, the dispersion solution for various orders, the name of the flat-field image and the sensitivity (flux per Å per electron per second) table are stored in a configuration file, which enables the full calibration of extracted spectra. For each instrumental configuration, the configuration files and all necessary calibration files for flat fielding and flux calibration can be downloaded from the WFC3 instrument website ([http://www.stsci.edu/hst/wfc3/analysis/grism\\_obs/wfc3-grism-resources.html](http://www.stsci.edu/hst/wfc3/analysis/grism_obs/wfc3-grism-resources.html)).

#### Background Subtraction

**aXe** has two different strategies for removal of the sky background from the spectra. The first strategy is to perform a global subtraction of a scaled "master sky" frame from each input grism image at the beginning of the reduction process. This removes the background signature from the images, so that the remaining signal can be assumed to originate from the sources only and is extracted without further background correction in the **aXe** reduction. Master sky frames are available for download from the **aXe** webpage.

The second strategy is to make a local estimate of the sky background for each beam by interpolating between the adjacent pixels on either side of the beam. In this case, an individual sky estimate is made for every beam in each science image. This individual sky estimate is processed (flat fielded, wavelength calibrated) parallel to the original beam. Subtracting the 1D spectrum extracted from the sky estimate from the 1D spectrum derived from the original beam results in the pure object spectrum. The second approach needs to account for the fact that the background of an observation

can vary during the course of an observation. As is the case for direct imaging, there can be a significant amount of dispersed HeI light as part of the background. Steps to mitigate this problem are described in [WFC3 ISR 2017-05](#).

### Output Products: Extracted Spectra

The primary output of **aXe** is a file of extracted and calibrated spectra, which is provided as a multi-extension FITS binary table with as many table extensions as there are extracted spectra. The table contains 15 columns, including wavelength, total and extracted and background counts and their errors, the calibrated flux and error, the weight and a contamination flag. The primary header of this "SPC" table is a copy of the header of the frame from which the spectrum was extracted

**aXe** also creates a 2-d "stamp" image for each beam. The stamp images of all spectra extracted from a grism image are stored as a multi-extension FITS (STP) file with each extension containing the image of a single extracted spectra. It is of course also possible to create stamp images for 2-d drizzled grism images.

### Handling the aXe Output

The output products from **aXe** consist of ASCII files, FITS images and FITS binary tables. The FITS binary tables can be accessed using the tasks in the `stdas.ttools` package and wavelength-flux plots, with error bars, can be plotted using `stdas.graphics.stplot.sgraph`.

When there are many detected spectra on a single image, a dedicated task **aXe2web** is available. **aXe2web** creates html pages consisting of direct image cut outs, stamp images and 1-d spectra for each extracted beam. This enables convenient browsing of large numbers of spectra or the publishing of **aXe** spectra on the Web with minimal interaction.




---

*Examples of these products can be found via the Hubble Legacy Archive. The ST-ECF ACS/WFC Grism Final Release (2010, July 6) on the HLA page above contains 47919 extractions from 32149 unique objects that have been uniformly reduced by the ECF team using the aXe software*

---

## 9.3.8 Accuracy of Slitless Spectra Wavelength and Flux Calibration

### Wavelength Calibration

The WFC3 grism dispersion solutions were established by observing both astronomical sources with known emission lines (e.g., the Wolf-Rayet star WR-14 and the planetary nebula Vy2-2; see WFC3 ISR [2009-17](#), [2009-18](#)) and ground-based monochromator sources (see WFC3 ISR [2009-01](#) and [2008-16](#)). The field variation of the dispersion solution was mapped by observing the same source at



different positions over the field. The internal accuracy of these dispersion solutions is good to  $\sim 0.25$  pixels for the IR grisms ( $\sim 6\text{\AA}$  and  $\sim 9\text{\AA}$  for the G102 and G141, respectively), and to  $\sim 1$  pixel ( $\sim 14\text{\AA}$ ) for the UVIS G280.

For a given object the accuracy of the assigned wavelengths depends most sensitively on the accuracy of the zero point and the transfer of the zero point from the direct to the slitless spectrum image. Provided that both direct and slitless images were taken with the same set of guide stars, systematic pointing offsets less than 0.2 pixels can be expected. For faint sources the error on the determination of the object centroid for the direct image will also contribute to wavelength error. Realistic zero point errors of up to 0.3 pixels are representative. The wavelength calibration of the G102 and G141 grisms were recently updated ([WFC3 ISR 2017-15](#)). The new aXe format calibration files also include the filter dependent wedge offsets that should be applied when pairing G102 and G141 observations with imaging obtained using a specific direct filter.

### Flux Calibration

The sensitivity of the dispersers was established by observing a spectrophotometric standard star at several positions across the field. The sensitivity (aXe uses a sensitivity tabulated in  $\text{ergs/cm}^2/\text{sec}/\text{\AA}$  per detected electron) was derived using data flat fielded by the flat-field cube. Results for the IR grisms show 4-5% differences in the absolute flux of spectra located near the center of the field as compared to those near the field corners. This is clear evidence for a large-scale variation in the overall illumination pattern in the grism flat-field data cubes. Additional field-dependent flux calibration observations are planned, which will enable such corrections to be implemented.

#### *UVIS Flux Calibration*

The sensitivity of the G280 grism was established by observing a spectrophotometric standard star at several positions across the field. The sensitivity (aXe uses a sensitivity tabulated in  $\text{ergs/cm}^2/\text{sec}/\text{\AA}$  per detected electron) was derived using data flat fielded by the flat-field cube. Please check the WFC3 Instrument Science Reports for updates.

#### *IR Flux Calibration*

The sensitivities of the G102 and G141 grisms were established by observing the white dwarf spectrophotometric standard stars GD153 and GD71 at several positions across the field (for example, see [WFC3 ISR 2009-17](#), [2009-18](#), and [2011-05](#)).

The flux calibration is primarily based on observations of GD153 at the center of the detector. Variation of the sensitivity over the field-of-view was measured by observing GD71 over a grid of nine points over the detector, which shows that the throughput falls off by about 2% in y direction and by about 4% in x direction to the edges of the FoV. The large-scale variation is included in the grism flat-field cube (see [WFC3 ISR 2011-05](#)). Regular monitoring of the flux calibration is performed, and has shown that the calibration has been stable to within 1% since the installation of the camera on HST ([WFC3 ISR 2012-06](#) and [2014-01](#)).

## 9.4 STSDAS and STSCI\_PYTHON Software

Software tools for working with WFC3 FITS files are available in the `stsdas` and `stsci_python` package. Legacy tools from **IRAF** such as `toolbox.imgtools.mstools` have been designed to maintain compatibility with pre-existing analysis software. The tools have either been written in ANSI-C or are **IRAF** CL scripts interfacing with pre-existing **IRAF/STSDAS** tasks. Some will be transitioned to the `python wfc3tools` package in a future release.

These tasks include tools for mathematical and statistical operations on science images and for analysis and display of raw and reduced data. In most cases, the utilities extend existing routines to include error and data quality propagation. These are the utilities of greatest interest to the user community. Under this category are several tasks described in Chapter 3 of the *Introduction to the HST Data Handbooks*, **msarith**, **mscombine**, **msstatistics**, **msjoin** and **mssplit**, along with a few other tasks we describe below, **ndisplay**, **markdq**, **mosdisplay**, **pstack**, **pstats**, **sampinfo**, **sampdiff**, and **sampcum**. The first five are found in the package `toolbox.imgtools.mstools`; the remaining ones reside in the `hst.calib.wfc3` (now deprecated - all `wfc3` calibration software maybe found in the `wfc3tools` and `HSTCAL` packages) and older **IRAF** `hst.calib.nicmos` package.

The tasks in the `toolbox.imgtools.mstools` package are particularly useful for working with individual WFC3 imsets. If you are not familiar with these tasks see *Working with FITS Imsets* in Chapter 3 of the *Introduction to the HST Data Handbooks*. Below we describe a few tasks of specific interest to WFC3 observers. For additional details and examples of these and other tools, please refer to the online help.

The following tasks are found in both the `wfc3` and `nicmos` **IRAF** packages: **mosdisplay**, **pstack**, **pstats**, **sampinfo**. Found only in the `nicmos` packager are **sampdiff**, **sampcum**, **ndisplay** and **markdq**. The latter two can be used for any HST dataset using multi-extension FITS format to store SCI, ERR and DQ arrays.

### **ndisplay and markdq**

The **markdq** task reads the data quality (DQ) array from a multi-extension image and marks the DQ flags on a previously displayed science image. Each flag value can be set independently to a different color or can be turned off. The **ndisplay** task combines the capabilities of the **IRAF** task **display** and the task **markdq**: it displays a science image and overlays the DQ flags according to a user-specified color-code. Both tasks are useful for locating specific DQ values, such as pixels flagged as saturated or marked as cosmic ray hits.

### **mosdisplay**

The **mosdisplay** task provides a convenient way to display images from all IMSETS of a WFC3/IR multiaccum image together as a mosaic in a single `ximtool` or `saoimage/ds9` window. The user may select which extension (e.g., SCI, ERR, DQ, SAMP or TIME) to display and can control the display threshold parameters or leave them to be automatically determined.

**pstack and pstats**

The **pstack** and **pstats** tasks plot all the samples of a specified pixel or image section, respectively, from a WFC3/IR multiaccum image as a function of sample time. These tasks can be used to track the time behavior of an image on a pixel-by-pixel basis. For example, the temporal positions of cosmic ray hits or the onset of saturation during the course of an exposure can be located for a particular pixel or set of pixels. The **pstats** task can be particularly useful for identifying anomalous data behavior, such as drifting bias levels or scattered light, which may cause the background level to vary substantially during the course of an exposure

**sampinfo**

The **sampinfo** task offers a convenient way to get readout-by-readout information about a WFC3/IR multiaccum image. It provides information about the overall readout sequence (**SAMP\_SEQ**, **NEXTEND**, **NSAMP**, and **EXPTIME**), and then for each imset of the multi-extension FITS file it lists the corresponding **SAMPNUM**, **SAMPTIME** and **DELTATIME** values. These can be useful bits of information when using non-standard processing techniques.

**sampdiff and sampcum**

The **sampdiff** task provides a convenient way to convert a WFC3/IR multiaccum image into a set of independent ‘first differences.’ Normally, each IMSET (readout) of a multiaccum image is the cumulative sum of the total exposure time prior to that readout. As such, the [sci,\*] images are not statistically independent. When analyzing multiaccum images, it is sometimes helpful to look at the data collected during each readout interval independently of that which was accumulated previously, i.e. by taking the difference of successive readouts. In this way, you can isolate readouts that have problems (e.g., major cosmic ray hits or moving objects, sudden changes in scattered light, etc.). The **sampdiff** task automates this process. Note that, in general, this is only really a sensible thing to do if the image has not been converted from counts to count rate by the **UNITCORR** step of **calwf3**! The **sampcum** task inverts this process, re-accumulating the first differences.

**Using These Tasks: An Example.**

As an example, you might want to inspect WFC3 data for anomalies occurring during individual readouts of an IR exposure using a procedure like this:

```
--> hedit ib3x01a1q_raw.fits[0] unitcorr=omit
--> calwf3 ib3x01a1q_raw.fits
--> sampdiff ib3x01a1q_ima.fits ib3x01a1q_fdiff.fits
--> mosdisplay ib3x01a1q_fdiff.fits 1 extname=sci number+
--> pstats ib3x01a1q_fdiff.fits[1:512,1:512]\
>>> extname=sci units=rate stat=midpt
```

In this example, the raw image is processed through **calwf3** with the `unitcorr` step turned off so that the data in the `_ima` file readouts are left in units of accumulating counts rather than count rate. You then take first differences with `sampdiff`, display the individual SCI extensions as a mosaic with `mosdisplay` to look for monster cosmic rays or other oddities in the readouts, and then use `pstats` to plot the median count rate (`units=rate`) per sample time in the image quadrant `[1:512,1:512]`.

---

## 9.5 Specific Tools for the Analysis of WFC3

This section describes existing tools and packages that can be used for the analysis of WFC3 data. Some of these tools are distributed as STScI affiliated packages, while others have been developed by STScI scientists for their own scientific projects, but have also been made available to the community. The latter type of software is not directly supported by the WFC3 team; thus users are directed to the software developers for assistance.

### 9.5.1 wfc3tools

**wfc3tools** is a python package containing several WFC3-specific tools. Online documentation for **wfc3tools** can be found on read the docs at:

<http://wfc3tools.readthedocs.io/en/latest/index.html>

The package is available on [github](#) and is also distributed on the STScI-maintained [AstroConda](#) channel. **wfc3tools** contains the python wrapper modules that call the **calwf3** pipeline executables (whose source code is written in C), as well as other auxiliary functions. The pipeline modules (**calwf3**, **wf3cte**, **wf3ccd**, **wf32d**, **wf3rej**, **wf3ir**) are described in detail in [Chapter 3](#) of this book. Here we briefly describe the other tools. The boldface paragraph titles correspond to the module name, and link to the read-the-docs resources which contain a more detailed documentation.

#### **embedsub**

Given an image specified by the user which contains a subarray readout, return a full-frame image with the subarray implanted at the appropriate location.

#### **pstat**

Plot statistics for a specified image section up the ramp of an IR MultiAccum image. Sections from any of the SCI, ERR, DQ, image extensions can be plotted. A choice of mean, median, mode, standard deviation, minimum and maximum statistics is available.

#### **pstack**

Plot the stack of MultiAccum sample values for a specified pixel in an IR multiaccum image. Pixels from any of the SCI, ERR, DQ, or TIME image extensions can be plotted.

#### **sampinfo**



Sampinfo prints information about a WFC3/IR MultiAccum image, including exposure time information for the individual samples (readouts). The global information listed (and the names of the header keywords from which it is retrieved) includes:

- the total number of image extensions in the file (NEXTEND)
- the name of the MultiAccum exposure sample sequence (SAMP\_SEQ)
- the total number of samples, including the “zeroth” read (NSAMP)
- the total exposure time of the observation (EXPTIME).

#### **sub2full**

Given an image specified by the user which contains a subarray readout, return the location of the corner of the subarray in a full frame reference image (including the full physical extent of the chip), in 1-indexed pixels. If the user supplies an X and Y coordinate, then the translated location of that point will be returned.

### **9.5.2 Standalone Fortran routines for CTE correction**

While the WFC3 team provides a python tool, `wfc3cte`, under the `wfc3tools` package, a standalone routine for cte correction of raw UVIS images is also available and documented here:

[http://www.stsci.edu/hst/wfc3/tools/cte\\_tools](http://www.stsci.edu/hst/wfc3/tools/cte_tools)

### **9.5.3 Cross-talk correction software**

As described in [Section 5.5.3](#), electronic crosstalk between the UVIS amplifiers during readout induces faint, negative, mirror-symmetric ghost images in the other quadrant of the same CCD chip. Software for cross-talk removal as well as a description of the analysis behind such software can be found here:

<http://www.stsci.edu/hst/wfc3/documents/ISRs/WFC3-2012-02.zip>

### **9.5.4 Grizli: Grism redshift & line analysis software for space-based slitless spectroscopy**

Grizli is not official WFC3 software but has been developed by WFC3 scientists. It is intended to provide some general techniques for manipulating HST slitless spectroscopic observations, providing software kernels to address questions such as: "How does the WFC3/IR G141 grism disperse the spectrum of a star/galaxy at pixel position (x,y) in my F140W direct image?".

Grizli, with examples and documentation can be found on [github](#).

### 9.5.5 PandExo: A community tool for transiting exoplanet science with JWST & HST

PandExo is not official WFC3 software, but WFC3 scientists have made significant contributions to its development. Similar to an exposure time calculator (ETC), PandExo is a transiting exoplanet noise simulator. It is based on Pandeia, the ETC for JWST, and has been expanded to include HST's WFC3 instrument.

PandExo, with examples and documentation can be found on [github](#).

### 9.5.6 IDL procedures for simulating trajectories of multi-lined spatial scans

The [WFC3 ISR 2017-06](#) describes simulations of spatial scans using a simple physical model of HST motions. The document contains an IDL code in the appendix that can be used both in designing detailed WFC3 observation in spatial scan mode, as well as for analyzing existing ones.

### 9.5.7 Satellite Trails Detection

The ACS instrument team has developed a code for finding satellite trails in their data, and flagging the interested pixels' DQ extension accordingly. The software is part of the acstools package and the detailed documentation be found here:

<http://acstools.readthedocs.io/en/latest/satdet.html>.

Flagging such trails can be useful e.g., in combining multiple images with Astrodrizzle. Disclaimer: the software is developed and tested only for ACS data, but should work on WFC3 data as well.

### 9.5.8 LINEAR: IDL and C tools for grism spectroscopy

LINEAR is a suite of IDL and C codes to extract and simulate slitless spectra for WFC3/IR observations with multiple roll angles. The details will be described in [Ryan, Casertano, & Pirzkal, 2018](#), *LINEAR: A Novel Algorithm for Reconstructing Slitless Spectroscopy* and users are welcome to contact the authors with questions.

### 9.5.9 Code for mitigation of variable IR background

[WFC3 ISR 2016-16](#) illustrates some possible strategies for dealing with IR variable background due to the HeI atmospheric line at 1.083. The ISR provides a full description of the methods, and the code is available at: [https://github.com/gbrammer/wfc3/blob/master/reprocess\\_wfc3.py](https://github.com/gbrammer/wfc3/blob/master/reprocess_wfc3.py)

## 9.6 References

- Bohlin, R., & Gilliland, R., 2004, *Hubble Space Telescope Absolute Spectrophotometry of Vega from the Far-Ultraviolet to the Infrared* [AJ](#), **127**, 3508
- Brown, T., et al, 2009 *WFC3 SMOV Proposal 11451: The Photometric Performance and Calibration of WFC3/IR*, [WFC3 ISR 2009-30](#).
- Cousins, A.W.J., 1974, *Standard Stars for VRI Photometry with S25 Response Photocathodes*, [MNRAS](#), **33**, 149.
- Hartig, G.F., 2009, *WFC3 SMOV Programs 11437/9: IR On-orbit PSF Evaluation*, [WFC3 ISR 2009-37](#).
- Hartig, G.F., 2009, *WFC3 SMOV Programs 11436/8: UVIS On-orbit PSF Evaluation* [WFC3 ISR 2009-38](#).
- Holtzman, J., et al. 1995, *The Photometric Performance and Calibration of WFPC2*, [PASP](#), **107**, 1065
- Johnson, H. L., Morgan, W. W., 1953, Fundamental stellar photometry for standards of spectral type on the revised system of the Yerkes spectral atlas, [ApJ](#), **117**, 313
- Kalirai, J., et al, 2009, *WFC3 SMOV Proposal 11450: The Photometric Performance and Calibration of WFC3/UVIS*, [WFC3 ISR 2009-31](#).
- Kalirai, J. S. et al., 2010, *WFC3 Pixel Area Maps*, [WFC3 ISR 2010-08](#).
- Koorneef et al., 1986, in *Highlights of Astronomy IAU*, Vol.7, p833, ed. J.-P. Swings
- Kuntschner, H., M. Kummel, J. R. Walsh, and H. Bushouse, 2011, *Revised Flux Calibration of the WFC3 G102 and G141 grisms*, [WFC3 ISR 2011-05](#).
- Kuntschner, H., H. Bushouse, M. Kummel, and J. R. Walsh, 2009, *WFC3 SMOV proposal 11552: Calibration of the G141 grism*, [WFC3 ISR 2009-17](#).
- Kuntschner, H., H. Bushouse, M. Kummel, and J. R. Walsh, 2009, *WFC3 SMOV proposal 11552: Calibration of the G102 grism*, [WFC3 ISR 2009-18](#).
- Kuntschner, H., H. Bushouse, J. R. Walsh, M. Kummel, 2008, *The TV3 ground calibrations of the WFC3 NIR grisms*, [WFC3 ISR 2008-16](#).
- Kuntschner, H., H. Bushouse, M. Kummel, and J. R. Walsh, 2009, *The ground calibrations of the WFC3/UVIS G280 grism*, [WFC3 ISR 2009-01](#).
- Maiz Apellaniz, J., 2007, *A Uniform Set of Optical/NIR Photometric Zero Points to be Used with CHORIZOS*, [ASPC](#), **364**, 227
- Oke, B., 1964, [ApJ](#), **140**, 689
- Ryan, R., Casertano, S., and Pirzkal, N., 2018, *LINEAR: A Novel Algorithm for Reconstructing Slitless Spectroscopy from HST/WFC3*, [Publ. Astron. Soc. Pac.](#) **130** 034501.
- Sabbi, E., 2012, *Proposal 11923-UVIS Filter Wedge Check*, [WFC3 ISR 2012-01](#).
- Sahu, K., Deustua, S., Sabbi, E., *WFC3/UVIS Photometric Transformations*, [WFC3 ISR 2014-016](#).
- Sirianni, M., et al., 2005, *The Photometric Performance and Calibration of the Hubble Space Telescope Advanced Camera for Surveys*, [PASP](#), **117**, 1049.

# WFC3 Spatial Scan Data

In this chapter . . .

10.1 Analysis of Scanned Data / 215

10.2 IR Scanned Data / 216

10.3 UVIS Scanned Images / 219

10.4 References / 220

---

## 10.1 Analysis of Scanned Data

Spatial scans enable observations of bright sources such as host stars of exoplanets, as well as high precision astrometry and photometry. However, the analysis of spatially scanned data obtained with HST WFC3 is different from that of nominal, staring-mode observations, for which an established pipeline is provided to the users, namely (**calwf3**, see [Chapter 3](#)).

For spatially scanned data the observers are required to customize a larger fraction of their analysis with respect to the typical staring mode of observation. In this section, we describe custom analysis flows for scanned A) IR spectroscopy, especially of exoplanet transits or eclipses, and B) UVIS and IR imaging. UVIS scanned spectroscopy is not recommended, due to order overlap.

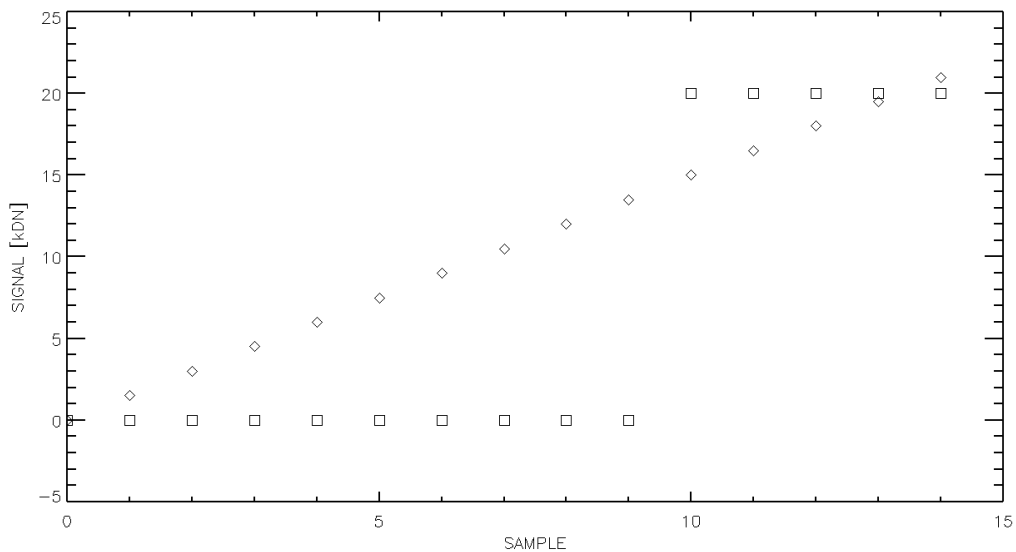
To begin their own custom analysis, we recommend observers use:

- \* \_ima.fits files for IR
- \* \_flt.fits or \_flc.fits files for UVIS observation

## 10.2 IR Scanned Data

Normally, **calwf3** constructs calibrated and cosmic-ray cleaned `flt.fits` files for IR data by fitting a straight line to the slope up-the-ramp of accumulating charge within each pixel. This method, however, is inappropriate for spatially scanned data where the charge accumulation in any given pixel crossed by a source occurs within a very short period of time and thus appears as a step rather than a ramp (see [Figure 10.1](#)).

**Figure 10.1: Schematic diagram of charge accumulation in a pixel sampled with the RAPID sequence for a source observed in staring mode (diamonds, in a ramp) or in spatially scanned mode (squares, in a step function).**



As a consequence, analysis of IR scanned data in the past has typically been done using the `ima.fits` files, which contain the individual readouts of the detector, adjusted for the appropriate reference pixel, dark and non-linearity corrections. However, starting with **calwf3** version 3.3 in early 2016, the `flt.fits` files for scanned data are constructed without the fit up-the-ramp (CRCORR is set to OMIT). The result is a calibrated science data file (`flt.fits`) consisting of the first-minus-last science extension from the MULTIACCUM `ima` file (where the individual reads are stored in reverse time order), a more reasonable representation of the image than the up-the-ramp fit. Observers with calibrated scan data predating 2016 may re-retrieve their files from the MAST archive to obtain the improved `flt.fits` files. Since CRCORR is OMIT, these calibrated files will contain cosmic rays that will require removal via traditional routines e.g., stacking of dithered images, Laplacian cosmic ray identification (e.g., LACosmic from van Dokkum), **Astrodrizzle**, and so on.

Alternatively, observers can of course continue using the standard `ima` files. In that case, an additional processing step is required: manually calculating differences of the Nth readout and the (N-1)th readout to form a set of images. Those difference images can be subsequently analyzed with custom procedures. As reported in [Section 3.3.9](#)

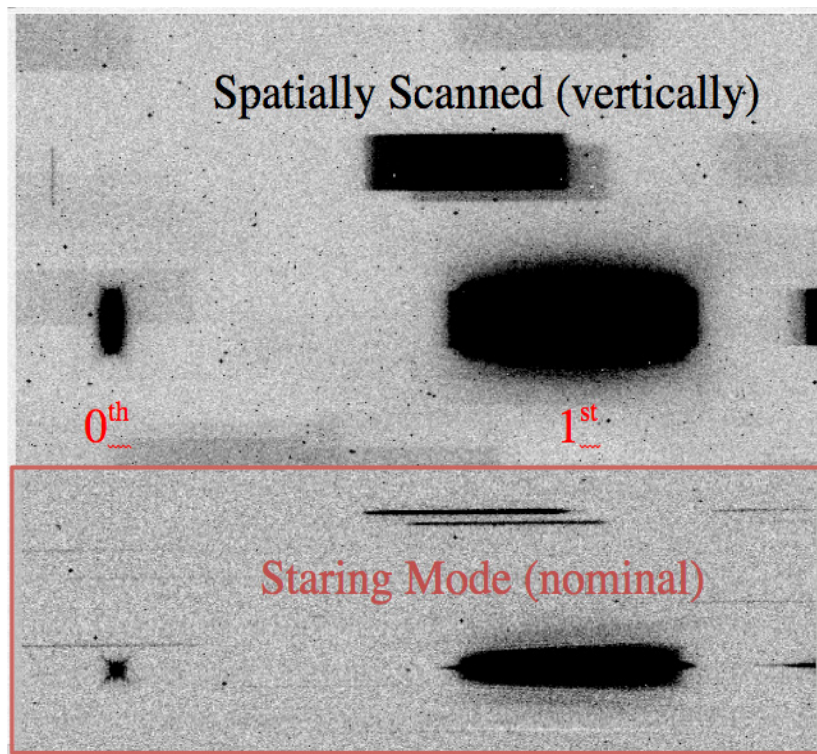
and in the note in [Section 3.3.10](#), depending on the values of the `UNITCORR` and `FLATCORR` switches, the ima file will report the average count (or electron) rate up to the given read or the total accumulated counts (or electrons) up to the given read. Given that WFC3/IR sampling sequences may have unevenly spaced readouts, converting from one to the other requires using the values of the readout timings (recorded in the ima image as either the `PIXVALUE` keyword of the `TIME` extension of each imset, or as the `SAMPTIME` keyword of the `SCI` extension of the same imset).

For the SPARS sample sequences specifically, the time interval between the 0<sup>th</sup> readout and the 1<sup>st</sup> readout is much shorter than the intervals between subsequent readouts; hence for SPARS data, the first interval probably should be discarded in subsequent analysis. For example, with a GRISM512 subarray and SPARS10 readout, the first interval is 0.85 seconds, whereas subsequent intervals are 7.92 seconds (see [WFC3 ISR 2006-06](#) or [Phase II Proposal Instructions](#)). Additional meta data related to spatial scans is available; in the `_spt.fits` file; an example block of keywords associated with spatial scans is listed in [Table 10.1](#). With calwf3 version 3.3 and later, all the UVIS and IR scan-related keywords formerly accessible only via the engineering file headers (`*spt.fits`), are now present in the calibrated science data headers (e.g., `*flt.fits`).

**Table 10.1: Spatial Scan Keywords in the `_flt.fits` files**

Keywords	Description
<code>SCAN_TYP= 'C'</code>	C:bostrophidon; D:C with dwell; N:N/A
<code>SCAN_WID=0.000000000000E+00</code>	scan width (arcsec)
<code>ANG_SIDE=9.000000000000E+01</code>	angle between sides of parallelogram (deg)
<code>DWELL_LN=0</code>	dwell pts/line for scan pointing (1-99,0 if NA)
<code>DWELL_TM=0.000000000000E+00</code>	wait time (duration) at each dwell point (sec)
<code>SCAN_ANG=2.248278045654E+02</code>	position angle of scan line (deg)
<code>SCAN_RAT=5.000000074506E-02</code>	commanded rate of the line scan (arcsec/sec)
<code>NO_LINES= 1</code>	number of lines per scan (1-99,0 if NA)
<code>SCAN_LEN=2.969249963760E+00</code>	scan length (arcsec)
<code>SCAN_COR='V'</code>	scan coordinate frame of ref: celestial,vehicle

**Figure 10.2:** A spatially-scanned spectrum labeled with its 0th and +1st order light, and compared to a nominal staring-mode slitless spectrum of the same field (red outlined inset); reproduced from [WFC3 ISR 2012-08](#).



### 10.2.1 IR Scanned Spectra

MAST provides the user with calibrated images taken in scanned mode. However the analysis of spatially scanned WFC3/IR spectroscopy (see [Figure 10.2](#) for an example) involves ad-hoc post-processing steps that are left to the users. Some guidelines for the analysis of spatially-scanned IR spectroscopy can be found in [WFC3-2012-08](#). Additionally, papers exist in the literature that illustrate custom data reduction procedures for the analysis of scanned data. The WFC3 team does not endorse of any specific paper, however the interested reader should search the literature for such examples and use their own judgement in adopting the reduction strategy best suited for their purposes



## 10.3 UVIS Scanned Images

For UVIS data, the calibrated flt/flc files can be used directly, just as for staring-mode observations.

### 10.3.1 Astrometry using UVIS Scanned Observations

There are several existing papers in the literature that illustrate the use of UVIS scan-mode data for astrometric measurements (e.g., [Riess et al 2014](#), [Casertano et al. 2016](#)). In these investigations, the authors have been able to achieve an accuracy of about 30 micro" (more than 10× that of pointed observations) in the measurements of trigonometric parallaxes. The interested reader is directed to such references for more details about the data analysis process.

### 10.3.2 Photometry of Bright Targets using UVIS Scanned Observations

In the case of photometry of bright, isolated sources, spatial scans have two key advantages over staring mode observations. First, the ability to collect millions of source photons per exposure without saturating is enabled by spreading the light over hundreds of pixels. Second, illuminating hundreds of pixels averages out spatially-dependent sources of noise such as flat-field errors and enables sampling of different pixel phases along the direction of the scan.

HST program 14878 is a Cycle 24 calibration program (ongoing at the time of this publication) intended to study the photometric repeatability of spatial scans of bright, isolated stars with WFC3/UVIS. Analysis of the first two identical visits of this program finds the photometric repeatability to be approximately 0.1% r.m.s. ([WFC3 ISR 2017-21](#)), an improvement of more than a factor of 5 over the traditional staring mode results.

An outline of the analysis procedure performed on program 14878 is summarized below (the aforementioned report contains additional details).

- Calibrated (\*\_flt.fits) products, processed with the CALWF3 calibration pipeline, are retrieved from the MAST archive. Vertical scans and corner subarrays were used in this program to mitigate CTE losses.
- Cosmic rays (CRs) are removed. An algorithm originally developed for CR rejection in STIS CCD images was adapted: it identifies cosmic ray hits in the scanned images and replaces them with an interpolated value from the surrounding 'good' pixels.



- Images are sky subtracted. The sky region is defined as all pixels excluding a 10-pixel border around the perimeter of the subarray, and a conservatively large  $400 \times 75$  pixel rectangular aperture around the source center. The pixel values in the sky region are sigma clipped (iteratively) and the mean of the remaining sky pixels is subtracted from the science array to remove the sky.
- The pixel area map is applied. This could be important if the position of the scan on the subarray drifts significantly between visits.
- A rectangular aperture is centered on the scan using `Photutils.RectangularAperture` is used. For higher precision, the overlap of the apertures with the science array is set to the ‘subpixel’ mode to allow for subpixel centering of the scans. Finally, `photutils.aperture_photometry` is used to sum up source counts.

---

## 10.4 References

- Deming, D., et al., *Infrared Transmission Spectroscopy of the Exoplanets HD209458b and XO-1b Using the Wide Field Camera-3 on the Hubble Space Telescope*, 2013, [ApJ](#), 774, 95.
- van Dokkum, P., 2001. *L.A. Cosmic., Laplacian Cosmic Ray Identification*.
- McCullough, P. & MacKenty, J., [WFC3 ISR 2012-08](#), *Considerations for using Spatial Scans with WFC3*.
- Petro, L. & Wheeler, T., [WFC3 ISR 2006-06](#) *New IR Detector Sample Times*.
- Reiss, A., Casertano, S., et al., *Parallax beyond a kiloparsec from spatially scanning the Wide Field Camera 3 on the Hubble Space Telescope*, 2014, [ApJ](#), 785, 2.
- Casertano, S., et al., *Parallax of galactic Cepheids from spatially scanning the Wide Field Camera 3 on the Hubble Space Telescope: the Case of SS Canis Majoris*, 2016, [ApJ](#), 825, 1.